Testing theories of baroclinic adjustment in the laboratory and in simple atmospheric models



Susie Wright

Worcester College

University of Oxford

A thesis submitted for the degree of

Doctor of Philosophy

Trinity 2019

Abstract

The mean state of the Earth's climate is the result of a balance between the destabilising effect of radiative forcing and the dynamics which transport heat through the atmosphere. The contribution of baroclinic instability to maintaining this balance is not quantitatively well understood. Two prominent groups of existing ideas which attempt to explain the effect of baroclinic eddies on the mean state are baroclinic adjustment and geostrophic turbulence theories. The former suggests that the efficiency of eddy transport increases rapidly with imposed forcing such that the system adjusts to some preferred neutral state and only small departures from this state are allowed. The latter implies that the efficiency of eddy transport is set locally by an eddy diffusivity which varies smoothly with the forcing.

This thesis describes the use of a new approach, centred on a novel configuration of a lab experiment, to provide insights useful for understanding the impacts of various instabilities on the dynamical equilibration of the thermal structure of the atmosphere. The lab experiment is a new rotating annulus configuration particularly suited to studying meridional heat transfer as its thermal structure is representative of that observed in Earth's atmosphere. Within this thesis we describe the development of a three dimensional simulation of this experiment using the dynamical core of the Met Office Unified Model. The main advantages of using this model are that the numerics can be tested against the experimental data and the same model can be used to simulate Earth-like atmospheres.

Our findings suggest that the theories of baroclinic adjustment and geostrophic turbulence may apply in different regimes which are described by the size of the baroclinic deformation radius relative to the domain size. We found this behaviour to be consistent between simulations of the annulus experiments and simulations of idealised planetary atmospheres.

Acknowledgements

First and foremost I would like to thank my supervisor, Peter Read, for his encouragement, advice and insight which were invaluable for all aspects of this project. Many thanks are also due to my supervisor Sean Milton and also to Tommaso Benacchio, Nigel Wood and the rest of the dynamics group at the Met Office for their help with taming the UM. I am also grateful to Paul Earnshaw for his help in setting up the Held Suarez model and Sylvie Su for laying the foundations for the two dimensional modelling. Thanks also to the MONSooN team for their help with computing resources and to both NERC and the Met Office for funding this project. Thanks must also go to all members of the Oxford GFD group, past and present, for enlightening discussions on various aspects of my work and theirs. Special mentions are required for Hélène Scolan for her work on the experimental aspects of the project and Roland Young for supporting the work with MORALs. I would also like to thank my examiners, Andrew Wells and Pablo Zurita-Gotor, for reading this thesis and providing useful comments and suggestions.

On a more personal note, I would not have made it to the end of this PhD were it not for the love, support and camaraderie of countless people. Oxford would not have been the same without the members of AGDC who have provided everything from burgers and beer to housemates to running buddies and caffeination. I am also very grateful to my friends outside of Oxford for providing much needed perspective and holidays, especially Ollie 'Bae' Stephenson for being my best physics friend. A special thank you also goes to George, Catherine and Nala for letting me share their beautiful home for the last month or so of writing up. I am also very grateful to Philip, who has made the last four years impossumbly wonderful. Finally, none of this would have been possible without the love and support of my family. Thanks to Kirsty for validating my excessive love of breakfast food. Grampie, to whom this thesis is dedicated, I am so humbled to be following in your footsteps. And last but not least, Mum and Dad to whom I owe everything. Mum, I am so grateful for all you do for all of us and Dad, I think all those years of bedtime science chat paid off. I hope you are both proud that I started in green group now I'm here.

To Grampie, the O.G. Dr. Wright and an inspiration in so many ways.

Statement of originality

Unless stated below, the entire content of this thesis is my own work.

Chapter 2: Most of the results from chapter 2 were published in Wright et al. (2017). As stated in that paper my personal contribution to the work was to run about two thirds of the simulations, perform most of the data analysis, write most of the manuscript and plot most of the figures. The model was adapted by my co-authors and they carried out the initial data collection for a single aspect ratio.

Chapter 4: All of the experimental data used in this work was collected by Hélène Scolan and Peter Read. Processing of the experimental data to produce vertical profiles and measures of the stratification was also carried out by Peter Read.

Chapter 6: Hélène Scolan also wrote the first version of the code for calculating the spectra and one dimensional structure functions. I then improved upon this initial version and used the code to analyse the simulations and experiments.

Chapter 7: Paul Earnshaw of the UK Met Office set up the basic Held Suarez configuration of the model used in chapter 7 and also wrote the code for calculating the Lorenz cycles presented in that chapter. I extended the initial version of the model to include the convective adjustment scheme, a new profile for the thermal forcing and the option of forcing the zonal mean flow and eddies separately.

Contents

1 Introduction **1**

1.1 Thermal equilibration of the extra-tropical atmosphere 3

1.1.1 The concept of baroclinic adjustment 5

1.1.2 Other means of eddy equilibration 9

1.2 Turbulence in the atmosphere 10

1.2.1 Geostrophic turbulence 12

1.2.2 Surface quasi-geostrophic dynamics 18

1.3 Annulus experiments as an analogue for the atmosphere 22

1.3.1 The classical annulus 22

1.3.2 A new annulus configuration 24

1.3.3 Heat transfer by free convection 25

1.4 Aims and overview of this thesis 27

2 2D simulations **31**

2.1 The numerical model 32

2.2 Model setup 35

2.3 Results 38

2.3.1 Non-rotating Flow 38

2.3.2 Rotating Flow Regimes 40

2.3.3 Heat Transfer 44

2.3.4 The Azimuthal Velocity Scale 47

2.4 Choice of non-dimensional parameter 48

2.5 Discussion 49

3 Adapting ENDGame **53**

3.1 ENDGame and the UM 53

3.1.1 The semi-Lagrangian advection scheme 54

3.1.2 The model grid 56

3.2 Changes to the model 58

3.2.1 Cylindrical geometry 59

3.2.2 Grid stretching 63

3.2.3 Boundary conditions 64

3.2.4 Viscosity and thermal diffusion . . . 69
3.2.5 The equation of state . . . 70
3.2.6 Adding a beta effect . . . 70
3.2.7 Parameterisation of non-ideal boundary conditions . . . 72
3.2.8 Convection scheme . . . 75
3.2.9 Choice of the numerical scheme . . . 76
3.3 Simulation setup . . . 77
3.4 Discussion . . . 78

4 Comparing simulation and experimental results 81
4.1 Flow regimes . . . 82
4.2 Total heat transport . . . 86
4.2.1 Nusselt number . . . 89
4.3 Stratification . . . 91
4.4 Resolution sensitivity . . . 99
4.4.1 Parameterising convection . . . 103
4.5 Discussion . . . 105

5 Analysis of the three dimensional simulations 109
5.1 Zonal mean diagnostics . . . 109
5.1.1 Temperature and zonal velocity . . . 110
5.1.2 Meridional overturning streamfunction . . . 112
5.1.3 Potential vorticity . . . 114
5.2 The criticality parameter . . . 121
5.2.1 Radial temperature gradients . . . 121
5.2.2 Isotherm slopes and criticality . . . 123
5.3 Eddy fluxes . . . 126
5.3.1 Mean and eddy heat fluxes . . . 127
5.4 Discussion . . . 132

6 Energy transfer in the annulus 135
6.1 Energy spectra . . . 136
6.1.1 Kinetic energy spectra . . . 137
6.1.2 Temperature variance spectra . . . 141
6.1.3 Depth dependence . . . 147
6.2 Spatial scales . . . 154
6.3 Structure Functions . . . 158
6.3.1 One dimensional structure functions . . . 160
6.3.2 Structure functions in three dimensions . . . 162
6.3.3 Discussion . . . 167

7 An idealised planetary atmosphere **171**
7.1 Model setup . . . 173
7.1.1 A conductive relaxation profile . . . 174
7.1.2 Parameter variation . . . 176
7.2 Zonal mean diagnostics . . . 178
7.3 Criticality . . . 179
7.4 Energy transfer . . . 185
7.4.1 Equator to pole temperature difference . . . 185
7.4.2 Heat fluxes . . . 188
7.4.3 Lorenz cycles . . . 190
7.5 Discussion . . . 193

8 Conclusion **197**
8.1 Overview of main results . . . 198
8.1.1 Science questions . . . 201
8.2 Future work . . . 204

Appendices

A The form of the diffusive term used in MORALS **211**

B Details of tests for cylindrical geometry **213**
B.1 Barotropic instability test in a cylinder . . . 213
B.2 Baroclinic instability test in a cylinder . . . 214

Be patient, for the world is broad and wide.

William Shakespeare, *Romeo and Juliet*

1 Introduction

The differential solar heating of the Earth's atmosphere, which results in a warm equator and cooler poles, is one of the most fundamental aspects of the planet's climate. This non-uniform heating directly drives the Hadley cell, characterised by strong convection in the tropics, and also the thermally direct polar cell (Schneider, 2006). Between these convectively dominated regions the extra-tropics support a meridional temperature gradient but remain statically stable in the vertical. Coupled with the Earth's rotation this extra-tropical gradient has the potential to become baroclinically unstable, giving rise to baroclinic eddies in the mid-latitudes which are a key contributor to heat and momentum transfer through the atmosphere (Vallis, 2006). Of course, these processes are not limited to Earth's atmosphere and exist in a variety of forms across the solar system and beyond (Read, 2011).

Complex global circulation models (GCMs) are generally able to reproduce the thermal structure of the Earth's atmosphere fairly accurately. However, this is unfortunately not because we have a good understanding of the underlying processes. Often it is because parameterisations used to represent unresolved processes are empirically calibrated and hence reproduce the observed structures by construction. This explains why GCMs for the Earth cannot generally be successfully applied to other planets or even Earth's palaeoclimate without modification (e.g. Mayne et al. (2014)). There is ongoing debate about how the Earth's thermal structure

equilibrates to its current observed form and what role the mid-latitude baroclinic eddies play in this process (Schneider, 2006; Zurita-Gotor and Lindzen, 2007). The potential for nonlinear eddy-eddy interactions and eddy-mean flow interactions and how these behave in the presence of radiative forcing and other atmospheric processes introduces significant complexity into the dynamics. In many ways the Earth's ocean dynamics behave similarly to the atmosphere in that baroclinic instability is an important agent of heat and momentum transport (e.g. Pérez-Pérez et al. (2010) and references therein). Hence, the oceans might be expected to equilibrate similarly. However, in this work we restrict our focus to the atmosphere.

In the current work we aim to explore some of the issues relating to the atmosphere's thermal equilibration using a novel approach of combining a study of baroclinic flows in a new laboratory experiment with numerical simulations. The laboratory experiment is a variation on the widely used rotating annulus (Read et al., 2015). This thesis details the computational side of this work although experimental results produced by colleagues in the lab are used for comparison where possible. Since the 19th century, when somewhat informal experiments took place, using cigar smoke to visualise the fluid (Vettin, 1857), the potential for studying analogues of atmospheric processes in the lab has been known. In the 1950's Hide (1953) (and independently Fultz et al. (1959)) carried out more systematic experimental studies which established the utility of lab experiments as a means of studying atmospheric flows and they have been widely used ever since (e.g. Mason (1975), Hignett et al. (1985), Read et al. (2015), Vincze et al. (2015), and von Larcher et al. (2018)). In many cases the experimental work has been complemented by numerical simulations to allow a wider range of phenomena to be measured and in some cases to validate the numerical formulations against data from the lab (e.g. Williams (1969), Read (2003), Pérez-Pérez et al. (2010), and Young and Read (2008)).

The novel rotating annulus configuration used in this thesis combines free convection, to represent the polar cell and tropical convection in the atmosphere, with a wide baroclinic zone where measurements of the equilibrated thermal structure may be taken (Scolan and Read, 2017). More details of the experimental setup

are given towards the end of this chapter. Our focus is on developing a numerical model for this new experiment from ENDGame, the dynamical core of the Met Office Unified Model (UM) (Wood et al., 2014). The UM is a numerical model of the atmosphere designed to be used across a wide range of applications and scales, from numerical weather prediction to climate modelling. It is used for operational forecasting by the UK Met Office and to our knowledge this is the first time an operational forecasting model has been used to simulate experiments in the lab. In addition to providing simulations of Earth's atmosphere on both global and regional scales, and on timescales ranging from a few days to hundreds of years, the UM has more recently been used for modelling the atmospheres of extra solar planets (Mayne et al., 2013). Furthermore, numerous idealised configurations of the UM exist for the purposes of testing and comparison with other numerical models as well as investigating fundamental aspects of geophysical flows (e.g. Mayne et al. (2013) and Wood et al. (2014)). The dynamical core, ENDGame (Wood et al., 2014), is the part of the model which discretises and solves the equations of fluid motion.

Use of this model allows us to validate some of the model's numerics against laboratory data. It also enables us to use the same model to simulate the lab experiment and atmosphere-like flows and hence gain some insight into how well the experiment behaves as an analogue to the atmosphere. In general, assuming that a model produces results consistent with an experiment, simulations can be used to produce more complete information on a flow than is possible to collect from experiments alone and this can provide deeper insight into the nature of the experimental flow. In the following sections we outline the existing literature which motivates our study and finish this chapter with a more detailed discussion of the aims of the thesis in light of this.

1.1 Thermal equilibration of the extra-tropical atmosphere

Currently, there exists no general theory for the equilibration of baroclinic eddies in the atmosphere and oceans. The factors which determine an eddy's ultimate

scale and how they themselves affect the equilibration of the mean state are not well understood. The goal of studies relating to this problem is not necessarily to provide full solutions to the fluid equations but to provide a closure relation which relates the eddy activity to the mean flow state. Existing theories which attempt to provide a closure relation fall into three main groups:

- **Baroclinic adjustment** - This was first proposed by Stone (1978) and is analogous to convective adjustment in the sense that baroclinic eddies are produced by instability and then act to stabilise the flow such that the mean state of the system is marginally supercritical to baroclinic instability.

- **Geostrophic turbulence** - Ideas in this vein are developed from homogeneous turbulence theories (Larichev and Held, 1995; Held and Larichev, 1996) and typically suggest that the size of equilibrated eddies is set by non-linear interactions between the eddies which can cause energy to flow from smaller to larger scales. They predict that the efficiency of diffusive eddy transport is determined locally by the eddy length scale.

- **Moist convection** - Theories in this group, pioneered by Juckes (2000), suggest that moist convection may be more efficient in setting atmospheric stratification than baroclinic eddies and that this is a dominant effect in the extra-tropics as well as the tropics. Results in this area have been mixed. Frierson et al. (2006) and Frierson (2008) found that moisture was an important component in setting the extra-tropical lapse rate although the former found that equilibrated eddy size was not much affected. On the other hand, Schneider and O'Gorman (2008) found that for Earth-like climates dry theories were consistent with the equilibrium stratification when moisture was present. We will not consider moisture further in this work as there is no analogue for it in the annulus experiment but we acknowledge that it may be an important factor to consider for the Earth's climate.

We consider the first two groups of theories in more detail below.

1.1.1 The concept of baroclinic adjustment

Baroclinic adjustment was first proposed by Stone (1978) as a means of closing the atmospheric equilibration problem. The concept was born from the observation that, on Earth, the mean slope of the isentropes is remarkably robust regardless of seasonal changes in the forcing. When a system is convectively unstable, convective instability acts to restore the system to a neutral state. Baroclinic adjustment proposes that baroclinic eddies undertake a similar process. In a baroclinically unstable fluid baroclinic eddies form and transport heat and momentum in such a way that the fluid is restored to marginal stability. This requires that the eddy fluxes vary strongly with the forcing so that they are able to counteract it.

Already this raises an important question: how does one define marginal stability for a baroclinic flow? In general, no necessary and sufficient condition for baroclinic instability is known. However, in the two layer, quasi-geostrophic model of Phillips (1951) one can derive the minimum shear for instability which is given by

$$U_c = \beta R_D^2. \tag{1.1}$$

$R_D = Nd/f_0$ is the Rossby deformation radius where N is the buoyancy frequency, d is the layer depth and the Coriolis parameter $f = f_0 + \beta y$ assuming motion on a β-plane. Defining the vertical shear, $U_s = U_1 - U_2$, as the difference in the velocity of the zonal basic state between the two layers, the mode is baroclinically unstable if the vertical shear exceeds U_c. Therefore, we can define a criticality, $\xi = U_s/U_c$, so that for $\xi > 1$ the model is baroclinically unstable and $\xi = 1$ represents a marginally supercritical state. Using the thermal wind relation

$$U_s = -\frac{gd}{f\theta_0}\partial_y\theta \tag{1.2}$$

one can rewrite the criticality in terms of the isentropic slope within the fluid

$$\xi = \frac{-f}{\beta d}\frac{\partial_y\theta}{\partial_z\theta}. \tag{1.3}$$

θ is the potential temperature and so we see that criticality is essentially the slope of the isentropes in units scaled such that the horizontal and vertical scales are

comparable. This means that for $\xi = 1$ an isentrope that leaves Earth's surface near the equator will meet the tropopause above the pole and this is broadly what is observed in the atmosphere (Stone, 1978).

Whilst this may seem a neat result, a number of problems are immediately identifiable. Firstly, the timescales associated with baroclinic instability are comparable with the timescales for diabatic heating in the atmosphere (Barry et al., 2000). This is very different to the convective adjustment scenario where convective processes occur significantly faster than the diabatic forcing and hence are able to set the stratification. A separation of timescales is required for rapid dynamical changes to adjust the mean state.

Furthermore, there is evidence that the two layer model itself does not actually equilibrate to a marginally supercritical mean state where $\xi = 1$. Using a two layer quasi-geostrophic model with truncation at high wavenumbers Salmon (1980) found that the system equilibrated to a strongly supercritical mean state. Vallis (1988) found a similar result in the two layer model when eddy-eddy interactions were significant but that the flow did equilibrate to marginal criticality in the case where nonlinear interaction between eddies was small. Also in the two layer model, Stone and Branscome (1992) found that although the model equilibrated to a supercritical state, this state was very robust to changes in the forcing with $\xi = 2.4$ over a wide range of parameters. Although this may indicate that the model equilibrates to some preferred state, a concept in accordance with the idea of baroclinic adjustment, there is no obvious physical significance of $\xi = 2.4$ as there was for $\xi = 1$. Later results in the two layer model from Zurita-Gotor and Lindzen (2006) showed a similarly robust equilibration to $\xi = 2.3$ but that this could be modified if large enough changes were made to the forcing.

Some attempt has been made to explain these results through the introduction of nonlinear baroclinic adjustment theory (Cehelsky and Tung, 1991; Welch and Tung, 1998). This suggests that the condition of $\xi = 1$ corresponds to the case where only the most unstable baroclinic mode interacts with the flow and dominates the heat transport. As the forcing increases this mode becomes saturated and the

next most unstable mode becomes the one to dominate the transport. This causes the criticality to increase to a value consistent with the stability condition for the new dominant wave. Therefore, there is not a single preferred equilibrium state to which the system adjusts but rather there are several possibilities for equilibrium. The one which is settled on depends on the forcing.

Despite all this interest in the two layer model it is not clear how applicable these results are to a continuous atmosphere. Unlike in the two layer model, there is no known necessary and sufficient condition for baroclinic instability in the continuous case. For geostrophic flow a necessary condition is provided by the Charney-Stern-Pedlosky (CSP) criteria (Charney and Stern, 1962; Pedlosky, 1964). This condition places a constraint on the structure of the quasi-geostrophic potential vorticity (QGPV),

$$Q = \nabla_h^2 \psi + f_0 + \beta y + \frac{\partial}{\partial z}\left(\frac{f_0^2}{N^2}\frac{\partial \psi}{\partial z}\right). \tag{1.4}$$

ψ is the geostrophic streamfunction and ∇_h is the horizontal component of the gradient operator. A full derivation of this result can be found in Vallis (2006). For a flow to be baroclinically unstable one of the following conditions must be fulfilled:

1. The meridional gradient of the potential vorticity, Q_y, changes sign within the domain.

2. The meridional potential temperature gradient, θ_y, at the upper boundary has the same sign as Q_y in the interior.

3. θ_y at the lower boundary has the opposite sign to Q_y in the interior.

4. θ_y at the lower boundary has the same sign as θ_y at the upper boundary when $Q_y = 0$ in the interior.

In the two layer model the top layer has a positive potential vorticity gradient by construction and hence the lower layer must have a negative PV gradient to fulfil the CSP conditions. In a continuously stratified atmosphere the internal vorticity gradient is generally positive due to the planetary vorticity and it is the negative

sign of the potential temperature gradient at the surface which causes the flow to be unstable. In this case there is no minimum shear required for instability.

However, the relevance of the two layer model to the continuous atmosphere may be elucidated by reformulating the criticality in a way that is relevant to the Charney model of baroclinic instability (Charney, 1947). In the Charney model a dynamical scale height

$$h = \frac{\Lambda f_0^2}{\beta N^2} \tag{1.5}$$

emerges from the non-dimensionalisation of the equations where Λ is the uniform shear of the background state (Vallis, 2006). From a simple rearrangement of equation 1.3 we find that

$$\xi = \frac{h}{d}. \tag{1.6}$$

When the flow is supercritical (i.e. $\xi \gg 1$ and $h \gg d$) the depth of the domain, d, provides a limit on the scale height and so becomes the relevant vertical length scale. Hence, Charney waves span the full depth of the domain and are considered to be 'deep waves'. In the opposite limit, where $h \ll d$, the waves are 'shallow' as they have a vertical scale much smaller than the depth of the domain. Held (1978) proposed that the deep waves are the most important modes for heat transport in a continuously stratified quasi-geostrophic system. Therefore, a baroclinic adjustment mechanism could involve the formation of these deep waves when the system becomes supercritical which would result in efficient transport of heat to return the system to a marginally supercritical state. The limited vertical resolution of the two layer model means that all waves span the full depth of the domain and so are effectively deep. Hence, the criticality condition of the two layer model could be expected to apply to the deep modes in the continuous model. Chai and Vallis (2014) revisited this interpretation and derived a scaling for the dependence of eddy size on criticality which connected the deep and shallow wave regimes. Their findings were not consistent with the baroclinic adjustment hypothesis as they found that criticality could be varied smoothly with the forcing and they inferred the existence of an inverse cascade for high criticality.

1.1.2 Other means of eddy equilibration

Thus far we have seen that a theory for the thermal equilibration of the extra-tropical atmosphere must account for the robustness of the isentropic slope as forcing changes with the seasons. However, a simple adjustment theory based on the criticality of the two layer model is not a satisfactory solution in all respects.

An alternative theory to Stone's baroclinic adjustment, but one which makes very similar predictions including that the system equilibrates to a state where $\xi = 1$, is given by Schneider (2004) and Schneider and Walker (2006). From zonal momentum balance they find that the eddy flux of surface potential temperature is balanced by the isentropic mass flux due to the eddy flux of potential vorticity in a primitive equation model (Schneider, 2005). By further assuming diffusive eddy flux closures for the potential vorticity and potential temperature and that the eddy diffusivity of these quantities is the same and independent of height they predicted that $\xi \approx 1$ in the equilibrated state. A diffusive closure presumes that the eddy flux is downgradient and proportional to the mean gradient of the field being transported by the flux i.e. $\overline{v'a'} = -D\partial_y \overline{a}$ where D is the diffusivity and a is some quantity being transported. Schneider and Walker (2006) demonstrated that an idealised primitive equation GCM with Newtonian cooling does equilibrate at $\xi \approx 1$ across a range of parameter space. One difference between this theory and the others we have discussed thus far is that it is derived for the primitive equations rather than a quasi-geostrophic system and hence the vertical stratification of the mean state may be adjusted as well as the horizontal thermal contrast. Although the prediction of $\xi = 1$ is the same as in baroclinic adjustment this theory has no implications for the baroclinic stability of the flow. An implication of the equilibration to $\xi = 1$ is that nonlinear eddy-eddy interactions are inhibited so energy cannot be transported upscale. We return to this point below in our consideration of geostrophic turbulence.

Contrary to the theory of baroclinic adjustment and the work of Schneider, numerous other authors have shown in both primitive equation and quasi-geostrophic models that atmosphere-like flows can equilibrate to a state where the criticality varies smoothly rather than settling at a constant $\xi \approx 1, 2.4$ or any other value. As

already mentioned, Zurita-Gotor and Lindzen (2006) found criticality could vary from 2.3 with sufficiently strong forcing in the two layer model and Zurita-Gotor (2007) found that this variation was well approximated by a diffusive closure. Zurita-Gotor (2008) showed that criticality could be continuously varied in a primitive equation model when the timescale for diabatic heating was changed and more recently other authors have corroborated this result and shown that variation in the criticality may also be achieved by changing other variables such as the applied equator to pole temperature difference or fluid properties (Zurita-Gotor and Vallis, 2009; Jansen and Ferrari, 2012; Chai and Vallis, 2014). To explain these results authors have turned to geostrophic turbulence theories to describe the flow equilibration and we now turn our attention to that.

1.2 Turbulence in the atmosphere

A rigorous definition of turbulence is difficult to come by but generally one knows it when one sees it. A turbulent flow consists of many eddies on a range of scales whose individual motion in space and time is unpredictable. In a flow which is forced on large scales, eddies will form at a scale commensurate with the forcing and interact non-linearly such that energy is transferred between scales. Hence, the energy will be transferred to smaller and smaller scales until it is dissipated by viscosity. Throughout this discussion on turbulence the concept of spatial scales in the flow is of great importance and thus we often consider the flow fields in spectral space. Using an appropriate spectral transform for the geometry of a problem not only simplifies the maths as the spectral basis functions are eigenfunctions of the Laplacian but also allows us to consider the flow fields as a function of wavenumber, the inverse of spatial scale.

A successful, heuristic description of turbulence was first presented by Kolmogorov (1941). Kolmogorov envisaged an isotropic, homogeneous, three dimensional turbulent flow. The flow is in a steady state meaning that the rate of energy injection equals the rate of energy dissipation. He also assumed that energy exchange is predominantly local, that is that energy exchange mostly occurs between similar

scales rather than, for example, very large wavenumbers interacting with very small wavenumbers. Given that energy is conserved there will be a so-called 'inertial range' over which a scale independent, constant flux of energy will exist between the injection and dissipation scales. Using a simple dimensional analysis, Kolmogorov found that within the inertial range the time averaged kinetic energy is given by

$$E(k) = C\varepsilon^{2/3}k^{-5/3} \tag{1.7}$$

where ε is the rate of energy injection, C is a universal constant and k is wavenumber. Although equation 1.7 is supported by many experimental results, it has never been derived directly from the Navier-Stokes equations.

In two dimensions the behaviour of turbulence is quite different. This is because in two dimensional flows there are two quadratic conserved quantities - total energy and total enstrophy - compared to energy only in three dimensions. Enstrophy is the square of the vorticity which is conserved because vortex stretching is impossible in a two dimensional flow. A corollary of the existence of two conserved quantities is that one expects to find two inertial ranges, one where enstrophy flows downscale from the injection scale to the dissipation scale and one where the flux of energy is from the injection scale to larger scales. Using dimensional arguments once again, one can show that in the inertial range where energy flows upscale the energy is given by

$$E(k) = C_1\varepsilon^{2/3}k^{-5/3} \tag{1.8}$$

and in the enstrophy inertial range the energy is given by

$$E(k) = C_2\eta^{2/3}k^{-3} \tag{1.9}$$

where η is the rate of enstrophy dissipation. C_1 and C_2 are constants which are presumed to be universal. A more complete discussion of both two and three dimensional turbulence and their relevance to geophysical flows can be found in many textbooks e.g. Vallis (2006). We now turn our attention to quasi-geostrophic turbulence which is relevant to both the atmospheres and oceans and something of a hybrid between turbulence in two and three dimensions.

1.2.1 Geostrophic turbulence

Geostrophic turbulence is found in flows which are rotating and stably stratified. The essential features can be understood via an analysis which begins with the quasi-geostrophic approximation. This approximation is valid for flows with small Rossby number (i.e. fast background rotation rate)

$$Ro = \frac{U}{fL} \tag{1.10}$$

where U is a typical velocity scale and L is a typical horizontal length scale in the flow. Throughout this thesis we will often refer to the thermal Rossby number

$$Ro_{th} = \frac{g\alpha_v \Delta T d}{f^2 L^2} \tag{1.11}$$

where we have approximated U using thermal wind balance. g is the gravitational acceleration, α_v is the thermal expansion coefficient, ΔT is the maximum temperature difference in the system and d is the depth of the domain. The quasi-geostrophic approximation also requires strong stratification as indicated by a small Froude number

$$Fr = \frac{U}{Nd} = \frac{Ro}{\sqrt{Bu}} \tag{1.12}$$

where $Bu = (R_D/L)^2$ is the Burger number. A key property of quasi-geostrophic flow is that the quasi-geostrophic potential vorticity (QGPV), Q, is conserved when advected by the horizontal geostrophic flow. A geostrophic flow is one where there is a balance between the Coriolis force and the pressure gradient. Hence

$$\frac{DQ}{Dt} = 0. \tag{1.13}$$

In the limit that the deformation radius, R_D, is much larger than the typical scales of motion in the flow this equation reduces to

$$\frac{D(\nabla_h^2 \psi + f_0 + \beta y)}{Dt} = 0 \tag{1.14}$$

and hence

$$\frac{\partial \nabla_h^2 \psi}{\partial t} + \mathbf{u} \cdot \nabla(\nabla_h^2 \psi) + \beta v = 0 \tag{1.15}$$

where $\nabla_h^2\psi$ is the relative vorticity. Non-dimensionalising equation 1.15 we can produce a balance between the advective term (the second term on the left hand side) and the β term (the third term on the left hand side) such that

$$R_\beta = \sqrt{\frac{V}{\beta}} = \sqrt{\frac{\sqrt{E.K.E._{bt}}}{\beta}} \tag{1.16}$$

where, in this case, the eddy velocity scale, V, is not equivalent to the thermal wind, U defined above. We define V as the root mean square of the vertically averaged (barotropic) velocity as derived from the barotropic eddy kinetic energy, $E.K.E_{bt}$, at the energy containing eddy scale. R_β is known as the Rhines scale. For scales less than the Rhines scale the advective term dominates and for scales larger than the Rhines scale the β-term dominates. Therefore, the Rhines scale represents a scale where there is a crossover between wave dominated and turbulence dominated behaviour. When the β term is large the flow becomes dominated by Rossby waves and these interact with the turbulence to produce zonal flows and potentially zonal jets (Rhines, 1975; Vallis and Maltrud, 1993).

The analogy between two dimensional and quasi-geostrophic turbulence is evident from consideration of the conserved quantities. Returning to equations 1.13 and 1.4 and this time retaining the stratification term but assuming constant f and N one can show that energy and enstrophy are conserved when integrated over the three dimensional domain (Vallis, 2006). Hence, we have two inertial ranges as in two dimensional turbulence, one where energy flows upscale from the forcing scale and one where enstrophy moves downscale. The equilibrium required to produce these inertial ranges relies on dissipation of energy at large scales and dissipation of enstrophy at small scales to balance the input of these quantities at the forcing scale. The mechanism by which energy is dissipated is one of the key differences between two dimensional and three dimensional turbulence. In three dimensions, fully developed turbulent flows with large Reynolds number (and hence low viscosity) have finite energy dissipation because the low viscosity is offset by an increase in vortex stretching (Vallis, 2006). In two dimensions, vortex stretching is not possible and hence energy dissipation by viscosity tends to zero as the Reynolds number

becomes large and energy is trapped at large scales. Hence, instead of energy being dissipated by small scale viscosity, it is dissipated by large scale sources of friction such as boundary layer drag in two dimensional turbulence.

Since the prediction of two dimensional turbulence for the dependence of energy on wavenumber was a dimensional argument (equations 1.8 and 1.9) it also holds here and hence the spectral slopes in geostrophic turbulence are also given by k^{-3} in the direct cascade and $k^{-5/3}$ in the inverse cascade. The difference is that in the geostrophic case this k represents a three dimensional wavenumber and so an inverse cascade in the horizontal is generally accompanied by an inverse cascade in the vertical which results in barotropisation of the flow. Notably these spectral slopes are not consistent with what is observed in the atmosphere and currently no satisfactory explanation for the atmospheric energy spectrum exists (Nastrom and Gage, 1985; Lindborg, 1999; Tulloch and Smith, 2006).

The overall mechanism of idealised geostrophic turbulence was first explored by Salmon (1978) in a two-layer model. Some large scale forcing sets up a baroclinically unstable flow and energy is channelled into scales close to the deformation radius by baroclinic instability, as predicted by linear theories. From here, enstrophy cascades downscale to a scale where the flow is non-geostrophic and it is dissipated. On the other hand, energy is cascaded to larger scales in the barotropic mode due to barotropisation of the flow. At the Rhines scale, where the β-effect becomes important, this energy is channelled into the zonal flow, potentially producing zonal jets. The cascade is eventually halted by frictional effects. This process is shown schematically in figure 1.1. From this description it is evident that for a geostrophic inverse cascade to exist in the flow there must be a scale separation between the deformation radius and the Rhines scale.

Sometimes the Rhines scale is referred to as the halting scale of the cascade but Sukoriansky et al. (2007) highlighted that the meaning of the Rhines scale depends on the flow regime under consideration and the dominant processes acting. Furthermore, they showed that under no circumstances does the Rhines scale actually halt the inverse cascade, rather it inhibits it. Dissipation is required to halt

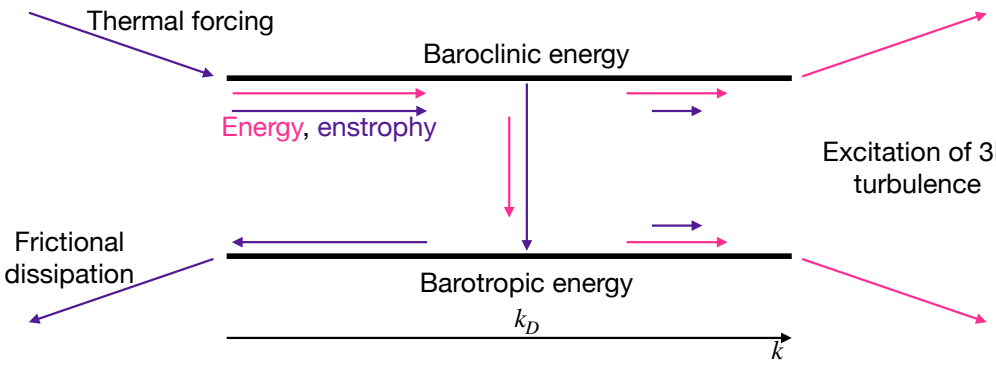


Figure 1.1: A schematic of two layer geostrophic turbulence. In the horizontal direction wavenumber increases from left to right. The upper level represents the baroclinic mode whilst the lower level represents the barotropic mode. Pink arrows represent energy transfer and purple arrows represent enstrophy transfer.

the cascade. For a friction dominated regime the Rhines scale has no particular relevance and the inverse cascade halting scale is set by the dissipation.

The utility of the Rhines scale as a prognostic for the equilibrated flow is limited by the fact that the eddy velocity scale, V, is not known a priori. Larichev and Held (1995) and Held and Larichev (1996) circumvented this problem by developing a scaling theory relating V to the velocity of the mean flow, U, which gives

$$\frac{V}{U} = \xi. \tag{1.17}$$

Combining this scaling with the definition of the Rhines scale (equation 1.16) and the definition of the criticality in the two layer model (equation 1.1)

$$\xi = \frac{R_\beta}{R_D}. \tag{1.18}$$

Hence, the criticality is also a measure of the separation between the Rhines scale and the deformation radius and consequently the extent of the inverse cascade. For flows where the criticality is maintained close to one, as in the theory and results of Schneider and Walker (2006), an inverse cascade would not develop and nonlinear eddy-eddy interactions would be suppressed. This is consistent with observations of Earth's atmosphere which suggest that an inverse cascade does not exist above the deformation scale (Shepherd, 1987; Lindborg, 1999; Cho and Lindborg, 2001). However, in Earth's ocean an inverse cascade of energy is observed (Scott and Wang,

2005) and evidence has also been found for an inverse cascade on Jupiter (Young and Read, 2017) which suggests these systems do not equilibrate to a marginally supercritical state despite having many features in common with Earth's atmosphere. Chai and Vallis (2014) provided evidence that for $\xi \approx 1$ there is a weakly nonlinear regime where eddies can increase in size before the onset of a fully developed inverse cascade at higher criticalities and that the Earth may lie within this regime.

It should also be noted that the scaling law of Held and Larichev (1996) strictly only applies when $\xi \gg 1$ as it relies on the assumption that a developed inverse cascade exists. Indeed, Lapeyre and Held (2003) found that the scaling law broke down for moderate criticalities. Using the arguments from the Charney model and the definition of criticality in equation 1.6, Held and Larichev (1996) suggested that in a continuous model dominated by the 'shallow' modes of Held (1978) the same scaling can be shown to hold for $\xi \ll 1$ and hence may hold for all values of ξ. However, for shallow modes, and more generally for subcritical flows where barotropisation does not occur, the scaling might not be uniform in the vertical. Schneider and Walker (2006) assert that, for Earth-like atmospheres, the pressure range of the troposphere is not large enough for significant vertical variation in any case.

Using mixing length assumptions and assuming that the eddy transport of heat in the fluid is diffusive, the scaling above can also be used to write the meridional eddy heat flux in terms of mean flow parameters. Assuming the eddy diffusivity, D may be written as the product of a characteristic eddy scale, $L_e = \xi R_D$ from above, and a characteristic eddy velocity, V above, the diffusive closure may be written as

$$\overline{v'\theta'} \approx -D\partial_y\overline{\theta} \approx -V\xi R_D\partial_y\overline{\theta} \approx -\beta\xi^3 R_D^3\partial_y\overline{\theta}. \tag{1.19}$$

The key difference between this closure and baroclinic adjustment is that here the eddy fluxes vary smoothly with the criticality rather than a particular value of criticality being preferred. However, Zurita-Gotor (2007) noted that, although this closure works well for the two layer model, the strong dependence on the criticality means that a small change in criticality causes a large change in the

eddy flux and this makes it difficult to distinguish between a baroclinic adjustment mechanism and a diffusive closure.

In a primitive equation model the stratification is determined by the dynamics whereas in the quasi-geostrophic case it is prescribed. Hence, for a non quasi-geostrophic model a closure is also required in the vertical direction. By assuming the eddies are adiabatic and hence the net eddy flux is directed along the isentropic slope such that

$$\frac{\overline{w'\theta'}}{\overline{v'\theta'}} \approx -\frac{\partial_y \overline{\theta}}{\partial_z \overline{\theta}} \tag{1.20}$$

Zurita-Gotor and Vallis (2009) found expressions for both the eddy meridional and vertical heat fluxes, the latter of which agreed with the scaling of Held and Larichev (1996). The introduction of variable stratification also raises the question of how equilibration by baroclinic eddies couples with the radiative forcing and convection.

More recently, Jansen and Ferrari (2012) used an argument similar to that of Schneider and Walker (2006) based on the isentropic zonal momentum balance in the primitive equations (although they also present a derivation in the quasi-geostrophic equations) to derive an expression for the criticality

$$\xi \approx \frac{f}{\beta d}\frac{\Psi}{D} \tag{1.21}$$

where Ψ is the mass transport over the surface layer which is the layer containing all isentropes which intersect the surface at some point. They approximate D using the scaling of Held and Larichev (1996) with the caution that this will not hold as criticality approaches 1. In Jansen and Ferrari (2013a) a similar scaling is calculated using the argument that the criticality is set via a balance of radiative forcing and adiabatic eddy heat flux and that the stratification is relaxed towards a neutral state where $\partial_z \theta = 0$. For both scalings they find good agreement with an idealised primitive equation model. Jansen and Ferrari (2013a) also highlights the importance of changes in the stratification and meridional temperature gradient separately as well as their ratio expressed as the criticality.

In the preceding sections we have traced the various strands of the literature discussing the thermal equilibration of the troposphere from the initial proposal of baroclinic adjustment by Stone (1978) to the present day. While theories based on geostrophic turbulence have shown promise in predicting the behaviour of eddies at high criticality they generally breakdown when $\xi \approx 1$. In part this is due to a lack of separation between the Rhines scale and deformation radius which means an inverse cascade cannot exist. Furthermore, in atmospheres which are slowly rotating or weakly stratified the quasi-geostrophic approximation may be inappropriate so it seems unlikely that geostrophic turbulence could be a universal solution. On the other hand, the prediction that the criticality equilibrates to a constant value, whether due to baroclinic adjustment or some other process, is violated by the results of many numerical studies but in agreement with others. It may be that these theories are each appropriate in different limits but if this is the case further work is needed to delineate the circumstances in which each is appropriate. Overall we can conclude that a general theory for the equilibration of the troposphere in the presence of baroclinic eddies remains elusive. Before we discuss our approach to this problem any further we take a brief detour to explore another form of turbulence, related to those discussed above, which will turn out to be relevant to the results presented in this thesis.

1.2.2 Surface quasi-geostrophic dynamics

In the quasi-geostrophic framework discussed above the potential vorticity is conserved along the geostrophic flow and the surface buoyancy, $b_s = f_0 \partial_z \psi|_{z=0}$, is conserved along the surface flow such that

$$\frac{\partial b_s}{\partial t} + \mathbf{u} \cdot \nabla b_s = 0. \tag{1.22}$$

Bretherton (1966) showed that the surface buoyancy acts equivalently to the potential vorticity in the fluid interior and this allows the two to be split such that the flow can be thought of as the sum of surface induced dynamics and interior induced dynamics (Lapeyre and Klein, 2006). The interior part of the solution

corresponds to the Charney model (Charney, 1947) where the flow is driven by the interior PV dynamics and the surface is characterised by uniform buoyancy. On the other hand, the surface part of the solution has $q = 0$ in the interior (this can also be generalised to constant q) and the flow is driven by the advection of buoyancy anomalies at the surface, assuming the domain to be semi-infinite above a single horizontal surface. This is the surface quasi-geostrophic (SQG) system (Blumen, 1978; Held et al., 1995; Lapeyre, 2017) and the governing equations are

$$Q = \nabla_h^2 \psi + \frac{\partial}{\partial z}\left(\frac{f_0^2}{N^2}\frac{\partial \psi}{\partial z}\right) = 0 \tag{1.23}$$

$$b_s = f_0 \frac{\partial \psi}{\partial z}\bigg|_{z=0} \tag{1.24}$$

$$\frac{\partial b_s}{\partial t} + \mathbf{u} \cdot \nabla b_s = 0 \tag{1.25}$$

where we have made the approximation that the Coriolis parameter, f_0, is constant.

Assuming constant stratification, i.e. constant $N = N_0$, the inversion relation between surface buoyancy and streamfunction can be derived from these equations using a horizontal spectral transform and written as

$$\hat{\psi} = -\frac{\hat{b_s}}{N_0 K} \exp\left(\frac{-K N_0 z}{f_0}\right) \tag{1.26}$$

where K is the modulus of the wavevector and $\hat{\cdot}$ denotes a two dimensional spectral transform of a variable (Scott, 2006). This result leads to a number of interesting properties of the SQG system:

- Structures decay exponentially away from the surface at a rate proportional to K. Hence, small scale structures decay quickly whereas large scale structures penetrate to greater depths. At depths greater than the scale of the largest surface mode the streamfunction is effectively zero. This also causes the kinetic energy spectrum to steepen with depth as larger wavenumbers decay more quickly.

- The dimensional decay constant is KN_0/f_0. Hence, for a surface disturbance to propagate throughout the entire depth of the domain it must have a

wavelength greater than the deformation radius. Note that this requires a modification to allow for a finite depth domain (Tulloch and Smith, 2006) and also relates to the mechanism of baroclinic instability in the Eady problem where the instability is caused by edge waves from two surfaces interacting.

- At the surface the kinetic energy is proportional to the potential energy, given by the square of the buoyancy (Lapeyre, 2017).

As in two dimensional turbulence SQG has two invariants, the total volume integrated energy

$$\mathscr{E} = \frac{1}{2}\int\int\int(\nabla\psi\cdot\nabla\psi)dxdydz = -\frac{1}{2}\int\int\psi_s\theta_s dxdy \tag{1.27}$$

and the surface potential energy

$$\mathscr{P} = \frac{1}{2}\int\int\theta_s^2 dxdy. \tag{1.28}$$

Here $\theta_s = b_s/N$ is the rescaled surface buoyancy where N is assumed to be constant. It is important to note that the energy invariant is the volume averaged energy, not the surface averaged energy and that, despite being controlled by the surface dynamics, the SQG system is three dimensional.

The relation between two dimensional turbulence and SQG turbulence has been explored by Pierrehumbert et al. (1994) and Smith et al. (2002). The presence of two invariants once again enables the existence of two cascades. The inverse cascade of total energy goes as k^{-3} and the surface potential energy goes as k^{-1} in the same range. In the inertial range where potential energy cascades to smaller scales the total energy follows a $k^{-8/3}$ slope and potential energy goes as $k^{-5/3}$. Given that the surface kinetic energy is proportional to the surface potential energy the kinetic energy spectrum at the surface has the same form as the potential energy. Schematics of these spectral shapes are shown in figure 1.2 alongside the equivalent spectra for 2D and 3D turbulence. In geostrophic turbulence the wave-turbulence crossover which inhibits the inverse cascade is a result of the background vorticity gradient due to the β-effect. For pure SQG turbulence the analogous effect is provided by a background buoyancy gradient (Held et al., 1995).

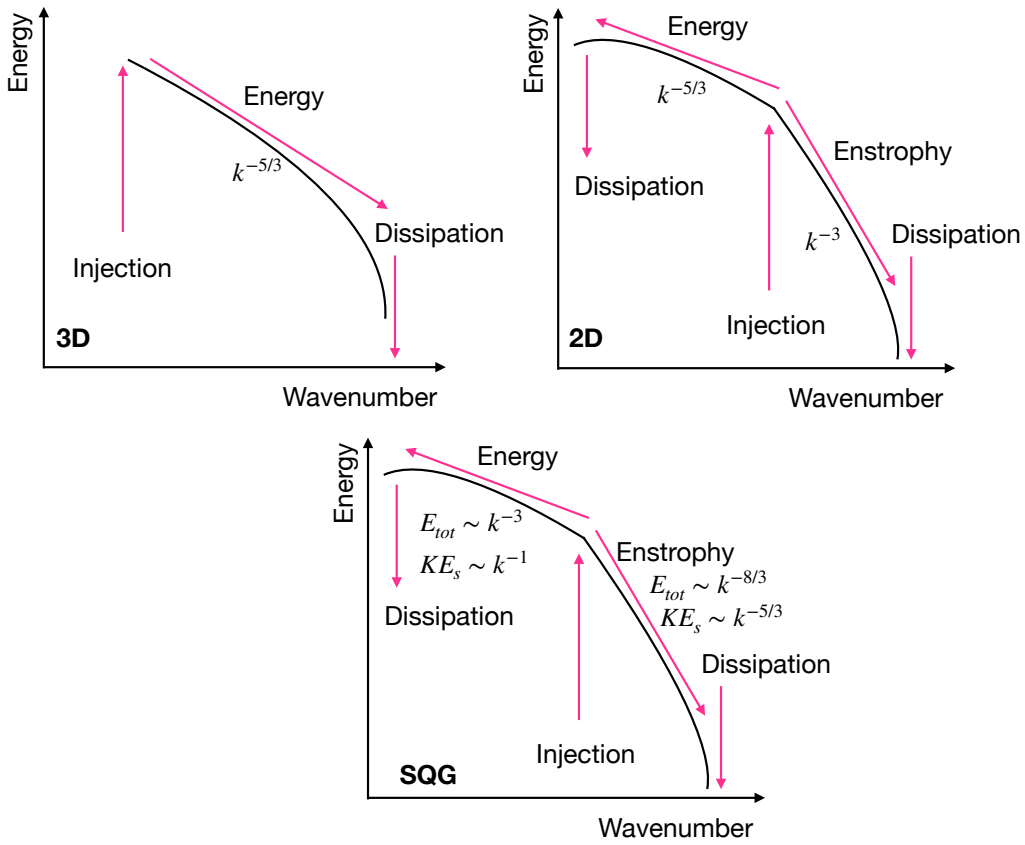


Figure 1.2: Schematic of the cascades in 3D turbulence (top left), 2D turbulence (top right) and SQG turbulence (bottom). The spectral shapes as functions of wavenumber in the inertial ranges are shown. In SQG the total volume averaged energy E_{tot} and surface kinetic energy, KE_s, have different shapes.

There is a precedent for the application of SQG theory to both the atmosphere and the ocean on Earth. Lapeyre (2017) and references therein discuss the applicability of SQG to the ocean and the importance of surface buoyancy to the dynamics of the upper ocean layers. At greater depths in the ocean the interior PV dynamics are a more important driving force. In the atmosphere, potential temperature anomalies on the tropopause and at the surface are important for driving the dynamics. Again a good review of work on this subject is included in Lapeyre (2017).

1.3 Annulus experiments as an analogue for the atmosphere

Having considered the issues surrounding the thermal equilibration of the atmosphere and the existing work on this topic we now consider how a lab experiment might provide a new approach to addressing this problem and how lab experiments have been used to explore aspects of geophysical fluids in the past. As we have discussed, whether a flow equilibrates to a preferred criticality or criticality varies smoothly seems to depend at least partly on modelling choices such as whether the quasi-geostrophic or primitive equations are used, the vertical resolution of the model and the heating formulation. One of the major benefits of using a lab experiment over a numerical model is that ambiguity due to choices of resolution, assumptions in the equations and parameterisations are removed. However, a lab experiment should not be thought of as a fundamentally different approach to an idealised numerical model. Both are simple systems which the modeller can use to explore aspects of atmosphere or ocean-like flows by changing parameters as they wish. It is useful to use numerical models alongside lab experiments to provide more complete information on the system which may not be easily measured in the lab. Throughout this work we shall refer to work in the lab as 'experiments' and numerical models as 'simulations' to differentiate the two.

1.3.1 The classical annulus

In its essentials the Earth's atmosphere, and the atmospheres of other planets, are stratified fluids, rotating at a constant rate and subjected to differential heating. Hence, a laboratory experiment that represents these aspects may be used as a simple analogue to the atmosphere that allows the phenomena resulting from these forcings to be studied in isolation.

The first systematic studies of this kind were carried out in the 1950's by Hide (1953) and independently by Fultz et al. (1959). Hide's experiment, known as the classical annulus experiment, consisted of two coaxial, vertically oriented cylinders, the outer of which was heated whilst the inner was cooled as shown in figure

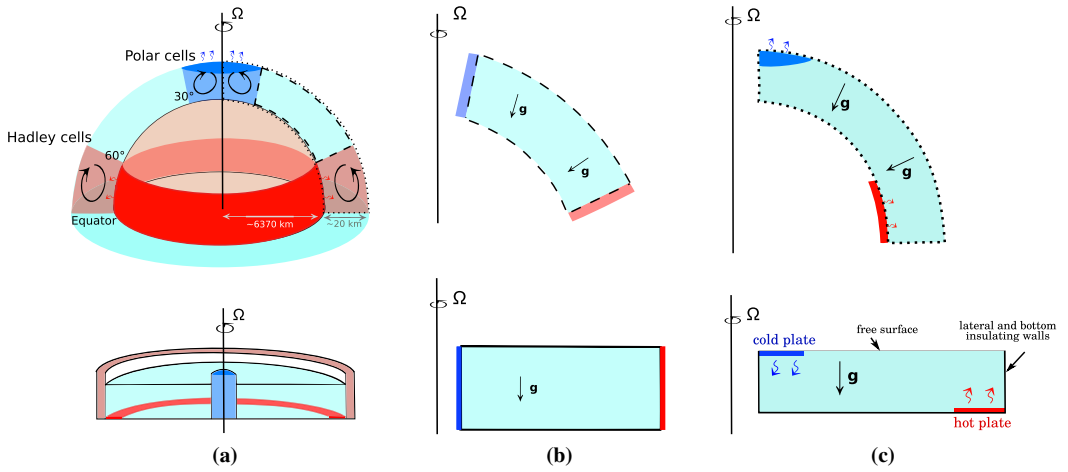


Figure 1.3: **(a)** An idealised view of the Earth's atmosphere with the dominant global heat source shown in red and the heat sink shown in blue. The analogous cylindrical lab experiment is shown below. **(b)** A schematic depiction of the atmosphere as represented by the classical annulus. A slice through the rz plane of the annulus is shown below with **g** showing the direction of gravitational acceleration in each case. The experiment is axisymmetric about the vertical rotation axis. **(c)** A schematic depiction of the atmosphere as represented by the new annulus configuration studied in this thesis. The rz slice below shows a sketch of the new experiment where the heat source and sink are displaced both horizontally and vertically. This figure is taken from Scolan and Read (2017).

1.3. A fluid was contained in the cavity between the two cylinders and the entire system was rotated at constant angular velocity. This fluid was affected by gravity, rotation and the applied temperature gradient which was in the same sense as the atmospheric temperature difference between the poles and the equator on Earth. Therefore, its behaviour was found to be analogous to the large scale dynamics of the atmosphere. Since these first studies many variations on this classical system have been used to investigate a diverse range of problems. Variations on the classical heating configuration have included an internally heated fluid (Hide and Mason, 1970; Read, 1986) and a horizontal temperature gradient across the base (Hignett et al., 1981). Usually the working fluid is water or an aqueous solution but air (e.g. Castrejón-Pita and Read, 2007), mercury and silicon oils (Fein and Pfeffer, 1976) have also been used. There are also many instances where the experimental work has been accompanied by numerical models as a non-invasive means of providing a measure of the flow and/or validating the model's numerics (e.g. Williams, 1969; Hignett et al., 1985; Read, 2003; Young and Read, 2008; Read et al., 2015).

In the classical annulus heat transport may be divided into two components, the axisymmetric overturning circulation and transport by eddies. Depending on the flow regime, which is set by the differential heating and rotation rate for a given experiment, the non-axisymmetric component may take the form of large scale baroclinic waves or smaller, more irregular eddies. The axisymmetric overturning is predominantly confined to the boundary layers (Read et al., 2015). On the vertical sidewalls where the heat source and sink are located there are thermal boundary layers while Ekman layers exist on the top and bottom boundaries due to the rotation. Ekman layers are horizontal boundary layers which exist in rotating systems and in the annulus the flow within them is characterised by a balance between the Coriolis force and friction (Vallis, 2006). As rotation increases the Ekman layers become thinner and the overturning circulation is throttled which results in a decrease in axisymmetric heat transport with rotation rate. Rotation also results in Stewartson layers forming on the sidewalls which may also contribute to throttling the flow. Stewartson layers are vertical boundary layers in rotating systems which contain strong horizontal shear. They are structured as two nested layers which together ensure matching between the interior flow and the boundary conditions and conserve mass by returning the fluid transported by the Ekman layer (Stewartson, 1957). Read (2003) found that the drop in axisymmetric heat transport due to throttling by the boundary layers could be largely offset by heat transport due to large scale low frequency baroclinic waves which form when the flow in the annulus becomes baroclinically unstable. This means that the total heat transport is almost independent of rotation rate but the partitioning between the eddy and mean heat fluxes changes. The mechanism behind the enhanced heat transport by the baroclinic waves is not yet theoretically well understood (Read et al., 2015).

1.3.2 A new annulus configuration

The experiment considered in this thesis is a novel variation on the classical annulus, the main difference being the configuration of heating and cooling. In our experiment the cooling takes place through a disk at small radii (r<0.1175m) on the top surface

of the fluid whilst a ring covering the outermost radii (r>0.388m) on the base provides the heating as shown in figure 1.4. The inner cylinder has a radius of 2.5cm. This arrangement of thermal forcing results in freely convecting regions at the sides of the tank with a baroclinic zone sandwiched between them. This is comparable to an idealised form of the structure of Earth's atmosphere in one hemisphere, as shown in figure 1.3. The motivation for this new configuration was to avoid the strong influence of the boundary layer overturning circulation in the classical annulus on the stratification of the fluid in the interior. The new configuration enables the interaction between baroclinic waves and the fluid stratification to be studied more comprehensively. The fluid used is either water or a mixture of 17% glycerol by volume in water to allow particles used for particle image velocimetry (PIV) to be neutrally buoyant. The new experiment can have either a flat bottom surface or a conical surface may be inserted to give depth variation with radius. This has an effect analogous to the planetary β-effect. The experiment has an open surface at the top and so the β-effect may also be enhanced by the centrifugal surface deformation at high rotation rates.

1.3.3 Heat transfer by free convection

In the classical annulus free convection does not take place and this is another difference between the modes of heat transport in the classical and new configuration. The convection may also play a role in setting the stratification. In the new annulus the heat source and sink are displaced both horizontally and vertically from one another and thus the configuration may be thought of as a hybrid of Rayleigh-Bénard convection (Chillà and Schumacher, 2012) and horizontal convection (Hughes and Griffiths, 2008). In the former the heat source covers the bottom surface of the domain whilst the heat sink is on the top surface. In the latter convection is caused by a heat source and sink on the same horizontal surface. In many previous studies of the heat transfer in these convective systems the goal has been to find scaling relationships between parameters representing the heat transfer (e.g. the Nusselt number, Nu) and external parameters (such as the Rayleigh number, Ra) as these

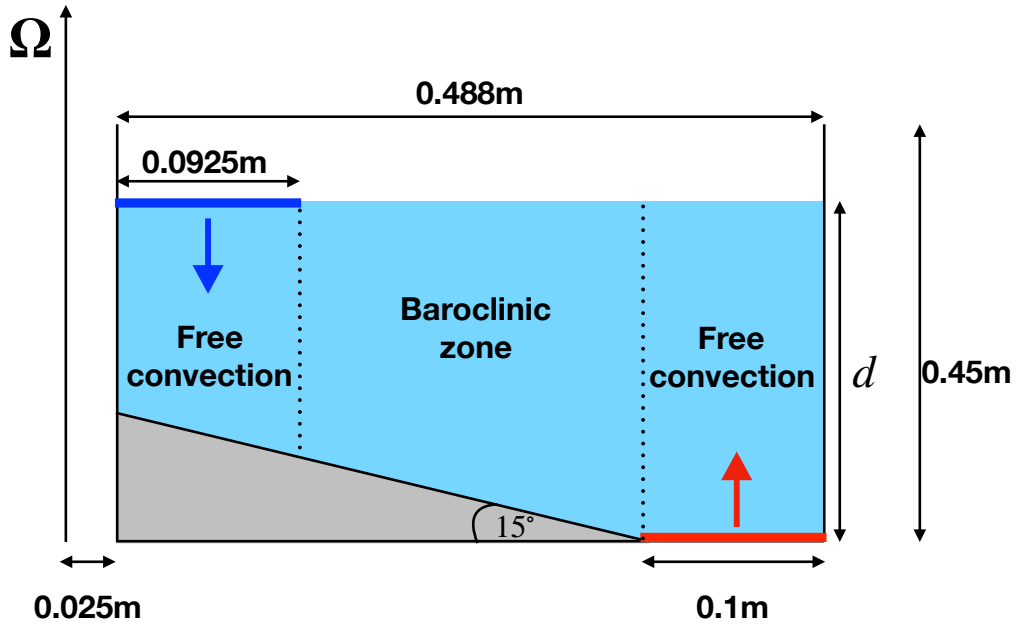


Figure 1.4: A sketch of the new experimental configuration in the rz plane. The heat source is shown in red, the heat sink in dark blue and the fluid in light blue. The sloping bottom can be removed to allow experiments where the depth is constant with radius. The freely convecting regions above and below the heat source and sink and the central baroclinic zone are delineated by dotted lines. Solid black lines represent solid, no slip boundaries.

scaling laws can be used to predict the behaviour of the system for a given set of external parameters. The Nusselt number,

$$Nu = \frac{q}{q_c} \tag{1.29}$$

is the ratio of total heat transfer, q, to heat transfer by conduction alone, q_c The Rayleigh number,

$$Ra = \frac{g\alpha_v \Delta T L^3}{\kappa\nu} \tag{1.30}$$

provides a measure of how vigorous the convection in the system is. L is the horizontal length scale, α_v is the thermal expansion coefficient, κ is the thermal diffusivity and ν is the kinematic viscosity. The scaling relationship is generally assumed to take the form $Nu \propto Ra^{\alpha}$ where the exponent is determined theoretically or empirically from experiment.

There is an extensive literature on the mechanisms of heat transfer and associated scaling laws for both Rayleigh-Bénard and horizontal convection in rotating and non-rotating systems (see e.g., Ahlers et al. (2009), Chillà and Schumacher (2012), and Hughes and Griffiths (2008) for reviews). Hignett et al. (1981) developed a theoretical framework for deriving this scaling law for the heat transfer in an annulus with a differentially heated base and found $\alpha = 1/5$. An exponent of 1/5 is also given by the Rossby scaling for non-rotating horizontal convection (Rossby, 1965), although the universality of this law has been questioned (Shishkina et al., 2016). The analysis of Hignett et al. (1981) has since been applied to an internally heated rotating annulus (Read, 1986) and the classical annulus configuration (Read et al., 2015) to give $\alpha = 1/4$, which is in agreement with experiment.

The value of α for Rayleigh-Bénard convection is still disputed; classical results predict $\alpha = 1/3$ (Malkus, 1954) or 2/7 (Shraiman and Siggia, 1990; Castaing et al., 1989) but values ranging from 1/4 to 1/3 have been observed and predicted by experiment and theory (Chavanne et al., 1997; Grossmann and Lohse, 2000). Over a large range of Rayleigh numbers, the heat transport was found to be well described by a phenomenological model proposed by Grossmann and Lohse (Grossmann and Lohse, 2000; Grossmann and Lohse, 2001; Grossmann and Lohse, 2002; Grossmann and Lohse, 2004; Grossmann and Lohse, 2011; Stevens et al., 2013) based on an assumption of low Reynolds number and laminar boundary layers. More recently this approach has also been applied to horizontal convection (Shishkina et al., 2016; Shishkina and Wagner, 2016). The model proposes that there is no universal scaling law for the Nusselt number but that α is dependent on the region of Rayleigh/Prandtl number space in which the experiment takes place (see Shishkina et al. (2016) Figure 2). This dependence on regime may be a result of the planform of the flow and whether it is dominated by plumes or large scale overturning.

1.4 Aims and overview of this thesis

The aim of the work detailed in this thesis was to use a novel approach to shed light on the process of baroclinic eddy equilibration in the atmosphere and, in

particular, understand whether baroclinic adjustment provides a framework that enables this equilibration to be understood in any or all dynamical regimes. Our novel approach has been to develop a model for a new rotating annulus experiment from ENDGame, the dynamical core of the Met Office UM. As discussed above it is generally useful to use a numerical model alongside an experiment but the use of ENDGame offers the particular benefit that the same model may be used to simulate an atmosphere. Using this model we have been able to study the dynamics of the system and how this fits in with existing theories of eddy equilibration relating to baroclinic adjustment and geostrophic turbulence. Unfortunately, a limitation of this work is that extensive experimental data does not currently exist, in particular we do not yet have velocity measurements to compare with our simulation data. However, more complete experimental data for comparison should become available in the near future and for the time being we are able to make recommendations for measurements to prioritise in future experimental work.

To focus the narrative of this thesis we pose the specific aims of this work as a series of questions and note how the thesis is structured to answer them.

1. **Can the novel annulus configuration be used as an analogue for Earth's atmosphere?**

   This question is first addressed in chapter 2 where we use an existing two dimensional model to produce simulations of the annulus experiment and use this to check that the form of the flow is in line with the principles used to design the experiment i.e. a baroclinic zone sandwiched between two freely convecting regions. The form of the flow is studied in more detail in chapters 4-6 and compared with an atmosphere-like flow in chapter 7.

2. **Can the ENDGame dynamical core be used to successfully simulate a laboratory experiment?**

   In chapter 3 we describe the modifications which were made to ENDGame to allow simulation of the lab experiment. In chapter 4 we validate this model

against the existing experimental data and also with some reference to the more established model used for the two dimensional simulations in chapter 2.

3. **How does heat transfer in the annulus scale with different experimental parameters and specifically how does this relate to baroclinic eddy activity?**

   We address this question in chapter 5 where we consider the form of the equilibrated flow in the three dimensional annulus simulations. The analysis is carried out with reference to the baroclinic adjustment and geostrophic turbulence frameworks as we try to ascertain which, if either, of these is most relevant to the annulus experiment.

4. **Is an inverse energy cascade from small to large scales observed and under what conditions does it emerge/is it suppressed?**

   The presence or absence of the inverse cascade is one of the distinguishing features between baroclinic adjustment and geostrophic turbulence. In chapter 6 we use a spectral analysis of the flow and structure functions to elucidate the conditions under which an inverse cascade may emerge or be suppressed.

5. **How do phenomena observed in the lab experiment scale to a more atmosphere-like configuration of the model?**

   In chapter 7 we present the results of idealised atmospheric simulations with a heating formulation designed with reference to the lab experiment. By computing some of the same diagnostics used in the lab experiment we are able to highlight similarities and differences between the two systems.

In chapter 8 we discuss how successful we have been in answering these questions and make suggestions for future work to extend the ideas presented here.

If your morals make you dreary, depend upon it they are wrong.

—Robert Louis Stevenson, *Across the Plains*

2 2D simulations

Before embarking on the development of a new model to study the annulus experiment a preliminary study was carried out using a well established two dimensional model. This had the multifold benefit of providing a point of reference for the forthcoming three dimensional simulations and a first view of the system's dynamics for less computational expense. A two dimensional model can be compared with a three dimensional system to quantify the effects of three dimensional features such as baroclinic waves and convective plumes. Read (2003) used this method to quantify the heat transfer due to non-axisymmetric effects by directly subtracting the simulated two dimensional contribution to heat transport from three dimensional laboratory measurements. If the ultimate goal of this thesis is to investigate how baroclinic turbulence exerts an influence on the background flow it is necessary to initially define this background state in the absence of baroclinic instability. With a view to making comparisons with data from the laboratory experiment and three dimensional simulations, the simulations were run using the same dimensions and system properties as in Scolan and Read (2017).

As noted in chapter 1 the new annulus experiment is something of a hybrid between horizontal and Rayleigh-Bénard convection. Hence we analyse the heat transport with reference to existing work on these two types of convection, assuming similarities will exist. The goal in many similar studies has been to find a scaling

relationship between the Nusselt number, Nu, and the Rayleigh number, Ra, of the form $Nu \propto Ra^{\alpha}$ where the exponent is determined theoretically or empirically from experiment.

Previous work on both horizontal and Rayleigh-Bénard convection has also addressed the merits and pitfalls of modelling convection in two dimensions. Schmalzl et al. (2004) found that at moderate Rayleigh numbers, with Prandtl number greater than unity and rigid boundary conditions, the behaviour of Rayleigh-Bénard convection was similar in two and three dimensional systems. van der Poel et al. (2013) extended this result to higher Rayleigh numbers and found that the global properties of the flow, including the heat transfer characterised by the Nusselt number, were again similar for 2D and 3D simulations for Rayleigh numbers less than 10^{10}. The experiments carried out in this chapter are at the upper limit of this range with Rayleigh numbers of around 10^{10}. In the case of horizontal convection many numerical studies have been carried out in the two dimensional limit and, despite some disagreements with experiment over the form of the flow, the scaling of the heat transfer with Rayleigh number is found to be the same as in three dimensions (Hughes and Griffiths, 2008; Ilicak and Vallis, 2012). At the lowest rotation rates experiments show an approximately axisymmetric flow in our annulus (Scolan and Read, 2017) and so two dimensional modelling might be expected to capture the fluid's behaviour fairly well in this regime. However, it is probable that as rotation rate increases and three dimensional features become more prevalent the results from two and three dimensional modelling would diverge.

2.1 The numerical model

The model used for the simulations in this chapter is MORALS (the Met Office Oxford Rotating Annulus Laboratory Simulation) which has been used extensively to model similar experiments in both two and three dimensions in the past (Farnell and Plumb, 1975; Hignett et al., 1985; Read et al., 2000). MORALS is a direct numerical simulation code which employs a finite difference scheme using a leapfrog method with Robert-Asselin filter for the integration. The centred finite difference method

used is accurate to second order in timestep and diffusion terms are represented by a Du Fort-Frankel scheme to maintain stability (Farnell and Plumb, 1975). Variation in the azimuthal direction was suppressed to give a two dimensional axisymmetric flow. The code solves the Navier-Stokes (Equation (2.1)), continuity (Equation (2.2)) and heat equations (Equation (2.3)) for an incompressible, non-hydrostatic, Boussinesq fluid in cylindrical co-ordinates

$$\frac{\partial \mathbf{u}}{\partial t} + \mathbf{u}\cdot\nabla\mathbf{u} + 2\boldsymbol{\Omega}\times\mathbf{u} - (\Omega^2 r\hat{\mathbf{r}} - g\hat{\mathbf{z}})\frac{\rho}{\rho_0} + \frac{\nabla p}{\rho_0} = \mathbf{D}, \tag{2.1}$$

$$\nabla\cdot\mathbf{u} = 0, \tag{2.2}$$

$$\frac{\partial T}{\partial t} + \mathbf{u}\cdot\nabla T = \nabla\cdot(\kappa\nabla T), \tag{2.3}$$

where $\mathbf{u} = (u, v, w)$ is the velocity in the r, ϕ, z directions respectively. p is the pressure and ρ_0 is a reference density. $\mathbf{D}$ is a viscous diffusive term which is more complex than the familiar $\nu\nabla^2\mathbf{u}$ term as it allows for spatial variations of the diffusion coefficient caused by the temperature field (Farnell and Plumb, 1975; Wright et al., 2017). The precise form of this term is given in appendix A. The equation of state for the density of the fluid, ρ, is given by

$$\rho = \rho_0(1 + \rho_1(T - T_{\text{ref}}) + \rho_2(T - T_{\text{ref}})^2) \tag{2.4}$$

where, in the current simulations, $\rho_0 = 1043$ kg m^{-3}, $\rho_1 = -3.07\times10^{-4}$ K^{-1} and $\rho_2 = -7.83\times10^{-6}$K^{-2} are constants and $T_{\text{ref}} = 22$°C is a reference temperature. The viscosity and thermal diffusivity vary similarly with temperature. The fluid parameters are chosen to match the 17% glycerol / 83% water mixture (by volume) used by Scolan and Read (2017).

The total heat transfer through the fluid is characterised by the Nusselt number (Equation (1.29)) which is the ratio of total heat transfer to that due to conduction alone. It is calculated from the conductive heat flux, $\mathbf{j}$, through the heat source and sink, which can be computed from the temperature field at any time as

$$\mathbf{j}.\hat{\mathbf{n}}_\mathbf{z} = -\kappa c_p \rho \nabla T.\hat{\mathbf{n}}_\mathbf{z} \tag{2.5}$$

where c_p is the heat capacity of the fluid and $\hat{\mathbf{n}}_\mathbf{z}$ is the unit vector in the z direction, i.e. the direction normal to the heat source or sink. This flux is integrated over the

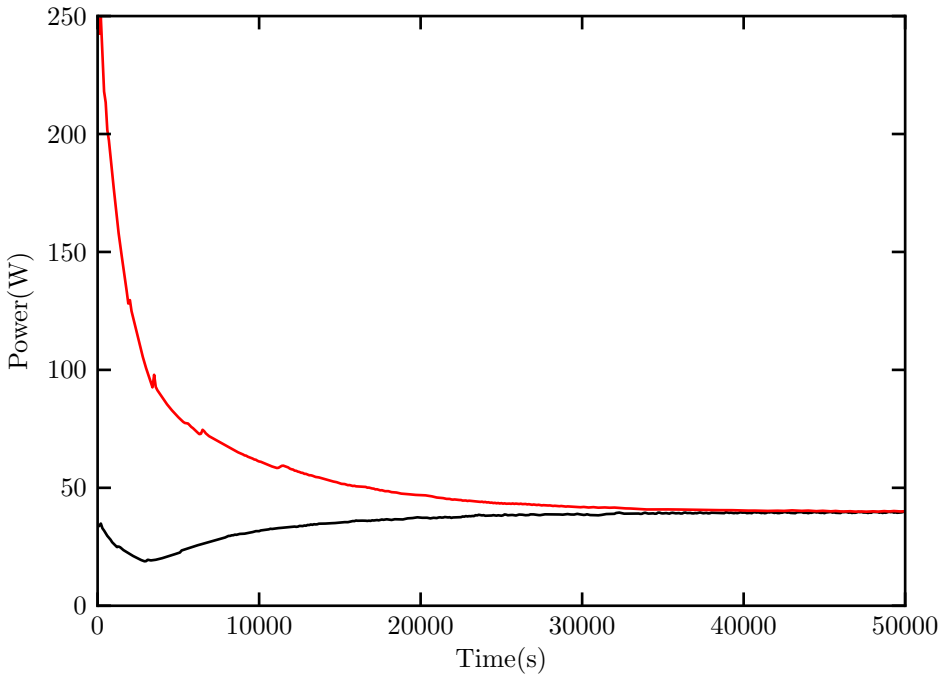


Figure 2.1: The time series of total power (W) for $\Delta T = 10$ °C, $\Omega = 1$ rad·s^{-1} and $d = 24.4$ cm. The red line shows the power dissipated by the heat sink and the black line the power input by the heat source, these converge after a stabilisation time of about 45,000 s.

area of the source or sink under consideration to give the power plotted in figure 2.1. The integrated power from the heat source should equal that dissipated by the heat sink once the model has equilibrated and thus the Nusselt numbers for the heat source and sink should also be equal. The conductive heat transfer (which excludes any heat transfer due to fluid motion) was calculated using a separate code, written by Roland Young, with a forward Euler solver and a significantly faster runtime than the full fluid model. This solved the thermal conduction equation for the transient adjustment of T towards the steady state in cylindrical co-ordinates

$$\frac{1}{r}\frac{\partial}{\partial r}\left(\kappa r\frac{\partial T}{\partial r}\right)+\frac{\partial}{\partial z}\left(\kappa\frac{\partial T}{\partial z}\right)=0. \tag{2.6}$$

after which the corresponding heat flux, $\mathbf{j_c}$, was computed and integrated over the area of the heat source or sink. To reduce any effect of fluctuations in the Nusselt number across the domain, the total Nusselt number is given by the average of the individual Nusselt numbers over the heat sink and source.

Parameter	Symbol	Present range	Units
Rotation rate	Ω	0–2	$\mathrm{rad{\cdot}s^{-1}}$
Temperature difference	ΔT	0.5–10	K
Fluid properties are listed at 20°C:			
Density	ρ	1044	$\mathrm{kg{\cdot}m^{-3}}$
Thermal expansion coefficient	α_v	2.76×10^{-4}	$\mathrm{K^{-1}}$
Kinematic viscosity	ν	1.71×10^{-6}	$\mathrm{m^2{\cdot}s^{-1}}$
Thermal diffusivity	κ	1.28×10^{-7}	$\mathrm{m^2{\cdot}s^{-1}}$
Channel geometry:			
Inner radius	a	0.025	m
Outer radius	b	0.488	m
Mean fluid depth	d	0.122, 0.244, 0.366	m
Non-dimensional:			
Ekman number (Equation (2.10))	Ek	$> 6 \times 10^{-6}$	
Prandtl number	Pr	12.6	
Rayleigh number (Equation (1.30))	Ra	3.3×10^9 – 6.7×10^{10}	
Aspect ratio	Γ	3.8, 1.89, 1.27	

Table 2.1: Parameters used in the experiments described in this chapter.

2.2 Model setup

To simulate the laboratory experiment of Scolan and Read (2017) the model is set up such that the fluid is contained between two upright, rigid, coaxial cylinders and a flat horizontal base. On the base, the region with $r \geq b - 10$ cm is heated to a constant temperature, T_b, and the innermost 9.25 cm of the upper surface is cooled to a temperature of T_a, hence $\Delta T = T_b - T_a$. In the simulation both boundaries are treated as isothermal whereas in the lab experiment the heat source is isoflux. Elsewhere, the boundaries are insulating so a temperature gradient of zero in the direction normal to the boundary is enforced. The velocity boundary conditions are no-slip everywhere, i.e. $\mathbf{u} = 0$ at the boundaries. This differs from the lab experiment where the top of the cylinder is a free surface. The form of the Ekman layer on the top surface will be modified by the presence of a free surface as opposed to a no slip boundary. However, a selection of simulations with a free slip upper boundary were run and this different boundary condition did not change the results presented in this chapter significantly.

To ensure adequate resolution of the boundary layers in the numerical simulation,

an Arakawa C grid (Arakawa and Lamb, 1977), which is stretched in r and z, is used. The stretching is such that 3 grid points lie within the thinner of the thermal and kinetic boundary layers. Tests with up to 9 points within the boundary layer were carried out but this higher resolution was found to produce a change of no more than 1% in Nu. All simulations contain 384 grid points in the radial direction and the number in the vertical direction scales with the depth of the fluid. For simulations with fluid depth $d = 12.2$ cm there are 96 grid points in the z direction and 192 and 288 respectively for simulations of height 24.4 cm and 36.6 cm. The maximum Reynolds number,

$$Re = \frac{UL}{\nu}, \tag{2.7}$$

for these flows is of the order of 10^4 and thus the Kolmogorov scale is

$$\eta \sim LRe^{-3/4} \sim 5 \times 10^{-4}\text{m}. \tag{2.8}$$

This scale is resolved within the boundary layers but not within the interior of the flow where the grid is coarser. Underresolving the Kolmogorov scale affects energy dissipation at the smallest scales within the flow but this is less dominant in the interior than in the boundary layers.

The parameters used for these experiments are listed in Table 2.1. Simulations were computed over a range of rotation rates, temperature differences and aspect ratios. Runtime for the simulations with the most gridpoints was approximately two weeks on a Dell Optiplex 9020 desktop. Data for the lowest aspect ratios at the highest rotation rates is not included as these simulations proved too expensive to compute with the available resources. The model was initialised with isothermal fluid ($T = 20$ °C, midway between the temperatures of the heat source and sink) which was immobile in the rotating frame. When the thermal and rotational forcing are applied the fluid enters a transient regime until the stabilisation time where the model reaches equilibrium. Figure 2.2 shows that convective plumes are resolved. The asymmetry between the intensity of the plumes over the heat source and sink is most likely due to the smaller area of the heat sink. A timestep of 0.01 s was chosen

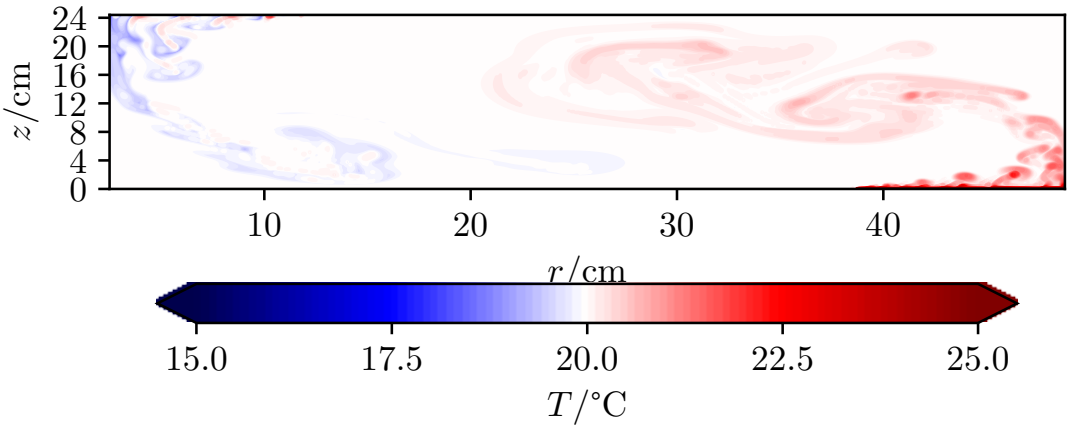


Figure 2.2: The instantaneous temperature field in the r, z plane after 100s of simulation time for a run with $\Delta T = 10$K, d=24.4cm and $\Omega = 0.01$rad s^{-1}. Convective plumes above the heat source and below the heat sink are resolved.

as we found this was the longest timestep that could be used whilst maintaining numerical stability. Most simulations were run for a total time of 50,000 s. Those runs which reached equilibrium more quickly were stopped after 30,000 s. Runs were judged to be equilibrated once the integrated power over the heat sink was within 1% of that over the heat source. Figure 2.1 shows that the run with $\Delta T = 10$ °C , $\Omega = 1$ rad·s^{-1} and $d = 24.4$ cm equilibrated within about 45,000 s.

In this chapter we characterise different flow regimes using the boundary layer ratio, P, as has been done in previous work (e.g.Hignett et al. (1981), Read (1986), Read (2003), and Read et al. (2015)).

$$P = \left(\frac{l_T}{l_{Ek}} \right)^2 \tag{2.9}$$

is the squared ratio of the non-rotating thermal boundary layer thickness to that of the Ekman layer (King et al., 2012; Hignett et al., 1981). The thickness of the thermal boundary in the non-rotating system is given by $l_T = L/2Nu_0$ and the Ekman layer thickness is given by $l_{Ek} = d\sqrt{Ek}$. Nu_0 is the Nusselt number of the non-rotating system and

$$Ek = \frac{\nu}{\Omega d^2} \tag{2.10}$$

is the Ekman number. Hence P is proportional to the rotation rate.

2.3 Results

2.3.1 Non-rotating Flow

Initially it is helpful to consider the behaviour of the convection without the influence of rotation. The non-rotating Nusselt number, Nu_0, is used to estimate the thickness of the thermal boundary layer which is in turn used to calculate the boundary layer parameter, P. It can also be used to normalise the Nusselt number for the rotating system. For these purposes it would be advantageous to have an external measure of the non-rotating Nusselt number rather than having to calculate it from simulations so we follow previous work in finding the exponent, α, discussed in chapter 1 from our simulated data.

Overall, the scaling exponent α appears to be close to 2/7 but has an aspect ratio dependence. The maximum difference in $Nu_0(Ra, \Gamma)$ at a given Ra for different aspect ratios is about 10% at the highest Rayleigh number. Table 2.2 gives the values of α for each of the different aspect ratios as well as the overall value calculated from a least squares fit. As illustrated in figure 2.3, data for the two lower aspect ratios were found to present a reasonable agreement with a scaling exponent of 2/7, as predicted both by Shraiman and Siggia (1990) and Castaing et al. (1989) for Rayleigh-Bénard convection and observed experimentally (Chavanne et al., 1997; Xu et al., 2000). For Γ=3.8 the scaling law is less clear but the 1/3 exponent seems to be more consistent with the data. This exponent has been predicted by Malkus (1954) for Rayleigh-Bénard convection and observed experimentally (see Malkus, 1954; Goldstein and Tokuda, 1980; Grossmann and Lohse, 2000).

The 2/7 exponent might be expected to be valid in the range of Rayleigh numbers for the present experiments ($\approx 10^9 - 10^{10}$) (Chavanne et al., 1997) and would suggest the existence of turbulent boundary layers as assumed in Shraiman and Siggia's model. The 1/3 scaling law suggests a more turbulent regime and a configuration with more independent behaviour of each plate and with heat transport which is independent of height (see Malkus, 1954; Chillà and Schumacher, 2012). This interpretation assumes that the current system behaves similarly to Rayleigh-Bénard

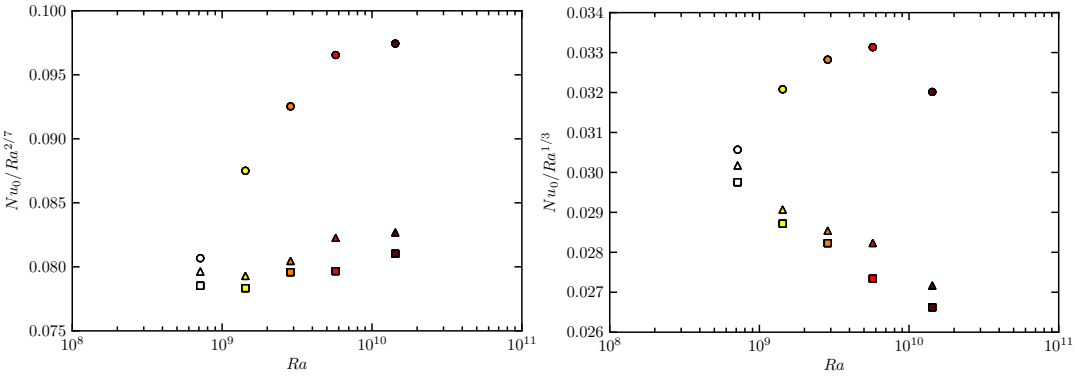


Figure 2.3: The dependence of the Nusselt number for the non-rotating system, Nu_0, on the Rayleigh number, Ra with left: compensation by a $Ra^{2/7}$ scaling law, right: compensation by a $Ra^{1/3}$ scaling law. Darker colours represent higher applied temperature differences, ○ for $\Delta T = 0.5°$ C, ● for $\Delta T = 1°$ C, ● for $\Delta T = 2°$ C, ● for $\Delta T = 4°$ C and ● for $\Delta T = 10°$ C. Shapes represent different aspect ratios, circles for $\Gamma = 3.8$ whilst $\Gamma = 1.9$ and $\Gamma = 1.3$ are represented by squares and triangles respectively.

convection. However, the complex role of the aspect ratio in such convective flow regimes is confirmed. The relevant length scale for defining the Rayleigh number is chosen to be the horizontal length of the domain as in horizontal convection, which renders the analysis independent of height. Tests using the vertical length scale were also carried out but these produced more scatter in the results, making it harder to define a scaling law. However, calculating the Nusselt number using the vertical length scale could be more appropriate as the thermal boundary layer is on the horizontal surface so its thickness is a vertical length. Given that the heat source and sink are displaced both horizontally and vertically it may be that a lengthscale calculated via a combination of the horizontal and vertical lengths would best capture the system properties. Despite use of the horizontal length scale as in horizontal convection, the measured exponent appears to be close to those previously found for Rayleigh-Bénard convection which suggests this system does behave as some hybrid of the two archetypal convection configurations.

As only three different aspect ratio values were tested it is not possible to rigorously determine a functional form for the dependence of the exponent on the aspect ratio. Both Funfschilling et al. (2005) and Sun et al. (2005) found the Nusselt number to be a weakly decreasing function of aspect ratio for Rayleigh-Bénard convection whilst Bailon-Cuba et al. (2010) found the Nusselt number to be a

Aspect Ratio, Γ	α
1.3	0.301 ± 0.003
1.9	0.297 ± 0.002
3.8	0.34 ± 0.01
All	0.329 ± 0.018

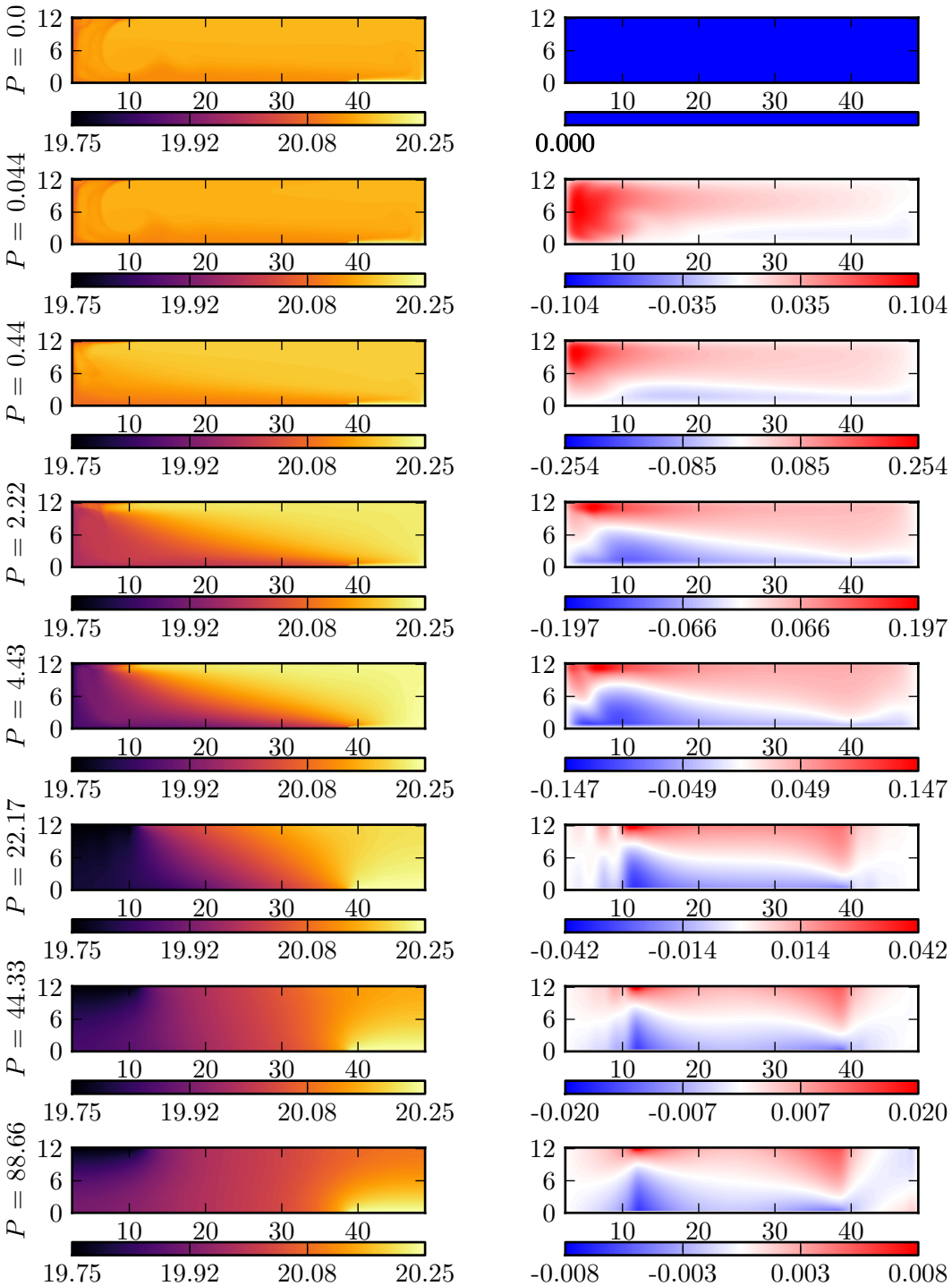
Table 2.2: Least squares fit parameters for the non-rotating Nusselt number vs. the Rayleigh number. α is the exponent in the power law $Nu_0 \sim Ra^{\alpha}$.

non-monotonic function for aspect ratios of order one and increasing for aspect ratios greater than one. From the current data it is not clear that the relationship between the Nusselt number and the aspect ratio is necessarily monotonic. In previous studies differences in flow patterns have been cited as an explanation of aspect ratio dependence (Bailon-Cuba et al., 2010; van der Poel et al., 2011; Puits et al., 2013) but observations of the temperature and velocity fields here do not reveal very different flow patterns for the different aspect ratios.

2.3.2 Rotating Flow Regimes

We now investigate the dynamical regimes and heat transfer in simulations with rotation. Using the definition of P from above, six axisymmetric flow regimes have been identified in previous annulus experiments (Hignett et al., 1981; Read, 1986; Read, 2003; Read et al., 2015). Figure 2.4 shows the temperature and azimuthal velocity fields for P ranging from 0 to approximately 90 for runs with $\Delta T = 0.5^{\circ}$ C and $\Gamma = 3.8$. The existence of a number of different equilibrated flow regimes, approximately equivalent to those found in previous studies, is evident:

1. No rotation ($P = 0$): A density current flows beneath the heat sink, down the side of the inner cylinder and along the base towards the heat source. A corresponding density current is not seen above the heat source, presumably because of the larger area of the hot plate. At high z and for $r \gtrsim 10$ cm the fluid interior is approximately isothermal at a temperature close to that of the hot plate. Since these fields are time averaged individual convective



(a) Temperature (° C) **(b)** Azimuthal Velocity (ms^{-1})

Figure 2.4: (a) r,z cross-sections of the equilibrated, time averaged temperature field for $\Delta T = 0.5$°C, $d = 12.2$ cm and the full range of rotation rates. The value of P for each run is shown on the left hand side. These correspond to rotation rates of 0, 0.001, 0.01, 0.05, 0.1, 0.5, 1 and 2 rad s^{-1}. (b) r,z cross-sections of the equilibrated, time averaged azimuthal velocity fields for the same runs.

plumes shown in figure 2.2 are not seen here. The azimuthal velocity is zero everywhere.

2. Weak rotation ($0.05 \lesssim P \lesssim 0.5$): The density current is reduced and replaced by a more uniform thermal gradient. Close to the inner and outer cylinders the isotherms are approximately vertical and confined to Stewartson layers which are a few centimetres thick and on the vertical boundaries. The azimuthal velocity is now non-zero and takes a maximum value near the top of the tank, outside the boundary layers but close to the inner cylinder. As the rotation increases this region of maximal velocity becomes more confined towards the top of the tank. Close to the bottom of the tank retrograde motion begins to develop. Using streaklines to visualise the flow, Scolan and Read (2017) showed that for weak rotation the flow in the experiment remains approximately axisymmetric.

3. Moderate rotation ($1 \lesssim P \lesssim 10$): For moderate rotation P is of order unity and thus the thicknesses of the thermal boundary layer and the Ekman layer are comparable. Free convection results in well mixed, approximately isothermal regions above and below the heat source and sink respectively. Sandwiched between these two convective zones is a baroclinic region with approximately uniformly sloping isotherms. This thermal structure has also been observed in experiments as shown by Scolan and Read (2017) (figure 6 of that paper). As before, prograde azimuthal velocity is seen close to the top of the tank and retrograde motion occurs near the bottom. The fastest velocities are observed at small radii. The azimuthal velocity begins to transition towards geostrophic balance as the rotation rate increases.

4. Strong Rotation ($P \gtrsim 20$): The Ekman layer thickness is less than that of the thermal boundary layer and thus the radial transport becomes inhibited. The suppression of vertical convection results in the replacement of the well mixed regions by statically unstable temperature gradients. The isotherms in the central baroclinic region steepen and, for the highest value of P, surpass the

vertical and slope in the opposite direction. The flow fields approach those expected for a purely conducting material as the rotation organises the flow via the Taylor Proudman effect and so mixing is suppressed (Vallis, 2006). The azimuthal velocity is now approximately zero in the regions directly over/under the heat source/sink but in the central zone an azimuthal flow which follows the applied rotation at the top of the tank and goes against it at the bottom is observed. This induces a thermal wind shear.

Read et al. (2015) identified changes in the slope of the isotherms as a function of P associated with transitions between different flow regimes. The isotherm slope, γ, is characterised by

$$\gamma = \int_{z=0}^{d}\int_{r=a+w_-}^{b-w_+}\left(\frac{\partial T}{\partial r}\Big/\frac{\partial T}{\partial z}\right)rdrdz\Big/\int_{z=0}^{d}\int_{r=a+w_-}^{b-w_+}rdrdz. \tag{2.11}$$

where w_- and w_+ are the widths of the heat sink and source respectively. Figure 2.5 shows the normalised isotherm gradient as a function of P. This is the ratio of the isotherm slope in the full flow to that in a purely conducting sample. The gradient is computed excluding the regions directly above/below the heat source/sink where the slope is non-linear. Low rotation rate data is excluded from the plot as figure 2.4 shows that for low rotation rates the interior of the fluid is approximately isothermal and so the isotherm slope is not meaningfully defined. Initially the isotherm gradient is approximately constant and at higher P it begins to increase with a slope of about 3/2 which is in good agreement with the prediction for the classical annulus (Read et al., 2015). This scaling of 3/2 begins at the point where rotation is sufficiently strong that Ekman layers containing a balance of friction and coriolis forces (meaning V scales as $P^{1/2}$) develop and the azimuthal vorticity equation is dominated by a balance of buoyancy and the Coriolis force such that $\gamma \sim fV$. For the classical annulus, the transition to this scaling is expected to occur at $P \approx Pr^{-2}$ (Read et al., 2015). Here the transition appears to have some aspect ratio dependence and occurs at higher values of $P = 1-10$. At high enough rotation rates the fluid stiffens and begins to behave as a purely conducting sample and so

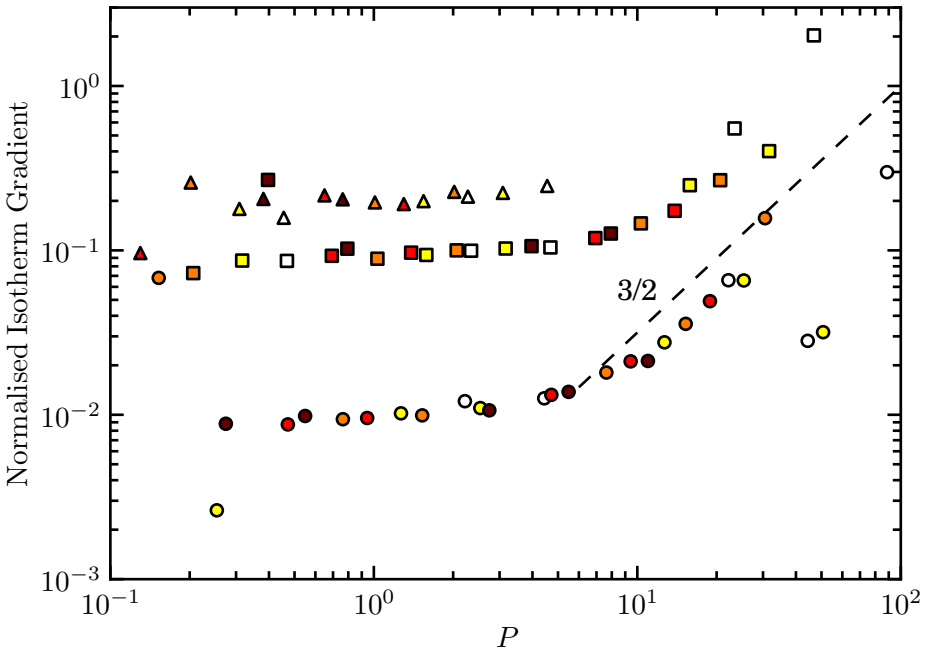


Figure 2.5: The isotherm gradient, normalised by the gradient of the conductive isotherms, as a function of P. Lower P data is not included as the interior of the annulus is approximately isothermal for low rotation and so the isotherm slope is not well defined. The dashed line shows the predicted dependence of the isotherm gradient on P and has a slope of 3/2. Symbols have the same meaning as in Fig. 2.3.

the normalised isotherm gradient is expected to tend to 1. However, more data at higher P would be needed to confirm this. An aspect ratio dependence of the isotherm slope is observed with lower aspect ratios giving steeper isotherms for the same value of P. Smaller aspect ratios in this case have a larger vertical separation between the heat source and sink. The isotherm gradient is closely related to the baroclinic supercriticality discussed in Chapter 1 and so will be studied further for the three dimensional systems in later chapters.

2.3.3 Heat Transfer

Figure 2.6 shows the variation in the normalised Péclet number, Pe, $Pe/Pe_0 = (Nu(\Omega) - 1)/(Nu_0 - 1)$, with P. Pe is the ratio of advective to conductive heat transfer and Pe_0 is the Péclet number of the non-rotating system. The clear trend is that the Péclet number remains close to that of the non-rotating system, until $P = O(1)$, when it begins to decrease rapidly with P. This transition occurs in the moderately rotating regime where the Ekman layer has a thickness comparable to

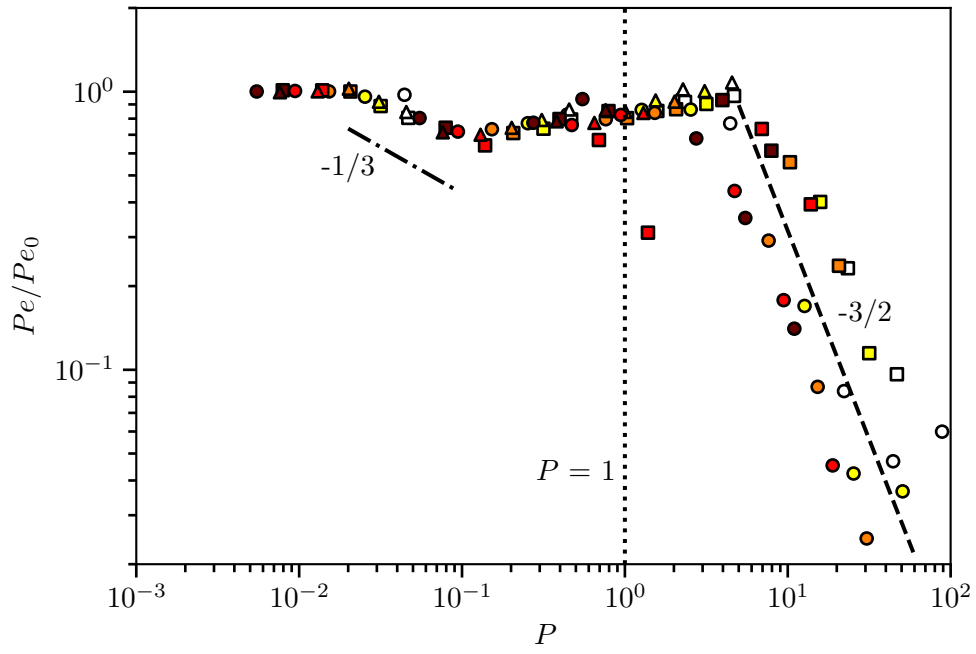


Figure 2.6: The reduced Péclet number $PePe_0^{-1}$ plotted against P. The dashed line has a slope of -3/2 which can be compared with the slope of the data points. The Nusselt number is expected to decrease at this rate for high P. The dashed-dotted line has a gradient of -1/3, this rate of decrease in the Nusselt number may be expected if Stewartson layers were throttling the flow. The vertical dotted line marks the point where the Ekman layer and thermal boundary layer have approximately equal thickness at $P = 1$. The symbols are the same as in Fig. 2.3.

that of the thermal boundary layer and thus begins to suppress radial transport. This behaviour has been observed in previous annulus experiments (Hignett et al., 1981; Hignett, 1982; Read, 1986). A least squares fit for $\log(Nu)$ vs. $\log(P)$ at high P gives a slope of -1.4 ± 0.1 and -1.3 ± 0.2 for $\Gamma = 3.8, 1.9$ respectively. These gradients are consistent with the -3/2 scaling found by Hignett (1982) and Read (1986). The Ekman mass transport is proportional to $v \cdot l_{Ek}$ (Vallis, 2006). At high rotation the azimuthal flow is governed by the thermal wind which results in $v \propto \Omega^{-1}$. Thus the mass transport, and hence the Péclet number, is proportional to $\Omega^{-3/2}$. For the highest aspect ratio (indicated by circular markers in figure 2.6) there appears to be another transition to a constant or slightly increasing Péclet number at $P \approx 50$. Although more data at higher P would be necessary to confirm this trend, it is notable that these data points correspond to the temperature fields

where the isotherms were observed to surpass the vertical.

Additionally, more subtle variation in the Péclet number is observed at low P. At $P \approx 0.02$ the Péclet number begins to decrease to a minimum of about 70% of the non-rotating value. The Péclet number then increases again to close to the non-rotating value before the rapid decrease with P begins. This was also observed in experiment by Scolan and Read (2017) despite the experiments being fully three dimensional compared to the axisymmetric simulations. A possible physical explanation may be offered by considering the temperature fields in figure 2.4.

The thickness of the inner Stewartson layer is given by $l_S = dEk^{1/3}$. For $P = 0.044$ the Stewartson layer thickness on the vertical sidewall is about 6-8cm, within the same order of magnitude as the approximately 10cm wide hot and cold plates. When P increases to 0.44 the thickness of the Stewartson layer approximately halves to about 3cm, less than half the width of the source/sink, and so the vertical motion is throttled, potentially reducing the heat transport. At higher values of P the heat transport is increased again as the regions above and below the heat source and sink become fully convective. The Stewartson layer thickness is proportional to $Ek^{1/3}$ and so the reduction in heat transport may be expected to go as $P^{-1/3}$. This value is possibly in agreement with the slope of the reduction observed in figure 2.6, as shown by the dashed-dotted line, but further investigation would be needed to fully support this argument.

For each of the three aspect ratios the general behaviour follows a similar trend. However, the value of P at which the transition to the regime where Pe is proportional to $P^{-3/2}$ occurs is a function of aspect ratio. Read (1986) predicted an aspect ratio dependence of the regime transitions for an annulus with internal heating and observed transitions occurring at lower P for higher aspect ratio in numerical simulations. Aspect ratio dependence of transitions between different behaviours has also been seen in Rayleigh-Bénard convection (Weiss and Ahlers, 2011). As the analysis stands P is independent of the height of the fluid. The aspect ratio dependence suggests that at higher values of P the depth of the fluid influences the heat transfer through the flow, perhaps because of the inhibition

of radial flow via the Taylor-Proudman effect. A full explanation for the aspect ratio dependence remains currently unknown.

2.3.4 The Azimuthal Velocity Scale

Following Read (1986) the azimuthal velocity scale, V, of the flow may be estimated by considering the volume averaged azimuthal kinetic energy per unit mass defined as

$$V = \left[\int_{z=0}^{d} \int_{r=a}^{b} v^2 r dr dz \Big/ \int_{z=0}^{d} \int_{r=a}^{b} r dr dz \right]^{1/2}. \tag{2.12}$$

The reduced azimuthal velocity scale plotted in figure 2.7 is derived via a scaling analysis of equations (2.1) and (2.3) in the weakly rotating regime to find the theoretical maximum of V. This is akin to Read (1986) but with heating on the horizontal surface as for our experiment. As with the Péclet number, the scaling of V is expected to change with increasing rotation (and hence increasing P) and such behaviour is observed in figure 2.7.

For very weak rotation, there is a balance of inertial and Coriolis forces and so, from the azimuthal momentum equation, it may be shown that $V = O(fL)$. Therefore it is expected that V should increase linearly with P as both P and f are proportional to the rotation rate. For slightly stronger, but still weak, rotation the Coriolis force balances viscous effects in the Ekman layer and thus the expected scaling of V can be found by equating these two terms in the azimuthal momentum equation. This gives $V = O(\kappa P^{1/2} N u_0^2 L^{-1})$, the transition to the shallower slope of 1/2 can be observed in figure 2.7 for $\Gamma = 1.3$ for $P \approx 0.04$. For $P = O(1)$ the azimuthal velocity scale reaches a maximum of $V = O(\kappa N u_0^2 L^{-1})$ before beginning to decrease. For $P > 1$ the azimuthal velocity is proportional to P^{-1}, which follows from thermal wind balance. These results are concurrent with those found from previous annulus experiments (Hignett et al., 1981; Read, 1986).

As in the case of the Péclet number there is clearly an aspect ratio dependence of the azimuthal velocity which has not been included in the analysis. The two lower aspect ratios collapse well onto a single line but the data for $\Gamma = 3.8$ gives a lower value for the scaled velocity for a given value of P. The dependence of

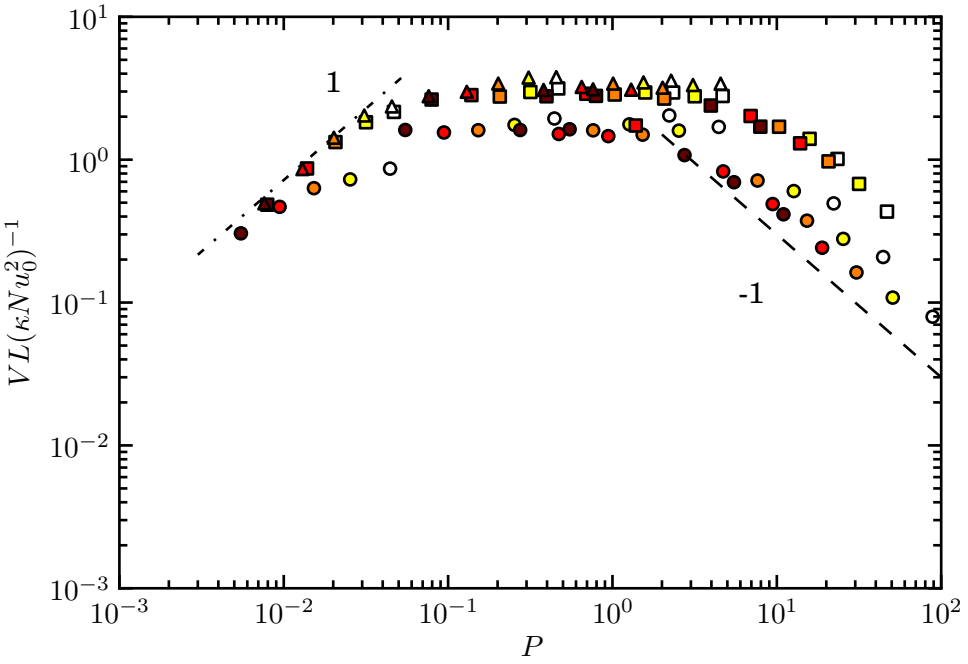


Figure 2.7: The azimuthal velocity scale, scaled by its theoretical maximum according to Read (1986), as a function of P. The dashed-dotted line has a gradient of 1 and thus it is clear that the azimuthal velocity scale increases approximately linearly with P at low P. The dashed line has a gradient of -1 showing that for $P > 1$ the velocity scale tends to the thermal wind scale. Symbols have the same meaning as in Fig. 2.3.

the transitions between regimes on the aspect ratio is less marked here than in the case of the Péclet number.

2.4 Choice of non-dimensional parameter

Throughout this chapter the boundary layer ratio, P, has been used as the independent parameter for identifying regimes and transitions in the system's behaviour. However, it has been noted that this parameter does not provide a unique prediction for any of the diagnostics considered and some ambiguity remains, particularly in relation to the aspect ratio. If the same parameters are considered as a function of thermal Rossby number the predictive power appears to be better, as shown in figure 2.8 where the data collapses onto a single line. The thermal Rossby number is the ratio of the inertial forces to the Coriolis force and thus is representative of the control of global force balance on the flow. Figure 2.8 shows that the transition from approximately constant to decreasing Péclet number occurs

at the same value of Ro_{th} for all parameters but this value is closer to $Ro_{th} = 0.1$ than $Ro_{th} = 1$, the point where the Coriolis force begins to dominate over inertial forces.

This is in contrast to what was found by King et al. (2009) and King et al. (2012) who suggested that, for rotating Rayleigh-Bénard convection, boundary layer control was more important than the global force balance in defining different flow regimes. The boundary layer ratio, P, has also been used to successfully diagnose regimes in previous studies using the classical annulus (Read et al., 2015). One possible reason for the reduced importance of boundary layer control in the current system is the diminished size of the heat sources and sinks. As they do not span the domain width it may be that the thermal boundary layer plays a lesser role in determining the dynamics of the entire system here. Furthermore, in both the classical annulus and Rayleigh-Bénard convection there is a single lengthscale which defines the separation between the heat source and sink. For our experiment, given the horizontal and vertical displacement of the heat source and sink, it seems likely that both the horizontal and vertical length scales are important but this is not encompassed by the definition of P used here. Based on these observations we use Ro_{th} as the control parameter for the analysis of the three dimensional simulations.

2.5 Discussion

Within this chapter we have explored and identified a number of distinct axisymmetric circulation regimes in the novel experimental configuration which combines statically unstable convection with large-scale overturning. The resulting flows include cases, at moderate rotation rates, where a stably stratified baroclinic zone, with sloping isopycnals and isotherms, is obtained between two convectively unstable regions adjacent to the laterally displaced heat source and sink. This flow structure was verified by the initial experimental results of Scolan and Read (2017). This flow may be thought of as an analogue to the Earth's atmosphere where vigorous convection takes place in the tropics, and to some extent in the polar regions, and the mid-latitude atmosphere is baroclinic.

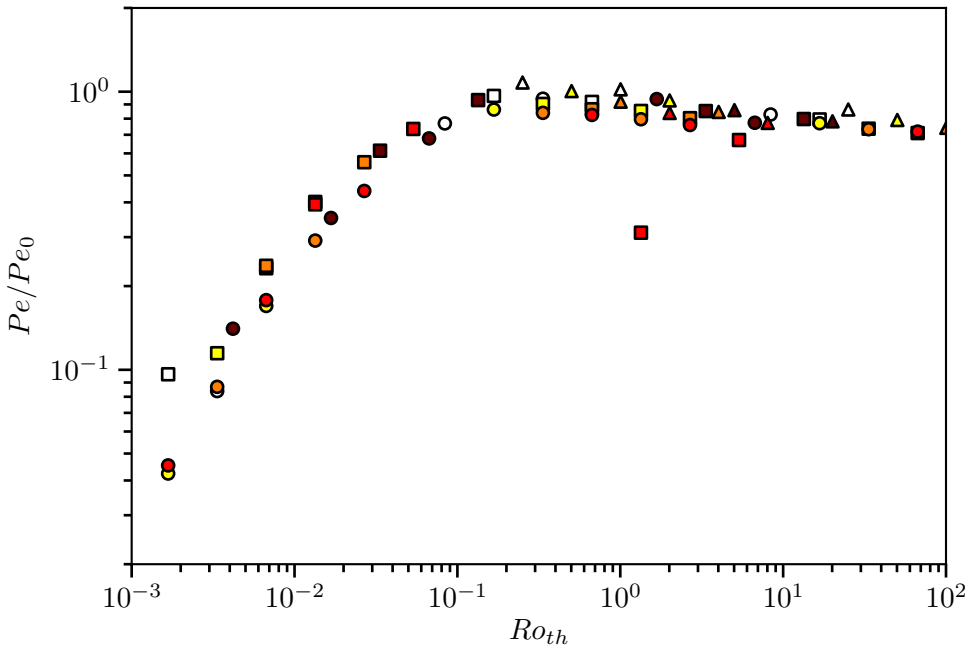


Figure 2.8: The normalised Péclet number $PePe_0^{-1}$ plotted against Ro_{th}. The symbols are the same as in Fig. 2.3.

The regimes identified herein are comparable to regimes (iii) - (v) of Hignett et al. (1981) and Read (1986) and Read et al. (2015). We found that many of the new system's properties scale with the boundary layer parameter in the same way as the properties of the classical annulus. These scalings may be derived by non-dimensionalising the fluid equations in two dimensions. For small values of P the gradient of the isotherms in the fluid is approximately constant with rotation rate but for $P \gtrsim 1$ the gradient scales as $P^{3/2}$. Heat transfer, characterised by the Péclet number, is also approximately constant at low P but decreases as $P^{-3/2}$ as P increases further. The change in scaling as P increases suggests that vigorous baroclinic instability is likely to occur for $P \gtrsim 1$ in the three dimensional system, as is the case in the classical annulus.

We also considered the system in comparison to the archetypal systems of Rayleigh-Bénard and horizontal convection. We found that heat transfer in the non-rotating system scales similarly with Rayleigh number to heat transfer in Rayleigh-Bénard convection although there is a dependence on the aspect ratio of

the domain in our system. This dependence is not fully understood and how the heat transfer varies with aspect ratio remains an open question. It seems some progress may be made by considering the rotating system as a function of thermal Rossby number rather than the boundary layer parameter. In previous work the boundary layer parameter was found to be the most useful control parameter but we found benefits to using the thermal Rossby number, perhaps because the thermal boundary layers do not span the whole domain in our system. Overall, despite many similarities in the scaling of the different parameters, the new system does not seem to behave exactly as any of the classical annulus, Rayleigh-Bénard and horizontal convection.

We now have a means of defining the background flow in the absence of baroclinic instability and thus a base state for comparison with the three dimensional simulations presented in later chapters. These comparisons will help to elucidate the effect of the baroclinic eddies on the flow in three dimensions. Furthermore, the sets of two dimensional simulations, at relatively high resolution hint at the form of the flow which might be expected in three dimensions and thus provide an initial sanity check for developing the three dimensional model.

Old endgame lost of old, play and lose and have done with losing.

— Samuel Beckett, *Endgame*

3 Adapting ENDGame

To progress further in our understanding of the dynamics in the annulus experiment, and hopefully in planetary atmospheres by extension, we improve on the two dimensional model of the previous chapter by developing a three dimensional model. As discussed in Chapter 1 the three dimensional model was adapted from the Met Office Unified Model (UM) with the aim of producing a hierarchy of models from annulus to planetary atmosphere using the same code base and to enable rigorous testing of the model against data from the lab.

3.1 ENDGame and the UM

The part of the UM required for modelling the annulus is the dynamical core, ENDGame (Even Newer Dynamics for General atmospheric modelling of the environment) (Wood et al., 2014). The dynamical core is the part of the model which discretises and solves the equations of fluid motion. ENDGame is a time semi-implicit, finite difference code with a semi-Lagrangian (SL) advection scheme. The equations solved in the original version of the model are the fluid equations

of motion for the atmosphere of a spherical, rotating planet given by

$$\frac{D\mathbf{u}}{Dt} + 2\boldsymbol{\Omega} \times \mathbf{u} = -c_p\theta_v\nabla\Pi + \mathbf{g} + \mathbf{S}^{\mathbf{u}}, \tag{3.1}$$

$$\frac{D\theta_v}{Dt} = S^{\theta_v}, \tag{3.2}$$

$$\frac{D\rho}{Dt} + \rho\nabla.\mathbf{u} = \mathbf{0}, \tag{3.3}$$

$$\rho = \left(\frac{p_0}{R}\right)\frac{\Pi^{\frac{1-\kappa}{\kappa}}}{\theta_v} \tag{3.4}$$

where it is assumed that the working fluid is dry air. ENDGame allows for the simulation of moist air or mixtures of aerosols but for modelling the annulus these are not needed. $\mathbf{u} = (u, v, w)$ is the fluid velocity, Ω is the angular velocity of the rotation of the planet, ρ is the air density, R is the gas constant, and c_p is the specific heat capacity at constant pressure. $\kappa = R/c_p$ and $\frac{D}{Dt} = \frac{\partial}{\partial t} + \mathbf{u}.\nabla$ is the standard Lagrangian derivative. θ_v is the potential temperature and $\Pi = (p/p_0)^\kappa$ is the Exner function where p_0 is a reference pressure. $\mathbf{S}^{\mathbf{u}}$ and S^{θ_v} are source/sink terms for momentum and heat respectively and the form of these terms can be set according to the application of the model.

$\mathbf{g}$ is the apparent gravity vector. This is calculated as the sum of the gravitational acceleration and the centrifugal acceleration. Hence, this vector is not parallel to the radial unit vector in spherical coordinates as would be expected for a purely gravitational force due to a spherical planet. Instead, it is perpendicular to surfaces of constant apparent geopotential - oblate spheroids in the case of the Earth. In general, in meteorological applications, due to the centrifugal force having a much smaller magnitude than the gravitational force close to the surface of the Earth, the surfaces of constant apparent geopotential are approximated as spheres to simplify the geometry. Alternative geometries such as similar oblate spheroids have been proposed (White et al., 2008) and ENDGame is written in such a way as to allow one to switch to such a co-ordinate system with relative ease (Wood et al., 2014).

3.1.1 The semi-Lagrangian advection scheme

In an Eulerian framework the fluid passes by a stationary observer who can measure its properties whereas in a Lagrangian scheme the observer follows a fluid parcel

through time and space and can hence map its path and characteristics. There are different advantages and problems with using each of these methods in a numerical model (Staniforth and Côté, 1991; Cushman-Roisin and Beckers, 2011). An Eulerian approach is more easily a victim of numerical instabilities if the timestep is not sufficiently small. However, whilst an Eulerian approach will have a grid which is fixed in time and evenly spaced across the domain to give sufficient resolution everywhere, a Lagrangian grid is time dependent with grid point density set by the number of fluid parcels in a particular place and hence the resolution is subject to the divergence and convergence of the flow. A semi-Lagrangian approach avoids this problem by changing the set of fluid parcels which are followed on each timestep. A set of fluid parcels are chosen such that they arrive at the model gridpoints at a given timestep, thus the gridpoints are termed the 'arrival points'. At an earlier time these fluid parcels were located at their 'departure points' and these points are found by integrating backwards along the parcel trajectory. In general the departure point will not lie on a grid point and thus, to find the value of a prognostic variable at the departure point, the field is interpolated from the surrounding gridpoints.

The interpolation required to find the prognostic fields at the departure points can introduce problems into the model. Primarily, it causes numerical diffusion. This may be limited by using higher order interpolation schemes (linear interpolation being the most diffusive) or higher resolution. However, using higher order interpolation can introduce a further problem. Interpolation using non-linear functions can introduce new, unphysical minima and maxima into the flow (e.g. Steffen (1990)). The property of conserving the flow shape including its minima and maxima is known as monotonicity. If a non-linear interpolation scheme is used to reduce the numerical diffusion and increase the accuracy of the interpolation it may also be necessary to use a monotonicity filter to limit the effect of under and over shoots, especially in regions where there are strong gradients in the fields.

Following the calculation of the fields at the departure points via interpolation the values of the fields at the arrival points must be found for the next timestep. This is achieved using an iterative method to solve a linear Helmholtz equation

derived from the spatially discretised fluid equations including source terms for heat, mass and momentum (Wood et al., 2014). Modifications to this part of the numerics were not necessary for modelling the annulus.

3.1.2 The model grid

ENDGame is a finite difference model and the equations are discretised on a staggered Arakawa-C grid (Arakawa and Lamb, 1977) in the horizontal and a staggered Charney-Phillips grid (Charney and Phillips, 1953) in the vertical. I,J,K are the maximum number of grid points in the longitude, latitude and height directions respectively. The vertical co-ordinate is height based and terrain following.

Halo points

A schematic slice of the staggered rz grid is shown in figure 3.1 with j being the index in the radial direction and k the index in the vertical direction. In general, due to the computational expense of the model, it is decomposed and run on multiple processors. This decomposition is only done in the horizontal direction. To enable communication between different processors, each decomposed part of the domain is surrounded by halo points. If figure 3.1 is considered as a part of the grid on a single processor these halo points are shown in fainter colours than the main grid. In the case of a limited area model (LAM), where at least one of the horizontal directions is not periodic, the processors at the edge of the domain do not have a neighbouring processor to swap information with. We refer to the halos outside the domain as external halos and if figure 3.1 is considered to be the entire domain these are shown by the fainter colours. External halos are, by default, filled with the same value of each field, F, as the outermost point inside the domain (i.e. $F_{j=-1/2,k=1} = F_{j=1/2,k=1}$ in figure 3.1). This has the effect of enforcing the gradient of every field normal to the boundary to zero. The exception is for the velocity perpendicular to the boundary which is set to zero to prevent mass loss from the domain. The boundary conditions at the top and bottom are set explicitly in calculations throughout the code as no halos exist at these boundaries.

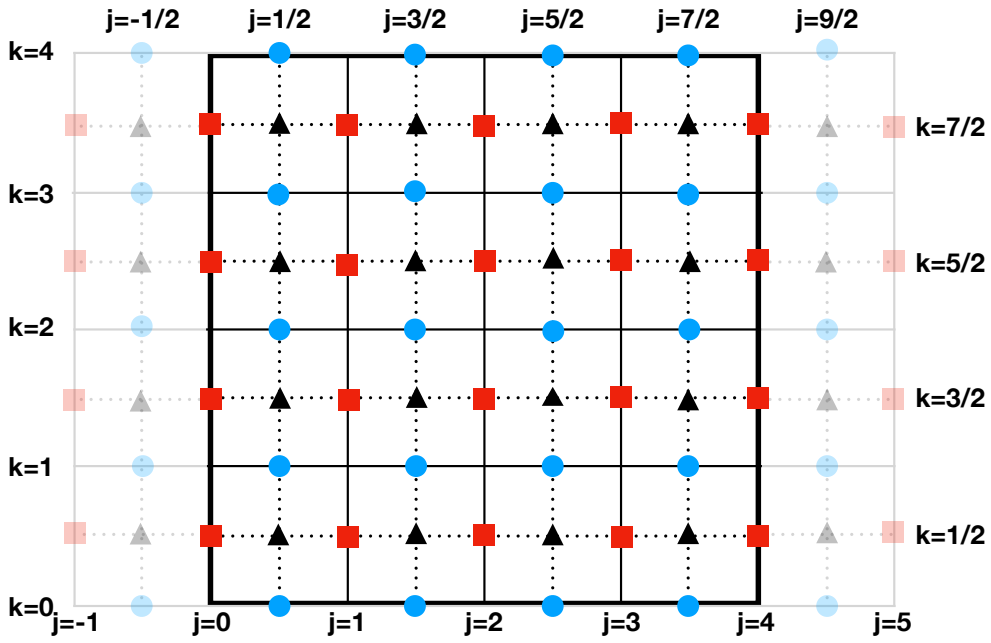


Figure 3.1: A schematic of the uniform model grid in the rz plane. It may be viewed as an entire domain with J=K=5 in both directions and only external halos shown. Alternatively it may be thought of as a part of the domain on a single processor with halos for communication with other processors shown and K=5 still because there is no decomposition in the vertical direction. The domain is shown in solid colours and one halo point for each type of gridpoint is shown in fainter colours. Halo points are those points where $j < 0$ or $j > 4$. T, θ_v and w are held at the points marked by blue circles. v is held at the points marked by red squares and all other fields are held at the points shown by black triangles.

The vertical grid

The UM uses a modified, terrain following vertical co-ordinate, η, for modelling the atmosphere above a planetary surface with orography (Wood et al., 2014). The terrain following vertical coordinate is not orthogonal to the horizontal coordinate surfaces (the r, θ planes in our cylindrical model) but the definitions of the velocity components, $\mathbf{u} = (u, v, w)$ remain the same and a new velocity $\dot{\eta} = \partial_t \eta$ is introduced. η surfaces flatten with altitude and are parallel to constant z surfaces above a specified height as shown in figure 3.2 where the orography is similar to that found

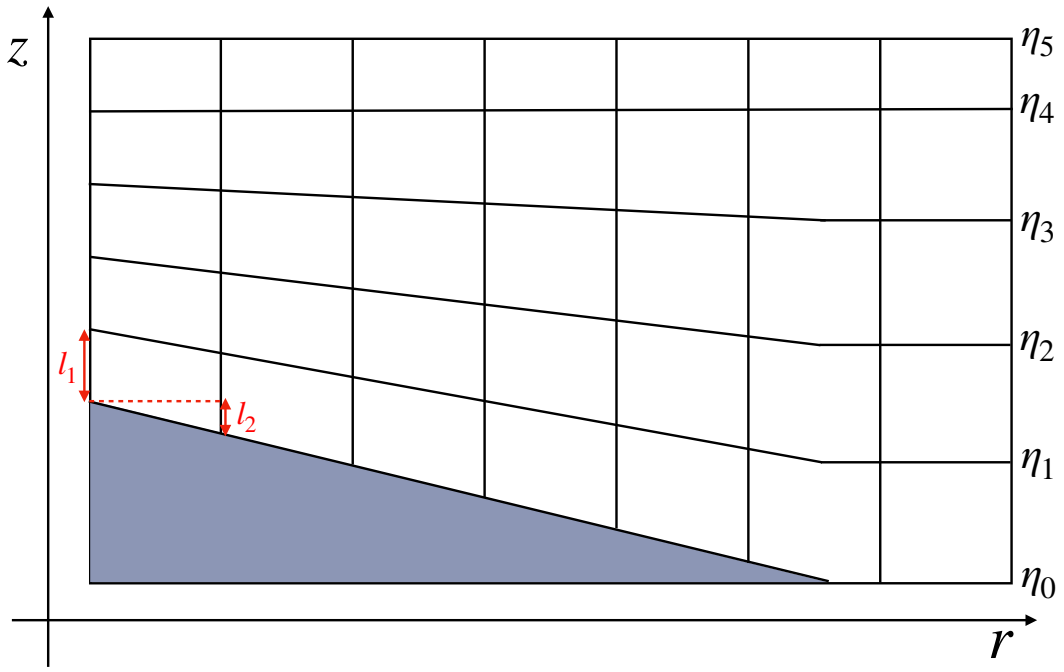


Figure 3.2: Schematic of the terrain following vertical grid. In the model the grid is staggered on full levels and half levels but here only full levels are shown for clarity. The η levels flatten as altitude increases. If the change in height of the cell from one side to the other, l_2, is greater than the depth of the cell, l_1, the simulation is likely to be unstable.

in the annulus experiment when a sloping base is used. The top level of the model is always flat. To maintain stability the orography cannot be too steep in the presence of high vertical resolution as the change in height across a grid cell (l_2 in figure 3.2) cannot exceed the change in z across the same grid cell (l_1 in figure 3.2). Figure 3.2 shows a uniform vertical grid but in general for weather forecasting the lower levels of the troposphere need to be modelled at the highest resolution. Thus the UM would generally be run with a grid that stretches such that the finest vertical resolution is found at the lowest model levels and then coarsens with altitude.

3.2 Changes to the model

The following sections outline the changes which have been made to ENDGame to allow simulation of the annulus experiment.

3.2.1 Cylindrical geometry

While a planetary atmosphere is spherical and generally requires maximum length scales of hundreds to thousands of kilometres, the annulus is cylindrical with maximum length scales of less than a metre and hence the model geometry must be modified. The geometry of the ENDGame domain is specified in terms of the metric factors of a curvilinear co-ordinate system. This provides a flexible modelling framework for a range of different scenarios. For example, the UM is traditionally run with a spherical geometry but higher accuracy may be obtained by using oblate spheroids to better represent the latitudinal variation of $\mathbf{g}$ (White et al., 2008). Furthermore, a shallow spherical shell geometry is used in some idealised situations (although the shallow co-ordinate system is not strictly a Euclidean sub-manifold) (Jablonowski and Williamson, 2006; Staniforth and Wood, 2013; Mayne et al., 2014) and a Cartesian geometry is sometimes used with limited area or channel models (Ullrich and Jablonowski, 2012).

Curvilinear co-ordinates are co-ordinate systems in three dimensions, (ξ_1, ξ_2, ξ_3), for Euclidean space in which the co-ordinate axes may be curved. For the purpose of modelling the annulus, a cylindrical curvilinear basis is most natural. For ease of comparison with the existing spherical geometry in the UM the vertical cylindrical co-ordinate, z, replaces the spherical radial co-ordinate, r_s, so that the gravitational acceleration vector remains aligned with the third co-ordinate axis. The cylindrical radial co-ordinate, r, replaces the latitude co-ordinate, ϕ, on the sphere and the longitude co-ordinate on the sphere, λ, remains angular but in the opposite sense, θ, to preserve a right handed co-ordinate system. The new cylindrical co-ordinate system is shown in comparison to the spherical system in figure 3.3.

For the cylindrical basis used here the co-ordinates are

$$\xi_1 = \theta \qquad \xi_2 = r \qquad \xi_3 = z. \tag{3.5}$$

They are related to a Cartesian system, (x, y, z) by

$$x = r\cos\theta \qquad y = -r\sin\theta \qquad z = z \tag{3.6}$$

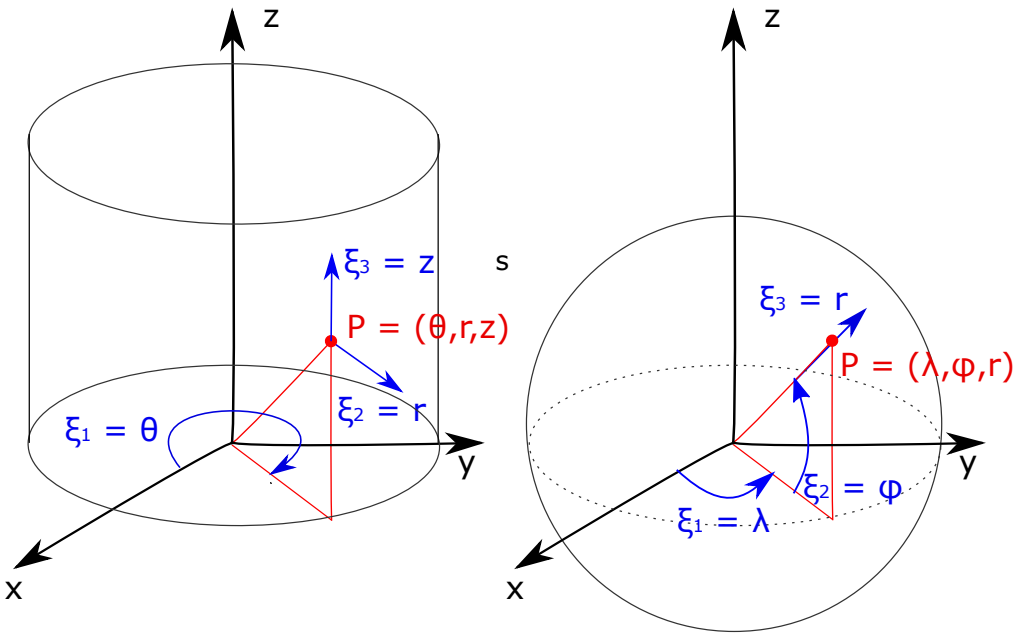


Figure 3.3: A comparison of the cylindrical co-ordinate system used for annulus modelling (left hand side) and the spherical co-ordinate system (right hand side) usually used for planetary modelling in the UM.

and thus the metric factors are

$$h_\theta = r \qquad h_r = 1 \qquad h_z = 1. \tag{3.7}$$

Following Wood et al. (2014) these expressions may be used to calculate expressions for the gradient, divergence and curl in cylindrical co-ordinates to be used in the fluid equations.

It should be noted that neither the cylindrical nor the spherical basis is global, the direction of the basis vectors changes in space. This has important consequences for the SL scheme as the local bases of the departure points and arrival points will be based on different unit vectors. The UM employs a rotation matrix method to express the components of vectors at the departure and arrival points in the correct form (Staniforth et al., 2010; Wood et al., 2010).

The final implication of using cylindrical geometry is that, contrary to the usual spherical formulation where the centrifugal force is combined with the gravitational acceleration into an apparent gravity term, the centrifugal force is included in its own right in the cylindrical case. On Earth, where the surface is deformed by

rotation into an oblate spheroid, the surface is defined by a co-ordinate surface if the horizontal co-ordinate surfaces are defined as being perpendicular to the apparent gravity (White et al., 2008). In cylindrical geometry, the centrifugal force deforms the free fluid surface into a parabola. However, the rigid base of the annulus is unaffected by this force and remains on a surface of constant z (if it is a flat surface). Therefore, in the cylindrical geometry it is simplest to include the centrifugal force separately from the gravity so that the pure gravitational acceleration vector remains aligned with z and the base remains perpendicular to z. The centrifugal force is given by the term $\mathbf{\Omega} \times \mathbf{\Omega} \times \mathbf{r} = (0, -\Omega^2 r, 0)$ which is added into the momentum equation (Equation (3.1)).

Testing the cylindrical geometry

After the cylindrical geometry was introduced it was tested to ensure that it was working as expected. The tests were run in a cylindrical domain on Earth-like lengthscales. Three stages of testing were carried out with increasing complexity. All were reproduced on at least two different processor decompositions to ensure the results were not affected by the model parallelisation. The three testing stages were:

- The model was initialised in solid body rotation with the expectation that the flow would not change in time. The rms velocity increased over time but remained well below the solver tolerance, 10^{-4}, over 100,000 timesteps for a range of resolutions.

- A uniform horizontal shear was introduced to the initial velocity profile to destabilise the flow. A barotropic flow may become unstable where there is a horizontal shear and instabilities are able to extract kinetic energy from the background state (Vallis, 2006). A necessary (but insufficient) criterion for barotropic instability is that the radial second derivative of the azimuthal velocity vanishes at some point within the domain (Cushman-Roisin and Beckers, 2011). Initialising the fluid with a velocity that was a sigmoidal function of radius, but independent of height, fulfilled this condition. In figure

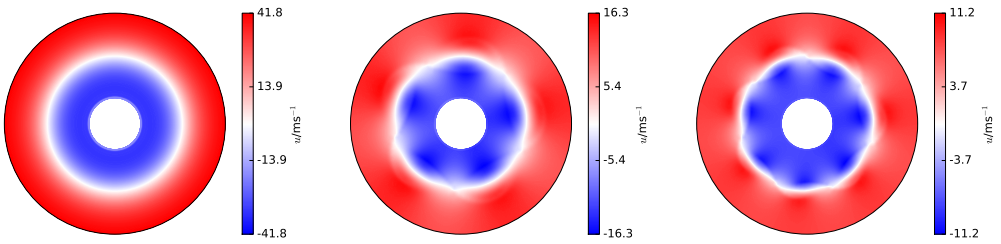


Figure 3.4: Snapshots of the azimuthal velocity fields after 20days at mid-height for the barotropic instability test in cylindrical geometry. The width of the shear zone in the initial velocity field decreases from left to right and hence the wavenumber of the resultant flow increases.

3.4 the width of the shear zone decreases from left to right. From left to right the shear zone width is proportional to 1, 1/4 and 1/6 and the wavenumber is proportional to 1,5,7. In an idealised system the wavelength of the disturbance is proportional to the width of the shear zone (Vallis, 2006). The wavenumber of the disturbance increases as the width of the shear zone decreases.

- A modified version of the Jablonowski baroclinic wave test (Jablonowski and Williamson, 2006) was carried out for cylindrical geometry. This was compared qualitatively to the results of carrying out the test in a spherical channel geometry, defined as a limited band of latitudes on the sphere. Qualitatively similar baroclinic waves were produced in both spherical and cylindrical geometry which suggests that the model responds as expected to analytically derived initial conditions for a cylinder. This test was used for a qualitative comparison only and comparable baroclinic waves for cylindrical and spherical geometry are shown in figure 3.5.

Further details of the latter two tests may be found in appendix B.

Spatial and temporal scales

It was also necessary to change the scale of the model. For spatial scales this is achieved trivially, by setting the grid spacing and initial parameters to values on the order of centimetres rather than kilometres. For temporal scales ENDGame is hard wired to prohibit timesteps of less than one second (or a non integer number of

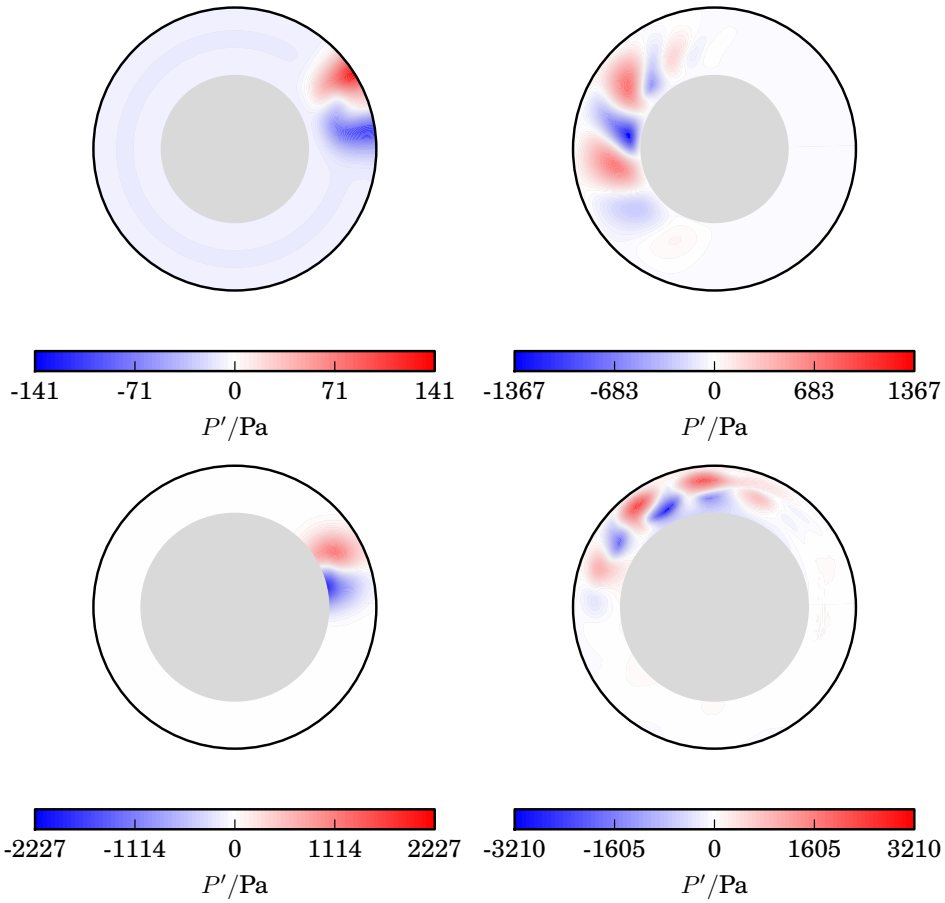


Figure 3.5: The pressure anomaly, $P' = (P - P_s)$Pa where P_s is the surface pressure, for the Jablonowski test in a spherical channel geometry (top) and a cylindrical geometry (bottom). The spherical channel The left hand column shows the field after 1 hour of simulation time and the right hand column shows the field after 10 days. A stereographic projection has been used to plot the spherical fields.

seconds) so that rounding errors do not become significant when the model is used for long climate integrations. To circumnavigate this, and allow the sub-second timesteps required for annulus modelling, a scaling factor is introduced to change the units of time used by the model.

3.2.2 Grid stretching

Due to the potential importance of boundary layers on the top, bottom and sidewalls of the annulus it is desirable to have higher resolution close to the boundaries. When modelling a planetary atmosphere it would usually only be the bottom boundary where higher resolution is required. Hence a new grid stretching function was added

to the code to allow for finer resolution at the top and bottom and also on the sidewalls. The function was chosen to be the same as that used by the MORALS model of chapter 2. The vertical grid is stretched via a mapping function such that a specified number of points lies within the thinner of the Ekman layer or the thermal boundary layer and the stretching is symmetrical about the centre of the domain (Farnell and Plumb, 1975). In the horizontal direction stretching is set so that a specified number of points lies within the Stewartson layer on the vertical boundary and the same function is used. Horizontal stretching would not generally be used in atmospheric modelling with the exception of using variable resolution to link a high resolution LAM with the coarser resolution model it is nested within (Tang et al., 2013).

3.2.3 Boundary conditions

The spherical geometry used in global planetary atmosphere modelling has periodic boundaries in both horizontal directions as the spherical surface is closed. Boundary conditions are required at the top and bottom of the atmosphere and for a system such as the Earth with complex interactions between land, flora, fauna, ocean and space these are far from trivial. In an operational forecasting model such as the UM it is also useful to be able to run limited area models over a smaller region of the globe. For realistic modelling of the Earth the lateral boundary conditions required by LAMs are taken from global models.

Kinetic boundary conditions

In the case of the annulus, the boundary conditions are specified analytically. The top of the domain, away from the cold plate, is modelled as a stress-free, rigid, impermeable boundary that approximates a free surface. Including a free surface that is able to deform would have been very complex within the existing model framework. Hence, the normal gradients of the tangential velocities are zero at the surface,

$$\left.\frac{\partial u}{\partial z}\right|_{z=d} = \left.\frac{\partial v}{\partial z}\right|_{z=d} = 0, \tag{3.8}$$

and $w = 0$ to avoid mass loss from the domain. The sides and bottom of the domain as well as the cold plate are no slip surfaces where $u = v = w = 0$. In the azimuthal direction the boundary condition is periodic as in the global model.

The default setting for an idealised LAM in ENDGame is to set the fields at any non-periodic boundaries to have zero gradient in the direction normal to the boundary. This is done by treating the halos which are used for data exchange between processors as ghost points as discussed in section 3.1.2. The value of each field at the first exterior ghost point is set equal to the value on the first interior grid points so there is no gradient across the boundary. For no slip side walls in the cylinder it is necessary to set the velocities tangential to the walls, u and w, to zero. The velocity perpendicular to the wall is already zero by default in the model to prevent mass loss from the domain. Due to the staggered horizontal grid u and w are not saved on the boundary grid points. Therefore, as above, the external halos are used as ghost points. The values of the azimuthal and vertical velocities outside the boundary are set to the negative of the fields on the first points inside the domain (e.g. $u_{j=-1/2} = -u_{j=1/2}$ in figure 3.1. This enables derivatives to be calculated on the boundary itself and ensures the value of the velocity interpolated onto the boundary is zero. To ensure these new boundary conditions are compatible with the semi-Lagrangian scheme, points on the no slip boundaries have their departure point set equal to their arrival point. Therefore, fluid parcels located on the boundaries never move from their initial positions and interact with the interior flow via diffusion only. The value of zero velocity at the boundary will also affect the interpolation of the fields onto any departure points which lie close to the boundary. For the top and bottom boundaries there are no halos to act as ghost points so the boundary conditions must be set in each calculation throughout the code.

Testing the kinetic boundary conditions

To test the no slip boundary conditions a series of spin up and down simulations were carried out (Greenspan and Howard, 1963; Benton and Clark, 1974; Duck and Foster, 2001; Park and Hyun, 2008). The fluid was initialised in solid body

rotation with some rotation rate, $\Omega_i = \Omega + \Delta\Omega$ where $\Delta\Omega$ may be positive or negative. At $t = 0$ the annulus is impulsively accelerated or decelerated to speed Ω and the fluid velocity subsequently decays as it readjusts to solid body rotation at the new rotation rate. For low Rossby number, $Ro = |\Delta\Omega/\Omega| \ll 1$, this process is expected to be linear (Park and Hyun, 2008) and thus the relative velocity of the fluid is expected to decay to zero exponentially on a timescale comparable with the Ekman spin down time given by

$$\tau = \Omega^{-1} Ek^{-1/2}. \tag{3.9}$$

This result was first derived for fluid contained between two infinite, horizontal plates (Greenspan and Howard, 1963). In the presence of vertical sidewalls a similar bulk timescale would be expected but the form of the flow at a given time would be expected to show more radial dependence (Weidman, 1976).

Hence, the decay time of the azimuthal velocity from the simulation data may be computed and compared with the Ekman spin down time. For linear spin down the azimuthal velocity field over time may be modelled as

$$\overline{u}(t) = \overline{u_0} \exp^{-t/\tau} \tag{3.10}$$

where $\overline{u}$ is the volume averaged azimuthal velocity, $\overline{u_0}$ is the value of $\overline{u}$ at $t = 0$ (Greenspan and Howard, 1963). Figure 3.6 shows the decay of the volume averaged azimuthal velocity for a simulation with $\Omega = 0.5\text{rads}^{-1}$ and $\Delta\Omega = -0.01\text{rads}^{-1}$. For the experiment with a no slip base and free slip sidewalls the decay is observed to closely follow the theoretical prediction given by equation 3.10. Using a linear fit to find the decay constant from the logarithm of the velocity gives $\tau = 147s$. This is close to the predicted value of 156s. For various rotation rates the time constant for the decay was found to be systematically lower in the simulation data than predicted by the theory, but still in good agreement. The systematic error may be due to numerical diffusion.

Figure 3.6 also shows the same simulation but with no slip sidewalls in addition to the no slip base. Here, the decay constant is observed to be smaller at $\tau = 107$s.

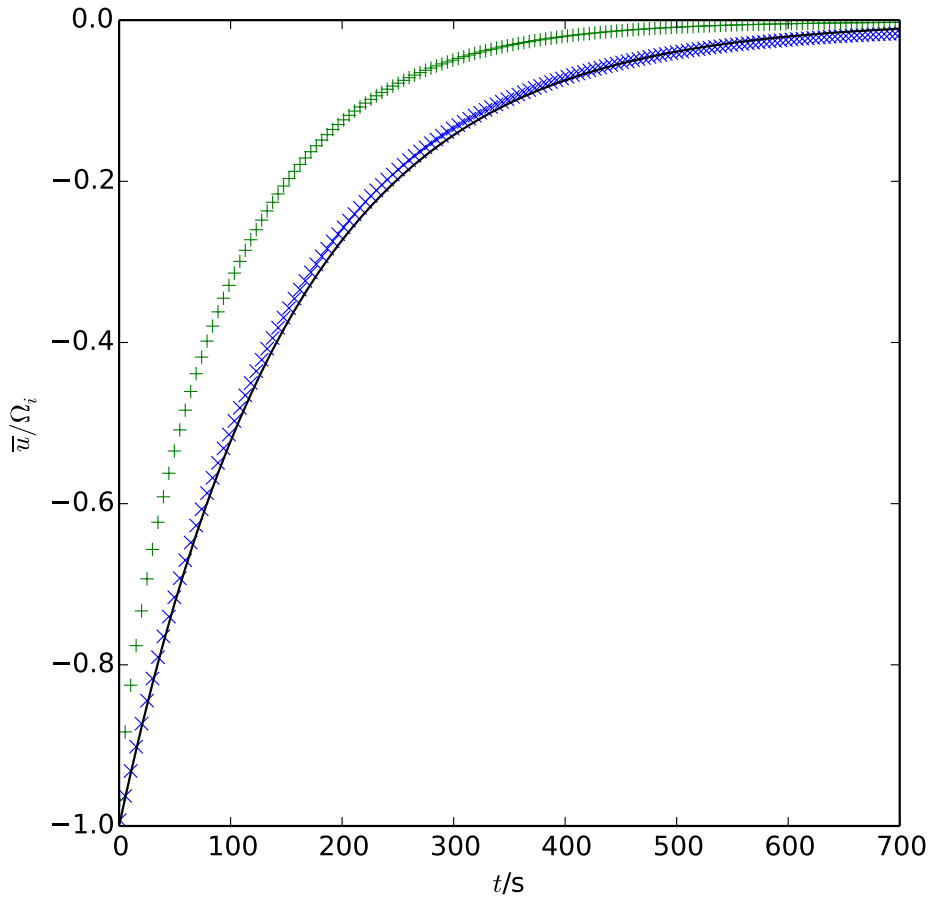


Figure 3.6: A time series of the volume averaged azimuthal velocity, $\overline{u}$, normalised by the initial rotation rate, Ω_i, for a spin up experiment. The fluid spins up from Ω_i=0.49rads^{-1} to Ω=0.5rads^{-1} which is a small enough change in velocity that the flow is expected to remain linear. The blue crosses ($\times$) represent a simulation with no slip bottom and free slip walls whilst the green plus signs ($+$) represent an experiment with the same parameters but no slip walls as well as a no slip bottom. The solid black line is a theoretical prediction for the decay given by equation 3.9.

This is possibly due to centrifugal instability induced by the no slip sidewalls (Weidman, 1976; Neitzel and Davis, 1981). Weidman (1976) found in experiments that, where spin down was initialised by a rapid deceleration such as the impulsive one used here, centrifugal instabilities would occur soon after spin down commenced leading to the formation of Taylor-Görtler vortices along the curved sidewall (Warn-Varnas et al., 1978; Neitzel and Davis, 1981; Kim and Kyun Choi, 2006). These vortices extract energy from the mean flow and increase momentum mixing, thus

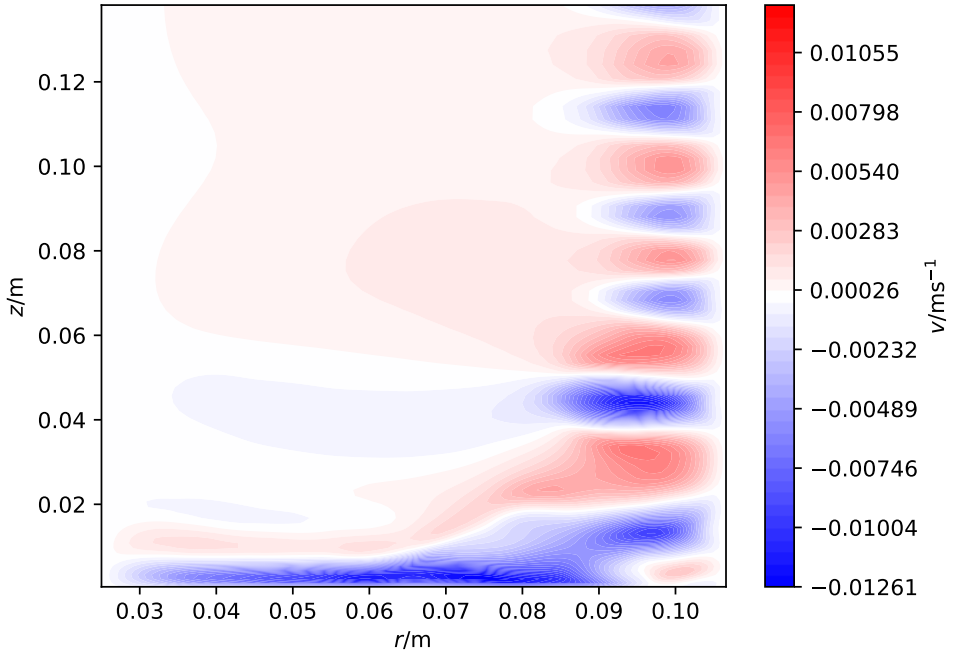


Figure 3.7: Snapshot of the radial velocity field, v ms^{-1}, in a simulation which is allowed to spin down to rest from an initial velocity of Ω_i=0.5rads^{-1}. The snapshot is shown 20s after rotation is halted. Taylor-Görtler vortices are observed on the outer wall only as the velocity on the inner wall is lower and hence the critical Reynold's number for instability is not surpassed. The vortices increase mixing and thus reduce the spin down time of the fluid.

reducing the spin down time. Figure 3.7 shows the existence of these vortices along the sidewall for a simulation with $\Omega_i = 0.5$rads^{-1} where the fluid is allowed to spin down to rest. For this simulation $Ro = 1$ so the flow is expected to be highly non-linear. For the small Rossby number simulation shown in figure 3.6 these strong vortices are not observed but the sidewalls may still induce some non-linear mixing.

Thermal boundary conditions

The heat sink used in the experiment is set to a constant temperature and thus requires an isothermal boundary condition in the model. The heat source in the experiment is set to supply a constant heat flux to the fluid which equates to a boundary condition of $\partial_z \theta_v = F_{in}$ where F_{in} is the constant applied heat flux. [1]

[1]Throughout the work on annulus modelling using ENDGame potential temperature will be used as the operational thermal variable but it should be noted that this is effectively equal to

The relation between applied flux and resulting temperature on the bottom surface is estimated using a one sided derivative. Elsewhere the boundaries are set to be thermally insulating which is the default thermal boundary condition in ENDGame.

3.2.4 Viscosity and thermal diffusion

In theory, it is possible to represent molecular viscosity and thermal diffusion explicitly in the annulus simulations but in practice it is too computationally expensive to resolve the Kolmogorov scale. As shown in section 2.2 the Kolmogorov scale for the annulus flows is on the order of 10^{-4}m. However, following previous simulations of annulus experiments we assume that the dissipation is adequately resolved at the available resolution which is on the order of millimetres. The molecular viscosity is represented by a Laplacian term added to the momentum equation (equation (3.1)). It is given by

$$\nu\nabla^2\mathbf{u} = \nu\nabla(\nabla\cdot\mathbf{u}) - \nu\nabla\times(\nabla\times\mathbf{u}) \tag{3.11}$$

where ν is the coefficient of viscosity which is assumed to be a constant and equal in the horizontal and vertical directions. To match the experiment we take $\nu = 1.62\times10^{-6}\mathrm{m}^2\ \mathrm{s}^{-1}$ throughout this work. The Laplacian is calculated using centred differences, exploiting the staggered grid. The exception is at the top and bottom boundaries where a one sided difference is used. Ghost points exist outside the lateral boundaries so a central difference method may still be employed there.

Thermal diffusion is implemented in a similar way to the viscosity, with the addition of a Laplacian term of the form

$$\kappa\nabla^2\theta_v = \kappa\nabla\cdot(\nabla\theta_v) = -\nabla\cdot\mathbf{F} \tag{3.12}$$

to the thermodynamic equation (equation 3.2). Here, $\kappa = 1.29\times10^{-7}\mathrm{m}^2\mathrm{s}^{-1}$ is the thermal diffusivity of the laboratory fluid which is again constant across all simulations in this work. $\mathbf{F} = -\kappa\nabla\theta_v$ is the conductive thermal flux.

temperature given the very small change in background pressure over the height of the annulus.

3.2.5 The equation of state

The working fluid used in the experiment is either water or 17% glycerol by volume in water (Scolan and Read, 2017). Conventionally these liquids are modelled as Boussinesq as in the MORALS model of Chapter 2. The default working fluid within the UM is air which is modelled using the ideal gas equation of state (equation (3.4)) and this is hard wired into the model such that modifying it would require significant modifications to the model architecture. From a dynamics perspective, the primary difference between an ideal gas and liquid water is their different volumetric thermal expansion coefficients, α_v. Thus, to simulate a water-like fluid within the ideal gas approximation, the mean temperature of the fluid is increased to the order of thousands of Kelvin so that the thermal expansion coefficient of the ideal gas is small.

A fluid may be approximated as incompressible if variations in density, $\delta\rho$, are small compared to the mean density, ρ_0, i.e. $\frac{\delta\rho}{\rho_0} \ll 1$ (Vallis, 2006). For an ideal gas in the annulus

$$\frac{\delta\rho}{\rho_0} \approx \frac{\delta T}{T} \tag{3.13}$$

where δT is the temperature variation and T is the mean temperature. For a gas at room temperature ($T \approx$300K) this gives a fractional density variation of about $(3 \times 10^{-3})\delta T$. However, for water, $\delta\rho/\rho \approx (3 \times 10^{-4})\delta T$. Thus, the mean temperature of the working fluid must be increased by a factor of 10 to around 3000K to simulate a fluid with a volumetric thermal expansion coefficient comparable to water. To maintain a density comparable to that of water within this approximation the specific gas constant, R, where $P = \rho RT$, is reduced commensurately.

3.2.6 Adding a beta effect

A sloping bottom is included in the annulus apparatus to emulate the beta effect. The similarity between a change in fluid depth in a barotropic fluid to a change in the Coriolis parameter with latitude may be shown by linearising the equation of conservation of potential vorticity

$$Q = \frac{\zeta + f}{d} \approx \frac{(\zeta + f)(1 - \delta)}{\overline{d}} \tag{3.14}$$

in an incompressible, inviscid fluid layer (Afanasyev and Wells, 2005). Here ζ is the relative vorticity, δ is a change in depth of the fluid layer and $\overline{d}$ is the mean depth. This linearisation assumes $\delta = d - \overline{d}$ and ζ/f are small. In a baroclinic fluid the effect is not exactly analogous to the β-effect because the sloping boundaries modify the zonally symmetric temperature field but Mason (1975) found only a small difference due to this effect. Thus, to define the beta effect in this system we use the same definition as for a barotropic flow following Bastin and Read (1999) where

$$\beta = \frac{2\Omega \tan \chi}{\overline{d}}. \tag{3.15}$$

$\overline{d}$ is the mean depth of the fluid. χ is the angle of elevation of the slope which is 15° in the experiment. The sloping cone only covers the insulating part of the base, the hot plate remains flat.

In the model the slope is implemented in the same way as orography in the full planetary atmosphere configuration. The height of the surface above $z =$ 0cm is given by the function

$$h = (r_{hot} - r) \tan \chi [1 - 0.5(1 + \tanh(100(r - r_{hot}) + 1))] \tag{3.16}$$

where $r = r_{hot}$ at the inner edge of the hot plate. This function is chosen as it smooths the discontinuity between the flat and sloping regions. This function is plotted in figure 3.8.

The presence of the sloping bottom presents some challenges to the model setup. Firstly, the depth of fluid close to the inner cylinder is approximately 2/3 of that close to the outer cylinder and thus the vertical resolution is significantly higher at small radii. Secondly, it has been recognised (e.g. Mahrer (1984) and references therein) that truncation errors in the pressure gradient term of the momentum equation can become significant in the presence of steep topography and fine resolution when a terrain following grid is used. Despite being most significant for the pressure gradient the error may also affect the horizontal gradients of other fields. Due to the grid stretching which provides fine resolution within the boundary layers these conditions are present in the simulations of the annulus. This meant

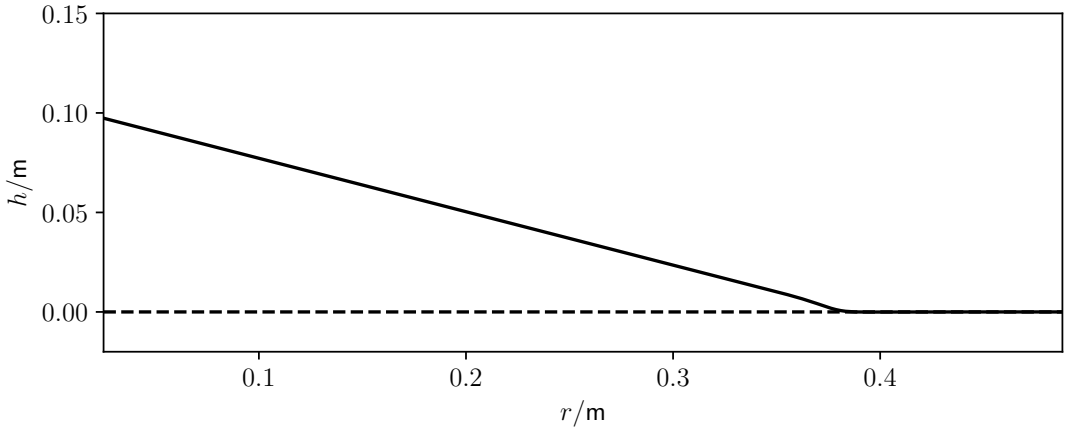


Figure 3.8: The function used to represent the sloping bottom used in the annulus. h is the height of the base above z=0m and r is the radial co-ordinate. The dashed line shows the topography in an experiment with a flat bottom.

that, given our 15° slope, the minimum fluid depth which can be used is around 25cm to keep the model numerically stable.

3.2.7 Parameterisation of non-ideal boundary conditions

In section 3.2.3 we prescribed all boundaries away from the heat source and sink to be thermally insulating. In reality the boundaries of the annulus are not perfect thermal insulators. In fact, Scolan and Read (2017) found that the total heat loss through the top surface via evaporation was of the same order of magnitude as the power input through the hot plate. Further heat is lost via conduction through the walls and base of the annulus and so, to achieve an accurate comparison between the experiment and the model, these effects must be taken into account.

Conduction through the sidewalls is modelled using a Newtonian heat flux condition, a method which has been used previously to simulate heat loss in classical annulus and rotating convection experiments (Walin, 1971; Rahm and Walin, 1980; Hyun, 1985; Min Hyun and Chun Hyun, 1987; Read et al., 2000). The heat flux applied at the sidewalls and the part of the base not covered by the hot plate is given by

$$\mathbf{n} \cdot \nabla\theta \mid_{fw} = s(\theta_e - \theta_{fw}) \tag{3.17}$$

where $\mathbf{n}$ is the unit vector normal to the boundary, the subscript fw denotes the fluid/wall interface and θ_e is the temperature of the environment outside the experiment i.e. in the lab.

$$s = \frac{\lambda_w}{\lambda_f d_w} \tag{3.18}$$

where λ_w and λ_f are the thermal conductivities of the wall and fluid respectively and d_w is the thickness of the annulus wall.

The heat flux due to evaporation is also parameterised. This is done by estimating the evaporative mass loss rate from the annulus and converting this to energy loss by multiplying by the latent heat of vaporisation. This energy loss is then imposed as a boundary condition on the upper boundary of the model. Following the simplest method of Shah (2012) the evaporative mass loss, E_0, in units of $\mathrm{kgm^{-2}hr^{-1}}$ is given by

$$E_0 = 0.00005(p_w - p_e) \tag{3.19}$$

where p_w is the saturation vapour pressure at the temperature of the fluid surface and p_e is the partial pressure of water vapour at the temperature and humidity of the external environment. The constant, 0.00005, is empirically derived and shown to fit well to observations of evaporation from still pools of water. We neglect the wind stress on the surface of the fluid as this is minimised in the experiment by surrounding the apparatus by a curtain. Shah (2012) also offers a second equation for the mass loss (equation 3 of that paper), however this one is slightly more complex in that the density of the air and fluid must be taken into account and within the parameter space used here the difference between the two formulae is negligible compared to the expected uncertainty in the lab measurements.

The saturation vapour pressure at the fluid surface is given by

$$p_w = p_{ref} \exp\left(\frac{L_v}{R_v}\left(\frac{1}{\theta_{ref}} - \frac{1}{\theta_v^*}\right)\right) \tag{3.20}$$

where subscript ref denotes reference values (taken to be at the boiling temperature of water), L_v is the latent heat of vaporisation of water and R_v is the gas constant

for water vapour (Andrews, 2000). Inputting the large mean temperatures used in the simulations into this equation will not yield sensible answers. Hence, the simulation temperatures, θ_v, are rescaled to be equivalent to lab temperatures using

$$\theta_v^* = T_{cold} + (\theta_v - \theta_{cold}) \tag{3.21}$$

where T_{cold} is the temperature of the cold plate in the lab, θ_{cold} is the temperature of the cold plate in the simulation and θ_v^* is the rescaled simulation temperature.

The partial pressure of water vapour in the environment, p_e, is calculated from the relative humidity of the lab, ϕ, which was measured as experiments took place using a hygrometer with an uncertainty of $\pm 4.5\%$. The humidity stayed approximately constant over time. We take

$$p_e = \phi p_{ref} \exp\left(\frac{L_v}{R_v}\left(\frac{1}{\theta_{ref}} - \frac{1}{\theta_e}\right)\right). \tag{3.22}$$

θ_e is the temperature of the air in the lab. The values of the parameters in this section which are used in simulation are shown in table 3.1. Figure 3.9 shows the non-dimensionalised surface temperature field of simulations where $\Omega = 0.025$ rads^{-1} with and without evaporative heat loss through the top surface. The non-dimensionalised temperature is defined as

$$\theta_v' = \frac{\theta_v - T_{cold}}{T_{hot} - T_{cold}} \tag{3.23}$$

such that for the cold plate θ_v'=0 and for the hot plate θ_v'=1. Enhanced convection cells and a lower surface temperature can be seen in the simulation where evaporative loss is present. For typical temperatures at the fluid surface the heat loss through evaporation amounts to about 50W. Scolan and Read (2017) found the heat loss in the experiment to range from 50-80W so the parameterisation is consistent with the lower end of this range.

In this parameterisation the long wave heat flux from the water surface has been neglected and no measurements have been made of this in the experiment either. It is possible that this heat flux could be significant and it may be worth measuring in future experiments and parameterising in the model if it is found to be similar in size to the evaporative heat flux.

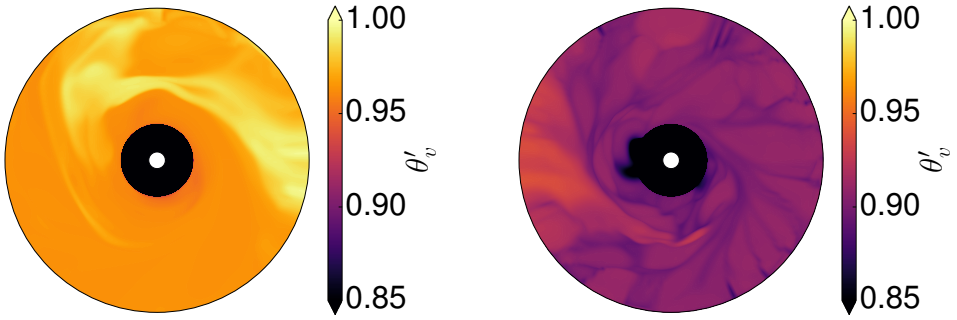


Figure 3.9: The top surface non-dimensionalised temperature fields for simulations with an insulating top surface boundary condition (left) and an evaporative top surface boundary condition (right). Both simulations have $\Omega = 0.025\text{rad } s^{-1}$.

Parameter	Symbol	Present value	Units
Conduction parameters:			
Environment temperature	θ_e	3639	K
Thermal conductivity of fluid	λ_f	0.6	W(mK)^{-1}
Thermal conductivity of wall	λ_w	0.2	W(mK)^{-1}
Wall thickness	d_w	0.01	m
Base thickness	d_b	0.05	m
Evaporation parameters:			
Lab relative humidity	ϕ	0.4	-
Water vapour gas constant	R_v	461.1	$\text{Jkg}^{-1}\text{K}^{-1}$
Latent heat of vaporisation of water	L_v	2.3×10^6	Jkg^{-1}
Reference saturation vapour pressure	p_{ref}	101.32×10^3	Pa
Reference temperature	θ_{ref}	373.15	K

Table 3.1: Parameters used in the schemes parameterising heat loss via conduction and evaporation from the annulus.

3.2.8 Convection scheme

For most simulations we assume the free convection under/over the heat sink/source is adequately resolved by direct numerical simulation but realistically the model cannot be run at high enough resolution to resolve the smallest convective scales. Therefore, to assess the impact of the unresolved convection, some simulations are run with a convective parameterisation. The Lambert-Lewis convection scheme (Lambert et al., 2017) available within the UM was modified to allow only dry convection. This scheme implements convective adjustment in a way which conserves the column integrated enthalpy while adjusting to the dry adiabatic lapse rate,

g/c_p, on a given timescale.

Convection is triggered in a column when $\theta_{k+1} - \theta_k < 0$ where k is the model level starting with $k = 0$ at the surface. The convective temperature increment is then calculated as

$$d\theta_{convection} = (\theta_{adj} - \theta_0)(1 - \exp(-\delta t/\tau_c)) \tag{3.24}$$

where θ_{adj} is the adjusted temperature given by the dry adiabatic lapse rate, θ_0 is the initial unadjusted temperature, δt is the model timestep and τ_c is the timescale for convection. In the simulations discussed in later chapters we take $\tau_c = 1000$s but the results were found to be quite insensitive to this choice. Once all increments have been calculated they are modified to enforce enthalpy conservation when the heat is integrated over the whole column. This implies kinetic energy generated by convection is dissipated on the sub grid scale such that the grid scale enthalpy is conserved.

3.2.9 Choice of the numerical scheme

As discussed in section 3.1.1 interpolation is an integral part of the semi-Lagrangian advection scheme and this can cause excessive numerical diffusion in the model if the spatial resolution or the order of the interpolation function is too low. However, using higher order interpolation functions can cause issues with the monotonicity of the fields. The different interpolation schemes and monotonicity schemes available within the UM were tested in conjunction with the annulus setup. It was found that a cubic Lagrange interpolation scheme in both the horizontal and vertical was the most suitable. A lower order linear method was unrealistically diffusive and higher order schemes did not produce significant changes to the results at greater computational expense.

In some simulations, the temperature in parts of the domain was observed to increase above the temperature of the hot plate, which is unphysical, given that the hot plate is the only heat source in the domain. This was most often observed close to the cold plate where the temperature gradients are strongest. To mitigate this, a

monotone filter was applied to the temperature field to maintain the temperature within the correct range. The monotone filter works by considering any valid semi-Lagrangian solution to be a superposition of a lower order diffusive solution and higher order oscillatory solution. In regions where the solution is judged to be oscillatory - and not associated with a correctly resolved turning point - the higher order part of the solution is discarded to maintain smoothness (Allen, 2018). Thus, unphysical oscillations of the flow fields and hence extraneous extrema are generally avoided. This method is called the posteriori monotone filter (PMF). There are however situations where this method can allow oscillatory behaviour to persist so the UM also includes a stricter monotone filter which forces the value of a field at a certain gridpoint to lie within the range of the field at the neighbouring gridpoints (Allen, 2018). This guarantees monotonicity but at the cost of increasing the numerical diffusivity and is called the strict posteriori monotone filter (SPMF). Simulations were run with both types of filter and in general it was found that the PMF filter was sufficient to prevent spurious temperature maxima developing.

3.3 Simulation setup

In the following chapters simulations of the annulus experiment produced using the model outlined here will be analysed. The main focus will be on how the dynamics change with rotation rate. However, a number of other factors such as resolution, numerical scheme and parameterisations are considered. Table 3.2 categorises the simulations which have been carried out. Within each set a range of rotation rates were tested. The heat loss column in table 3.2 refers to whether heat is lost through the boundaries of the annulus or whether they are insulating. The details of the parameterisation scheme are discussed in section 3.2.7. The convection column describes whether the convection in the annulus is parameterised by the convective adjustment scheme outlined in section 3.2.8.

Using the grid stretching discussed in section 3.2.2, a minimum of three grid points are located within the thinner of the thermal boundary layer and the horizontal Ekman layer in all simulations. This is the same boundary layer resolution

Set	Resolution (θ, r, z)	χ	T_{cold} K	P_{hot} W	d cm	Heat loss	Convection	Filter
A	196×144×85	0°	3639	20	30	None	None	PMF
B	392×195×85	0°	3639	20	20	None	None	PMF
C	196×144×85	15°	3639	20	30	None	None	PMF
D	196×96×85	15°	3634	80	30	None	None	SPMF
E	196×144×85	15°	3634	200	30	Yes	None	PMF
F	196×144×85	15°	3639	20	30	None	Yes	PMF
G	196×144×85	0°	3639	20	20	None	None	PMF

Table 3.2: Sets of simulations carried out using the model described in this chapter. Settings not mentioned in this table are the same for all simulations. No heat loss means the boundaries are insulating away from the heat source and sink. The convection column reads 'Yes' for simulations where a parameterisation scheme is used for convection in the fluid. The filter is the monotone filter used with the semi-Lagrangian interpolation.

used in chapter 2. Hence, the resolution of the boundary layer is similar to that in the 2D simulations. However, the stretching is more exaggerated and the interior resolution is lower in the 3D simulations as fewer grid points are used in each co-ordinate direction to reduce computational expense.

All simulations were run with a timestep of 0.01s and for a total simulated time of between 10 and 15hrs to ensure the runs had equilibrated. The model was run on MONSooN (Met Office and NERC Supercomputing Nodes) and Monsoon2 following the upgrade to the system in April 2017. These are both part of a Cray XC-40 high performance computing system. Using this system a typical 15hrs of simulation time for the annulus at lower resolution (i.e. not set B in table 3.2) took approximately 5 days to run on 28 nodes with 36 CPUs per node.

3.4 Discussion

This chapter has described the adaptation of ENDGame to make it suitable for modelling the annulus experiment of Scolan and Read (2017). The model geometry was changed to allow for the use of cylindrical co-ordinates and novel forcing terms were added to the momentum and heat equations. The model boundary conditions were modified to reflect the rigid, no slip walls of the annulus experiment and the free surface at the top. The same grid stretching function used in the MORALs

model was introduced to allow the boundary layers to be well resolved. Isothermal, isoflux and insulating thermal boundary conditions were added in the required locations. The mean fluid temperature was increased by approximately a factor of ten to give a similar volumetric thermal expansion coefficient to the working fluid in the lab without changing the equation of state. The model now includes options for a sloping or flat base, parameterised heat loss through the boundaries and different choices for the numerical scheme. Where possible these changes have been tested in isolation and the main shortcomings of the numerics, non-monotone behaviour and excessive numerical diffusion, have been considered. Finally, the settings used for the simulations discussed in the following chapters have been summarised.

During the development of the model significant problems with numerical instability were encountered. As described already, these often manifested themselves as a runaway heating of the fluid at the cold plate. These were most common at the lowest rotation rates where velocity was highest. However, increasing the resolution did not prevent these problems from occurring and quickly became prohibitively expensive. As described above, we used the monotonicity filters available within the UM to prevent these spurious maxima from developing.

However, we ultimately found that the model would only remain numerically stable when very small timesteps were used. The Courant-Friedrichs-Lewy condition gives a necessary condition for convergence when solving partial differential equations numerically. Generally if the Courant number,

$$C = \Delta t \left(\frac{u}{\Delta x} + \frac{v}{\Delta y} + \frac{w}{\Delta z} \right) \leq 1 \tag{3.25}$$

the numerics should remain stable. Δt is the timestep and $\Delta x, \Delta y, \Delta z$ are the grid spacings in each of the co-ordinate directions. For the semi-Lagrangian, semi-implicit scheme used here one would expect values of C larger than one to be tolerable. For our simulations we find that, for the largest timestep where stability was maintained, $C \approx 0.5$. The timestep itself, 0.01s, is equal to that used in the 2D MORALs simulations in chapter 2 despite those simulations using higher spatial resolution. The reason for this remains unknown.

For the purpose of comparing these simulations with the lab experiment there is one clear discrepancy remaining. The top level of the model is constructed to be horizontal and thus parabolic deformation of the fluid by the centrifugal force is not possible. In the lab experiment, at high rotation rates, the deformation can be appreciable with changes in fluid depth of up to 5cm. As the depth changes in the same sense as the sloping bottom this deformation results in a stronger β-effect in the experiment than in the simulations.

Never trust anything that can think for itself if you can't see where it keeps its brain.

— Arthur Weasley, *Harry Potter and the Chamber of Secrets*

4

Comparing simulation and experimental results

Now we move on to analysing the three dimensional simulations of the experiment produced using the model developed in the previous chapter. The main aim of this chapter is to compare the results of the simulations with measurements from the experiment to provide some validation of the numerical model. Currently, the available data from the experiment is limited to information about the temperature field as particle image velocimetry (PIV) analysis of the velocity fields has not yet taken place. Measurements of the temperature field in the experiment were made using an infra-red (IR) camera which observed the top surface of the flow and a number of thermocouples and thermistors within the flow. The thermocouples were arranged to measure temperature over the full depth of the experiment at one horizontal position in the baroclinic zone and one horizontal position over the heat source. Thermistors were embedded in each of the heat source and sink and used to measure their temperatures (Scolan and Read, 2017). From these thermal measurements we are able to compute the total temperature difference that emerges between the isoflux heat source and isothermal heat sink. We can also calculate the mean stratification within the flow and diagnose the flow regimes that exist at different rotation rates. We consider these aspects of the flow in this

chapter and we also investigate some modifications to the numerical model which attempt to improve the agreement between simulation and experiment. From the IR camera images we are also able to calculate temperature variance spectra at the top surface of the flow but we present these in chapter 6 alongside a more extensive spectral analysis of the simulations.

4.1 Flow regimes

We begin by considering the regimes which categorise the behaviour of the flow in the annulus and how the experimental and simulated flows fit into these. The annulus in this study is ultimately governed by the same control parameters as the classical annulus experiment and thus one might expect it to exhibit similar behaviour. In chapter 2, we found that some of the scalings in the two dimensional simulations were similar to predictions for the classical annulus. The flows in the classical annulus may be characterised as belonging to a number of different regimes (Hide and Mason, 1975). Figure 4.1 shows the regime diagram in thermal Rossby number/Taylor number space for the series of lab experiments and numerical simulations studied within this thesis. Figure 10 of Scolan and Read (2017) shows a comparable regime diagram for experimental runs without a sloping base. The presence of the sloping bottom does not appear to have much effect on the regime diagram. The regimes observed can be categorised in broadly the same manner as those found in the classical annulus. We find that the transitions between the three regimes are approximately consistent between the lab experiments and the simulations. Broadly, the three regimes identified in the classical annulus (and also here) are:

1. Axisymmetric regime (Panel A in figure 4.1): In this regime the flow is approximately symmetric about the rotation axis as it is stable to baroclinic instability and so eddies and waves are not observed. This regime can be further divided into two separate axisymmetric sub-regimes (Hide and Mason, 1975). In the lower symmetric regime the temperature difference is very low and the flow is diffusion dominated. The upper axisymmetric regime exists

below some critical thermal Rossby number where the rotation rate is very low and the temperature difference is moderate which gives an axisymmetric flow dominated by thermal wind balance in the interior. In our simulations the axisymmetric flows belong to the upper symmetric regime.

2. Regular wave regime (Panels B, C and D in figure 4.1): Here the flow becomes unstable and large scale waves are observed. Their wavenumber, m, increases with rotation rate and decreases with applied temperature difference. Assuming the wavenumber is proportional to the inverse of the deformation radius, as predicted by the Eady model (Eady, 1949), we expect

$$m \sim \frac{f}{Nd} \sim \Omega \Delta T^{-1/2} \sim Ro_{th}^{-1/2}. \tag{4.1}$$

The wavenumbers observed for different sets of parameters are comparable between the experiments and the simulations. It is also possible for the wavenumber of a given flow to change over time. In our simulations and in the lab experiment a wavenumber vacillation is observed for $\Omega \approx 0.1$rad/s where a flow starting out with wavenumber 2 or 3 transitions to wavenumber 3 or 4. Weng and Barcilon (1988) found this effect to be the result of wave-mean flow interactions. In previous studies two other kinds of wave vacillation, amplitude and structural, have also been identified (Pfeffer and Chiang, 1967). Amplitude vacillation is an approximately periodic variation of the wave amplitude whilst structural vacillation involves a periodic tilting of the wave peaks/troughs and generally occurs close to the transition to irregular flow. We do not study these phenomena in this work in any further detail but note that amplitude vacillation has been observed in both the experiments and simulations .

3. Irregular regime (Panels E-G in figure 4.1): At high enough rotation rates the flow becomes fully irregular and is characterised by turbulent dynamics. The wavenumber spectrum becomes broader and more continuous rather than peaking at discrete values corresponding to the regular waves of the regime

above. We also note that the flow in this regime exhibits local horizontal shear instabilities characterised by filamentary structures and these features are known to be prevalent in systems governed by SQG dynamics. These properties will be discussed in more detail in chapter 6.

We find that the transition from a stable state to the onset of baroclinic instability occurs at $Ro_{th} \approx 6$ which corresponds to a Burger number of about 0.5 for the simulations. This is consistent with what is found in the lab (Scolan and Read, 2017) but also with the prediction of Hide and Mason (1975) for the transitional Burger number in the classical annulus using the Eady model. For our annulus the Eady model gives a critical Burger number of 0.44. It should be noted that in the classical annulus any agreement with the Eady model could be coincidental as the flow is dominated by an interior PV gradient rather than temperature gradients on the horizontal boundaries. The PV structure of our experiment appears to be in better agreement with the Eady model as the PV gradient on the boundaries dominates over the interior contribution which is close to zero (see section 5.1.3). A more appropriate idealisation of the classical annulus may be the instability of an internal baroclinic jet which was considered by Bell and White (1988).

A notable difference between the appearance of the flows here, both in simulation and experiment, and those in the classical annulus is that here we observe small scale hot spots at the outermost radii. These are likely to be the remnants of convective plumes which have risen above the heated plate. These are observable in the flows in panels B and G in figure 4.1. The convective plume tops near the outer boundary delineate a region to which, in general, the large scale, low frequency baroclinic waves do not spread. This confinement of the baroclinic waves is observed in both experiment and simulation and suggests that the waves will be less affected by the existence of the boundaries than in the classical annulus.

In the two dimensional experiments of chapter 2 the transition to a flow where heat transport was severely inhibited by increasing rotation rate (characterised by rapidly decreasing Nusselt number) was found to occur at $Ro_{th} \approx 0.1$. This is where we see the transition from large scale regular baroclinic waves to irregular,

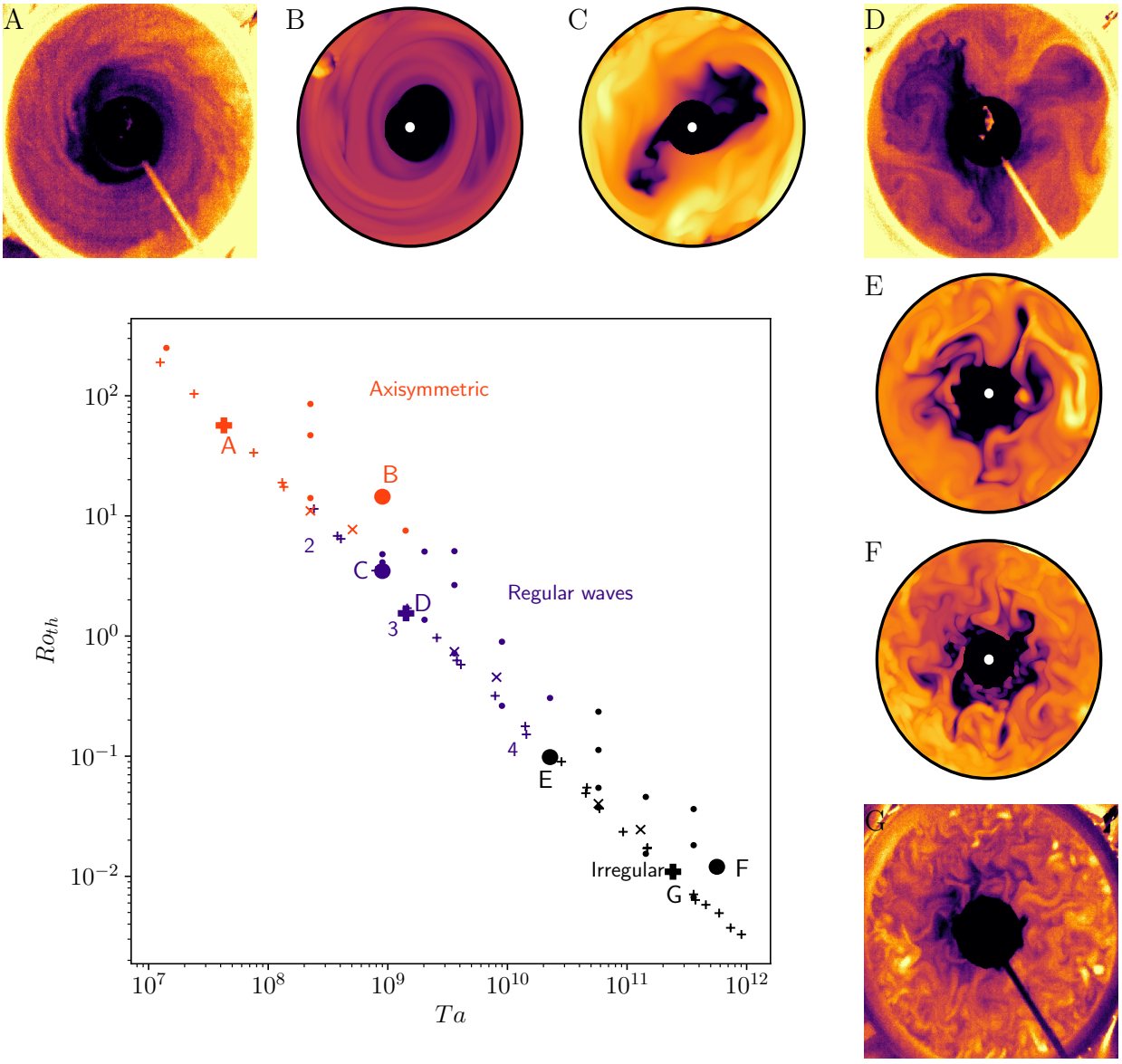


Figure 4.1: The region of Taylor/thermal Rossby number space spanned by the lab experiments with a sloping bottom (+), 3D simulations with a flat bottom (×) and 3D simulations with a sloping base (•). Orange, purple and black points indicate the axisymmetric, regular wave and irregular regimes respectively. Panels A-G show examples of the top surface temperature field across the parameter space. Panels A, D and G show snapshots of the temperature field on the top surface of the lab experiment recorded by a thermal imaging camera. The others correspond to simulation runs. The alphabetical order of the panels corresponds to decreasing Rossby number and the corresponding points in parameter space are highlighted by larger markers in the regime diagram and labelled by the same letters as the panels.

turbulent flow in the three dimensional simulations and experiment. Figure 2.4 shows the appearance of sloping isotherms in the rz plane of the two dimensional

simulations at a similar thermal Rossby number to where we see the appearance of large scale baroclinic waves in the 3D simulations. This suggests there is at least qualitative agreement between the 2D and 3D simulations.

4.2 Total heat transport

To quantify the total heat transport in the annulus a slightly different method must be used to that used in chapter 2 to calculate the Nusselt number. In the two dimensional simulations all boundaries were insulating apart from the heat source and sink which were both isothermal. Hence, the emergent flux through the heat source and sink was related to the total heat transport through the system.

In the three dimensional simulations the heat sink is isothermal whilst the heat source is isoflux. In simulations where the other boundaries are insulating (sets A,B,C,D,F in table 3.2) this means that, at equilibrium, the total flux through the cold plate is equal to the total flux through the hot plate. Hence, the integrated flux through any $r\theta$ or $z\theta$ surface is equal to the flux applied through the hot plate and thus the total flux through the system is constrained. The temperature of the cold plate is fixed and so it is the temperature of the hot plate, and hence ΔT, which adjusts according to the heat transfer through the system. A smaller ΔT would imply that heat is transported more efficiently by the fluid. Here we take ΔT to be the difference between the cold plate temperature and the spatially and temporally averaged temperature of the hot plate. At equilibrium the average temperature is approximately constant in time.

For Rayleigh-Bénard convection with isoflux boundaries

$$Nu = \frac{dP_{hot}}{c_p \rho A \kappa \Delta T} \tag{4.2}$$

where P_{hot} is the total power through the heat source and A is the horizontal cross sectional area of the domain (Otero et al., 2002). Via similar arguments we also expect the Nusselt number for our system to be proportional to the inverse of ΔT although the constant of proportionality is different to that of Rayleigh-Bénard convection because of the different geometry.

It should be noted that the arguments above apply only to simulations where the boundaries away from the heat source and sink are insulating. Set E has heat transfer through all boundaries in the system and this must be taken into account when calculating the Nusselt number. In this case, the method of integrating the flux over the boundaries used in chapter 2 may be a more appropriate measure of the Nusselt number but we do not consider this further here.

Figure 4.2 shows the temperature difference between the heat source and sink in the simulations and the experiment as a function of rotation rate. In the experiment ΔT remains approximately constant for all rotation rates until $\Omega \approx 1$rad/s where it begins to increase. Less efficient heat transport at high rotation rate is consistent with suppression of convection via the Taylor-Proudman effect and a reduction in the mean overturning circulation.

Heat loss via evaporation and conduction, which can be as high as 50% of the input power through the hot plate in the experiment, is likely to affect the total heat transport (Scolan and Read, 2017). This is not accounted for in simulations A, C and D but set E has the same input power as the experiment and parameterised heat loss through the boundaries so would be expected to be the best match to the experimental data. However, the temperature difference in simulations from set E is higher than in the experiment and there is also a large reduction in ΔT with Ω in the range $0.05<\Omega<0.2$ which is absent in the experiment. Amongst other things, the discrepancy between the simulations and the experiment may suggest a shortcoming in the boundary heat loss parameterisation. This will be discussed further in section 4.3.

Simulations in sets C and D also exhibit this strong reduction in ΔT over a similar range of rotation rates. This is also the range of Ω where regular baroclinic waves are seen. The magnitude of the drop in ΔT is approximately proportional to the applied heat flux at the hot plate. At the highest rotation rates, within the irregular turbulent regime, the simulated ΔT becomes roughly constant and then increases slightly with Ω, which is more consistent with the trend in the experimental data.

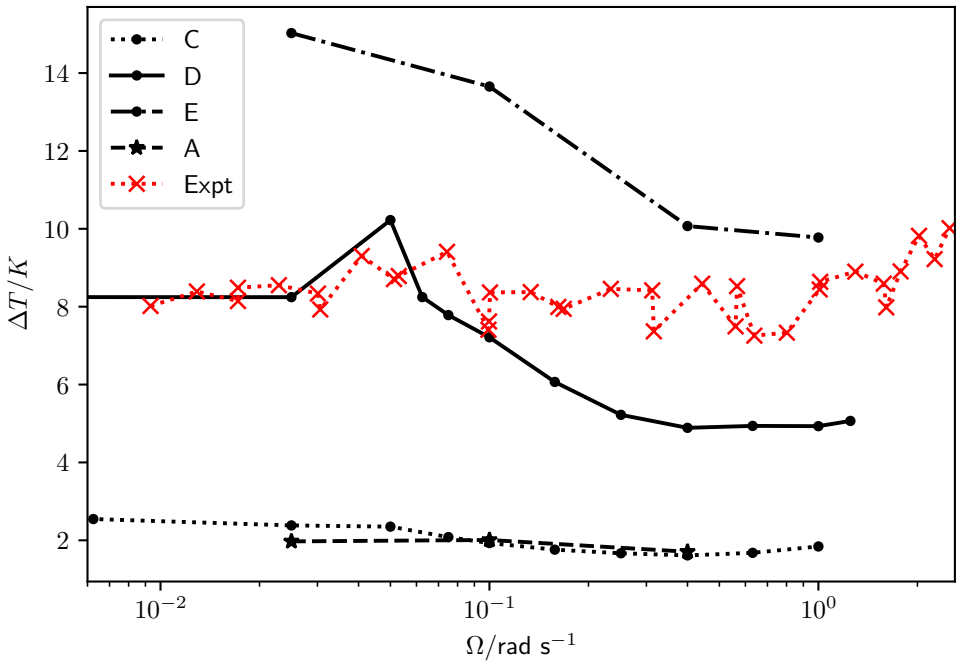


Figure 4.2: The variation in the temperature difference between the hot and cold plate, ΔT with rotation rate, Ω for various sets of simulations and the experimental data. The different sets of simulations have different input power at the hot plate.

One possible explanation for the spurious behaviour of ΔT with rotation rate in the simulations is that convection is not sufficiently resolved. Due to convergence of the model grid as $r \to 0$, the resolution is coarser at large radii where the heat source is located. At the largest radii the azimuthal resolution is approximately two orders of magnitude greater than the Kolmogorov scale. Furthermore, when the slope is present, the vertical resolution in the interior of the flow is also lower at larger radii as the flow is deeper there although the resolution of the boundary layers on the top and bottom surfaces is the same everywhere.

In Rayleigh-Bénard convection it has been shown that the Nusselt number is very sensitive to the resolution (particularly in the boundary layer but also in the interior) and Nu is overestimated when the flow is under resolved (see Shishkina et al. (2010) and references therein). Also, higher Rayleigh number flows require a larger number of gridpoints in the boundary layer to accurately compute the Nusselt number. The Rayleigh number is almost a factor of ten lower for set C

(10^9) than set D (10^{10}) and so the simulations with greater applied heat flux in set D may be more affected. The grid is stretched such that there are always three points within the thinner of the kinetic or thermal horizontal boundary layer. This was sufficient in the two dimensional simulations of chapter 2 but in three dimensional Rayleigh-Bénard convection Stevens et al. (2010) found that at least ten points were needed within the thermal boundary layer at these high Rayleigh numbers. The aspect ratio of the grid cells may also contribute to this problem as they are wider in the horizontal direction than in the vertical. These ideas will be explored further at the end of this chapter.

4.2.1 Nusselt number

For comparison with the results from the 2D simulations in chapter 2 we calculate the Péclet number for some of the 3D simulations. As discussed above, in the case where the boundaries away from the heat source and sink are insulating, the Nusselt number can be computed directly from the total temperature difference. Here, we calculate the Nusselt number as

$$Nu = \frac{\Delta T_{cond}}{\Delta T} \tag{4.3}$$

where ΔT_{cond} is the temperature difference between the hot and cold plate when the system is only conducting. ΔT_{cond} was calculated using the same forward Euler solver as in chapter 2 but with boundary conditions modified to match those used here.

As in chapter 2 the Péclet number is given by $Pe = Nu - 1$ and this is the ratio of advective to conductive heat transport. The Péclet numbers for simulations in sets C and D are plotted in figure 4.3 as a function of the boundary layer ratio P. Also shown are the equivalent results from the 2D simulations with depths of 24.4cm and 36.6cm.

Set C shows a trend in Pe/Pe_0 with P which is similar to that seen in the 2D data. However, the heat transfer is always higher in the 3D simulations. In part this is a consequence of the spurious reduction in ΔT discussed above. However, it has also

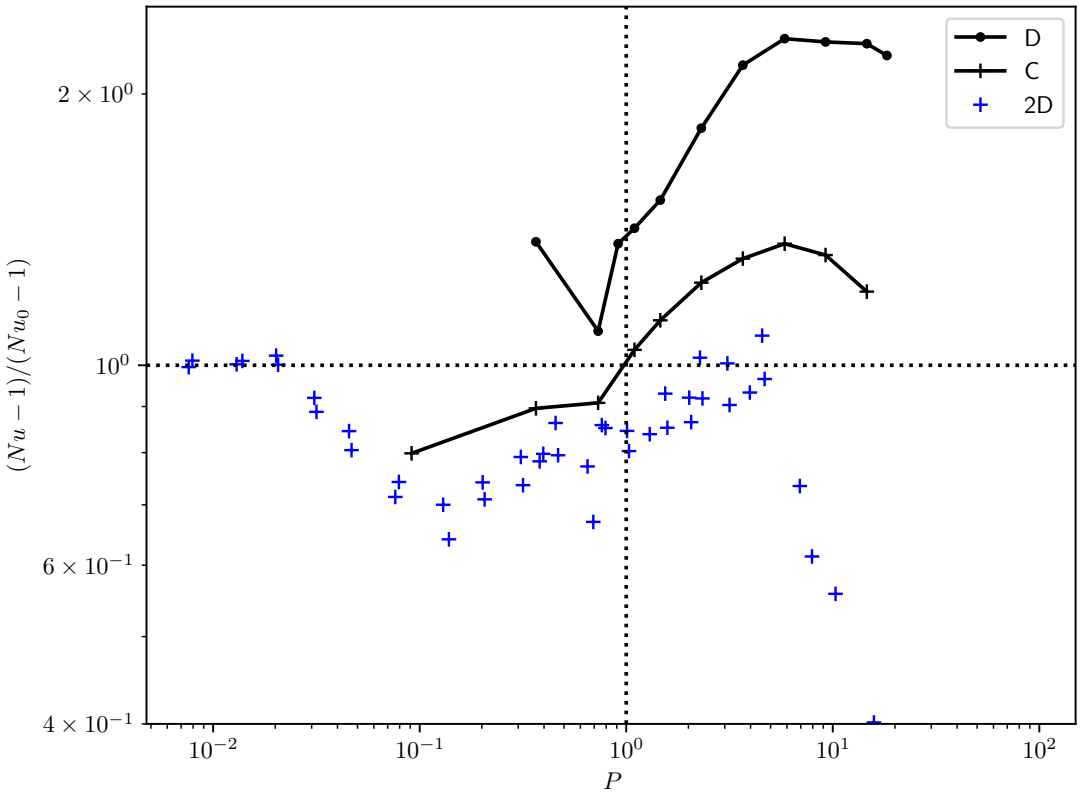


Figure 4.3: The variation in normalised Péclet number, $Pe/Pe_0 = (Nu-1)/(Nu_0-1)$, with the boundary layer parameter, P, for datasets C and D from the 3D simulations and the 2D simulations of chapter 2. Nu_0 and Pe_0 are the non-rotating values of the Nusselt number and Péclet number respectively. The vertical dotted line represents $P = 1$ i.e. where the thermal boundary layer and Ekman layer have a similar thickness. The horizontal dotted line represents Pe=Pe_0.

been found that the Nusselt number is larger in three dimensions than two in non-rotating Rayleigh-Bénard convection (van der Poel et al., 2013). For $P > 1$ the heat transport in three dimensions becomes significantly greater than in two dimensions and the heat transport is enhanced beyond that of the non-rotating system.

Weiss and Ahlers (2011) found that in rotating Rayleigh-Bénard convection the Nusselt number could be increased beyond the non-rotating value when Ekman suction was able to efficiently transport heat out of the boundary layer. Figure 4.4 shows the relative vorticity and temperature anomalies at the top of the Ekman layer under the cold plate for the simulation in set C with the highest Nusselt number. There is some evidence of vortical structures which correlate with cold temperature anomalies. This suggests that Ekman suction may also be acting to

increase the heat transport here. However, due to the low density of vortices and the lack of a similar, large increase in heat transfer in the experiment we conclude that this mechanism is not dominant in setting the heat transfer. We do note that in the experimental work of Scolan and Read (2017) there appears to be a slow increase in Nu at low rotation rate which could be consistent with this mechanism but further investigation would be needed to confirm this. It would not be possible for vortices to form in two dimensions so this effect would not be present in the 2D simulations.

In the classical annulus the baroclinic wave activity increases at a sufficient rate to compensate for the reduction in heat transport due to the suppression of the overturning circulation as rotation rate increases. This means that the Péclet number remains approximately constant with rotation rate (Read, 2003). The presence of baroclinic waves and eddies is one reason why the heat transport is higher in three dimensions than two dimensions but here it is not offset by a commensurate decrease in the mean overturning. In general we find that the zonal mean circulation is very weak in our simulations (see chapters 5 and 6). This may also be a product of insufficiently resolving the convection as the zonal mean circulation is thermally direct.

4.3 Stratification

Another measure which can be compared between the experiments and simulations is the stratification of the fluid. This is important in the current context as the vertical temperature gradient is used to calculate the criticality parameter which is commonly used to characterise regimes of thermal equilibration (see chapter 1). In the experiment vertical temperature gradients are measured by an array of thermocouples equally spaced along a vertical probe (Scolan and Read, 2017). One of the probes is situated at mid-radius to measure the vertical temperature profile in the baroclinic zone. The other is positioned over the middle of the hot plate to measure the temperature profile in the convective zone. They measure the temperature profile over time at a single radial and azimuthal position and this is subsequently averaged in time.

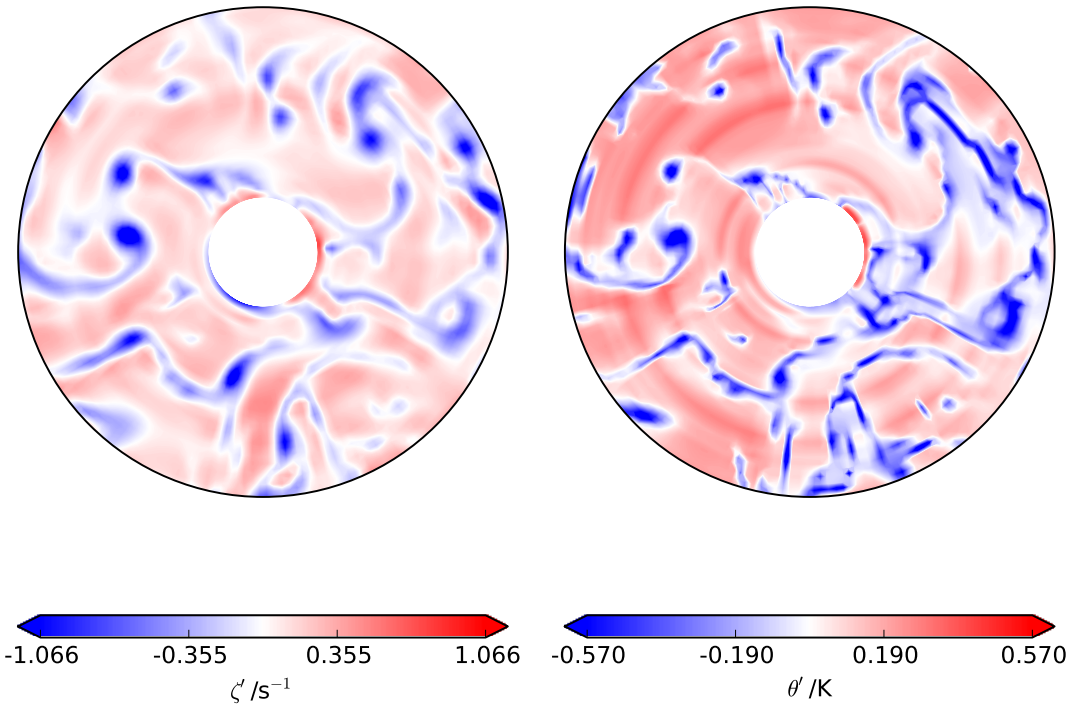


Figure 4.4: The relative vorticity (left) and temperature (right) deviations from the zonal mean at the top of the Ekman layer under the cold plate for the simulation from set C with $\Omega = 0.4$rad/s.

Small vertical temperature gradients could indicate one of two scenarios. Firstly, if vertical mixing in the flow is very efficient, the vertical temperature gradient will be low. For example, this is likely to be the case in regions where free convection is dominant and is able to adjust the flow towards a convectively neutral profile. Secondly, when rotation is very strong the fluid 'stiffens' due to the Taylor-Proudman effect as described in chapter 2 so convective heat transfer is suppressed and the isotherms tend to the conducting profile which is approximately vertical and so the stratification is again reduced.

Vertical temperature profiles from simulations with parameterised heat loss at the boundaries (set E) are shown in figure 4.5 and profiles from the lab experiment spanning a similar range of Rossby numbers are shown in figure 4.6. Simulations without parameterised heat loss are shown in figure 4.7, these

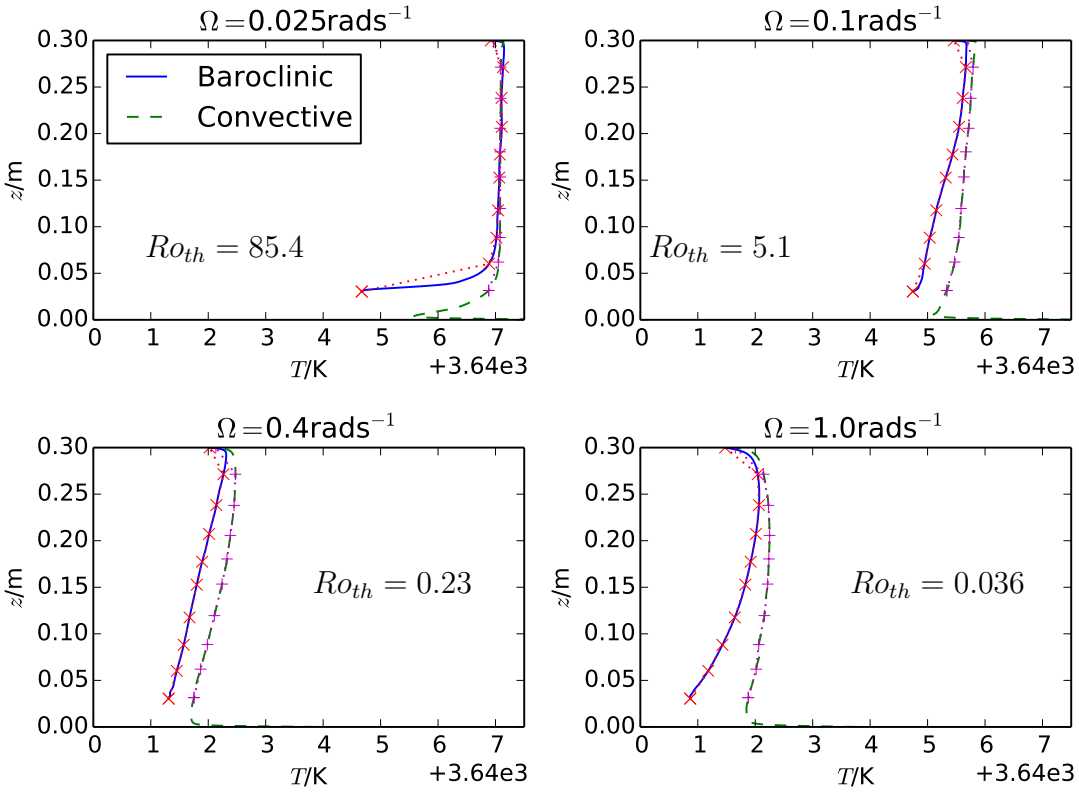


Figure 4.5: Time averaged temperature in the annulus at a fixed azimuth and radius as a function of depth for runs in set E where heat loss through the boundaries is parameterised. The solid blue line shows the temperature at midchannel, $r = 0.2565$m, in the baroclinic zone. The dashed green line shows the temperature over the centre of the hot plate in the convective zone, $r = 0.438$m. The crosses, + and ×, mark the depth of the thermocouples used to measure the temperature in the experiment and so the dotted lines joining these represent the profiles which would be observed if the same fields were present in the lab.

simulations are from set C.

The broad trend, seen in both the experiments and the simulations is that in the convective region of the flow the temperature field is quite well mixed and close to being isothermal. In the baroclinic zone the flow is more stratified and the strength of the stratification increases with the rotation rate. The experimental data is more noisy than the simulations which may indicate that there is fine scale detail not being properly resolved by the simulations. Alternatively, the experimental runs have not have fully equilibrated or the noise is an artefact of the experimental measurement system. The simulations were run for up to 15hours of simulation time to reach an equilibrated state but running all experiments for this long is not

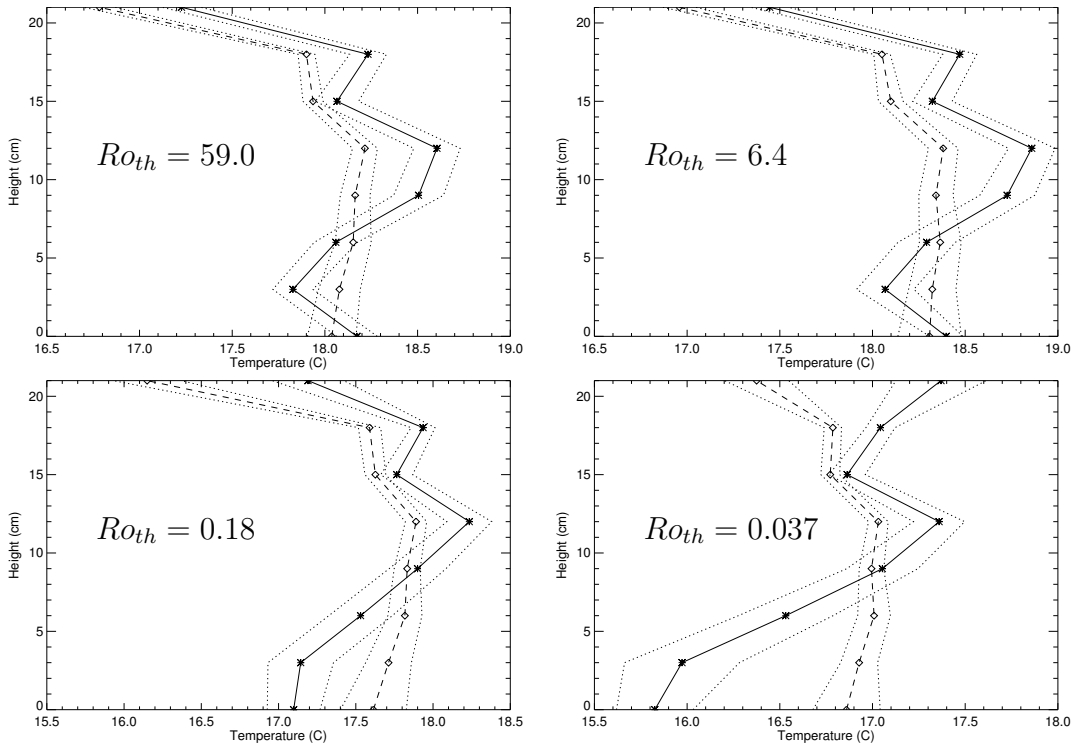


Figure 4.6: Vertical temperature profiles in the baroclinic and convective zones measured in the experiment. The solid line shows the vertical temperature profile in the centre of the baroclinic zone and the dashed line represents measurements taken over the centre of the hot plate. The dotted lines indicate the uncertainty. The points on each line mark the positions of the thermocouples used to collect the data. These plots and the corresponding data were produced by Peter Read.

practical in the lab. There is a notable, systematic deviation in the experimental profiles shown in figure 4.6 between the heights of 12cm and 15cm. This could be a systematic error resulting from insufficient calibration of the thermistors and may warrant further investigation in future experimental work.

Other similarities between the simulations and experiments include a cooling of the bulk mean temperature as rotation rate increases and an increasing difference between the temperature of the baroclinic zone and the convective zone at small z as rotation rate increases. However, in the experiments, the temperatures of the baroclinic and convective zones converge at larger z whereas in the simulations a larger difference remains at almost all depths.

In the experiments, and the simulations at higher rotation rate, a temperature inversion is observed close to the top of the tank although this is far more pronounced

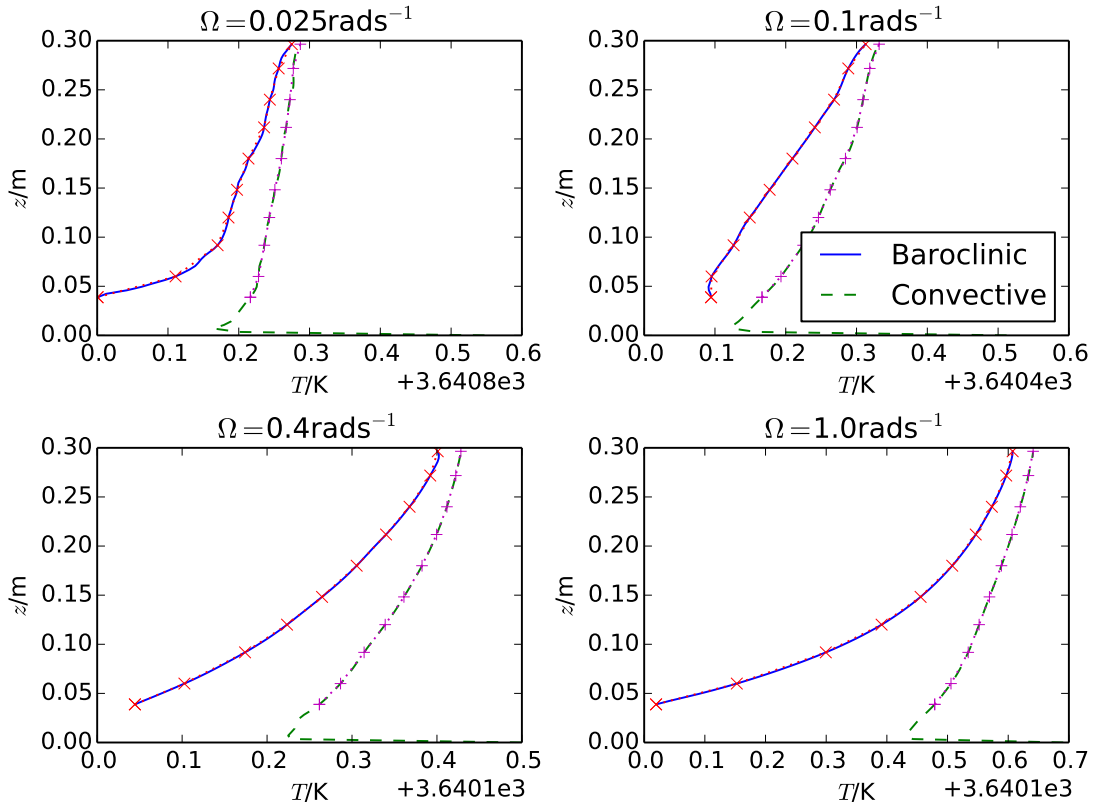


Figure 4.7: The equivalent of figure 4.5 for simulations in set C where heat loss from the boundaries is not parameterised. Away from the heat source and sink all boundaries are insulating. Symbols and lines have the same meaning as in figure 4.5.

in the experimental data. The inversion is seen in both the convective and baroclinic zone (except at the highest experimental rotation rate where the top of the tank is stably stratified in the baroclinic zone) and extends to a depth of 3cm in the simulations and 7cm in the experiments. This feature is thought to be primarily due to evaporative cooling from the top of the tank. It is not observed in simulations with an insulating top surface (figure 4.7). Although the experiment is shielded by a curtain to reduce wind stress, this will not be removed entirely and this effect, which enhances evaporation, is not accounted for in the simulations which could partly explain why the temperature inversion is generally stronger in the experiment.

In the simulations this inversion appears to strengthen with rotation rate which may be consistent with mixing becoming less efficient as rotation rate increases. However, in the experiments shown here the inversion is weaker at the highest

rotation rate but this may be due to the lower mean temperature of the fluid which would result in less evaporation. The difference between the truly free top surface in the experiment and the simulated 'free' surface may also play a role in modifying the flow near the top of the tank.

At the lowest rotation rate shown the simulations produce a strong vertical temperature gradient near the bottom surface due to a cold density current which runs down the inner wall and onto the sloping base. This is not observed in the experimental profiles shown here where the surface is actually slightly warmer than the fluid directly above it for low rotation. However, it is observed in the measurements of Scolan and Read (2017) (Figures 6-8 of that paper) using the flat bottomed annulus at the lowest rotation rates when the fluid was allowed to equilibrate for 1 - 2.5hours. It was not observed when the fluid was only allowed to equilibrate for 20 minutes. This may suggest that the experimental data shown here was not allowed to equilibrate for long enough.

Stratification in the baroclinic zone

To summarise the trends in stratification with the forcing we compute gradients from the profiles discussed above using a linear fit to points where 6cm$\leq z \leq$15cm so that regions close to the horizontal boundaries and the temperature inversion at the top are not included. The same method is then used to calculate the gradient from the experimental data for comparison. Other means of calculating the gradients in the simulations, for example a volume average over the baroclinic zone as used in chapter 2, yield similar results with changes affecting the absolute values by a small amount but not the trends in the data.

Figure 4.8 shows the vertical temperature gradients measured in the middle of the baroclinic zone from the experiments and equivalent gradients from both the 3D simulations using the UM and the 2D simulations of chapter 2. The gradients are normalised by $\Delta T/d$ so that the different datasets may be compared. This normalised gradient can also be thought of as the ratio of the Burger number to the thermal Rossby number. Set E, where the boundary heat loss is parameterised,

is highlighted with a line joining the points as this would be expected, a priori, to provide the best model of the experimental data. Only those 2D simulations with $d = 24.4, 36.6$cm are shown as these are most similar to the depths of 20-30cm used for the simulations and experiments. The three data sets (experiments, 2D and 3D simulations) show similar trends with decreasing thermal Rossby number:

- At the highest thermal Rossby numbers ($Ro_{th} > 10$), where the flow is axisymmetric, the vertical temperature gradient in the simulations is close to zero and approximately constant. In this regime the flow was previously shown to be approximately isothermal in the interior where the gradient is calculated. There is good agreement between the two dimensional simulations and three dimensional simulations (both with and without parameterised heat loss from the boundaries) as might be expected in this region where the three dimensional flow is approximately axisymmetric. However, the gradient observed in the experiment is higher than that seen in the simulations. This may suggest that some non-axisymmetric features are not being resolved by the three dimensional simulations.

- At $Ro_{th} \approx 10$ for the axisymmetric runs, and $Ro_{th} \approx 1$ for the other data sets, the temperature gradient begins to increase. This transition is coincident with the appearance of baroclinic waves in the experiments and 3D simulations as shown in figure 4.1. For $Ro_{th} \approx 0.01$ the stratification in the 3D simulations and experiment appear to converge. The increase in the vertical gradient is due to the rotation becoming strong enough to resist the buoyancy forces and thus causing the isotherms to slope at an angle to the horizontal.

- In the two dimensional data a peak in stratification is reached at $Ro_{th} \approx 0.05$ and at lower thermal Rossby numbers than this the gradient decreases rapidly as the fluid stiffens due to the Taylor-Proudman effect and mixing due to the overturning is throttled by the narrowing of the Ekman layer. Therefore the thermal structure of the fluid tends to the conductive solution where the isotherms are close to vertical as discussed in chapter 2. The experiments and

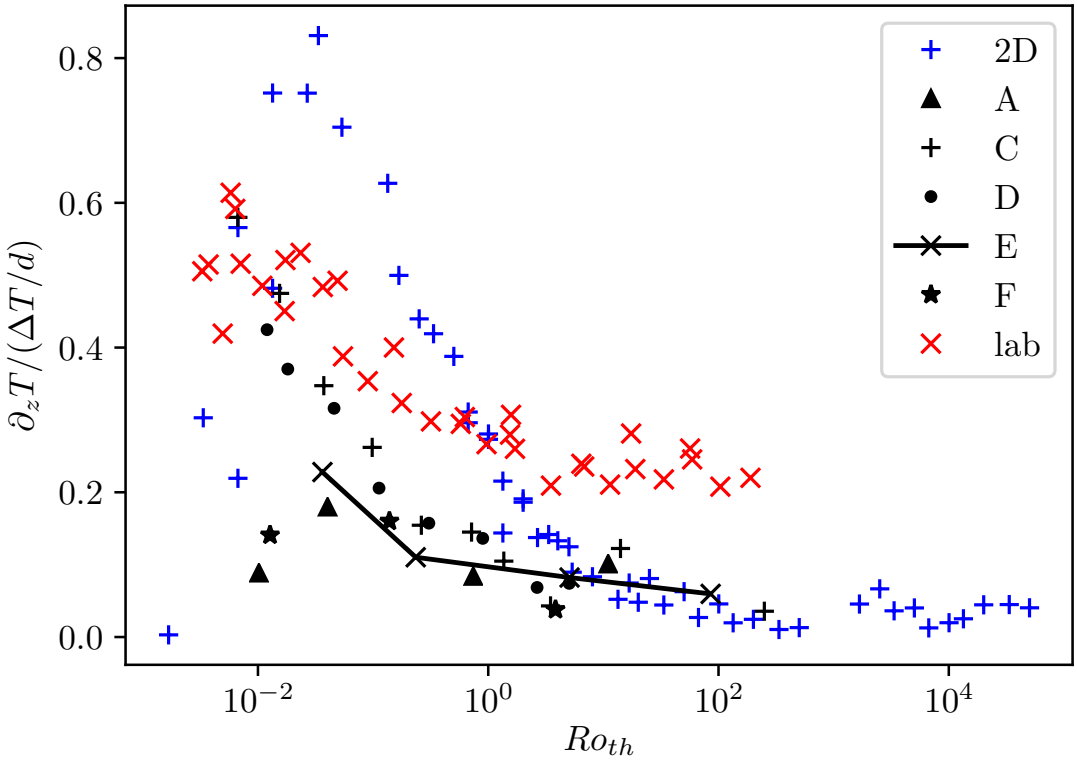


Figure 4.8: The average normalised vertical temperature gradient in the baroclinic zone as a function of thermal Rossby number for the various datasets discussed in this thesis. Red × symbols represent data from the lab experiment, blue + represent the 2D simulations of chapter 2,and other points represent 3D simulations using the UM. The letters in the legend correspond to the datasets described in table 3.2.

3D simulations do not reach low enough Ro_{th} to confirm whether a similar trend exists.

The main discrepancy identified between the simulations and the experiments from the analysis thus far is that, within the baroclinic zone at low to moderate rotation rates, the stratification is generally weaker in the simulations than in the experiment. This is true of both the stable stratification in the interior of the domain and the unstable stratification close to the top surface.

Stratification in the convective zone

The vertical temperature gradient in the freely convecting region above the hot plate may be measured in the same way as that in the baroclinic zone. These measurements are shown in figure 4.9. In general the gradients in this region are

much smaller than those in the baroclinic zone due to efficient mixing towards a convectively stable profile by the free convection. The overall trend in the experimental data is a slow increase in the stratification down to $0.1 < Ro_{th} < 1$, after which the temperature gradient reduces and for $Ro_{th} < 0.01$ the fluid is unstably stratified. Inhibition of convection and suppression of the advective heat transport in the Ekman flow at high rotation rates causes this unstable stratification.

A similar trend is seen in the simulated data where stratification increases as thermal Rossby number decreases from large values down to $Ro_{th} \approx 0.02$ where the temperature gradient begins to decrease. However, the gradient is up to four times larger than that seen in the experiment except at the lowest rotation rates. This may suggest that the free convection is not well represented by the simulation and so convective mixing does not neutralise the temperature gradients as effectively as in reality. Convection on the scale of the numerical grid produces higher stratification in the convective region. However, the simulation underestimates the stratification it in the baroclinic zone.

Runs where heat loss from the boundaries is parameterised are highlighted with a solid line joining the points and seem to provide the closest match to the experimental data. There is good agreement between the experiment and simulations for $Ro_{th} > 1$ and then a peak in the simulated stratification at a Rossby number of $0.1 < Ro_{th} < 1$, albeit at a gradient approximately twice that measured in the experiment. At higher thermal Rossby number the stratification is reduced again. This suggests that accounting for heat loss is important, at least for accurately simulating this region of the flow which is near the sidewall and hotter than the environment so prone be more affected by the boundary conditions than the central baroclinic region discussed above.

4.4 Resolution sensitivity

In the interest of model validation we briefly consider the effect of resolution on the equilibrium flow properties studied in this chapter. As discussed in chapter 3 excessive numerical diffusion is a potential disadvantage of a semi-Lagrangian

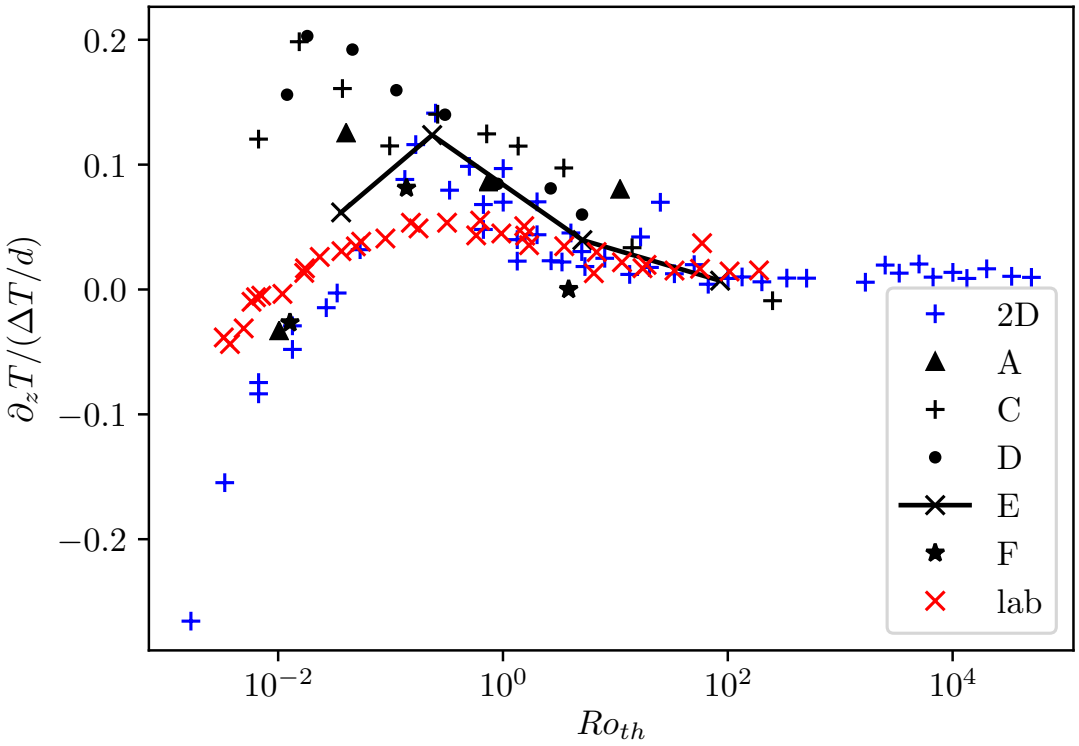


Figure 4.9: The average vertical normalised temperature gradient in the convective zone as a function of thermal Rossby number for the various datasets discussed in this thesis. Symbols are the same as in figure 4.8.

advection scheme but the effect of this is reduced at higher resolution as interpolation becomes more accurate. We have also suggested that we may be under-resolving the free convection above and below the heat source and sink. However, computational expense is also a concern and a balance must be struck between finding sufficient resolution to accurately model the flow without requiring excessive computation time and resources.

High resolution simulations with 394×192×85 grid points in the zonal, radial and vertical directions respectively were carried out at low (0.025rad/s), medium (0.1rad/s) and high rotation rates (0.4rad/s) (set B in table 3.2). This is twice the zonal resolution used in the other simulations presented in this work. In the vertical the same number of grid points was used but the height of the fluid was reduced from 30cm to 20cm so the resolution was increased. These tests were run with a flat bottom, a flux of 20W through the hot plate and insulating boundary conditions

away from the heat source and sink. For comparison, identical simulations were run at the lower resolution of 196×144×50. It should be noted that these high resolution simulations have around half the resolution of the two dimensional results presented in chapter 2 but any higher in three dimensions would be prohibitively expensive. Unfortunately, this means that, at its most coarse, the higher resolution grid spacing is still around an order of magnitude greater than the Kolmogorov scale. To maintain stability the timestep had to be reduced from 0.01s in the lower resolution simulations to 0.003s in the higher resolution simulations. The higher resolution three dimensional simulations took about two weeks of walltime to simulate 10hrs using 72 nodes on the Met Office supercomputer MONSooN. The lower resolution three dimensional simulations could simulate 10hrs in about four days on 28 nodes on MONSooN. The poor scalability is due primarily to the shorter timestep required as resolution increases. The timestep is particularly limited due to the convergence of the azimuthal grid at small radii.

Figure 4.10 shows that for most parameters characterising the thermal properties of the flow there is little difference between the lower and higher resolution simulations. In general the discrepancies are smaller than the uncertainty associated with how these parameters are averaged over the flow. Crucially, the trends in the parameters as a function of rotation rate generally remain the same.

The largest differences are seen at the lowest rotation rate where velocity is highest and the free convection is vigorous and three dimensional. The vertical temperature gradient within the convective zone, $(\partial_z T)_C$, is the parameter most changed by the increased resolution. At low rotation rates increasing the resolution approximately halves the convective temperature gradient, bringing it closer to what is observed in the experiment. However, the gradient is higher at $\Omega = 0.4$rad/s for the higher resolution simulations than at low resolution. Due to the small scales of motion involved in convection it is unsurprising that this part of the flow is the most difficult to model accurately. This result suggests that doubling the resolution may not be sufficient to accurately simulate it at all rotation rates which is unsurprising given that the Kolmogorov scale remains far from resolved. It is

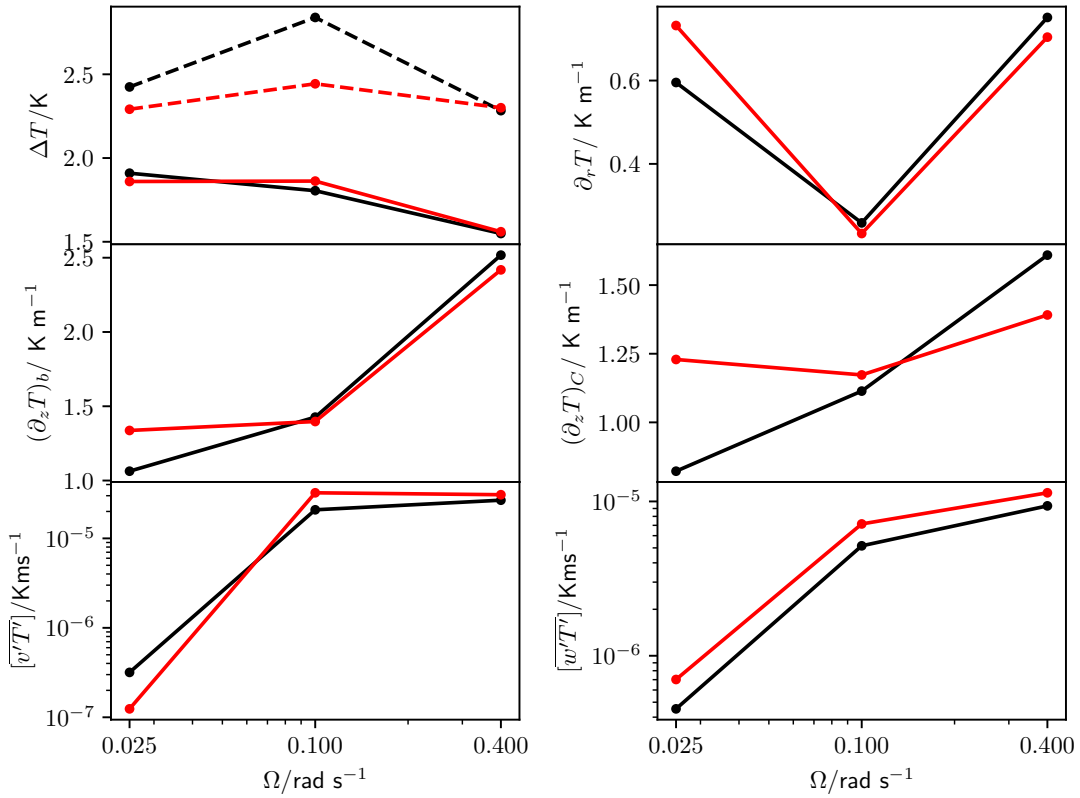


Figure 4.10: The various parameters that characterise the mean thermal state of the flow as a function of rotation rate for higher and lower resolution simulations. The red lines represent the lower resolution simulations and the black lines represent runs at higher resolution. Clockwise from top left the parameters shown are the mean temperature difference (solid line) and the maximum temperature difference (dashed line) between the hot and cold plate, the meridional temperature gradient in the baroclinic zone, the vertical temperature gradient in the convective zone, the peak integrated vertical eddy flux, the peak integrated meridional eddy flux and the vertical temperature gradient in the baroclinic zone.

also notable that, as resolution increases, the vertical eddy heat flux is reduced by a factor of 2-3. This heat flux is dominated by convection and thus this result suggests that heat transport through the fluid, particularly in the vertical direction, is affected by under resolving the convection.

However, despite our previous suggestion that underresolved convection may cause unrealistically small values of ΔT, the higher resolution simulations show almost the same mean ΔT at all rotation rates as the lower resolution simulations. For a more stringent test of the effect of resolution on the model we require a set of simulations using the same parameters as the experimental runs. A more systematic

review of a wider range of resolutions within the simulations would also be useful.

4.4.1 Parameterising convection

As outlined above, the stratification in the convective zone is resolution dependent and quite different in the experiment and the simulations. We also suggested that insufficient resolution of the free convection could contribute to spuriously large Nusselt numbers. The relatively large stratification observed in the convective zones of the simulations thus far suggests that sub-grid scale convection may be important for heat transport and mixing the convective zone towards neutrality. This effect may be exacerbated over the heat source compared with the heat sink because of the divergence of the grid which gives lower azimuthal resolution at larger radii and the presence of the slope which means the vertical resolution is higher at smaller radii. To quantify the effects of these small scale features we briefly investigate the effect of using the convective adjustment parameterisation scheme discussed in section 3.2.8 to parameterise them.

The zonally and temporally averaged temperature and zonal velocity fields with and without convective parameterisation for two different rotation rates are shown in figure 4.11. The zonal velocity is almost entirely unaffected by the parameterisation. However the temperature field is altered quite significantly as temperature gradients are reduced by the convective adjustment. The stratification in the baroclinic zone and convective zone is marked in figures 4.8 and 4.9 respectively by black stars. In the convective zone the parameterisation scheme reduces the stratification significantly, bringing the magnitude and variation with Ro_{th} closer to what is seen in the experiment.

In the baroclinic zone the stratification is also reduced in the presence of the parameterisation scheme, increasing the discrepancy between simulation and experiment. The time averaged fields are stably stratified in the baroclinic zone and the convective adjustment does not act on stable columns. Baroclinic waves and eddies are still produced in much the same way as in the absence of the convection scheme. Since the experimental flows are well mixed above/ below the

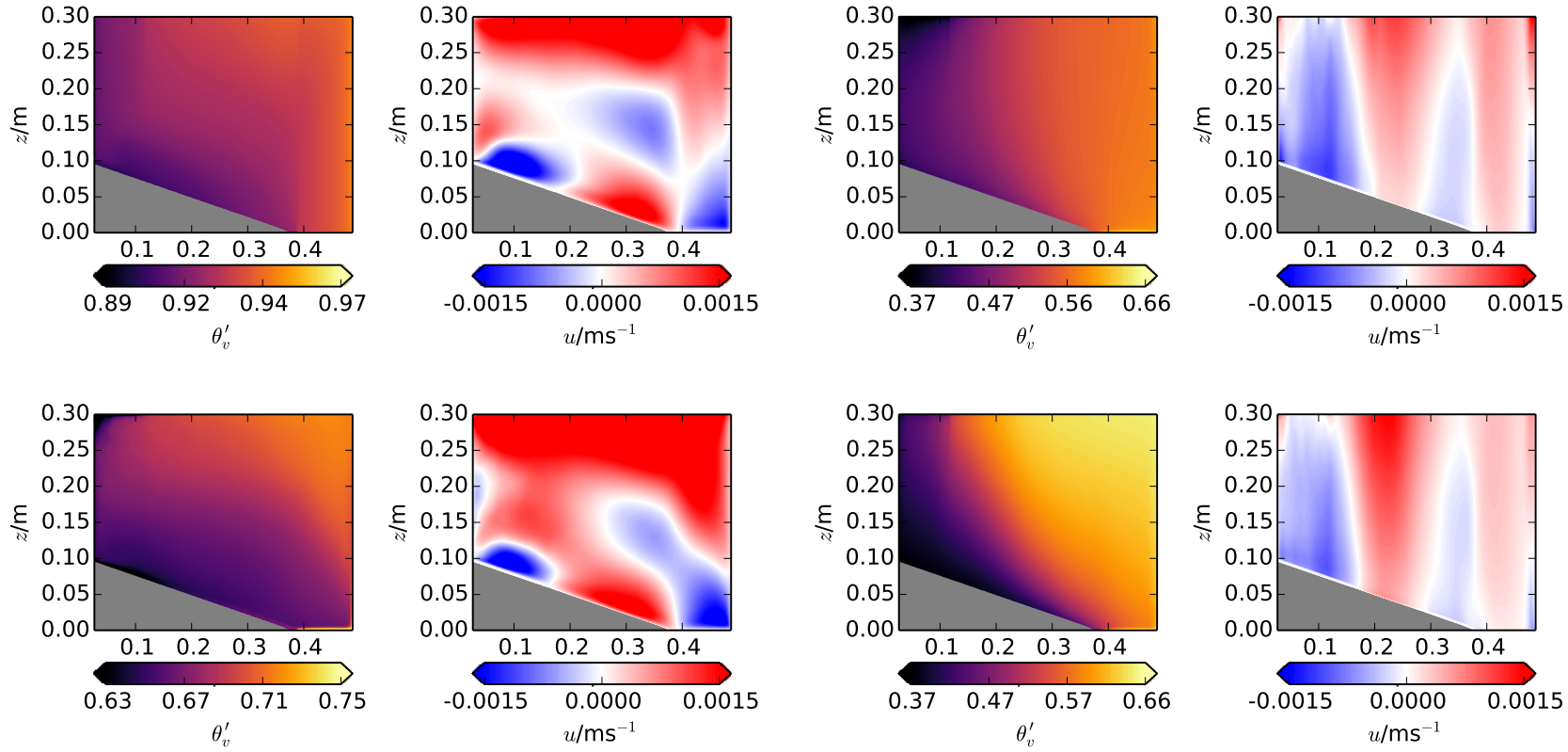


Figure 4.11: The zonally and temporally averaged non-dimensionalised temperature and zonal velocity for simulations with idealised boundary conditions and a sloping bottom. The top row have a convective adjustment scheme switched on (set F) and the bottom row are initialised with exactly the same parameters but no adjustment scheme (set C). The two left hand columns show simulations where $\Omega = 0.05$rad/s and the two right hand columns have $\Omega = 1$rad/s.

heat source/sink it seems unlikely that some physical process is feeding back from the convective zone to reduce the stratification in the baroclinic zone. Instead the convective adjustment is probably acting to reduce local unstable stratification in the instantaneous flow and thus increasing the mixing and decreasing the gradients in the baroclinic zone.

Figure 4.12 shows ΔT as a function of Ω for simulations in set C and the simulations in set F which include parameterised convection. Although set F only includes three datapoints, these results suggest that the convective parameterisation does improve the trend in total temperature difference by removing the sharp decrease in ΔT with Ω which was discussed in section 4.2. This provides further evidence that partly resolved convection may be responsible for the unexpected behaviour in the overall heat transport.

The fact that this convective adjustment scheme increases the discrepancy between the stratification in the experiments and simulations in the baroclinic zone suggests it may not be a good choice for this problem. However, some form of parameterisation for sub-grid scale convection may be necessary to achieve a level of mixing more similar to that seen in the experiments. One problem with the parameterisation considered here is that it is not affected by rotation whereas we have seen that as rotation increases convection is suppressed. One direction for future work may be to implement a more complex parameterisation scheme which better accounts for the rotation such as a mass flux, plume-based model (e.g. Cheinet (2003)).

4.5 Discussion

In this chapter we have compared various features of the flows in the 3D simulations of the annulus with measurements from the lab experiment. Promisingly, the qualitative flow features seen in the experiment are reproduced by the model as are transitions between the various flow regimes. These were also found to be in agreement with the predictions made by Hide and Mason (1975) using the Eady model. Hence, the model passes the first, most basic tests as to whether it is able to

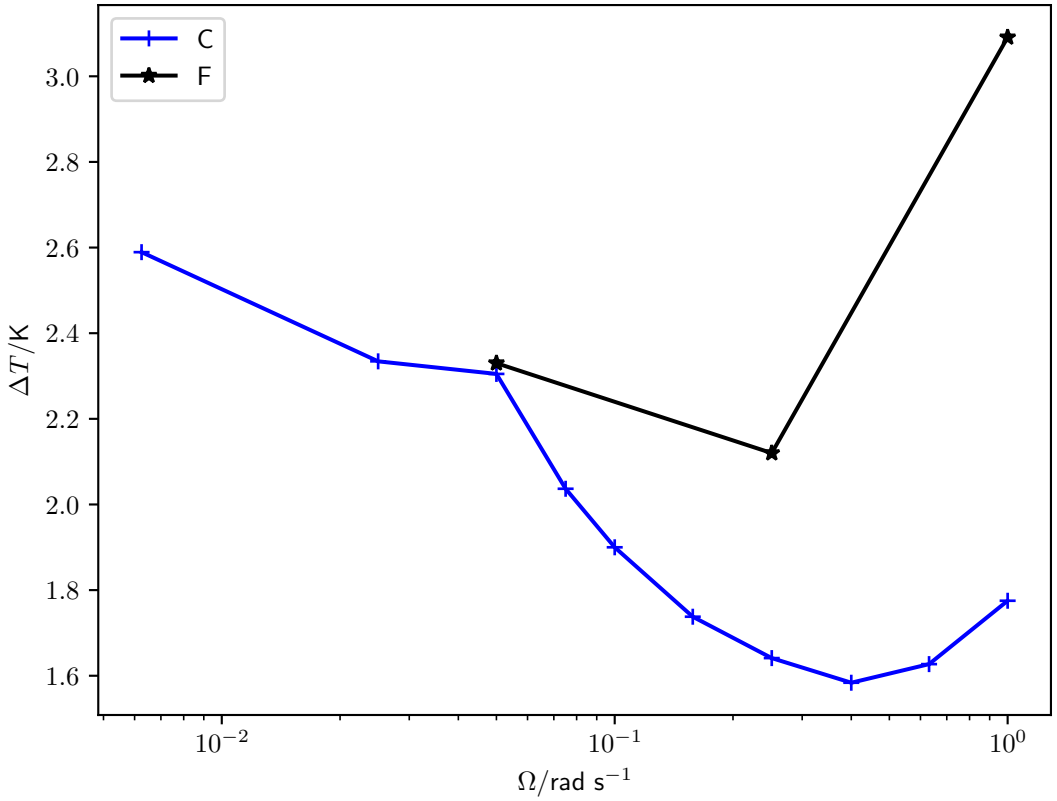


Figure 4.12: Mean temperature difference, ΔT, between the heat source and sink in the annulus as a function of rotation rate, Ω, for simulations with parameterised convection (F) and without (C).

successfully reproduce the types of flows seen in the experiments. As in the classical annulus we observe axisymmetric flows, large-scale, low frequency baroclinic waves and irregular, turbulent behaviour in both the experiment and simulations.

The first major disagreement between the model and the simulations was flagged by the trend in temperature difference between the hot and cold plate with rotation rate. In the experiment, ΔT stays approximately constant with a small increase at the highest rotation rate. Contrary to this, the simulations generally show a sharp decrease in ΔT at moderate rotation rates. A smaller ΔT would suggest more efficient heat transport through the flow and the Nusselt number is proportional to the inverse of ΔT. This apparent large increase in heat transfer was negated by introducing a convective parameterisation scheme

into the simulations. Based on this, and previous results from Rayleigh-Bénard convection, we suggest that convection is under resolved in our simulations and this means the Nusselt number is overestimated.

A more sophisticated convection scheme might improve our model further as the basic adjustment scheme used here does not account for the suppression of convection as rotation rate increases. This aspect of our work is an area which may merit further investigation and closer comparison with the experimental results to more precisely quantify the effect of only partially resolving the convection on the simulations. Models which operate within the 'grey zone', where convection is partially resolved, are an active area of research in numerical weather prediction as modern computational resources allow global models to operate at higher and higher resolutions (Roode et al., 2019). Our results suggest that insufficient resolution of convection within these models could significantly impact the representation of heat transport.

We also computed the stratification within both the convective and baroclinic zones from the simulations to compare with available experimental data. The stratification in the baroclinic zone is best represented by the simulations at higher rotation rates whereas in the convective zone this is where the greatest discrepancies between the experiment and simulations lie. In general, the baroclinic stratification was lower in the simulations whereas the stratification in the convective zone was higher. Increasing the resolution as far as possible within the computational resources available did not yield an obvious improvement. Implementing the simple convective parameterisation scheme reduced the magnitude of the convective zone stratification but also limited the stratification in the baroclinic zone. However, parameterising the heat loss due to evaporation and conduction from the boundaries of the simulations did improve the representation of some qualitative features of the experimental flows although quantitative agreement was still lacking.

Life need not be easy, provided only it was not empty.

— Lise Meitner

5 Analysis of the three dimensional simulations

In this chapter we extend our analysis of the 3D simulations. The motivation behind this analysis is to study whether the heat transfer and thermal equilibration can be explained within the baroclinic adjustment paradigm or whether an alternative explanation is required. Initially, we focus on various zonal mean fields to gain a better understanding of the overall structure of the flow in the equilibrated state at different rotation rates. Following this we combine calculations of the meridional temperature contrast in the equilibrated system with the stratification data from section 4.3 to compute the criticality parameter, ξ. We also consider how eddy fluxes contribute to the transport of heat and vorticity through the system. Currently, the diagnostics considered here cannot be computed from the experimental data. However, in the future, once PIV data becomes available or more extensive temperature measurements are collected a more complete comparison would be possible.

5.1 Zonal mean diagnostics

As the forcing in our annulus is axisymmetric it is illuminating to consider zonally averaged diagnostics. In this section we specifically consider the temperature, zonal

velocity, meridional overturning streamfunction and vorticity fields.

5.1.1 Temperature and zonal velocity

Figure 5.1 shows the zonally averaged, non-dimensionalised temperature and zonal velocity fields in simulations with a sloping bottom at three different rotation rates - one from each of the regimes discussed in section 4.1. As was seen in the 2D simulations, the isotherm slope increases with rotation rate in the central baroclinic zone. Noting the different colour scales in each of the plots it is evident that as rotation rate increases the fluid supports larger temperature gradients in both the vertical and radial directions.

At the slowest rotation rates there is a fast prograde velocity near the top of the tank at approximately mid-radius. As rotation rate increases the overall velocity scale is reduced and alternating regions of prograde and retrograde motion appear. These velocities persist into the convecting regions of the flow where the velocity was found to be close to zero in the two dimensional simulations. At the highest rotation rate a banded structure appears in radius which is approximately barotropic. This is associated with the formation of zonal jets (see section 6.2).

Figure 5.2 shows an equivalent set of runs to figure 5.1 where the base is flat (set A). The velocity field at the lowest rotation rate looks quite similar to the low rotation rates in the two dimensional simulations. However, the two dimensional simulations used different boundary conditions on the upper surface - all boundaries were no slip whereas here the top surface is free slip.

The addition of the sloping bottom to the experiment causes a β-effect analogous to that due to the latitudinal variation of the Coriolis force on a spherical planet. This provides a restoring force which allows the propagation of planetary scale waves. The difference between the flat bottomed runs and the sloping bottom runs is greatest at high rotation rate where the β-effect is largest. Without the sloping bottom, at the highest rotation rate, a strongly unstable temperature gradient is observed in the convective zones, as was seen in the 2D simulations.

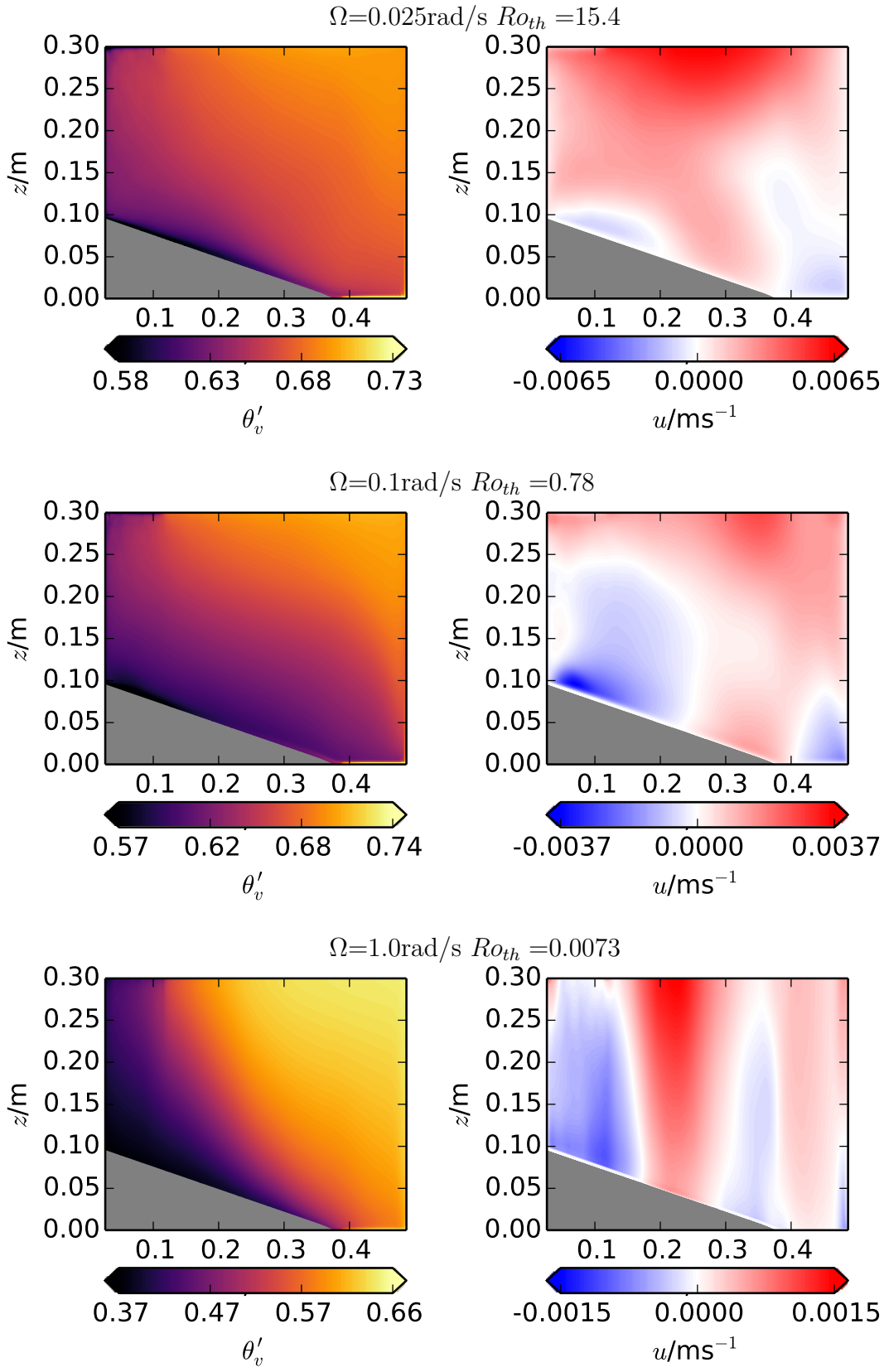


Figure 5.1: Zonal and time mean temperature (left) and zonal velocity fields (right) for runs at different rotation rates. These runs are from set C in table 3.2 and thus have idealised boundary conditions and a sloping bottom.

The alternating regions of prograde and retrograde motion which are suggestive of zonal jets are not seen without the β-effect.

At the slowest rotation rates, in both figure 5.1 and figure 5.2, there is a fast prograde velocity near the top of the tank. In the 2D simulations this was maximal under the cold plate whereas here the maximum is observed outside of the cold plate on the top surface. Scolan and Read (2017) showed the existence of fast moving fluid under the cold plate for low rotation rates in the experiment using dye streaks but the velocity was not quantified. In simulations where the applied flux through the hot plate is higher, which results in higher ΔT and hence higher Ro_{th}, we do see this structure in the simulations (see figure 5.3). Scolan and Read (2017) suggested that this intense region of prograde flow may be dynamically similar to the polar vortex seen on slowly rotating planets such as Titan and Venus.

5.1.2 Meridional overturning streamfunction

Figure 5.4 shows the Eulerian, overturning meridional mass streamfunction, defined as

$$\psi = -\int_z^d [\overline{v}] r dz' \tag{5.1}$$

for a number of different rotation rates. $[\cdot]$ denotes a zonal average and $\bar{\cdot}$ a time average. The simulations with the sloping bottom in the top two rows are taken from set C while the lower rows show flat bottomed simulations from set A. Other than the inclusion of the topography these simulations are identical and so any differences are due to the presence of the slope. Multiple overturning cells are observed with the number of cells increasing and the width of the cells and their strength decreasing with rotation rate for both flat and sloping bottom simulations. This is similar to the behaviour of the Hadley circulation in a planetary atmosphere as rotation rate is increased (Wang et al., 2018).

In the classical annulus the strong overturning circulation is confined to the sidewall boundary layers (e.g. figure 1.16 of Read et al. (2015)). Evidence of multiple cells and a greater role of the interior fluid in our simulations suggests that the new annulus configuration meets its goal of producing dynamics which are not

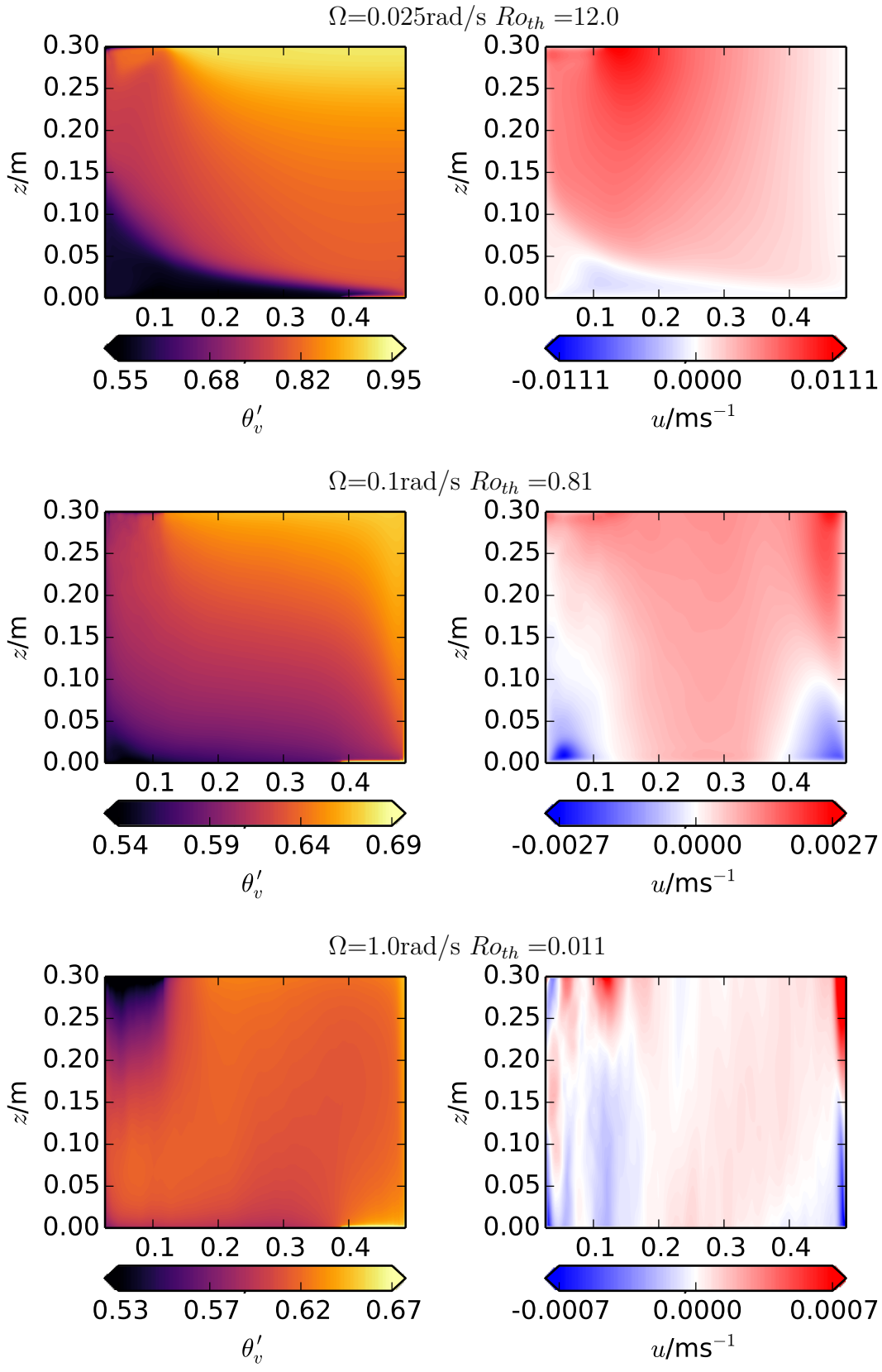


Figure 5.2: Zonal and time mean temperature (left) and zonal velocity fields (right) for runs at different rotation rates. These runs are from set A in table 3.2 and thus have idealised boundary conditions and a flat bottom. Aside from the absence of the sloping bottom these runs have the same setup as those shown in figure 5.1.

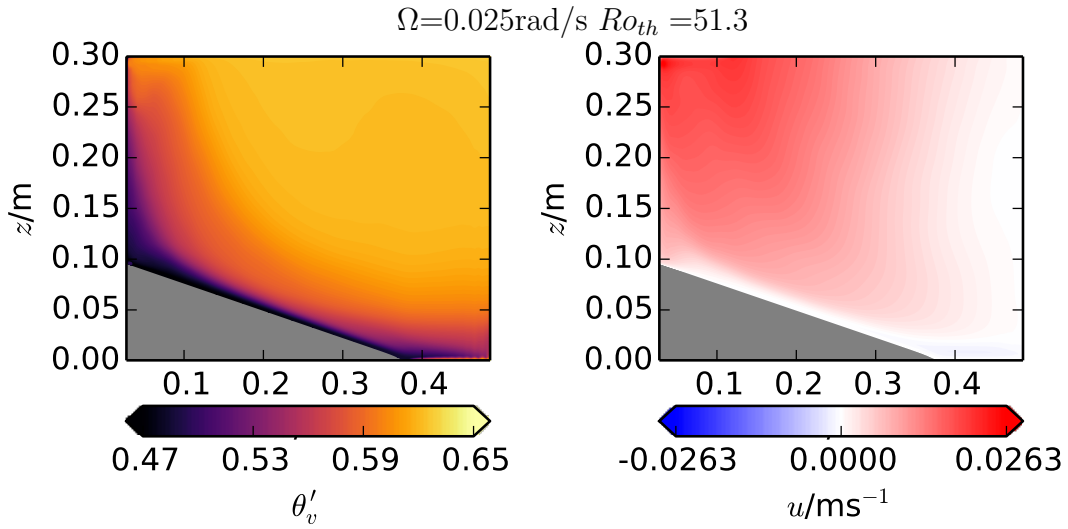


Figure 5.3: The zonally and temporally averaged temperature and zonal velocity field for a simulation with high thermal Rossby number where the zonal velocity maximum occurs underneath the cold plate.

as controlled by the boundary layers as in the classical setup. However, in all but the lowest rotation rate simulations, the streamfunction takes a maximum on the outer wall of the annulus and the width of this maximum region decreases with rotation rate. This may indicate that the Stewartson layers on the sidewall are confining the flow to a narrower layer as their width decreases with rotation rate.

At $\Omega = 0.025$rad/s the sloping bottom appears to make quite a significant difference to the form of the streamfunction. In the flat bottomed simulation a single, anticlockwise overturning cell spanning the entire domain is observed. However, once a slope is introduced a strong clockwise circulation is setup above the bottom of the slope. In general the overturning is stronger when the sloping bottom is present, presumably because the presence of the slope accelerates downslope density currents.

5.1.3 Potential vorticity

Ertel's potential vorticity is given by

$$q = \frac{\omega_a . \nabla \theta_v}{\rho} \tag{5.2}$$

where the absolute vorticity is given by $\omega_a = \nabla \times \mathbf{u} + 2\Omega$. Ertel's PV is conserved along isentropic surfaces. In the primitive equations it is analogous to QGPV in

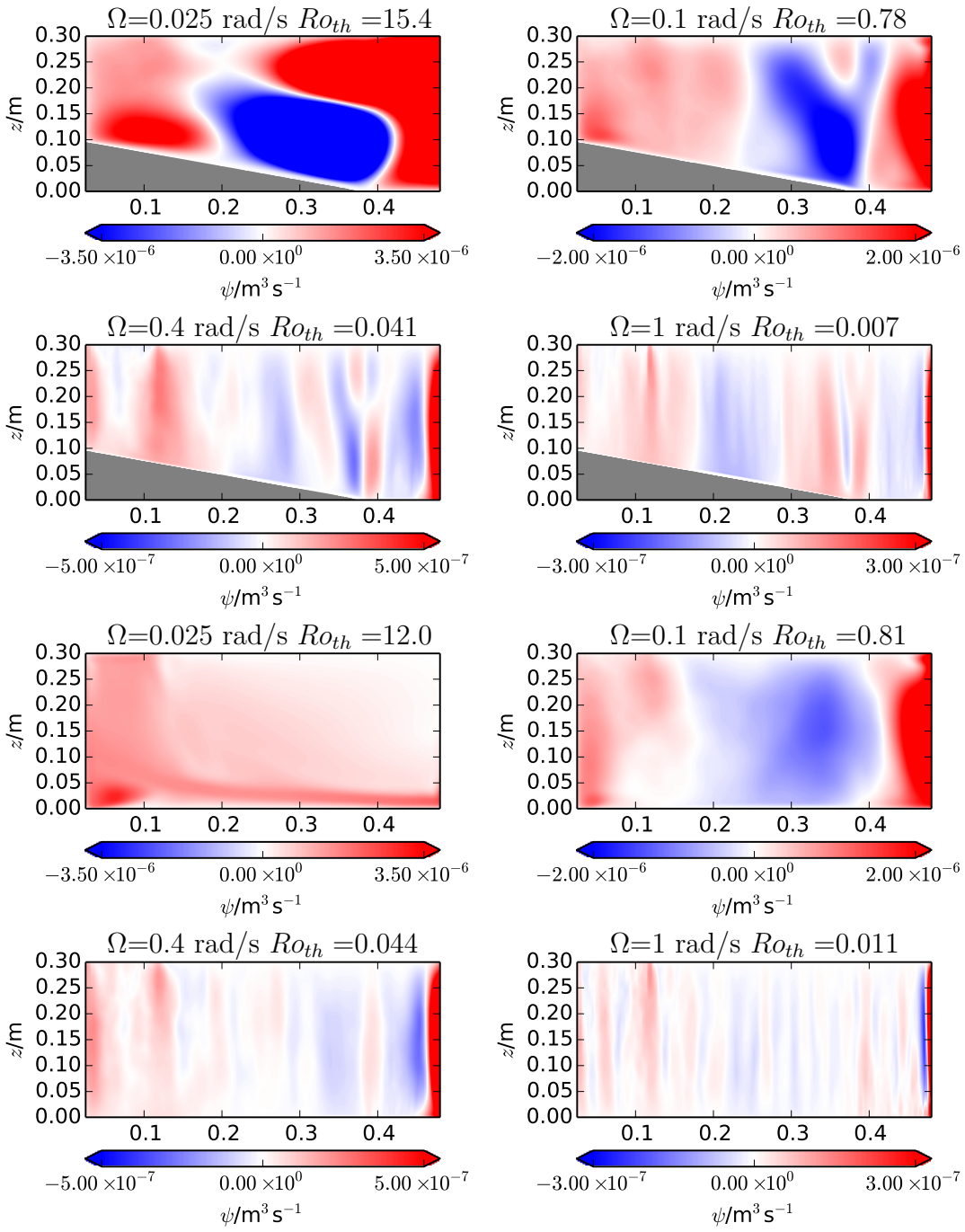


Figure 5.4: The meridional mass overturning streamfunction, ψ, shown for simulations from set C (top two rows) and set A (bottom row). A positive streamfunction represents anticlockwise motion whilst a negative streamfunction means the fluid is moving in a clockwise sense.

a quasi-geostrophic system and the two may be related using quasi-geostrophic scaling on isentropic surfaces to reduce equation 5.2 (Vallis, 2006). The freely convecting regions within our annulus are not consistent with the quasi-geostrophic approximation and so we first use the Ertel PV as a measure of the potential vorticity distribution across the entire annulus in simulations from set C.

Figure 5.5 shows how the zonally and temporally averaged Ertel potential vorticity field varies with rotation rate. The PV here is normalised by Ω (which is directly proportional to β) so that the different rotation rates may be compared. At the lowest rotation rate the potential vorticity is concentrated on the horizontal boundaries and directly under the cold plate. For moderate rotation rates the highest PV is located at the boundaries and interior PV is homogenised. As rotation rate increases the horizontal boundaries remain dominant but the interior flow also contains increasing PV.

Figure 5.6 shows snapshots of the horizontal PV field on the top surface of the flow and at mid height for simulations with $\Omega = 0.1, 1$rad/s. The mid-height fields are shown in the right hand column. Although the magnitude of the PV perturbations are on the order of 1% of those on the top surface there is evidently still a PV structure to the flow in the interior. The correlation between the structure of the field at different depths is not particularly strong apart from at the highest rotation rates where there is some anti-correlation. For $\Omega > 0.4$ rad/s the correlation coefficient is roughly -0.7 whereas it is between -0.3 and 0 for lower rotation rates. This may be compared with figure 5.7 where the deviation of the temperature field from the zonal mean outside of the cold plate is shown for the same simulations on the same levels. There are similarities between the vorticity and temperature anomaly fields, for example a wavenumber 4 pattern is clearly seen at both depths and in both fields for $\Omega = 0.1$rad/s. Furthermore, there is clearly a strong coherence of the large scale buoyancy structures at the two depths in the flow. This coherence in the temperature structure and the dominance of the boundaries in the PV fields suggests that surface quasi-geostrophy may be a relevant framework for the analysis of this system.

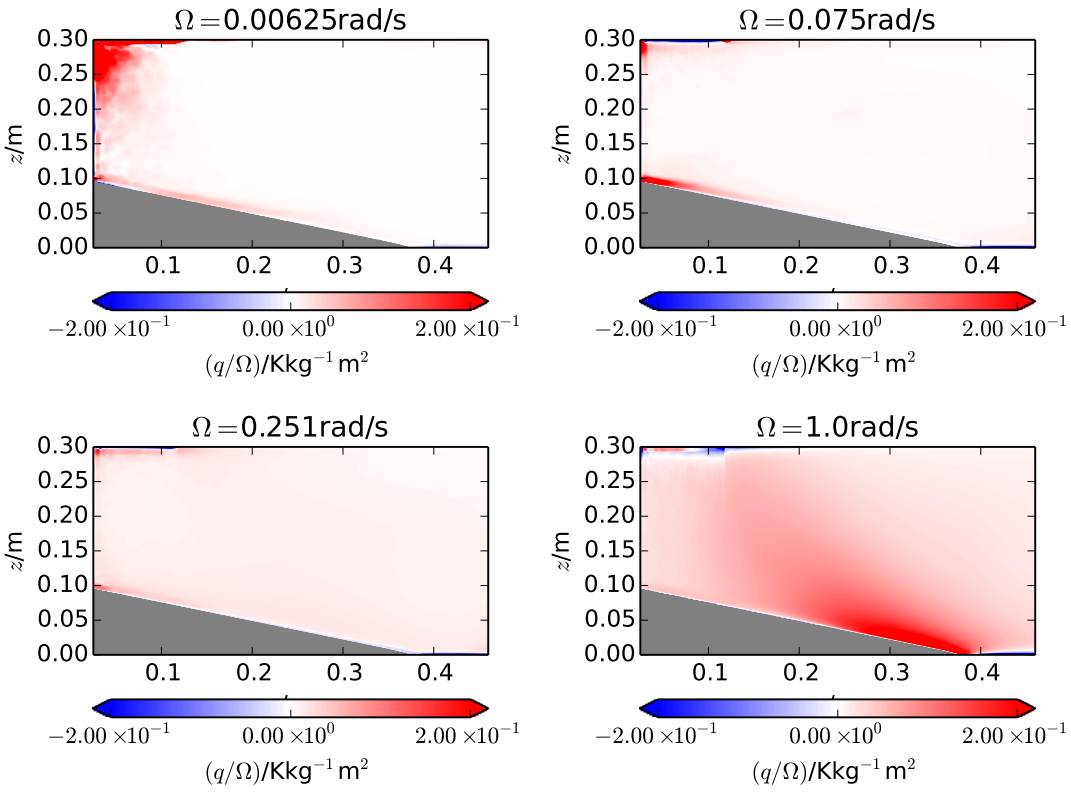


Figure 5.5: The time and zonal average of the potential vorticity, q for simulations in set C at different rotation rates. The fields are normalised by Ω.

Recall from chapter 1 that within the quasi-geostrophic framework a necessary (though insufficient) criterion for baroclinic instability is that one of the Charney-Stern-Pedlosky (CSP) criteria (Charney and Stern, 1962; Pedlosky, 1964) must be fulfilled. If baroclinic adjustment is a correct interpretation of the dynamics and the eddies neutralise the mean state to baroclinic instability, the eddies must mix the PV to the extent that the mean flow is stable. In the atmosphere the surface temperature gradients are clearly not homogenised and it has been suggested that neither are the interior PV gradients (Zurita-Gotor and Lindzen, 2007). However, this is not necessarily an argument against baroclinic adjustment if other processes such as dissipation play an important role, as may be the case in the surface boundary layer. We now consider the quasi-geostrophic potential vorticity (QGPV) of simulations in set A in light of the CSP criterion. The QGPV is estimated

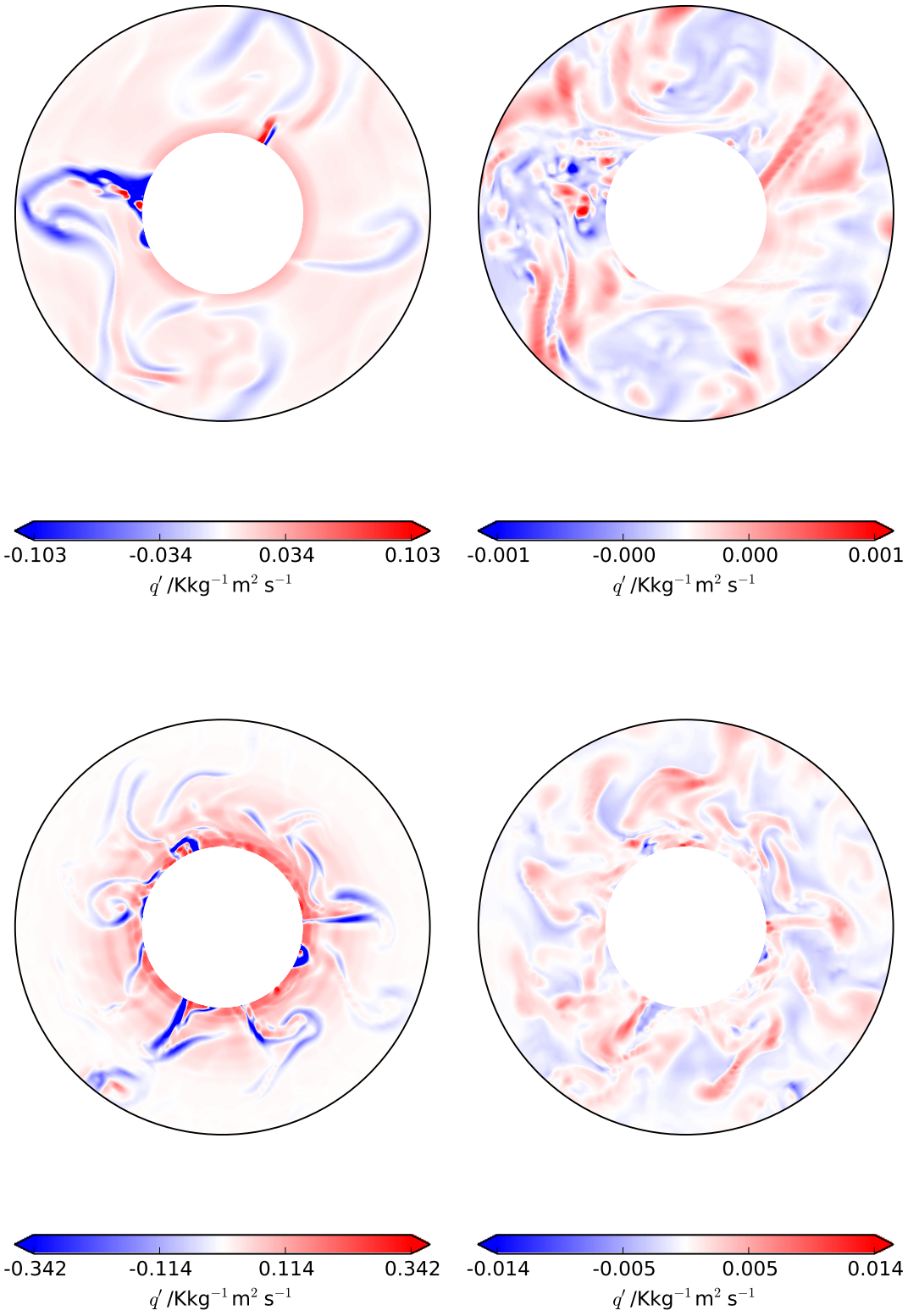


Figure 5.6: Instantaneous snapshots of the potential vorticity deviation from the zonal mean on the top surface of the fluid (left hand column) and at mid-height (right hand column). The top row shows simulations where $\Omega = 0.1$rad/s and the bottom row shows simulations with $\Omega = 1$rad/s. Only radii outside the cold plate are shown.

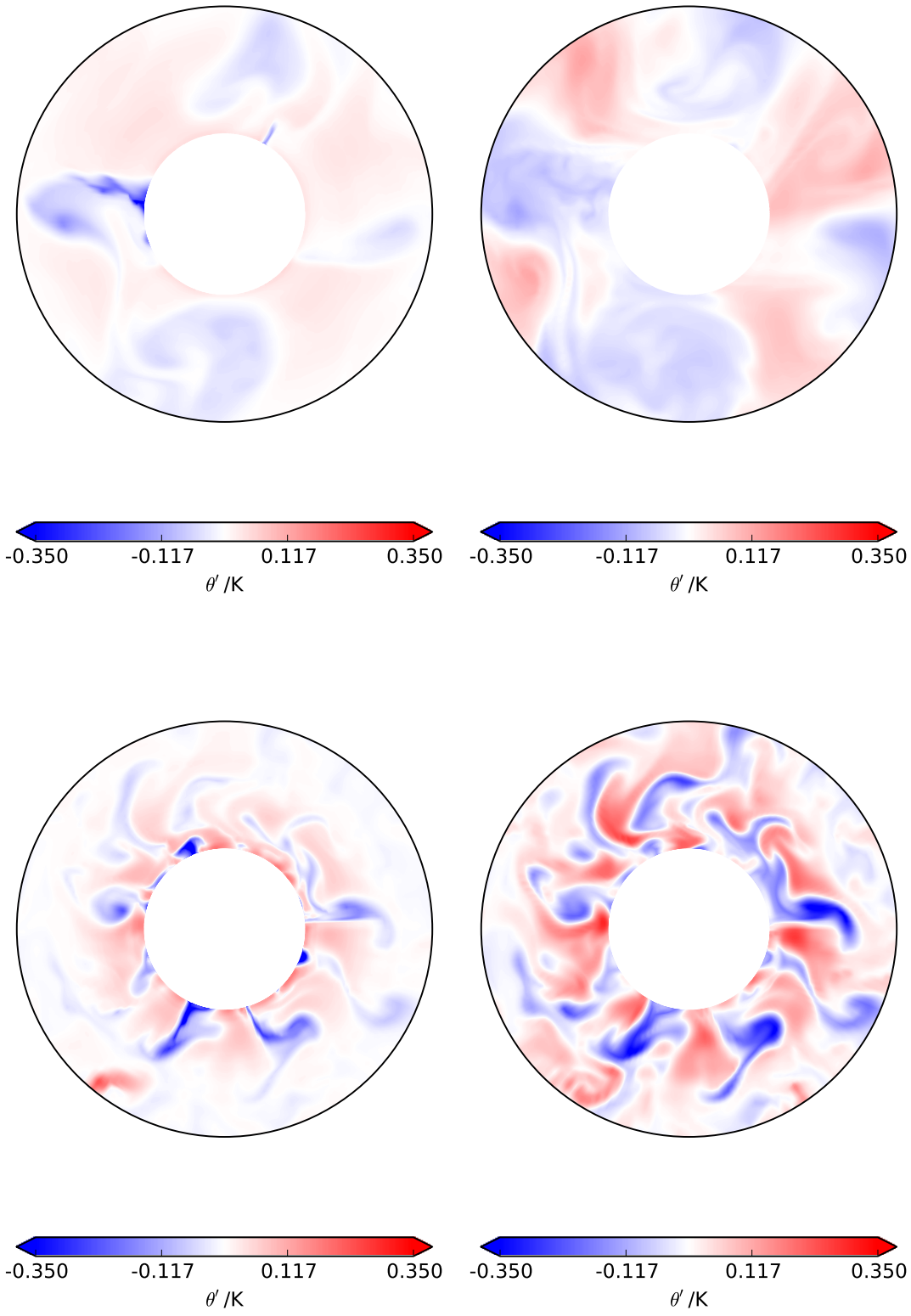


Figure 5.7: Instantaneous snapshots of the temperature deviation from the zonal mean on the top surface of the fluid (left hand column) and at mid-height (right hand column). The top row shows simulations where $\Omega = 0.1$rad/s and the bottom row shows simulations with $\Omega = 1$rad/s. Only radii outside the cold plate are shown.

following Pérez-Pérez et al. (2010) as

$$q = f + \frac{1}{f\rho_0}\left[\frac{1}{r}\frac{\partial}{\partial r}\left(r\frac{\partial p'}{\partial r}\right) + \frac{1}{r^2}\frac{\partial}{\partial \theta}\left(\frac{\partial p'}{\partial \theta}\right)\right] - \frac{f}{g\alpha_v\rho_0}\frac{\partial}{\partial z}\left(\frac{\partial p'/\partial z}{\partial \tilde{T}/\partial z}\right) \tag{5.3}$$

where $p'/(\rho_0 f)$ is the quasi-geostrophic streamfunction, $\tilde{T}$ is the temporally and horizontally averaged temperature field and p' is the deviation of the pressure from the temporally and horizontally averaged pressure field. The freely convecting regions are neglected and averages are taken over the central baroclinic zone. Figure 5.8 shows the vertical profiles of the meridional gradient of QGPV in the centre of the baroclinic zone for simulations in set A with high rotation as this is a requirement for the validity of the QG approximation.

In the simulation where $\Omega = 0.4$rad/s the QGPV gradient is approximately zero in the interior of the fluid and the sign change which is required for instability is manifest in the oppositely signed QGPV gradient on the top and bottom boundaries. This configuration is similar to the QGPV distribution in the Eady model where the interior PV gradients are equal to zero and the flow is governed by advection of potential temperature anomalies on the boundaries (Eady, 1949). The temperature anomalies on the boundary are dynamically equivalent to a delta function or 'sheet' of PV located on the boundary (Bretherton, 1966). In the simulation where $\Omega = 1$rad/s the PV structure is slightly more complex. Although the gradients on the boundaries are of opposite sign and large magnitude, there is also a sign change in QGPV gradient in the fluid interior. This may suggest that, in this case, a number of modes of instability are possible. However, it should be noted that the CSP criteria are derived from linear theory and thus may not be fully descriptive of the complex non-linear flows seen in the annulus at high rotation rates. The very strong QGPV gradients on the boundaries support our previous assertions that SQG theory may be able to provide a description of certain aspects of the flow in the annulus.

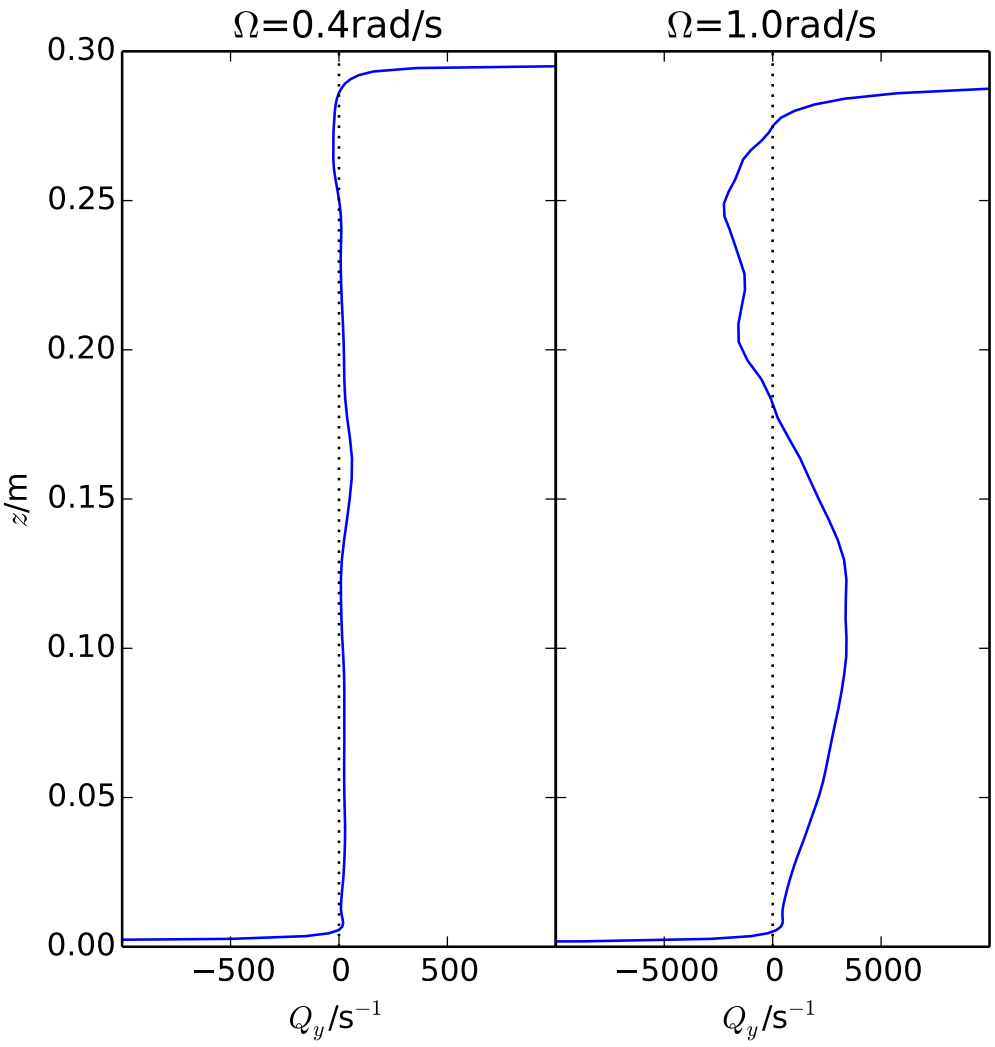


Figure 5.8: The vertical profile of the zonally and temporally averaged radial gradient of quasi-geostrophic potential vorticity, Q_y, at mid radius for two of the highest rotation rates. The black dotted line marks Q_y=0.

5.2 The criticality parameter

5.2.1 Radial temperature gradients

Thus far, in the experiment, temperature measurements have been made at only one radial position within the baroclinic zone and so the radial temperature gradient within the fluid cannot be determined. However, this quantity is of interest for calculating the isotherm slope and criticality of the fluid and so we proceed to measure it from the simulations. In future it would be possible to measure in

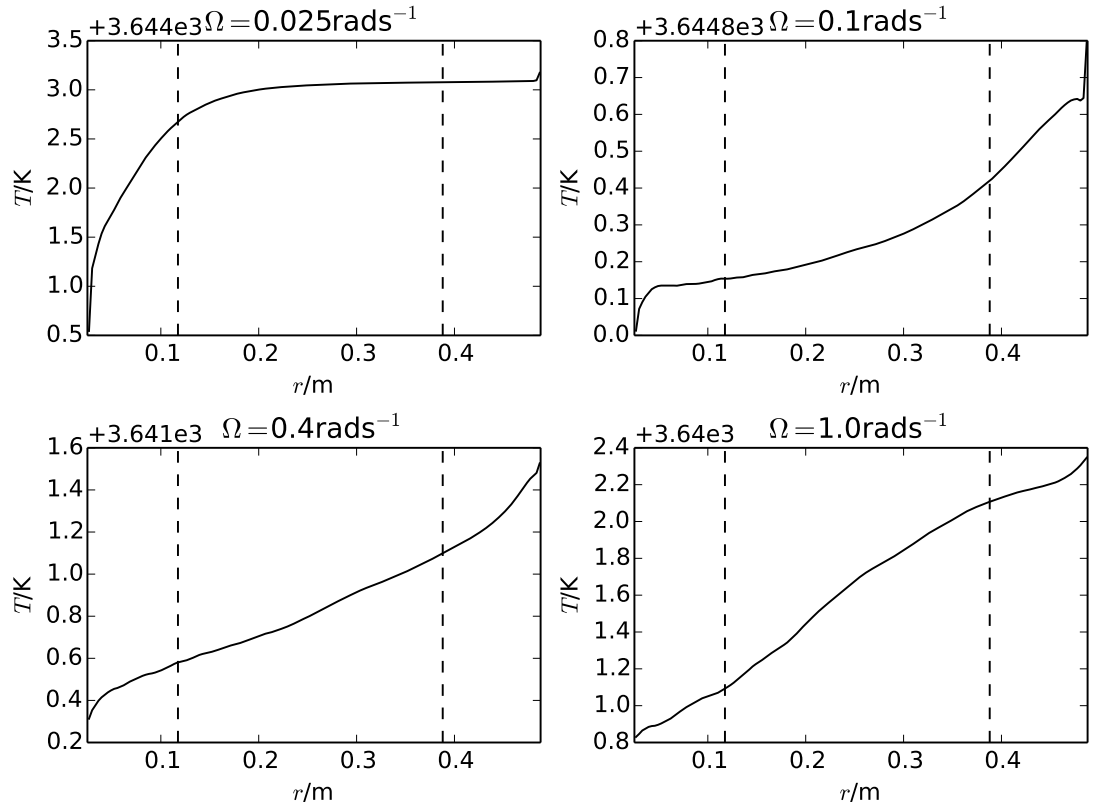


Figure 5.9: The temporally and zonally averaged radial temperature profiles at mid height in simulations from set E at a number of different rotation rates. The dashed lines show the limits of the central baroclinic zone.

the experiment if more than one thermal probe were setup within the baroclinic zone. Examples of the radial temperature profiles at mid-height for simulations in set E where boundary heat loss is parameterised are shown in figure 5.9 with dashed lines delineating the baroclinic zone. At the slowest rotation rate the fluid is approximately isothermal other than under the cold plate where temperature changes rapidly with radius due to the cold gravity current running down the inner wall. For the other runs the temperature gradient is approximately uniform across the baroclinic zone, with temperature increasing towards the outer wall. Unlike in the 2D runs (see figure 2.4) where the convective zones were approximately isothermal in radius at moderate rotation rate we observe strong radial gradients across the convective zone in most of the simulations.

The radial temperature gradients across the baroclinic zone at mid-height for

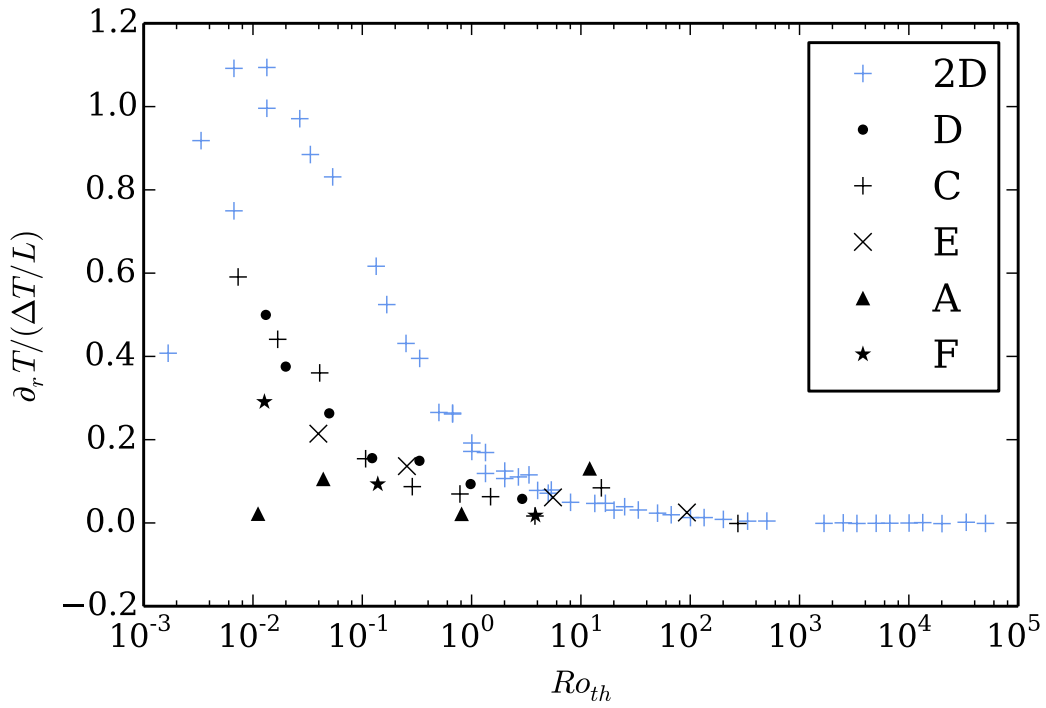


Figure 5.10: The radial temperature gradient across the baroclinic zone at mid-height in both the 2D and 3D simulations with symbols representing different sets of simulations shown in the legend.

a range of 2D and 3D simulations are summarised in figure 5.10. As with the vertical stratification, there is good agreement between the 2D and 3D runs at low rotation rates but, once the flow becomes baroclinically unstable, the radial gradient is lower in 3D. This indicates that the eddies increase mixing and hence reduce the thermal gradients in the interior of the fluid. The gradients increase with rotation rate as heat transfer becomes suppressed by the rotation. The overall trend is very similar to that seen in the vertical stratification.

5.2.2 Isotherm slopes and criticality

The criticality parameter has received much attention in the literature due to the prediction by baroclinic adjustment theories that the fluid adjusts to a state with $\xi \approx 1$ as outlined in chapter 1. Having investigated the horizontal and vertical temperature gradients individually we are now in a position to compute

the isotherm gradients and hence the criticality for the data from the simulations. In our simulations the ratio

$$\frac{f}{\beta d} = \frac{\overline{d}}{d \tan \chi} = 3.29 \tag{5.4}$$

is constant so the criticality is proportional to the isotherm gradient. Note that, unlike on the Earth where the ratio f/β is approximately equal to the planetary radius, in the annulus it is 2-3 times the horizontal length scale. The exact value of the criticality is somewhat dependent on the averaging used to calculate the vertical and radial gradients. However, the maximum variation is found to be on the order of 5% and the trends in the data remain essentially the same whichever calculation is used. For the data shown in this section all calculations are averaged over the mid-channel region of the annulus cavity where 8cm$<z<$22cm and 15.65cm<r<25.65 cm. Thus, the convective zones and the horizontal boundary layers are excluded from the calculation.

Figure 5.11 shows the criticality via a plot of bulk vertical temperature difference, $d\partial_z T$, against bulk radial temperature difference, $\frac{f}{\beta}\partial_r T$. The dashed line represents $\xi = 1$ with supercritical flows lying below the line and subcritical flows above. From the analysis in section 4.3 we know that the flows with higher bulk temperature differences correspond to flows at higher rotation rate for simulations in a given set. Although there is some spread in the data the broad trend is that $\xi \approx 1$ when the radial temperature gradient is small and the flow becomes increasingly supercritical as rotation rate increases. Although both the vertical and radial bulk temperature differences increase with rotation rate, the faster increase in the radial gradient leads to larger criticality.

Figure 5.12 shows the criticality as a function of the Rossby deformation radius normalised by the width of the baroclinic zone, a. This is equal to the square root of the Burger number. The Rossby radius is the scale where baroclinic instability is generated. Hence, when the ratio R_D/a is close to one the size of the domain limits the ability of baroclinic waves and eddies to form. The runs which have $R_D \approx a$ are those within the axisymmetric regime where no baroclinic instability

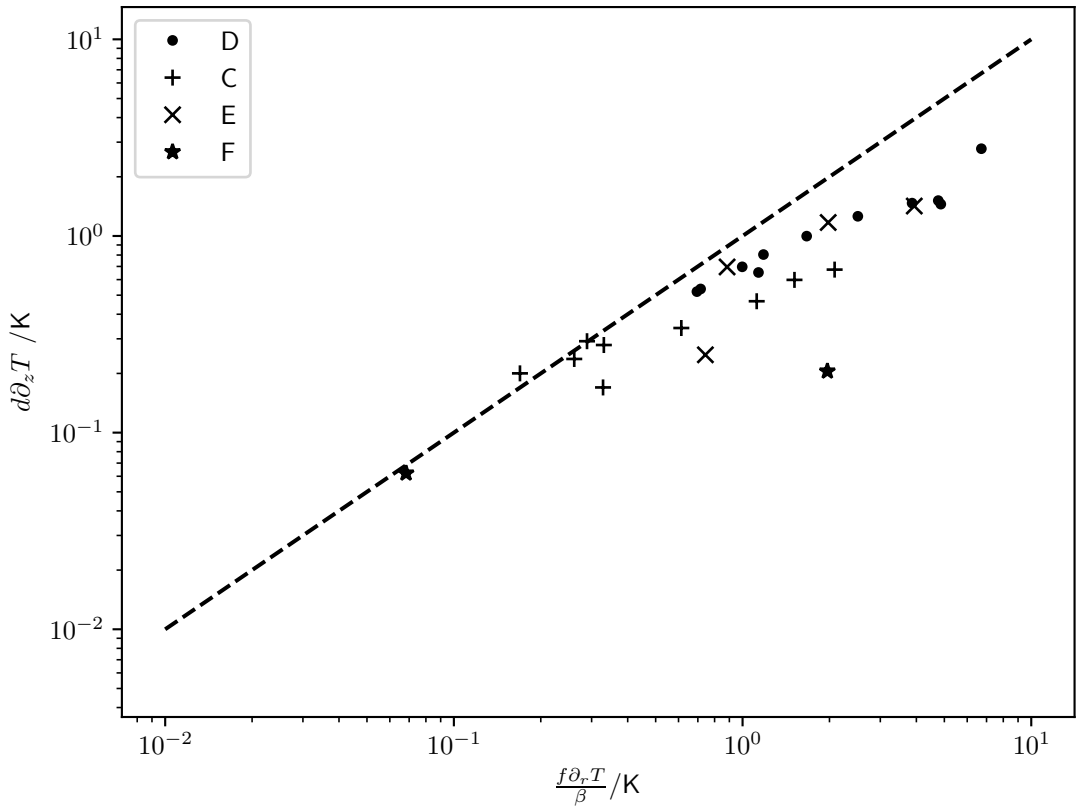


Figure 5.11: The bulk vertical temperature difference, $d\partial_z T$, against bulk radial temperature difference, $\frac{f}{\beta}\partial_r T$. Symbols represent simulations from different sets labelled by letters C-F. The black dashed line shows where $\xi = 1$. Below the line flows are supercritical and above it flows are subcritical.

occurs. Due to efficient mixing by the mean overturning circulation, the interior of the fluid is approximately isothermal here so the criticality is not well defined as both vertical and radial temperature gradients are close to zero.

At smaller values of R_D/a, for runs in the regular wave regime, the criticality is approximately constant with a value slightly larger than one for sets D and E and approximately one for set C. This suggests that the equilibrium value of the criticality has some dependence on the applied temperature difference as the main difference between these simulations is the larger applied heat flux at the heat sink in sets D and E.

For $R_D < 0.2a$ the supercriticality begins to increase such that $\xi \sim R_D^{-3/4}$. This

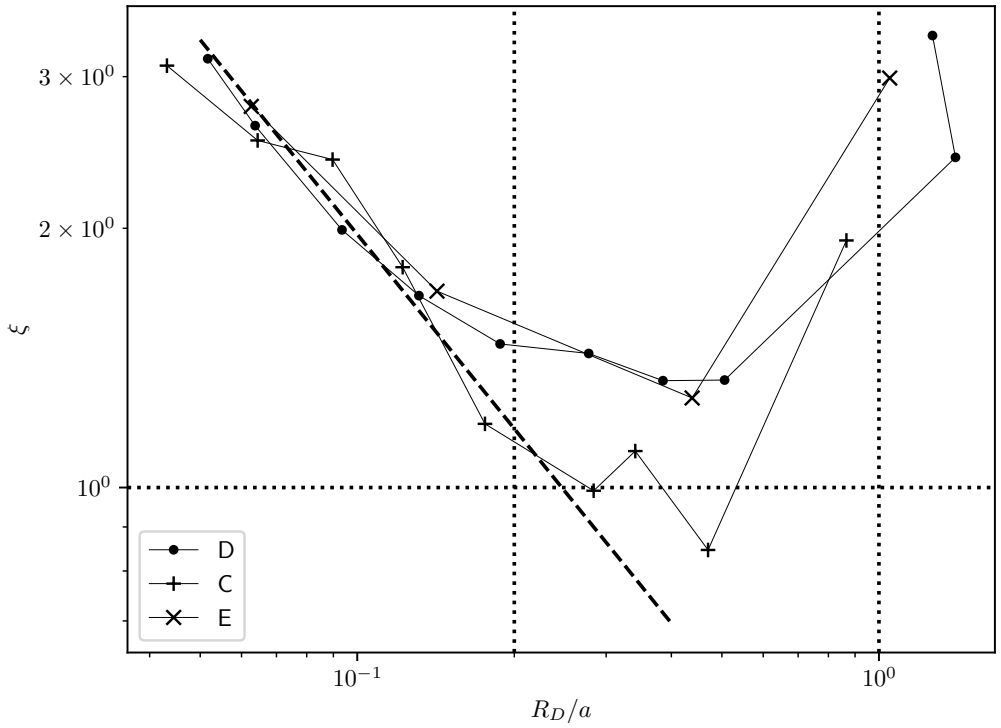


Figure 5.12: The criticality, ξ, as a function of the Rossby deformation radius, R_D, normalised by the width of the baroclinic zone, a. The dotted horizontal and vertical lines indicate where $\xi = 1$ and $R_D = a$ respectively. The black dashed line has a slope of -3/4.

is in line with the prediction of Jansen and Ferrari (2012) for the scaling of the criticality parameter in the regime where the flow is supercritical which was outlined in chapter 1. In this regime the flow is irregular and turbulent. Our result is in good agreement with much of the recent work on the variation of the criticality parameter in primitive equation systems where it has been found that the criticality is resistant to change in certain regimes but can vary strongly when large enough changes are made to the forcing (Schneider, 2004; Zurita-Gotor and Vallis, 2011; Jansen and Ferrari, 2012; Jansen and Ferrari, 2013a).

5.3 Eddy fluxes

The transport of heat through the system which results in the equilibrated structure outlined above can be characterised by the heat flux in each of the co-ordinate

directions which may be further separated into contributions from the eddies and from the zonal mean, background flow. A Reynolds decomposition allows any single variable to be written as $v = [\overline{v}] + \overline{v^*} + v'$ where $[\cdot]$ denotes a zonal mean, $\bar{\cdot}$ denotes a time mean, $\cdot^*$ denotes a departure from the zonal mean and $\cdot'$ denotes a departure from the time mean. Hence

$$[\overline{vT}] = [\overline{v}][\overline{T''}] + [\overline{v^*T^*}] + [\overline{v'T'}]. \tag{5.5}$$

T'' is the deviation from the horizontal mean temperature or the rz plane mean temperature in the case of the vertical flux. The first term on the right of equation 5.3 is the heat flux due to the mean flow and the second and third terms are the stationary and transient eddies respectively. Due to the axisymmetric topography we do not observe stationary waves in the annulus.

5.3.1 Mean and eddy heat fluxes

The mean heat fluxes and combined stationary and transient eddy heat fluxes are shown in figure 5.13 for simulations from set C. Rotation suppresses the overturning Hadley-like circulation and so the mean fluxes fall with rotation rate and become increasingly confined to the boundaries. The dominant vertical eddy heat flux is under the cold plate and is likely due to convection rather than baroclinic activity. In contrast the meridional eddy heat flux has an approximately constant magnitude everywhere outside of the boundary layers where it goes to zero because of the no slip boundary conditions. The overall effect of the eddies is to transport heat upwards and to smaller radii at all rotation rates.

The heat fluxes for all rotation rates in set E are summarised in figure 5.14. The heat flux at each value of Ro_{th} is summarised by the peak integrated value in Watts. For the meridional flux this is calculated as

$$F_{max} = \mathrm{Max}\left(\int_0^d \int_0^{2\pi} \rho c_p \overline{v'T'} r d\theta dz\right) \tag{5.6}$$

where Max indicates that the maximum value is taken. For the vertical heat flux we follow the same procedure but integrating over $r\theta$ surfaces rather than $z\theta$

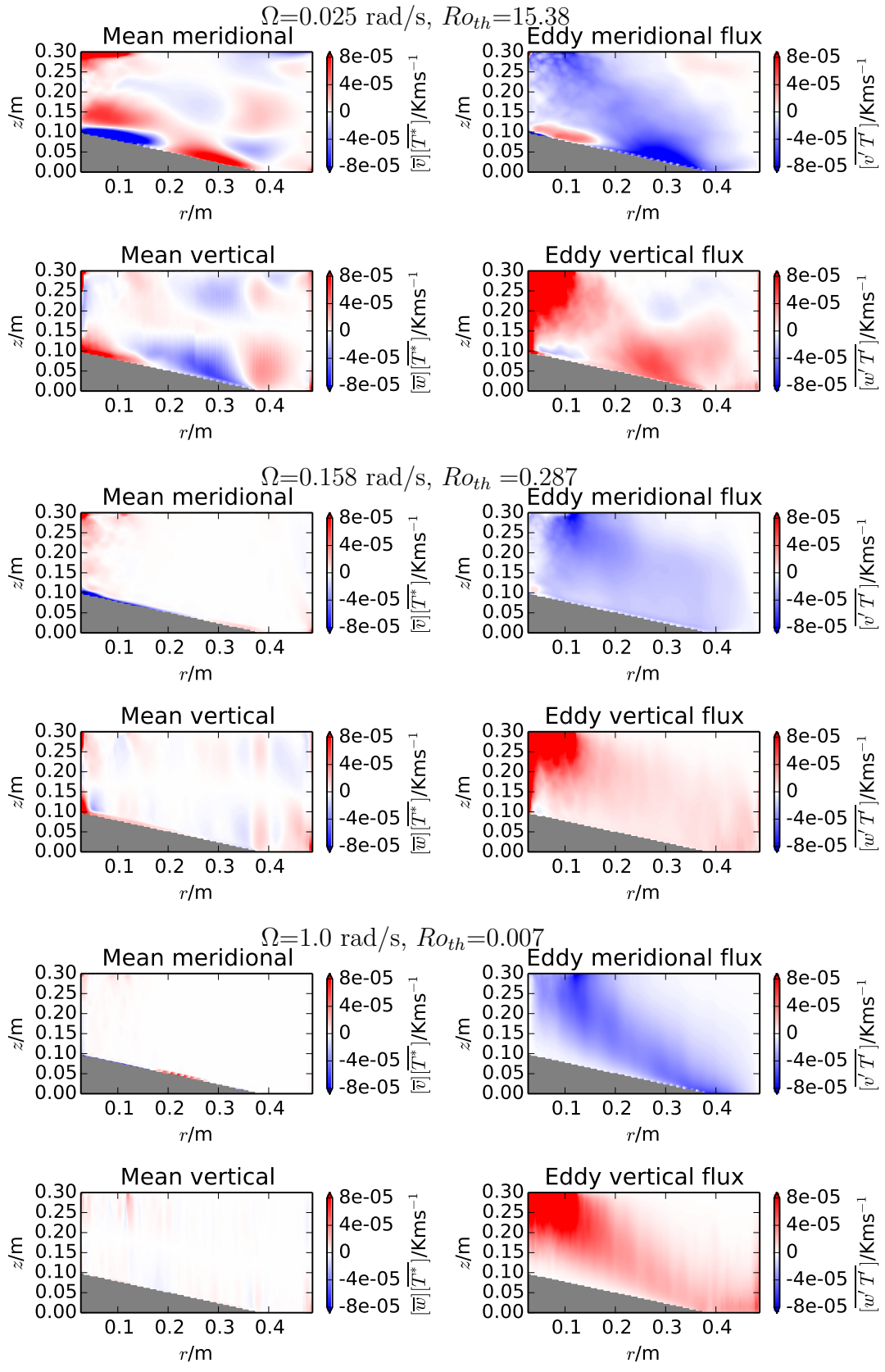


Figure 5.13: Zonally and temporally averaged mean and eddy heat fluxes in the vertical and meridional directions in the rz plane for low, moderate and high rotation rate simulations in set C.

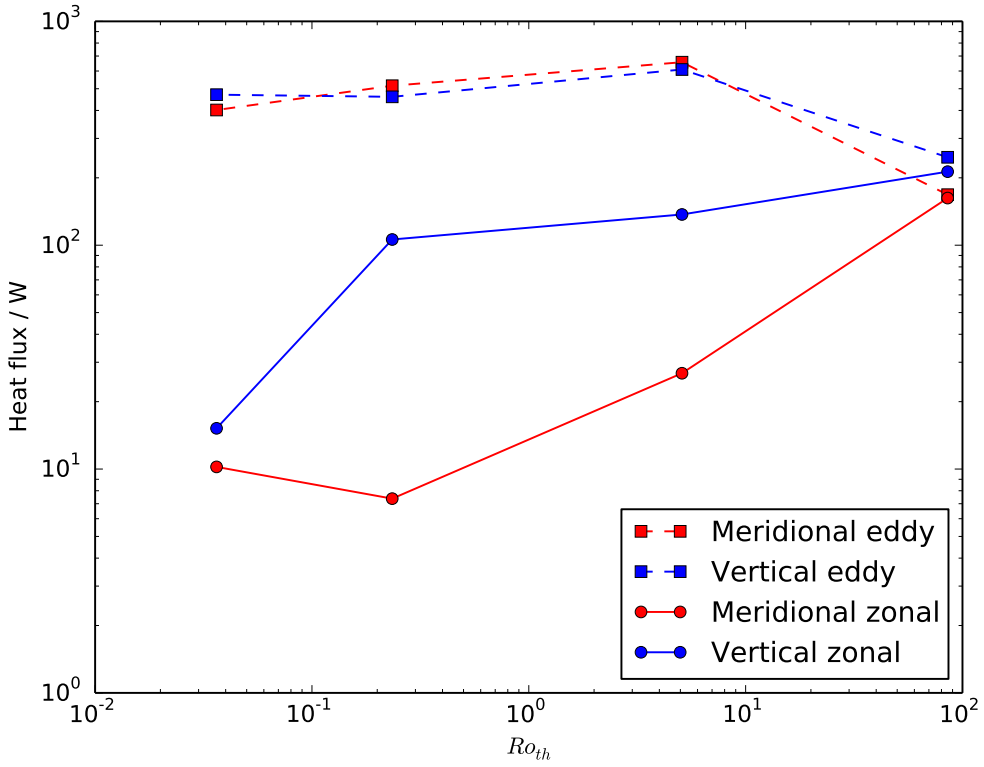


Figure 5.14: The peak mean meridional (red) and vertical (blue) heat fluxes (solid lines with circular markers) and peak eddy meridional and vertical heat fluxes (dashed line with square markers) for simulations in set E. Reference to a 'zonal' flux in the legend means the flux due to the non eddy component of the flow.

surfaces. As expected, the heat flux due to the mean overturning decreases with increasing rotation. The rate of decrease is faster for the meridional flux than in the vertical direction, probably because the contribution to the vertical flux from the convection remains quite strong, even at higher rotation rates. At all but the lowest rotation rate the eddy heat flux dominates over the mean flux and the vertical and meridional components are quite similar. An increase in the eddy flux is seen at the onset of baroclinic instability but otherwise it varies very little with rotation rate compared to the flux due to the mean flow.

That the eddy fluxes are adiabatic and hence transport heat along the isotherms is confirmed by figure 5.15. The isotherm gradient as a function of the ratio between

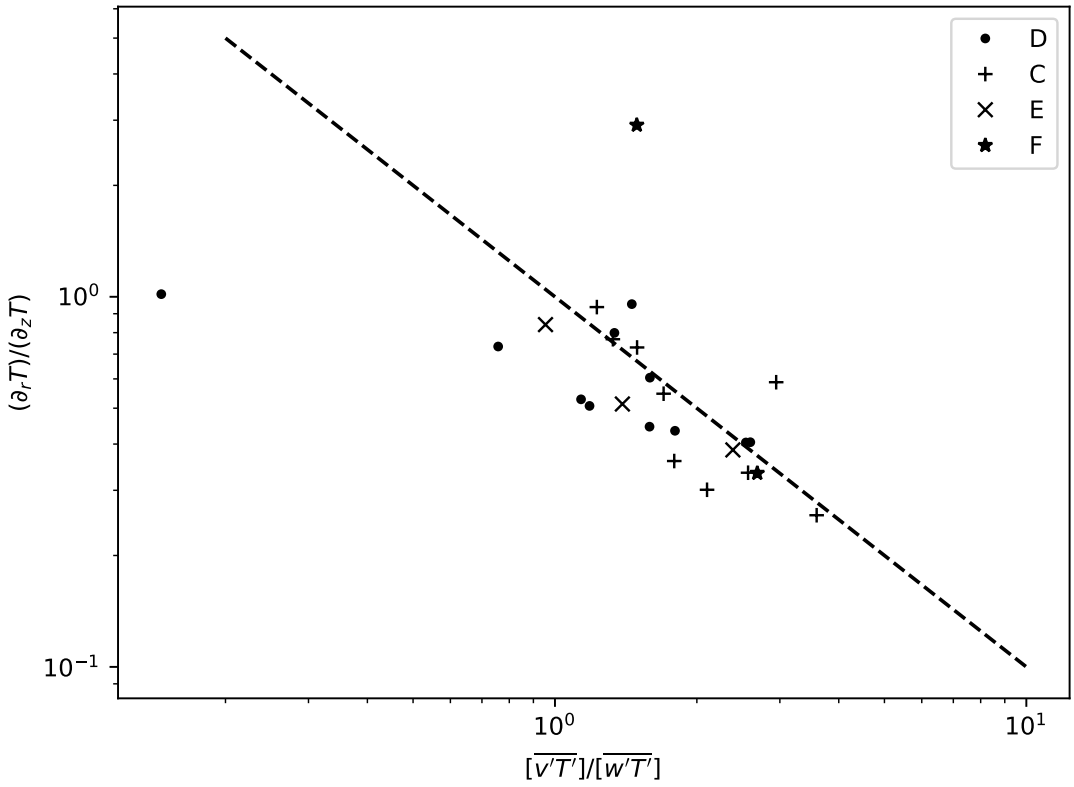


Figure 5.15: The absolute value of the isotherm gradient versus the ratio of the meridional to the vertical eddy heat flux from simulations. The equation of the solid line is $y = 1/x$.

meridional and vertical flux is shown for a range of simulations. The scaling

$$\frac{\overline{w'T'}}{\overline{v'T'}} \approx \frac{\partial_r T}{\partial_z T}. \tag{5.7}$$

suggests that the overall eddy heat flux is directed along the isentropes. Zurita-Gotor and Vallis (2009) showed via a local energy balance that this relation is expected to hold for adiabatic eddies. It is notable that this relation appears to hold across the simulations, regardless of the flow regime.

As discussed in chapter 1, the idea that eddy fluxes behave in a diffusive manner by carrying out down gradient transport is used ubiquitously as a means of eddy-mean flow closure. It is commonly employed as an assumption in parameterising eddies and has also been invoked in deriving predictive frameworks for the equilibrated mean state of the atmosphere based on geostrophic turbulence and mixing

length assumptions (Larichev and Held, 1995; Held and Larichev, 1996; Zurita-Gotor and Lindzen, 2007; Zurita-Gotor and Vallis, 2009; Jansen and Ferrari, 2012). However, Pfeffer et al. (1980) and Pérez-Pérez et al. (2010) found that eddy heat fluxes do not necessarily transport heat downgradient in the manner of Fickian diffusion in the classical annulus in the regime where fully developed baroclinic waves exist. In the previous section we found that, at large Burger numbers, our data appears to follow the scaling of Jansen and Ferrari (2012) which relies on the diffusive closure of Held and Larichev (1996).

Figure 5.16 shows the spatial correlation coefficient between the meridional eddy flux and the meridional temperature gradient as a function of R_D/a for a range of simulations. The correlation is calculated in the baroclinic zone excluding the boundary layers. If the eddies behave as Fick's law of diffusion we expect a strong negative correlation between the two fields as

$$\overline{v'T'} = -D\frac{\partial T}{\partial r} \tag{5.8}$$

where D is the eddy diffusivity.

For R_D/a>1 and $R_D/a < 0.1$ the correlation is observed to be strong and negative between the two fields, indicating that a diffusive closure may be an appropriate representation of the eddy fluxes. $R_D/a < 0.1$ is the range for which the scaling of Jansen and Ferrari (2012), which is based on a diffusive closure, appeared to hold. At the lowest rotation rate in set C the correlation is close to zero which may be because ΔT is much lower for simulations in that set resulting in much smaller radial temperature gradients that would not be compatible with diffusive behaviour by the eddies. For the range where we found the criticality to be approximately constant, $0.2 < R_D/a < 1$, the correlation is generally weak and, in some cases, positive which suggests up gradient transport. In this regime the flow is dominated by regular, large scale baroclinic waves and a lack of downgradient, diffusive transport was previously found in flows where these waves dominate (Pfeffer et al., 1980; Pérez-Pérez et al., 2010). Hence it is not surprising that the scaling of Jansen and Ferrari (2012) breaks down in this regime. The absence of diffusive

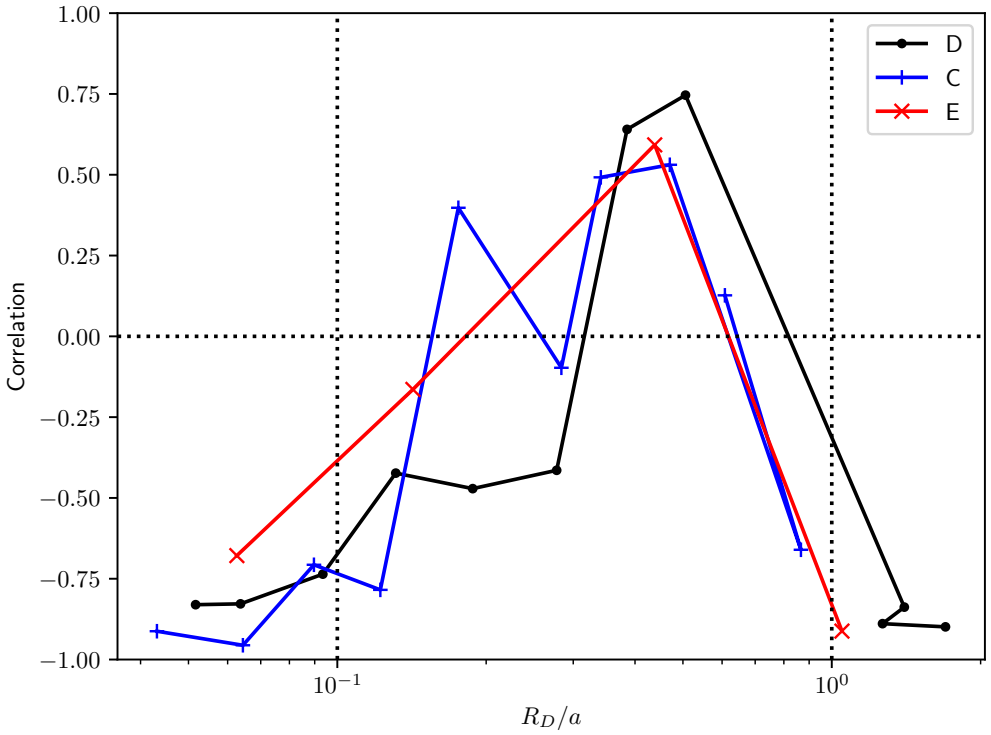


Figure 5.16: Spatial correlation coefficient between the radial eddy heat flux ($v'T'$) and the radial temperature gradient $\partial_r T$ as a function of the normalised deformation radius, R_D/a for simulations in sets C, D and E.

behaviour in the presence of large scale baroclinic waves suggests that turbulence closures which begin with the assumption that the relation in equation 5.8 holds are only suitable for some regimes in the current experiment.

5.4 Discussion

In this chapter we have investigated various aspects of the simulated flow in the annulus, paying particular attention to diagnostics relevant to theories of thermal eddy equilibration. We found that, in the simulations, both the stratification and radial temperature gradients in the baroclinic zone increase with rotation rate. The increase in stratification is the slower of the two and hence the criticality diverges from a constant value as rotation rate increases. Ultimately, in the limit of very strong rotation, the temperature gradients are expected to tend to those of the

conducting solution which has very weak unstable stratification and some finite radial gradient which is approximately proportional to ΔT. This state places a theoretical maximum on the criticality that can be accessed in this system but this is large due to the small vertical temperature gradients in the conductive state. To verify our calculations of supercriticality it would be useful to have a measure of the radial temperature gradient across the baroclinic zone in the experiment.

The observed increase in criticality at high rotation rates can be understood by considering how the deformation radius changes with rotation. At the lowest rotation rates the deformation radius is similar to the size of the domain and so baroclinic instability is suppressed. Criticality does exceed one in this regime but this is probably due to convection being the dominant instability and acting to neutralise the vertical gradients, thus increasing the criticality.

Once the deformation radius is less than 20% of the width of the baroclinic zone the criticality increases rapidly. This increase is concurrent with the prediction of Jansen and Ferrari (2012) that $\xi \sim R_D^{-3/4}$. This is based on a diffusive closure where the diffusion coefficient is reduced as the deformation scale decreases. The increasing criticality suggests that at these scales non-linear eddy-eddy interactions become important and an inverse cascade may exist. These phenomena will be further investigated in the next chapter. The regime where increasing criticality is seen is coincident with the existence of the irregular wave regime described in chapter 4.

At intermediate values of the deformation radius there is some evidence that the criticality saturates to an approximately constant value. In this regime it was also found that the horizontal eddy fluxes do not obey a downgradient diffusive closure and the flow is dominated by large scale, regular baroclinic waves with low frequency. The constancy of the criticality in this regime may suggest that some form of baroclinic adjustment is taking place. In previous studies these large scale waves were found to be very efficient agents of heat transport (Read, 2003).

We also studied the potential vorticity structure of the flow. This revealed that the PV field is dominated by the temperature gradients on the horizontal boundaries with the interior PV gradient being much smaller - although non zero.

This structure is consistent with the homogenisation of the PV field by baroclinic eddies in the interior for at least some rotation rates. For the highest rotation rate investigated there was non-zero PV gradient and a sign change in the QGPV gradient in the flow interior. The potential vorticity structure identified here is similar to the PV structure of the Eady model (Eady, 1949) and the related surface quasi-geostrophic (SQG) equations (Blumen, 1978; Held et al., 1995). Classically the SQG equations describe a semi-infinite domain containing constant PV bounded above or below by a surface upon which buoyancy anomalies are advected by the geostrophic velocity. It is this motion of anomalies on the surface which drives the flow. When the semi-infinite domain is replaced by a finite depth volume, one obtains the system described by the Eady model. As with QG theory, SQG applies to flows with strong rotation and strong stratification and so is not expected to be relevant to the full range of simulations shown here. The coherence of the large scale temperature structure with depth in our flows is also suggestive of SQG dynamics where structures decay away from the surface at a rate proportional to their wavenumber. In the next chapter we will continue to investigate the relevance of SQG dynamics to this system.

And little whorls have lesser whorls
And so on to viscosity.

— Lewis Fry Richardson

6

Energy transfer in the annulus

The results of the previous chapter suggested that the behaviour of the criticality is dependent on the size of the deformation radius relative to the size of the domain. In chapter 1 we also noted the importance of the criticality as a measure of the extent of any inverse cascade in the flow. Conversely, if non-linear eddy-eddy interactions are active and result in an inverse cascade the criticality will deviate from the constant value predicted by baroclinic adjustment. To explore these observations further we turn to a representation of the flow in spectral space to investigate how energy is concentrated at different spatial scales and how it is transferred between these scales.

We have already suggested that SQG, described in chapter 1 may be a particularly relevant framework for the dynamics observed in our annulus. However, we approach the diagnosis of the spectral properties of the experimental flows with caution as they are substantially different from the heavily idealised situations dealt with by this theory. For example, turbulence theories generally assume that energy and enstrophy are input and dissipated at a localised wavelength and that there is a well defined inertial range between the sources and sinks of energy and enstrophy. This is unlikely to be the case in our system where both baroclinic instability and convection act as energy sources and evaporation from the top surface of the experimental flow adds an additional complication to the energetics near the top surface. To diagnose the direction and rate of energy transfer in the inertial range

we use third order structure functions. The advantage of this approach is that they are relatively simple to calculate and, in the future, once PIV data is available from the experiment, they can be used to infer the energy transfer in the lab flows as well.

6.1 Energy spectra

The diagnostic fields are transformed to spectral space by expanding them in terms of a set of orthogonal basis functions suitable for the geometry of the domain. These are given by the eigenfunctions of the Laplacian in the relevant coordinate system. It can be shown that in the annulus the appropriate functions are given by a Hankel transform which consists of a Fourier transform in the azimuthal direction and a Bessel decomposition in the radial direction (Wordsworth et al., 2008). Hence, any single valued field, ϕ, defined in the annular (r,θ) plane may be expanded in terms of the orthogonal basis set

$$\phi(r,\theta) = \sum_{m=-\infty}^{m=+\infty} \sum_{n=1}^{n=\infty} \phi_{mn} K_{mn} = \sum_{m=-\infty}^{m=+\infty} \sum_{n=1}^{n=\infty} \left(\phi_{mn}^{J} J_m \left(\gamma_{mn} r\right) + \phi_{mn}^{Y} Y_m \left(\gamma_{mn} r\right) \right) e^{im\theta}. \tag{6.1}$$

J_m and Y_m are Bessel functions of the first and second kind respectively and γ_{mn} is a constant which represents the total wavenumber. m and n are the dimensionless zonal and radial wavenumbers respectively. γ_{mn} may be determined numerically for a given set of boundary conditions (Mushref, 2010). For simplicity we restrict the calculation to two dimensions. Since measurements cannot be easily taken in the vertical plane in the experiment this does not impede comparison between the experiments and simulations. A standard fast Fourier transform is used to first transform in the azimuthal direction and then we follow the method of Wordsworth et al. (2008) to calculate the Bessel decomposition in the radial direction and apply the boundary conditions.

In this chapter we consider the spectrum of temperature variance and that of horizontal kinetic energy. The temperature variance is a measure of buoyancy and hence the available potential energy. For the simulations both these spectra may be computed at all depths throughout the flow. For the experiment, the top surface

temperature variance spectra can be calculated from infrared camera images. In the future, once PIV data from the lab experiment is made available, it would also be possible to compute the kinetic energy at different levels in the experiment.

6.1.1 Kinetic energy spectra

The horizontal kinetic energy is calculated by transforming the zonal and radial components of the velocity separately and then summing the squares of the results. We calculate the kinetic energy in the horizontal plane so that it may be compared with future PIV measurements from the experiment which are taken using horizontal light sheets. Given that the magnitude of density fluctuations are relatively small across the horizontal plane it is thought that the spectra would not change significantly if they were calculated on isopycnal surfaces.

2D spectra

We begin by considering the two dimensional spectra where the energy is given as a function of both the zonal and radial wavenumbers. $m = 0$ represents the zonal component of the flow and the $m \neq 0$ component is due to the non-axisymmetric eddies.

Figure 6.1 shows the two dimensional kinetic energy spectra on the top surface of the flow for simulations from set C at a range of rotation rates. We focus on the top surface as this is where the temperature variance spectra can be measured in the experiment using the IR camera. Also, the investigation of the PV in section 5.1.3 revealed that the temperature gradients on the boundaries dominate over the interior PV gradients and thus the top boundary is likely to be dynamically important. The signature of each of the flow regimes identified in chapter 4 can be seen in these spectra. At the lowest rotation rates, the kinetic energy is dominated by the $m = 0$ component as the flow is axisymmetric. For $Ro_{th} < 10$, $m \neq 0$ components become stronger, indicating the presence of large scale, low frequency baroclinic waves. For example, where $Ro_{th} = 3.4763$ an $m = 2$ wave is dominant and for $Ro_{th} = 1.3652$ the $m = 3$ wave dominates, although the contribution from $m = 2$ remains strong.

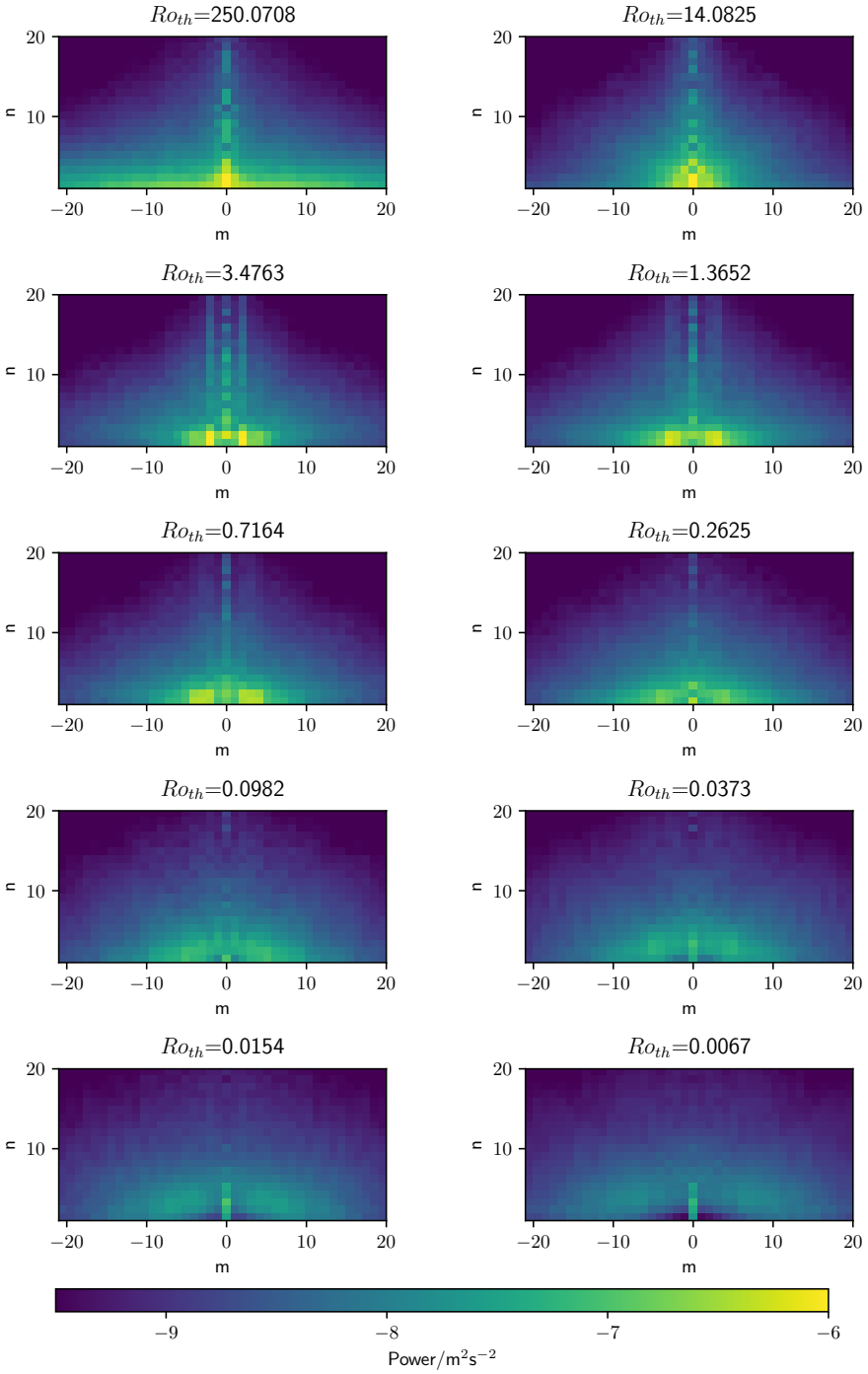


Figure 6.1: Two-dimensional kinetic energy spectra from the top surface of the flow in simulations from set C at different thermal Rossby numbers. Non-dimensional zonal wavenumber, m, is shown along the x axis and non-dimensional radial wavenumber, n is shown along the y axis. The colour scale is logarithmic and hence the colour bar labels correspond to the logarithm (base 10) of the power.

Where $Ro_{th} < 0.1$ there is no longer a localised dominant wavenumber and energy is spread across a range of scales with $m, n \lesssim 5$. The $m = 0$ mode becomes stronger again as Ro_{th} decreases which may indicate the formation of zonal jets.

1D spectra

Now we consider the spectra as a function of total wavenumber, $k = \gamma_{mn}$, only. γ_{mn} is approximately proportional to n and varies weakly with m for a given n. The one dimensional spectra are calculated from the two dimensional spectra shown above by binning the power into intervals of γ_{mn} and dividing by the bin width to produce a power density. The residual spectrum is defined as the part of the total spectrum where $m \neq= 0$ and the zonal component has $m = 0$.

Figure 6.2 shows the top surface kinetic energy spectra for simulations in set C at different rotation rates plotted together for comparison. Guidelines showing slopes of -5/3, -2 and -3 are shown for the purpose of guiding the eye rather than to necessarily suggest that these are the slopes followed by the spectrum. The peak of the residual, and hence the total spectrum, moves to a larger wavenumber as rotation rate increases and the peak becomes sharper. The peak may be associated with an injection or dissipation scale in the flow and possible measures of these scales will be discussed in section 6.2. The slope of all three components of the spectra become slightly shallower as the rotation rate increases. Overall, we find the total spectra follow a power law of approximately k^{-2}, slightly steeper than -5/3 for low to moderate wavenumbers and a power law slightly shallower than k^{-3} at larger wavenumbers.

To assess the impact of the beta effect on the flow we briefly compare the spectra from simulations in set C where there is a sloping bottom to those in set A with a flat bottom. Figure 6.3 shows the top surface kinetic energy spectra for three different rotation rates in sets C and A. A slope of -5/3 is shown as a guide but the spectra are generally found to be slightly steeper than this. At the moderate rotation rate of $\Omega = 0.1$rad/s the spectra are very similar in both cases. At the lowest rotation rate, $\Omega = 0.025$rad/s, the slope of the total spectrum is similar in

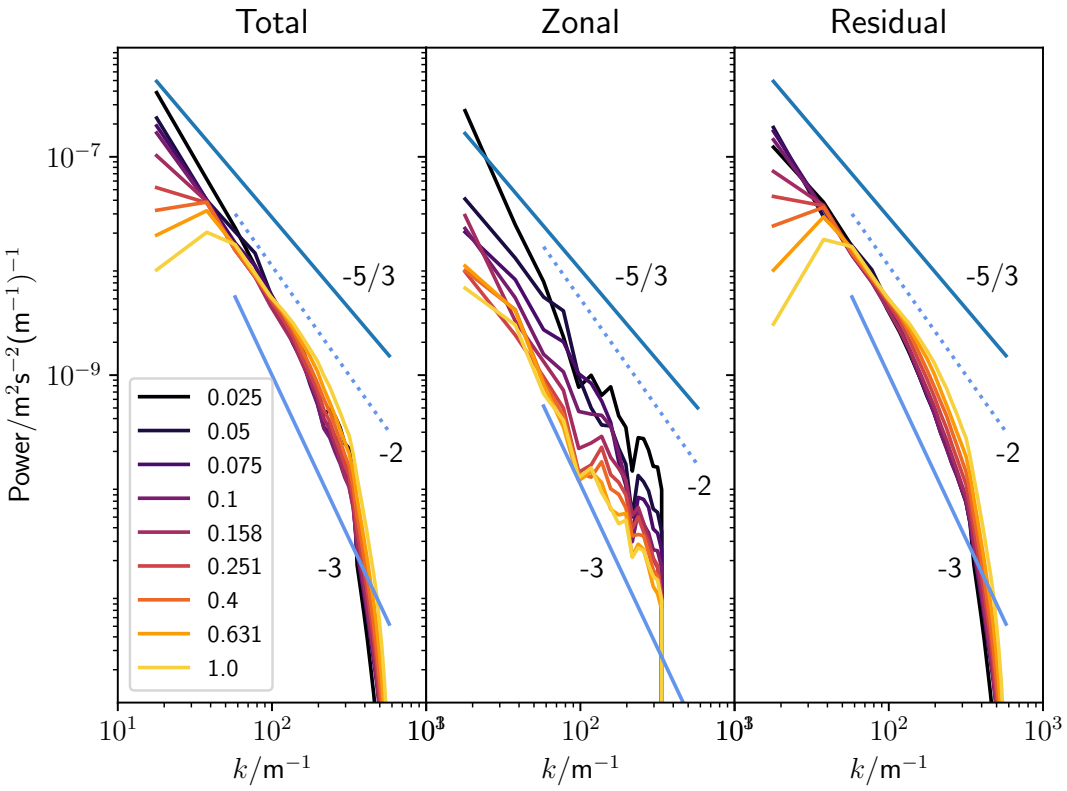


Figure 6.2: Kinetic energy spectra as a function of total wavenumber for simulations from set C. The left hand panel shows the total spectrum whilst the central panel shows the zonal ($m = 0$) component and the right hand panel shows the residual ($m \neq 0$) component. Slower rotation rates are shown in darker colours with the numbers in the legend referring to the rotation rate of each simulation in units of radians per second. Slopes of -5/3, -2 and -3 are shown on each plot as a guide for the slope of the spectrum.

both cases but when the sloping bottom is present the residual spectrum has a slightly higher magnitude than the zonal spectrum whereas the zonal component dominates in the simulation where the base is flat. The acceleration of fluid down the slope does change the form of the overturning circulation quite significantly as shown in chapter 5. When the flat bottom is present a single overturning circulation spans the entire domain whereas the presence of the slope causes this to breakdown into multiple cells. At the highest rotation rate, the spectrum for the simulation with a flat bottom is very flat. It is not clear why this is the case given that the only major differences between the sloping and flat bottomed simulations is the presence of the beta effect in the former and a lower emergent stratification in the latter. An irregular, turbulent flow is observed at the highest rotation rate in the

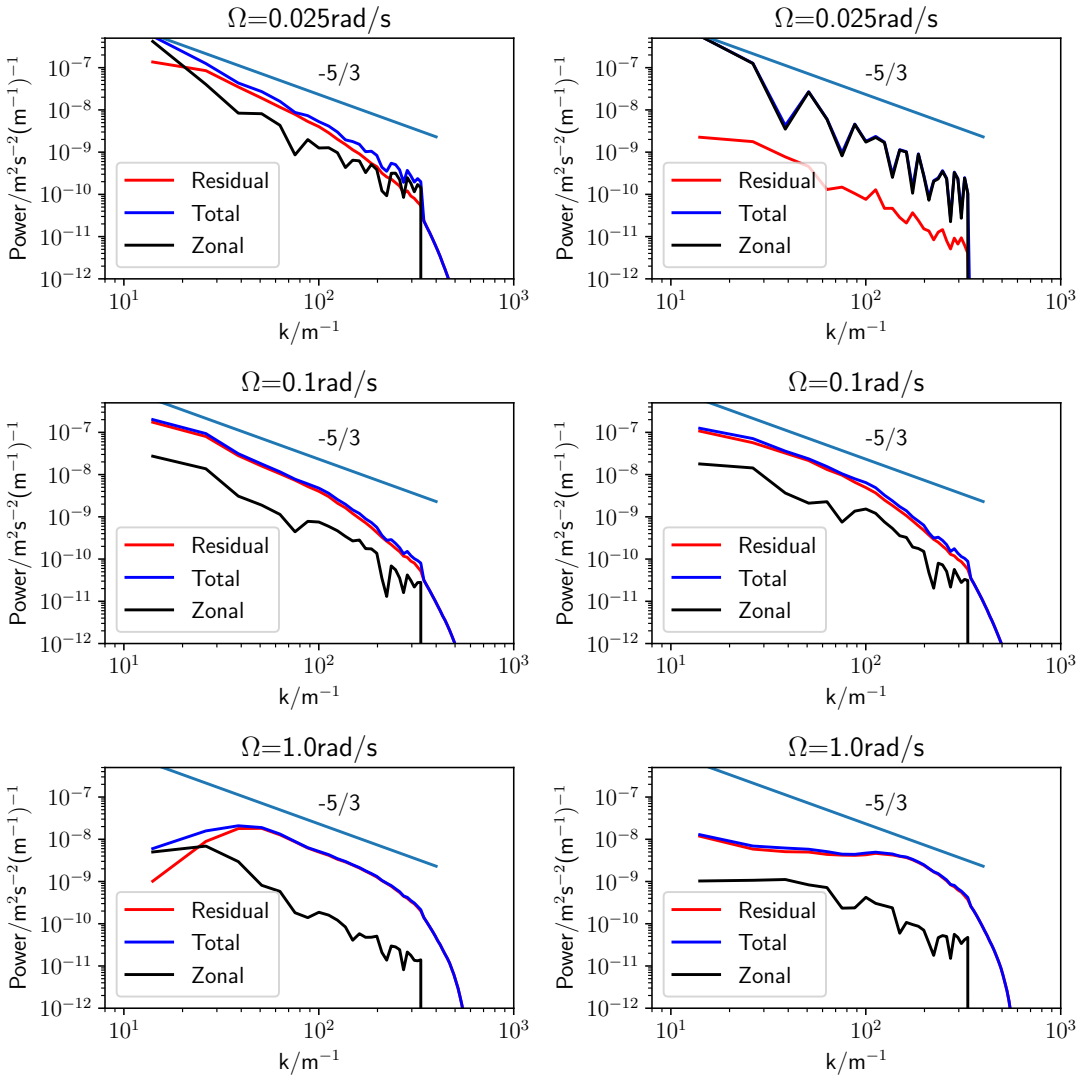


Figure 6.3: Kinetic energy spectra taken from the top surface of simulations from set C (left hand column) and set A (right hand column) at three different rotation rates. Runs in set C include a sloping bottom whereas the runs in set A have a flat base. The zonal component ($m = 0$) is shown by the black solid line, the residual component ($m \neq 0$) is given by the red solid line and the blue solid line gives the total spectrum. The light blue straight line shows a slope of -5/3.

flat bottomed case whereas zonal jets are observed in the sloping bottom simulation.

6.1.2 Temperature variance spectra

The temperature variance field is given by $T_v = (T - T'')^2$ i.e. the squared deviation of the temperature from the horizontal mean. Hence, it is proportional to the square of the buoyancy and proportional to the available potential energy.

2D spectra

Figure 6.4 shows the two dimensional temperature variance spectra for the top surface of the lab experiment at different rotation rates. These are somewhat noisier than the simulated spectra shown in figure 6.5 although some of this may be due to enhanced convection driven by evaporation from the top surface. Figure 6.6 shows the top surface temperature variance spectra for simulations with parameterised heat loss due to evaporation. For $n = 1$ there is weak power in a broad range of zonal modes which is not seen in the simulated spectra with insulating boundary conditions and this is also observed in the spectra from the experiment. For both the experimental and simulated spectra there is a depletion of energy where $n > m$ (away from the region of the spectra affected by evaporation) and an enhancement along the line $m = n$. This isotropic enhancement could represent a preference for isotropic eddies across a range of scales. However, the mechanism by which this would occur is unclear and it is notable that the enhancement is weaker in the experimental flow than in the simulations. Furthermore, it is not observed in the kinetic energy spectra as might be expected if it were related to the presence of isotropic eddies. Both the simulations and experiments have maximum power in the $m = 0$ mode for all rotation rates.

1D spectra

We compare the experimental data with simulations from set E in figure 6.7. Simulations in set E have the evaporative heat loss from the upper surface of the flow parameterised and the same input heat flux at the hot plate as the experiment. However, note that the rotation rates in each case are slightly different. A number of similarities can be observed between the experimental and simulated flows. In both cases there is a flattening of the residual spectrum at low wavenumber which becomes more pronounced as the rotation rate increases. This suggests that an injection or dissipation scale in the flow is moving to higher wavenumber as rotation rate increases. There appears to be little variation with rotation rate in the slopes of the spectra, particularly in the experiment where the total and zonal components

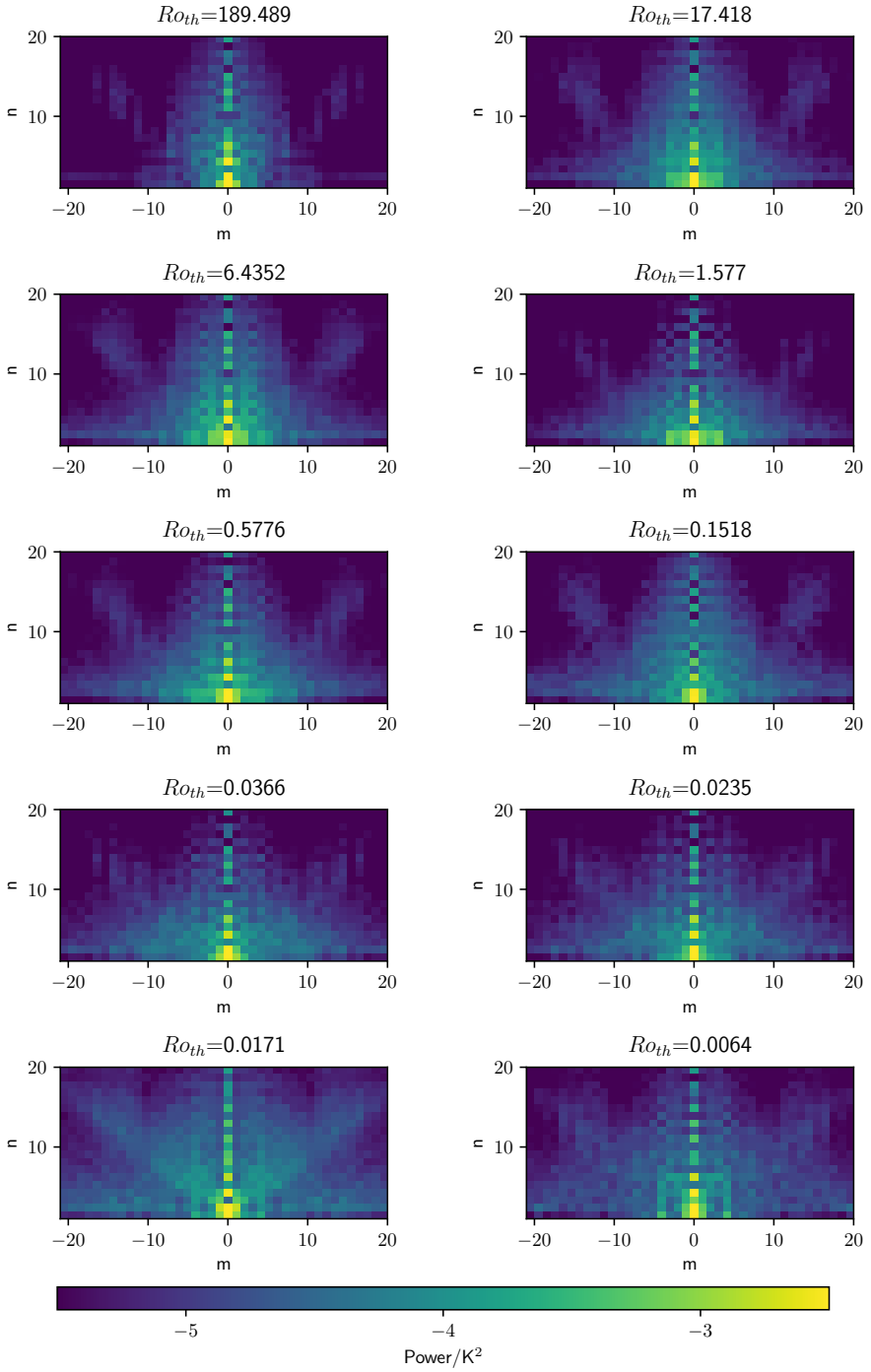


Figure 6.4: Two-dimensional spectra of the temperature variance on the top surface of the flow calculated for data from the experiment at different thermal Rossby numbers. The temperature variance is calculated from infra red camera images of the top surface of the flow. Zonal wavenumber, m, is shown along the x axis and radial wavenumber, n is shown along the y axis. The colour scale is logarithmic and hence the colour bar labels correspond to the logarithm (base 10) of the power.

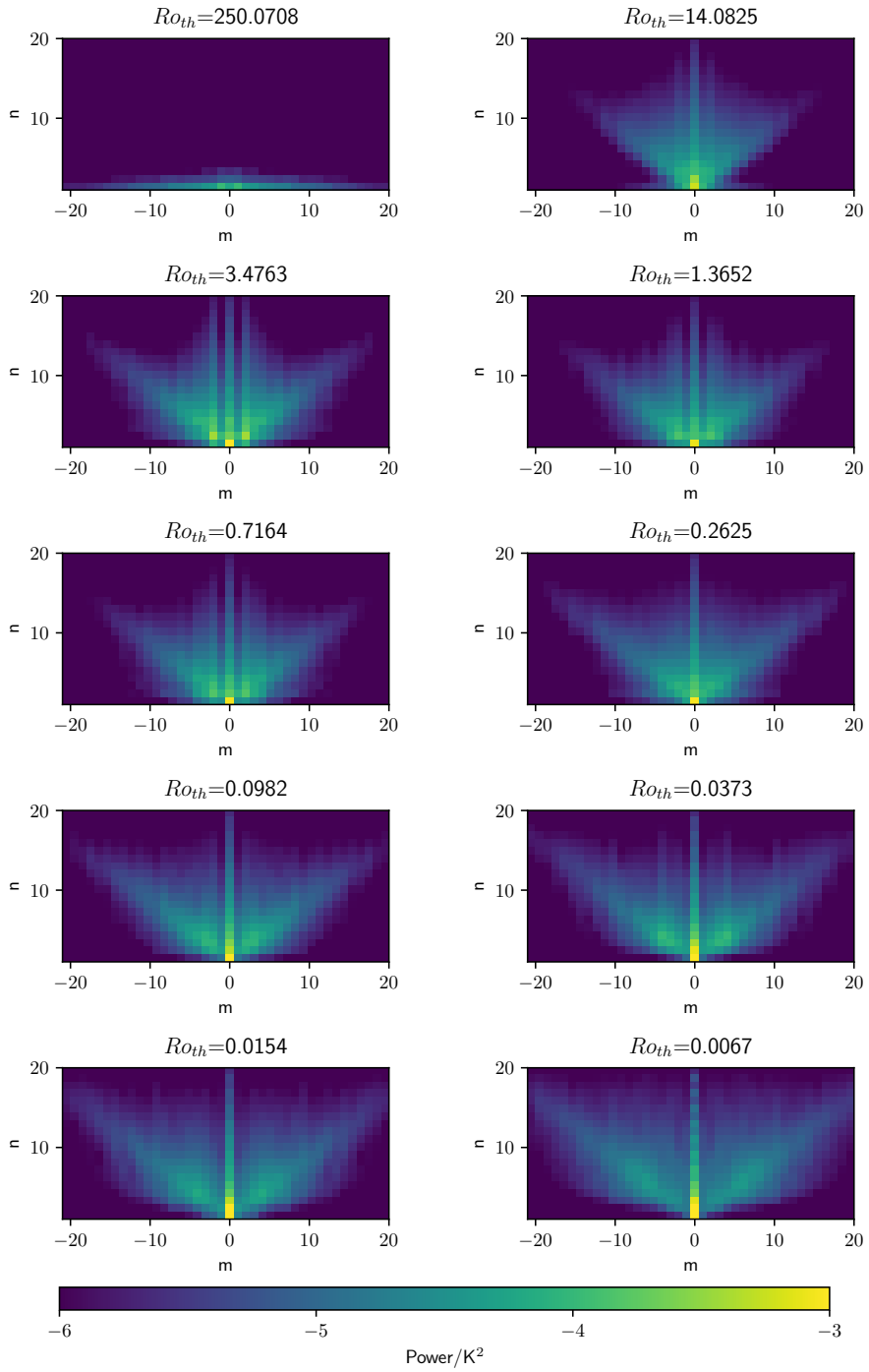


Figure 6.5: The equivalent of figure 6.4 for simulations in set C at different thermal Rossby numbers. Zonal wavenumber, m, is shown along the x axis and radial wavenumber, n is shown along the y axis. The colour scale is logarithmic and hence the colour bar labels correspond to the logarithm (base 10) of the power.

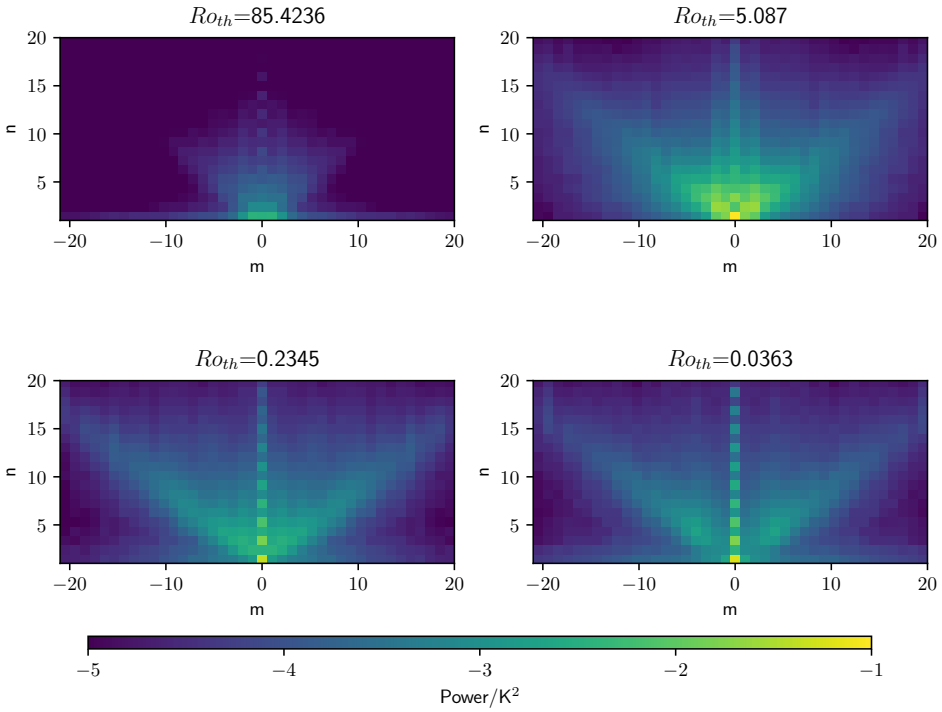


Figure 6.6: The equivalent of figure 6.4 for simulations from set E where heat loss from the boundaries is parameterised including the evaporation from the top surface.

are very robust. The shape of the total temperature variance spectrum in the simulations is similar to that of the total kinetic energy spectrum.

The slope of the total spectrum in the experiment is found to be close to -2 but it is generally steeper in the simulations of set E (see table 6.1 for precise values). There is a steepening of the spectrum at high wavenumber in the simulated data (for $k > 100$) which is not seen to the same extent in the experiment. This may be due to the resolution limit in the simulations where the smallest resolved scale in the zonal direction is about 1cm at the outer radius. In general the zonal component in the simulations is weaker than in the experiments relative to the residual component. The zonal mean component of the heat flux was also found to be very weak in chapter 5. This apparent systematic under estimation of the mean overturning could be a consequence of under resolving the free convection which is expected to drive the thermally direct overturning.

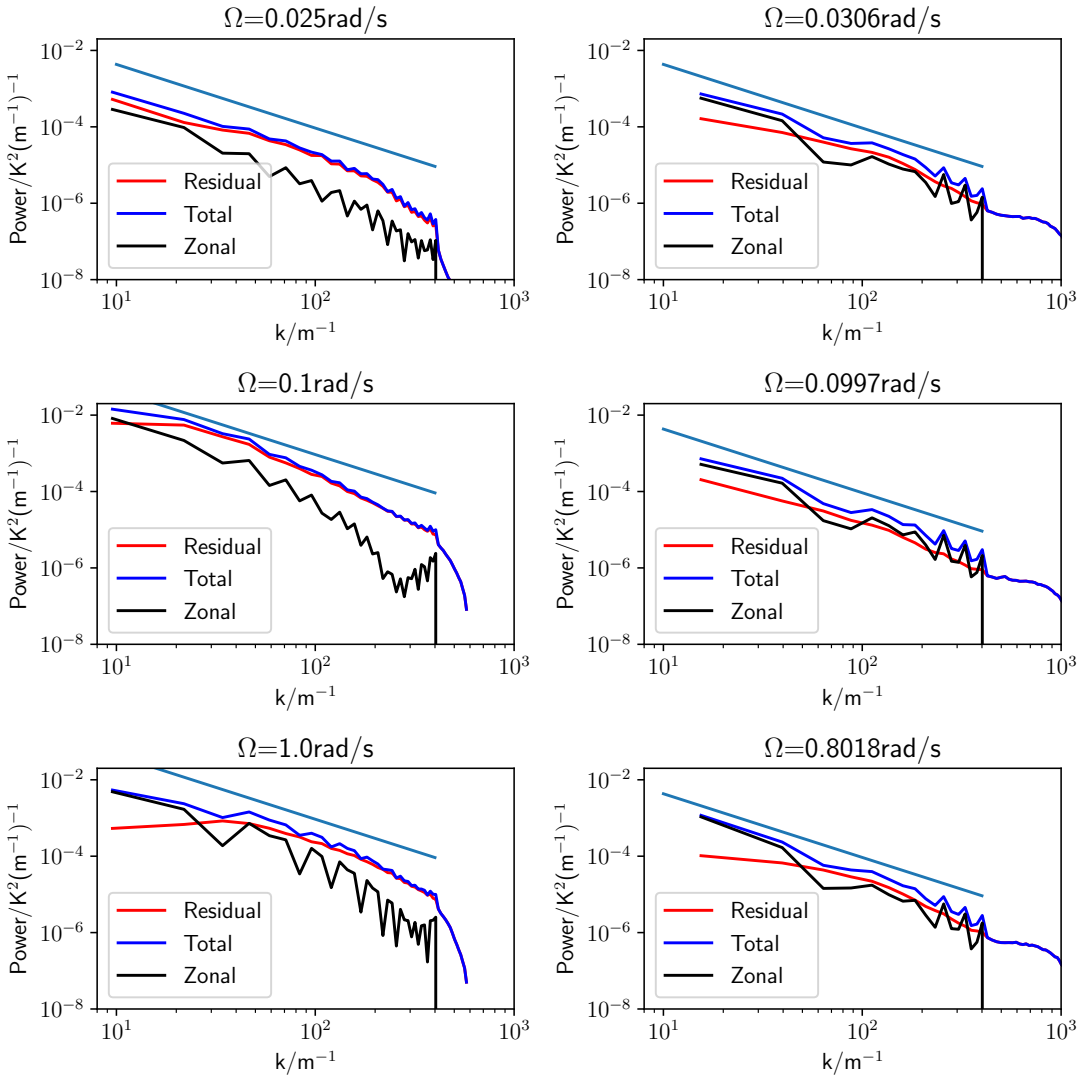


Figure 6.7: A comparison of temperature variance spectra taken from the top surface of simulations from set E where the evaporative heat loss is parameterised (left hand column) and the experiment (right hand column). The different panels show different rotation rates increasing downwards. Note that the rotation rates are not the same in the experiments and simulations. The zonal component ($m = 0$) is shown by the black solid line, the residual component ($m \neq 0$) is given by the red solid line and the blue solid line gives the total spectrum. The light blue line shows a slope of -5/3 as a guide.

Ro_{th}	Total	Zonal	Residual
93.3	-2.4 ± 0.1	-2.8 ± 0.3	-2.4 ± 0.1
56.6	-2.0 ± 0.4	-1.8 ± 0.7	-2.2 ± 0.2
5.55	-2.63 ± 0.04	-4.3 ± 0.3	-2.47 ± 0.03
6.43	-2.1 ± 0.3	-2.0 ± 0.6	-2.3 ± 0.2
0.04	-2.28 ± 0.08	-3.3 ± 0.4	-2.01 ± 0.07
0.04	-2.0 ± 0.3	-1.9 ± 0.6	-2.1 ± 0.1
93.3	-2.6 ± 0.1	-1.9 ± 0.3	-3.0 ± 0.1
5.55	-2.7 ± 0.06	-2.4 ± 0.2	-3.0 ± 0.1
0.04	-2.0 ± 0.1	-2.4 ± 0.2	-2.0 ± 0.1

Table 6.1: Values for the spectral slopes in experiment (rows shaded grey) and in simulations where heat loss through the boundaries is parameterised (set E, rows with white background). Slopes are calculated by linear regression between wavenumbers 30 and 300 and the standard error of the regression is shown. The top section of the table shows values for temperature variance spectra in simulations and experiments and the bottom section shows the slopes of the kinetic energy spectra in the simulations.

6.1.3 Depth dependence

Thus far we have only considered the spectra for the top surface of the flow. In part this was motivated by the fact that the infra-red camera images allow this diagnostic to be calculated for the data from the lab experiment. However, we have also noted throughout the preceding chapters that certain characteristics of the flow suggest that an SQG framework may provide an appropriate description of the dynamics close to the top surface. In chapter 5 we found that the interior PV gradients in the annulus are much weaker than those near the upper boundary and that the flows seen in both the simulations and experiments suggest the existence of local horizontal shear instabilities characterised by filamentary structures which produce their own secondary instabilities. Both these factors are characteristic of SQG dynamics (Lapeyre, 2017). In this section we attempt to make a more quantitative comparison between the characteristics of the flow in the annulus and SQG dynamics. It should be noted that this is motivated by observations of the flow which suggest some SQG like qualities rather than a desire to produce a fully descriptive model of the flow dynamics.

In SQG the advection of buoyancy anomalies on the top surface controls

the dynamics of the entire flow so the characteristics of the top surface are of great importance. In pure SQG the kinetic energy at the surface and surface buoyancy spectra are expected to be proportional to one another with spectral slopes of -1 at low wavenumber and -5/3 at high wavenumber. These inertial ranges correspond to the inverse cascade of total energy and the direct cascade of buoyancy variance respectively. However, in previous work on SQG dynamics, under various arrangements of forcing and dissipation, the buoyancy variance spectra in the direct cascade have been found to be steeper than $k^{-5/3}$, with a slope closer to -2 (Pierrehumbert et al., 1994; Sukhatme and Pierrehumbert, 2002; Celani et al., 2004; Capet et al., 2008). In the simulations we generally found the buoyancy variance spectra to be steeper than -2 but the experimental spectra had slopes of around -2 for $30\text{m}^{-1} < k < 300\text{m}^{-1}$ which could be consistent with an SQG direct enstrophy cascade.

Another characteristic of SQG flow is that features decay exponentially away from the surface at a predictable rate. Hence, we complete our investigation of the spectra by considering how they vary with depth in the annulus simulations. The skin depth of water for penetration by IR radiation is on the order of 1mm so the infrared camera only allows us to study the top surface of the experiment. Thus we cannot provide a comparison between the experiment and the simulations at deeper levels in the flow. There are horizontal light sheets on three different levels deeper down in the experiment and so once PIV data is available some quantification of the depth variation of the kinetic energy spectra in the experiment will be possible.

Figure 6.8 shows the variation in the kinetic energy and temperature variance with depth over the top 2.5cm of the flow in a simulation where $\Omega = 0.631\text{rad/s}$ from set C. Simulations from set C have idealised, insulating boundaries away from the heat source and sink. Lighter colours represent the spectra further from the top surface. The kinetic energy spectrum evidently steepens smoothly with depth. The power in the spectrum decays with depth at all wavenumbers but at a faster rate for larger k which results in a steeper spectrum. The temperature variance spectra are less smooth but a similar decay with depth is observed from the second level

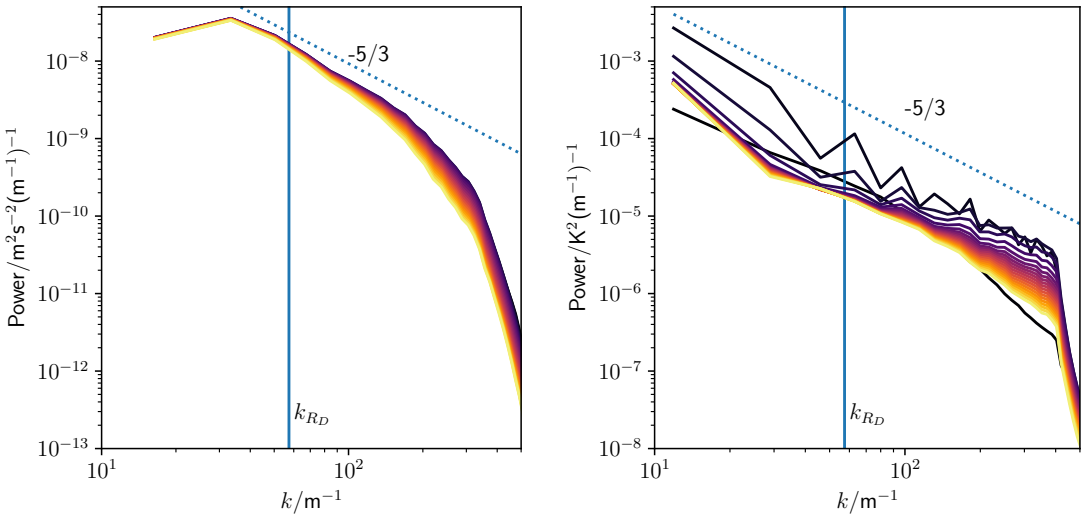


Figure 6.8: The left hand panel shows the kinetic energy spectra for all levels where 30cm$<z<$27.5cm in a simulation from set C where Ω =0.631 rad/s. The colours of the lines representing the spectra lighten with depth such that black represents z=30cm and yellow represents z=27.5cm. The right hand panel shows an equivalent representation of the temperature variance spectra over the same range of depths in the same simulation. Also shown is a slope of -5/3 for comparison (blue dotted line) and the wavenumber corresponding to the Rossby deformation radius, k_{R_D} (blue solid line).

from the top. Only the spectra over the top 2.5cm of the flow are shown here but we find that the decay slows down and eventually plateaus for depths greater than 5-10cm from the surface. As shown in figure 5.7 we find that large scale features in the horizontal temperature field are coherent throughout the depth of the flow.

In the temperature variance the top level actually has a lower spectral power density than the levels immediately below it. This is found to be the case across all simulations. It is also notable that the top surface spectrum steepens towards a slope of -3 at high wavenumber whereas the spectra at lower levels retain a slope of -5/3 to -2 throughout the entire wavenumber range. The top level spectrum has a form very similar to the surface kinetic energy spectrum whereas at lower levels the shape is quite different to the kinetic energy and more consistent with the temperature variance spectra from the experiment where steepening at high wavenumbers is not observed. We tentatively suggest that the dramatic change in the temperature variance at lower levels may be due to small scale convective features resulting from the cold plate. These would not be present on the top surface

where the cold plate is located but might be expected to increase the temperature variance in general and especially at small scales at greater depths.

To test whether this decay is consistent with SQG theory we measure the rate at which the spectra decay with depth. In the case of the temperature variance we ignore the top level for this purpose and assume that the decay at lower levels is unaffected by the presence or absence of convection. As discussed in chapter 1, the spectral horizontal transform of the buoyancy in SQG theory is given by (Scott, 2006; Lapeyre, 2017)

$$\hat{b} = \hat{b}_s \exp\left(\frac{-N_0 k z}{|f_0|}\right) \tag{6.2}$$

and the equivalent kinetic energy is given by

$$\hat{E} = \hat{E}_s \exp\left(\frac{-2N_0 k z}{|f_0|}\right) \tag{6.3}$$

where $\hat{E}_s$ and $\hat{b}_s$ are the spectral transforms of the kinetic energy and the buoyancy at the surface respectively. Therefore, controlling for k and z, one would expect the decay constants of both the kinetic energy and temperature variance spectra to equal $2N/f$.

We also note that, with the correct scaling, SQG predicts that $\hat{E}_s = \hat{b}_s$ and so one would expect the surface kinetic energy and surface buoyancy spectra to be proportional to one another (Lapeyre, 2017). We have observed that, within the approximately linear part of the spectrum which may indicate the existence of an inertial range and allowing for quite large uncertainty in the spectral slopes, the slopes of -5/3 to -2 are generally consistent between the simulated temperature variance and kinetic energy spectra. Both sets of spectra also steepen towards a slope of around -3 at higher wavenumbers though this may be due to resolution constraints.

Figure 6.9 shows the measured decay constants from the kinetic energy and temperature variance spectra plotted alongside the average value of $2N/f$ for simulations in set C as a function of thermal Rossby number. At the lowest rotation rates SQG would not be expected to hold as a small Rossby number is a prerequisite assumption for any kind of quasi-geostrophy. For $Ro_{th} < 0.1$ there

is a convergence between the three measurements of the decay constant which suggests that the decay of the spectra follows the prediction of SQG theory. At this point it is not clear whether this result also applies to the experiment as the evaporation at the top surface causes unstable stratification there and the convection modifies the temperature field at the top surface. We do find a similar decay, with a consistent decay constant, in simulations where the evaporation from the top surface is parameterised (bottom panel of figure 6.9). However, as discussed in section 4.3 our parameterisation gives an unstable stratification near the surface which is much weaker than in the experiment.

The results presented thus far in this section suggest that aspects of the simulated flows are similar to the characteristics of an SQG flow. However, there are numerous discrepancies between the idealised SQG setup and our experiment. Firstly, it should be noted that SQG theory is developed under the assumption of a semi-infinite domain whereas our annulus is bounded by both a top and bottom boundary. In addition to having a finite domain size our simulations also contain a background meridional temperature gradient which is not present in a standard SQG setup. These conditions are more similar to the setup of the Eady problem than pure SQG (Eady, 1949). The original Eady problem contains a background buoyancy gradient and top and bottom boundaries but neglects the beta effect and does not allow for variable stratification. Subsequently, various authors have modified the original problem to include these extra complications, for example Williams (1974) allowed for variable stratification and Lindzen (1994) included a β-effect. However, perhaps the defining characteristic of Eady-type models which is retained in these extensions is an interior PV gradient which is equal to zero. This characteristic is approximately represented in our simulations given the large PV gradients at the boundaries but the interior PV gradient is not identically zero. In the Eady problem, SQG type edge waves from the two bounding surfaces interact to produce instabilities. Hence, the Eady model could provide a more useful starting point than standard SQG to develop a theoretical description of the annulus dynamics.

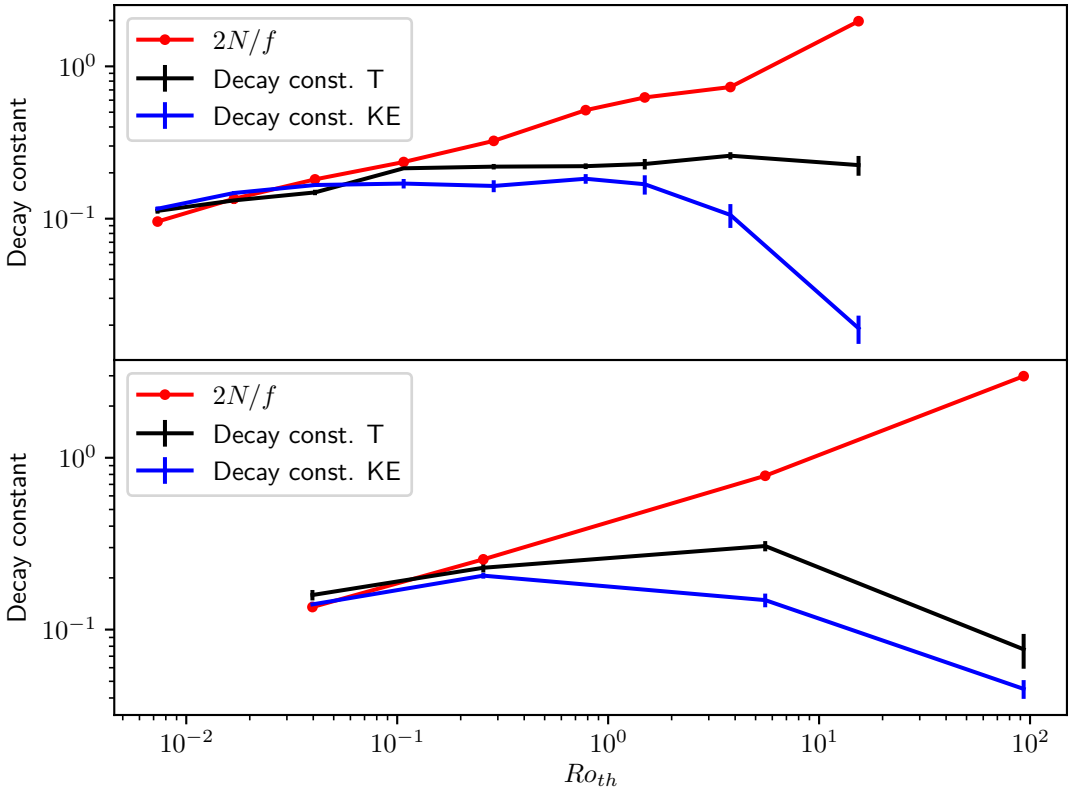


Figure 6.9: The decay constant of the spectral energy with depth for a given wavenumber (averaged over wavenumbers in the range $20<k<200$) compared to the value of $2N/f$ for the simulations in set C (top panel) and set E (bottom panel). The blue line shows the decay constant calculated from the kinetic energy spectrum and the black line shows the decay constant of the temperature variance spectrum. The red line shows the average value of $2N/f$ from the simulated flow. The error bars on the decay constants are calculated from the standard error on the least squares fit.

Previous studies of SQG dynamics have attempted to incorporate a background buoyancy gradient into the equations (Held et al., 1995; Smith et al., 2002). The background buoyancy gradient, Λ, which is present in our annulus and in the Eady model provides a restoring force which may allow Rossby-like waves to propagate (Smith et al., 2002). This is evident from the SQG buoyancy equation given by

$$\frac{Db}{Dt} + \Lambda \frac{\partial \psi}{\partial x} = 0 \tag{6.4}$$

which is analogous to the vorticity equation in QG dynamics. To complete our discussion of SQG characteristics in the annulus we briefly consider the effect of

this background gradient on the flow.

When the Λ term is comparable in size to the advection term there is a crossover between wave and turbulence dominated behaviour (Sukhatme and Smith, 2009). This is analogous to the situation discussed in section 1.1 for geostrophic turbulence and thus one might expect the formation of zonal jets when the background temperature gradient is sufficiently large. The wave-turbulence crossover occurs at a scale analogous to the Rhines scale which is set by the background thermal gradient, Λ, rather than the background vorticity gradient, β. Assuming isotropy, the dispersion relation for an edge wave in SQG turbulence can be derived from equation 6.1.3 and is given by $\omega = -\Lambda$ (Held et al., 1995). Equating this with the advective frequency, taking $U(k)$ to be the surface kinetic energy [1],

$$\omega_{ad} = (k^3 U(k))^{1/2} = \varepsilon^{1/3} k \tag{6.5}$$

gives a characteristic wavenumber for wave turbulence crossover as

$$k_\Lambda \approx \left(\frac{\Lambda^3}{\varepsilon}\right)^{1/3}. \tag{6.6}$$

The advective frequency is given by the inverse of the eddy turnover time which may be derived from dimensional considerations (Vallis, 2006).

Equation 6.1.3 can be compared with the equivalent expression for geostrophic turbulence

$$k_\beta \approx \left(\frac{\beta^3}{\varepsilon}\right)^{1/5} \tag{6.7}$$

which is derived similarly by equating the Rossby wave dispersion relation with the advective timescale (Vallis, 2006). Alternatively, taking the advective frequency to be the ratio of a typical eddy velocity to eddy lengthscale, we find

$$L_\Lambda = \frac{U}{\Lambda} \tag{6.8}$$

which may be compared to equation 1.16.

[1] $U(k)$ is the spectrum of surface kinetic energy which is proportional to the surface temperature variance spectrum. The total conserved energy, $E(k)$, is the volume averaged sum of kinetic and potential energy and so is not the appropriate measure to estimate the eddy turnover time.

Thus, an inverse cascade might be expected up to L_Λ where the cascade is depleted by anisotropic transfer into the zonal mode. Within this inverse cascade the zonal component of the kinetic energy is expected to scale as k^{-3} which is shallower than the k^{-5} law expected for QG turbulence. The zonal spectra shown in figure 6.3 are generally shallower than -3. The zonal flows produced by this mechanism would be expected to be surface intensified rather than barotropic as in in the case of geostrophic turbulence. We do not observe a zonal jet structure similar to those in figure 6.10 at the surface or elsewhere in runs without the sloping bottom. Furthermore, where jets are observed they are approximately barotropic rather than surface intensified. Hence, it is likely that the background potential vorticity gradient provided by the slope rather than the background temperature gradient is playing a role in jet formation here. Therefore, despite the apparent relevance of SQG to some aspects of the dynamics in the annulus, it is far from a complete description and geostrophic turbulence is likely to provide a better description of the jet formation process.

6.2 Spatial scales

As discussed in chapter 1 and in the previous section, transitions in the spectral behaviour of turbulent flows can often be described by a characteristic length scale. For example, in a well defined inertial range, energy or enstrophy is injected at a particular scale at one end of the range and dissipated at a range of scales at the other end. In the current setting, where we predict baroclinic instability is a major source of eddy kinetic energy, one might expect the deformation radius to provide a good prediction of the injection scale. Furthermore, if the flow is geostrophically turbulent, one would predict that energy produced by baroclinic instability at the deformation radius would cascade upscale to the Rhines scale to be channelled into the zonal component to produce jets. The criticality can be estimated by the ratio of the Rhines scale to the deformation radius and so provides a measure of the extent of the inertial range of this inverse cascade. The first evidence that jet formation may be present in some of our simulated flows is given by the time averaged barotropic

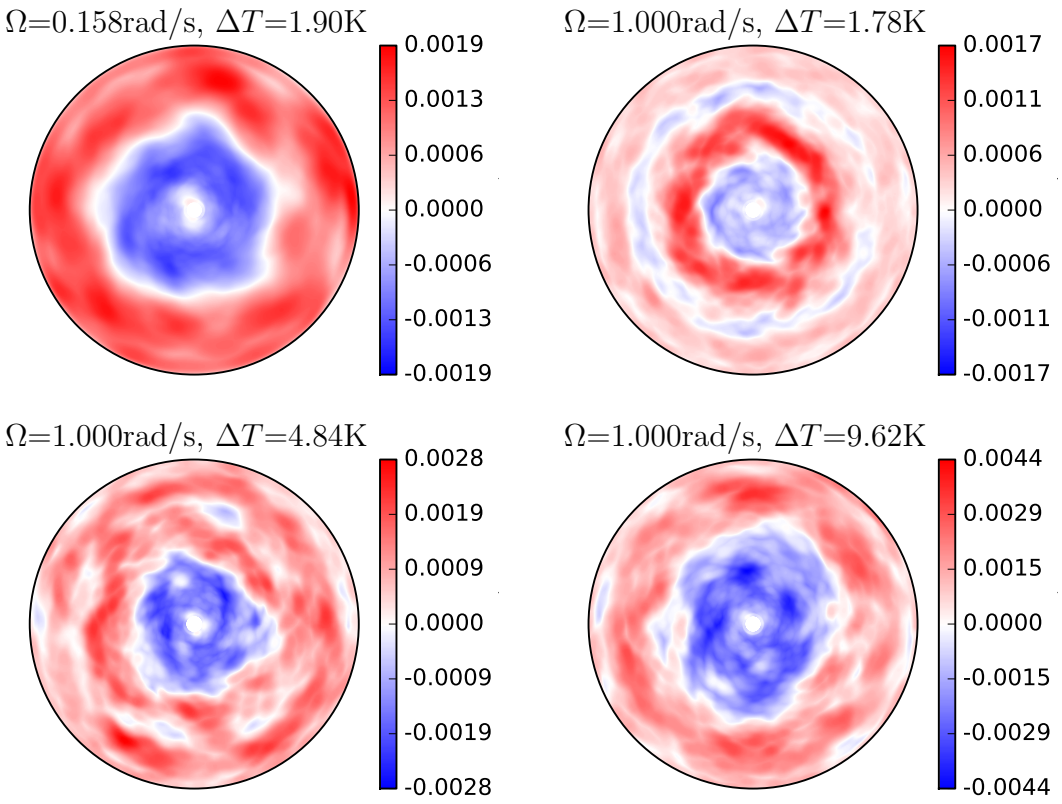


Figure 6.10: The barotropic temporally averaged zonal velocity in simulations from set C (top row), set D (bottom left) and set E (bottom right). Set E has heat loss at the boundaries parameterised and a high input heat flux to match the experiment. Set D has lower radial resolution, a different monotone filter and a higher input heat flux than set C.

zonal velocity fields where the emergence of persistent, zonally symmetric structures is observed as rotation rate increases for simulations in set C (figure 6.10). At the highest rotation rates, clearly defined multiple jets are not observed for simulations in sets E and D where the applied temperature difference is higher.

We calculate the energy containing wavenumber of the eddies, k_E, from the residual kinetic energy spectrum, $E_r(k)$ as

$$k_E^2 = \frac{\sum_k E_r(k)dk}{\sum_k k^{-2}E_r(k)dk}. \tag{6.9}$$

This gives a value of energy containing wavenumber which is typically closer to the peak of the spectrum than a wavenumber defined using the first moment of the spectrum (Schneider and Walker, 2006). However, the wavenumbers calculated using each of these definitions are found to differ by no more than 10% for our

spectra. In figure 6.11 this scale ($R_E = 1/k_E$) is compared with the deformation radius and Rhines scale across simulations in sets C, E and A. Set A simulations do not include a sloping bottom and hence there is no beta effect so the Rhines scale is not defined. In the lab experiment the top surface is free so deforms under the influence of the centrifugal force at high rotation rates. This produces a slope in the same sense as the sloping bottom but on the top surface. Therefore there would be a β-effect at high rotation rates in the lab even without the sloping base.

We find that both R_β and R_d decrease with rotation rate and the separation between the two scales increases with rotation rate. The increasing separation at faster rotation rates is consistent with the increasing criticality seen in chapter 5. The maximum separation at low rotation rates gives $R_\beta/R_D \approx 3.$ which is also consistent with the maximum criticality found in chapter 5. The Rhines scale gives a good prediction of the energy containing scale for $Ro_{th} < 0.1$. However, in interpreting this result it should be noted that the value for β used here is only an estimate for baroclinic flow. In the runs without a sloping bottom the eddy scale at the highest rotation rate is significantly larger than the deformation radius but this does not tell us much as the deformation radius does not appear to be a good predictor of the energy containing scale at any point.

At $Ro_{th} > 10$ the flow does not exhibit baroclinic instability and so one would not expect the energy containing length scale to relate to either the Rhines scale or the deformation scale. It is notable that the energy containing scale is quite insensitive to thermal Rossby number in all the sets of simulations considered here. In all cases the energy containing length scale is much smaller than the domain size so it is unlikely that this is imposing some limit. At low rotation rates in particular the energy containing scale may be set by convection rather than the baroclinic eddies. If the characteristic scale of convection is similar to the Rhines scale at high rotation rates this could result in an energy containing scale which is fairly insensitive to rotation. However, further investigation would be needed to confirm this. For the very lowest rotation rates where the flow is

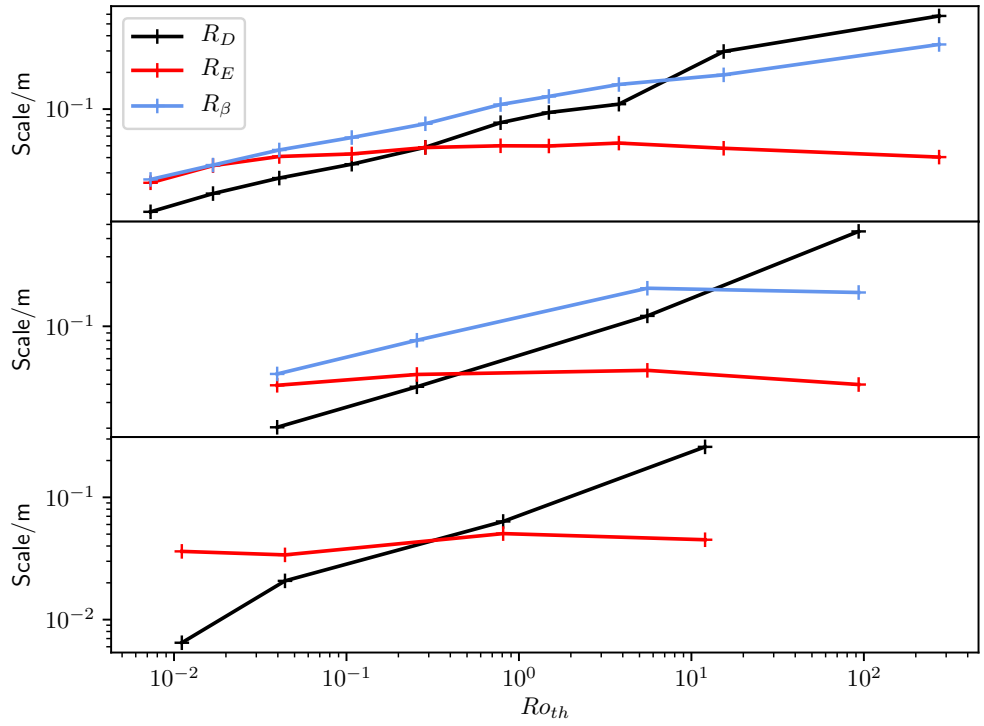


Figure 6.11: Variation of the Rhines scale (blue), Rossby deformation radius (black) and the energy containing scale (red) with thermal Rossby number. The top panel shows simulations from set C, the middle panel shows simulations from set E where non-insulating boundary conditions are used and the bottom panel shows simulations with a flat bottom from set A.

axisymmetric the residual spectrum is probably not a useful measure as the energy is mostly concentrated in the zonal mode.

These results suggest that, at high rotation rate an inverse cascade could be causing energy to become concentrated at the Rhines scale. We shall investigate this further in the following section. At lower rotation rates one would not expect the Rhines scale to be relevant as the rotation rate is not high enough for the β term in the vorticity equation to be comparable with the advection. It is also possible, in principle, for an inverse cascade to be halted by the domain size if there is no beta-effect or if the Rhines scale is larger than the domain. However, it is unlikely that this is the case here as the typical scale of the eddies is an order of magnitude smaller than the size of the domain.

6.3 Structure Functions

While the spectra indicate at which spatial scales energy is concentrated and the spectral slopes may give some indication of the underlying dynamics, they cannot be used to diagnose the direction of energy transfer between scales. Here, structure functions, which are calculated from the covariance of velocity as a function of separation, will be used to provide this diagnosis. The other approach which is commonly used to diagnose the transfer of energy between scales, particularly in planetary atmospheres, is spectral flux calculations (e.g. Augier and Lindborg, 2013; Young and Read, 2017; Read et al., 2018). In the annulus it is relatively simple to derive a spectral transfer term for the azimuthal direction (Wordsworth et al., 2008) but in the radial direction the triad coefficients must be calculated using Bessel functions which makes the algebra more complicated.

Hence, we choose the simpler approach of calculating structure functions which has the additional benefit that the same analysis may be easily applied to PIV data from the lab experiment when it becomes available. As our flows are anisotropic we attempt to calculate structure functions in all three dimensions but with data from the lab experiment only two dimensional calculations on the horizontal plane would be possible as no measurements of velocity can be taken in the vertical. A number of recent studies have used data from lab experiments to compute two dimensional structure functions and hence diagnose the energy transfers in the flow (Lamriben et al., 2011; Campagne et al., 2014; Gomes-Fernandes et al., 2015; Valente and Vassilicos, 2015).

A scale by scale energy budget equation for inhomogeneous flows can be derived directly from the Navier-Stokes equation following Valente and Vassilicos (2015). Starting with the Navier-Stokes equations in Cartesian co-ordinates at two separate points in the flow, $\mathbf{x} = \mathbf{X} + \mathbf{r}/2$ and $\mathbf{x}' = \mathbf{X} - \mathbf{r}/2$, where the velocities are $\mathbf{U} + \mathbf{u}$ and $\mathbf{U}' + \mathbf{u}'$ respectively with upper case U representing the mean flow and lower

case u representing the eddy component, one can derive

$$\begin{aligned}\frac{\partial\overline{\delta q^2}}{\partial t}+\left(\frac{U_k+U_k'}{2}\right)\frac{\partial\overline{\delta q^2}}{\partial X_k}+\frac{\partial\overline{\delta u_k\delta q^2}}{\partial r_k}+\frac{\partial\delta U_k\overline{\delta q^2}}{\partial r_k}=\\ -2\overline{\delta u_i\delta u_k}\frac{\partial\delta U_i}{\partial r_k}-\overline{(u_k+u_k')\,\delta u_i}\frac{\partial\delta U_i}{\partial X_k}-\\ \frac{\partial}{\partial X_k}\left(\overline{\frac{(u_k+u_k')\,\delta q^2}{2}}\right)-\frac{2}{\rho}\frac{\partial\overline{\delta u_k\delta p}}{\partial X_k}+\\ \nu\left[2\frac{\partial^2}{\partial r_k^2}+\frac{1}{2}\frac{\partial^2}{\partial X_k^2}\right]\overline{\delta q^2}-2\nu\left[\overline{\left(\frac{\partial u_i}{\partial x_k}\right)^2}+\overline{\left(\frac{\partial u_i'}{\partial x_k'}\right)^2}\right].\end{aligned}\tag{6.10}$$

$\overline{\delta q^2}=\overline{(\delta u_i)^2}$ where $\delta u_i=u_i-u_i'$, $\delta U_i=U_i-U_i'$ and the subscript denotes the co-ordinate dimensions with implicit summation over the indices. $\overline{\delta q^2}$ is the second order structure function and is a representation of the kinetic energy distribution in the space of separations. This is related to the eddy kinetic energy spectrum in spectral space via a convolution with a function of wavenumber and separation (Davidson, 2015).

Conceptually this equation may be understood by considering a three dimensional space of separations where spheres centred on the origin are surfaces defined by $|\mathbf{r}|=c$ where c is a constant. The three dimensions represent separations between points in each of the three physical spatial dimensions. Within this space of separations the kinetic energy is distributed over the different scales as $\overline{\delta q^2}(\mathbf{r})$. Transfers of kinetic energy between scales are given by the flow of $\overline{\delta q^2}$ through the spherical surfaces of constant $|\mathbf{r}|$.

Interpretation of the various terms in this equation is given by Valente and Vassilicos (2015). For the time being we assume that for sufficiently small separations the fluid is homogeneous. Therefore, all terms on the right hand side except for the dissipation vanish as does the fourth term on the left hand side (Lamriben et al., 2011; Gomes-Fernandes et al., 2015). Hence the equation reduces to

$$\frac{\partial\overline{\delta q^2}}{\partial t}+\left(\frac{U_k+U_k'}{2}\right)\frac{\partial\overline{\delta q^2}}{\partial X_k}+\frac{\partial\overline{\delta u_k\delta q^2}}{\partial r_k}=-4\epsilon.\tag{6.11}$$

For stationary turbulence, as in our system, the time derivative vanishes. In homogeneous flow $1/2(U_k+U_k')=U_k$ and this term represents advection of δq^2

by the mean flow. The third term on the left hand side is the non-linear transfer of energy by eddy interactions. It is this non-linear transfer that we shall focus on in the subsequent analysis. If an inverse cascade exists $\epsilon < 0$ and so the left hand side of equation 6.11 must be positive.

By assuming isotropy as well as homogeneity, equation 6.11 can be reduced to the well known 4/5 law of Kolmogorov (1941)

$$\langle \delta u_L \delta u_L \delta u_L \rangle = -4\epsilon r/5 \tag{6.12}$$

where δu_L is $\delta \mathbf{u}$ projected along the separation vector of the two points (i.e. the longitudinal structure function) and ϵ is the mean dissipation rate of kinetic energy (Lamriben et al., 2011). Angular brackets denote averaging. Assuming the existence of an inertial range (where ϵ is constant) the mean dissipation is equal to the mean rate of energy input and hence the rate of energy flow through the inertial range. Hence, the sign of ϵ gives the direction of the energy cascade, where it is positive the cascade is downscale and where it is negative the cascade is upscale. This expression can also be used to estimate the magnitude of ϵ from the calculation of the structure functions. In the subsequent analysis we begin by using this reduced form and then attempt to account for the anisotropy of the flow using the full three dimensional form of the equation.

6.3.1 One dimensional structure functions

Despite having already acknowledged that our data is neither isotropic nor homogeneous we begin by calculating structure functions in one dimension since this is a standard diagnostic which has previously been used to diagnose the cascade directions in lab experiments (e.g. Galperin et al. (2016)) and planetary atmospheres (e.g. (Cho and Lindborg, 2001; Young and Read, 2017)). We also note that the discussion above has only considered the equations in Cartesian form whereas we wish to diagnose energy transfer in the radial and azimuthal directions of a cylindrical system. Deriving equation 6.10 in cylindrical geometry involves complex algebra and introduces new terms into the problem. Since we only consider small

separations between points we assume that the use of a local Cartesian basis with radial co-ordinate r and azimuthal co-ordinate $r\theta$ is a reasonable approximation.

In our experiment and simulations the time averaged fields are approximately axisymmetric as shown in figure 6.10. Therefore, in the first instance, we construct structure functions along horizontal circles at a given r and z as the velocity fields are approximately locally isotropic and homogeneous in the zonal direction. In this case the distance, $r_s = r\Delta\theta$, between points is equal to the arc length along the circle, where $\Delta\theta$ is the angular separation of the two points. Hence, the longitudinal velocity difference, δu_L, is given by the difference in zonal velocity between the two points and the transverse velocity difference, δu_T, is given by the difference in radial velocity. Structure functions are calculated in this way for each radius and then averaged over all radii within the baroclinic zone. Following the 4/5 law (equation 6.12) the sign of the third order longitudinal structure function will indicate whether the cascade is up or downscale (negative if downscale). It should however be noted that, in addition to isotropy and homogeneity, the 4/5 law assumes the existence of an inertial range with a -5/3 spectral slope. Our spectra appear to show the existence of this feature at some scales in some cases but a true inertial range may not exist as there are multiple sources and sinks of energy in the system which may act across a range of scales.

Figure 6.12 shows the longitudinal structure functions, $\langle \delta u_L^2 \rangle$ and $\langle \delta u_L^3 \rangle$, for different rotation rates at the top surface and at mid-height in our simulations. At separations greater than 10cm the diagnostic is not useful as the flow at different points becomes uncorrelated and the assumption of homogeneity fails on large scales. For smaller separations than this the third order structure functions are negative except for at the two highest rotation rates. At mid-depth the structure functions are positive for all resolved separations for $\Omega = 1$rad/s and all but the smallest for $\Omega = 0.631$rad/s which suggests an inverse cascade is present. On the top level the two highest rotation rates also exhibit positive structure functions where all others are negative. However, in this case they do not extend down to the smallest resolved separations but become negative at a scale of 3-4cm. This is of the same

order as the deformation radius. The divergence of the cascade in both directions at this scale may suggest an energy input is present there.

Consistent with the findings of section 6.1.3 the structure functions steepen with distance from the top surface (not shown) as small scale features decay quickly away from the surface. For reference, in figure 6.12, we show the slopes predicted by equation 6.12. On the top surface the slopes of the structure functions at the highest rotation rates are quite close to those predicted by the theory but at lower rotation rates they are steeper. The structure function slopes are found to be steeper than the predictions for all rotation rates at mid-depth. It is not unduly surprising that the measured structure functions deviate from the quantitative predictions of the theory as there are many discrepancies between our system and the idealised assumptions which the theory relies on.

6.3.2 Structure functions in three dimensions

We now proceed to calculate the structure functions in three dimensions. For this analysis to be useful we need to consider separations in the radial, azimuthal and vertical directions in the annulus rather than in an arbitrary Cartesian basis. Therefore, we approximate the separations in each direction using a local Cartesian basis in the horizontal plane such that $\mathbf{r} = (\delta r, r\delta\theta, \delta z)$. There is some ambiguity about the value of r which should be used to weight the angular separation. Since we cannot assume homogeneity across radii in the annulus we calculate the structure functions in radial bands and use the centre of the band as a reference radius, r_c, and hence $\mathbf{r} = (r_\theta = r_c\delta\theta, r_r, r_z)$.

We compute the structure functions for points where 0.1965m$<r<$0.3165m and $z > 0.24$. This region is a channel near the top of the middle of the baroclinic zone. Within this range we expect the flow to be reasonably homogeneous and so we are able to average over the separations between all points. Once the structure functions have been calculated we interpolate to a spherical co-ordinate system in the space of separations following previous work (Lamriben et al., 2011; Campagne et al., 2014; Gomes-Fernandes et al., 2015; Valente and Vassilicos, 2015). Axial

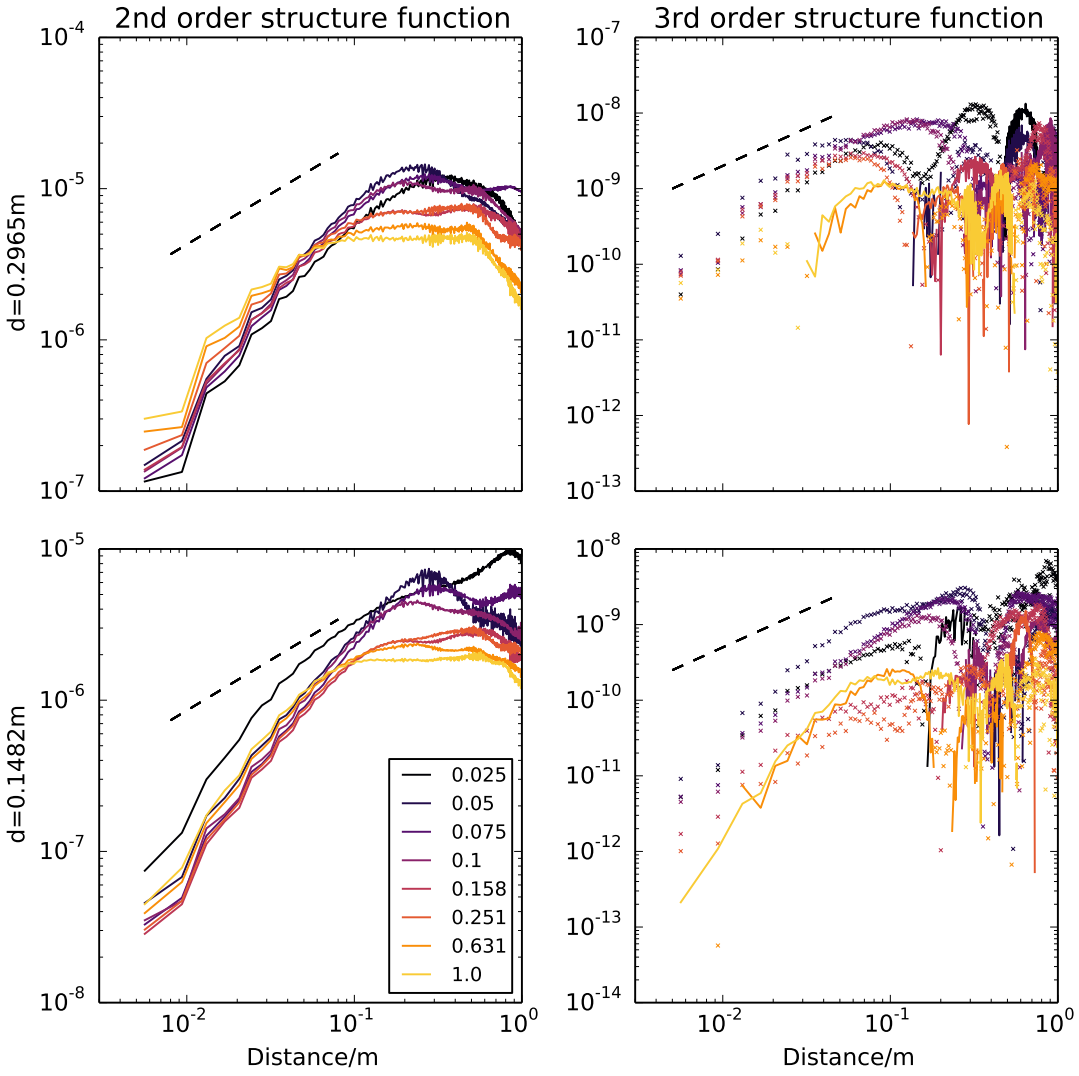


Figure 6.12: Second order (left hand column) and third order (right hand column) longitudinal structure functions in the zonal direction for simulations in set C at various rotation rates. Solid lines show positive values and points represent negative values, colours represent different rotation rates given in radians per second in the legend. In the left hand column the dashed line shows the power law $r_s^{2/3}$ and in the right hand column the dashed line is proportional to r_s.

symmetry within the sphere is expected if the statistics have converged given that the turbulence is stationary so only a quarter of it is shown in the following plots.

Second order structure functions

Lamriben et al. (2011) used this method to diagnose the anisotropic energy transfers induced in a fluid by rotation. As would be expected the flow was found to approach invariance along the rotation axis with increasing rotation and hence two dimensionality. Figure 6.13 shows the second order structure function for various rotation rates in the plane $r_\theta = 0$ as a function of vertical and radial separation. As expected, as rotation rate increases, the energy distribution becomes more anisotropic and depleted along the rotation axis but is quite isotropic at the lowest rotation rate. This indicates the increasing two dimensionality of the flow as rotation rate increases.

In contrast, we find that at all rotation rates the energy distribution between the radial and zonal directions is fairly isotropic as shown in figure 6.14. At the lowest rotation rate there is a slight depletion of energy along the zonal axis due to the flow being axisymmetric in that case.

Third order structure functions

The radial part of the divergence of the third order structure function in the spherical co-ordinate system in the space of separations gives the non-linear eddy transfer of energy between scales and hence when this value is positive it indicates that an inverse cascade is present. Figure 6.15 shows the third order structure function, $\overline{\delta u_k \delta q^2}$ in the horizontal plane, $r_z = 0$ as arrows and the radial component of its divergence as shading. This is the energy transfer due to nonlinear interactions only and from equation 6.10 we know there are other transfers which contribute to the overall energy distribution in the flow. The y axis represents separations in the azimuthal direction whilst the x axis shows separations in the radial direction.

Consistent with what was seen in section , we find there is a direct cascade of energy at all resolved scales for low rotation rates. The nonlinear transfer vectors point approximately along the radial direction towards the origin which suggests

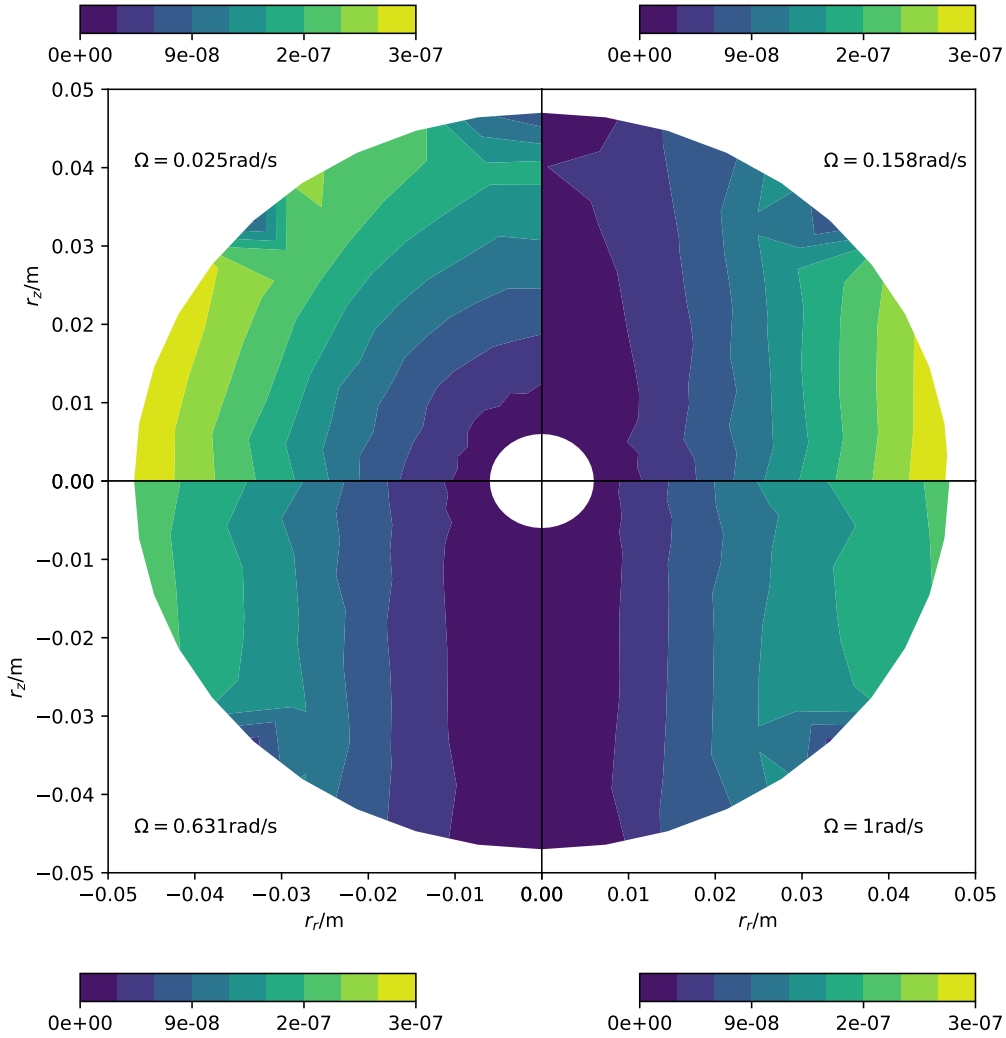


Figure 6.13: The second order structure function, $\overline{\delta q^2}$, in the plane $r_\theta = 0$ for a number of different rotation rates. The y axis shows displacements in the vertical direction and the x axis shows displacements in the radial direction. The structure functions are calculated at a reference radius of 0.2565m and a reference height of 0.296m in the annulus.

that this inverse cascade is approximately isotropic in the horizontal plane. For $\Omega = 1$rad/s there is an inverse cascade for scales larger than about 1cm in the radial direction and 3cm in the zonal direction and this is also approximately consistent with what was seen in one dimension. For Ω =0.631rad/s the radial transfer is much stronger than the zonal transfer but the overall transfer is downscale. The maximum scale represented here, 5cm, is close to where the change of sign in the one dimensional structure function was found for this rotation rate.

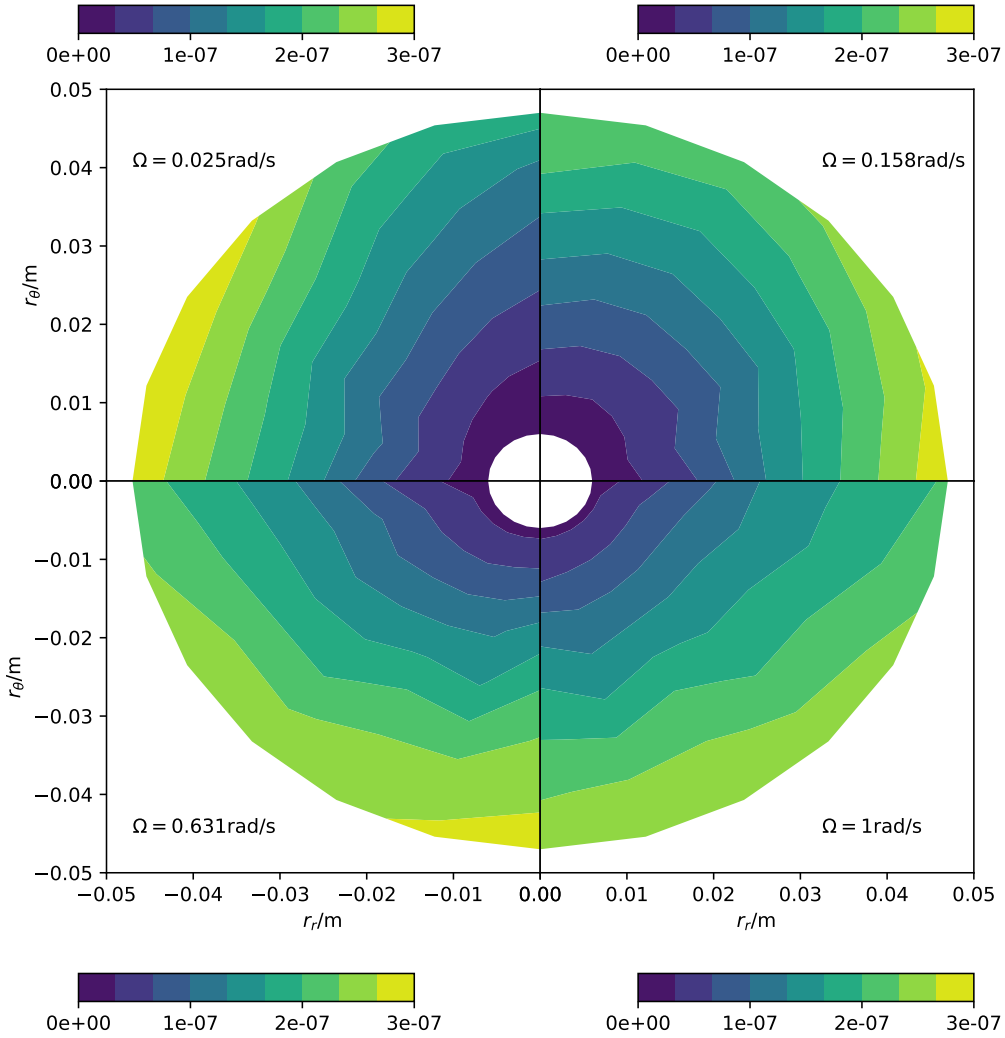


Figure 6.14: The second order structure function, $\overline{\delta q^2}$, in the plane $r_z = 0$. for four different rotation rates. The y axis shows displacements in the zonal direction and the x axis shows displacements in the radial direction. The structure functions are calculated at a reference radius of 0.2565m and a reference height of 0.296m in the annulus.

This work on three dimensional structure functions is preliminary and more extensive analysis is required to verify the results. The method appears to have some potential for analysing anisotropic cascades in this context. However, a more thorough investigation of the extent to which the flow can be considered homogeneous and the extent to which the statistics have converged would be useful. It would also be interesting to calculate the other terms in equation 6.10 and how their magnitude compares to the non-linear transfer. In principle, one could also

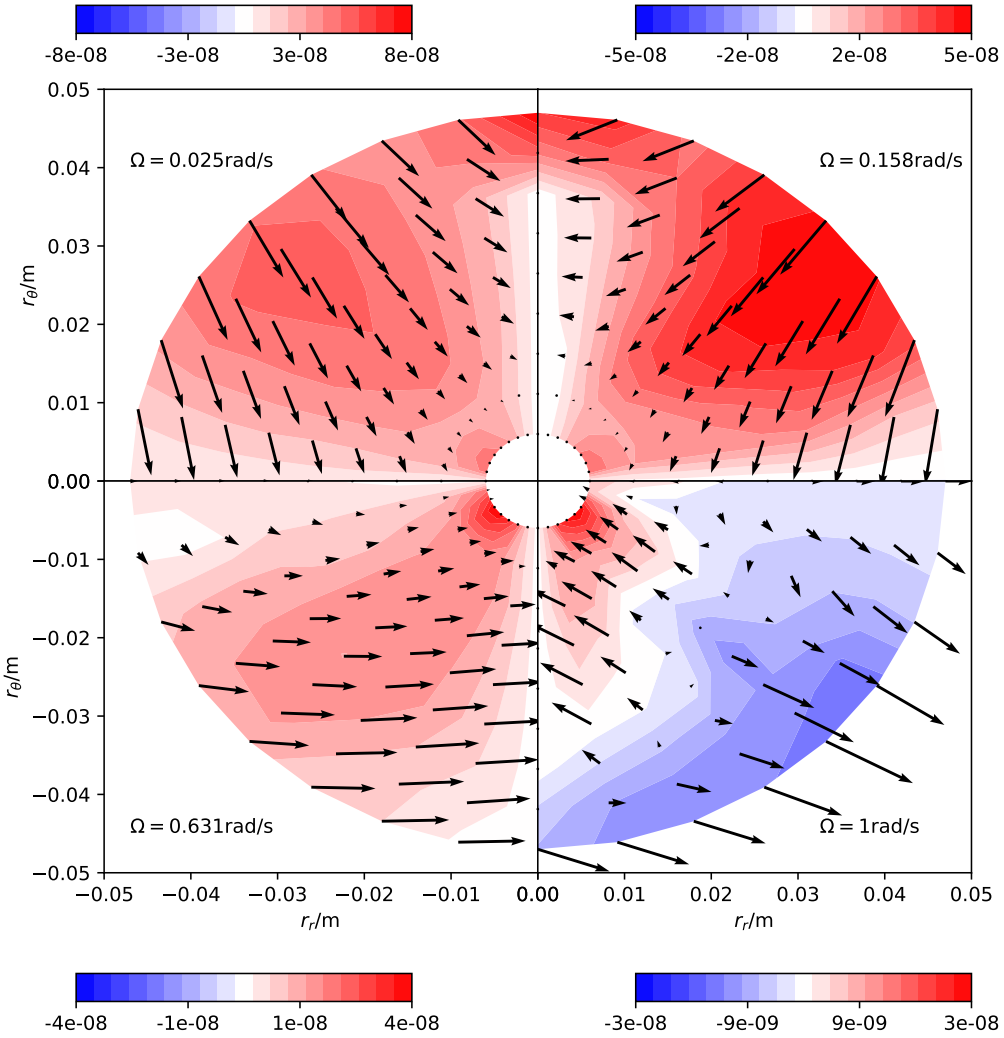


Figure 6.15: The third order structure function, $\overline{\delta u_k \delta q^2}$, in the plane $r_z = 0$. The arrows show the direction of energy transfer and the shading shows the magnitude of the radial part of the divergence of the structure function.

apply this method to the enstrophy cascade by computing a version of equation 6.10 from the temperature equation.

6.3.3 Discussion

In this chapter we have investigated the flows within the annulus in spectral space and considered the non-linear energy transfers in the flow resulting from the presence of the eddies. From the two dimensional spectra of kinetic energy the regimes associated with different regions of parameter space which were discussed

in chapter 4 are clearly evident. Once the spectra are reduced to one dimension there is no strong change in the spectral slopes with rotation rate but the peak of the residual spectrum shifts to higher wavenumbers as rotation rate increases. This peak, which is associated with the energy containing scale of the eddies is well predicted by the Rhines scale at high rotation rates. The form of the kinetic energy spectrum and the temperature variance spectrum are found to be broadly similar on the uppermost level of the flow.

The slopes of the spectra, for both kinetic energy and temperature variance, are found to be between -2 and -3 in the simulations. At higher wavenumbers the spectrum steepens towards a slope of approximately -3 but this may be associated with a limit set by the resolution. In the experiment we find a slope of -2 extends throughout the accessible wavenumber range and there is no clear steepening at higher wavenumbers. The zonal component of the spectrum is found to be weaker in the simulations compared to the experiments. We suggest this may be due to the simulations under resolving the convection which was discussed as a potential problem in chapter 4. The evaporation from the top surface of the experiment is a source of uncertainty as there are some inconsistencies between the experimental results and our parameterisation. It would be beneficial to verify the kinetic energy spectra against PIV measurements in the future, particularly as the kinetic energy field is likely to be less affected by the evaporation than the temperature and PIV would allow exploration of the flow below the top surface.

The spectra also shed further light on whether the flow adheres to the dynamics of the SQG system as was suggested from the vertical structure of the potential vorticity and the filamentary nature of the surface potential temperature field. The similar form of the temperature variance and kinetic energy spectra on the surface is suggestive of SQG although the temperature spectrum below the uppermost level of the flow is found to be quite different to these. The slopes of the spectra do not match those predicted by SQG theory but not too much weight should be put on this point as differentiating between different slopes from the spectra and identifying inertial ranges is somewhat subjective when there are many factors

which mean our system deviates from the idealised theory. These factors include a finite domain size, regions of free convection, non constant PV in the interior and a background meridional temperature gradient.

The most compelling evidence of SQG behaviour is the decay of the surface spectra with depth. The decay constant is close to that predicted by theory at high rotation rates. In the temperature variance spectrum this decay is evident from the second level from the top, but the top surface has a different spectral shape and lower power density than the levels immediately below. We suggest this may be due to the presence of convective features at lower levels. Unfortunately, due to the need for boundary conditions in calculating the spectra we cannot diagnose the baroclinic and convective regions of the flow separately.

Finally, we used structure functions to diagnose the direction of kinetic energy transfer between scales in the annulus. This method has the advantage of being simple to implement in annular geometry and with future experimental data. Calculation of one dimensional structure functions in the baroclinic zone suggested the presence of an inverse cascade for rotation rates above 0.4rad/s. The scaling was not in agreement with the predictions of Kolmogorov's 4/5 law but this is unsurprising given that the turbulence in our experiment is neither homogeneous nor isotropic. Given the range of processes which input and dissipate energy from the system it is unlikely that inertial ranges exist in an idealised form. The structure functions did not show an inverse cascade for $\Omega = 0.4$rad/s even though the energy containing scale of the eddies was close to the Rhines scale in that simulation. This may suggest that the weakly nonlinear regime identified by Chai and Vallis (2014) is increasing the eddy scale without involving an inverse cascade here.

The existence of an inverse cascade at the highest rotation rates is consistent with our result from the previous chapter that the flows in the annulus can become supercritical at high rotation rates. We also note that we observe alternating zonal jets in the flows where an inverse cascade is seen. At moderate rotation rates, where we found the criticality of the flows to be approximately constant,

the energy containing scale of the eddies is less than or similar to the deformation radius and no inverse cascade is observed.

Illusions are to the soul what atmosphere is to the earth.

— Virginia Woolf, *Orlando*

7

An idealised planetary atmosphere

The work detailed in chapter 3 which was required to adapt a model of the atmosphere to a model of the annulus demonstrates the many differences which exist between flows in these two settings. This inevitably leads to the question of how useful the lab experiment can be as an analogue for a planetary atmosphere and whether the phenomena we have observed thus far in the annulus translate to the atmosphere. One of the motivating factors behind using the UM as a model for the annulus was to enable us to use the same numerical system to study both the experiment and the atmosphere. In this chapter we demonstrate this by using the UM in a simple, atmosphere-like configuration. We aim to use the results of these simulations to investigate whether the properties of the atmosphere-like flows are comparable to those we have seen thus far in the annulus. To this end, the configuration of thermal forcing we use in these atmosphere-like models is inspired by that used in the annulus. By the end of this chapter we will have produced a hierarchy of models from two dimensional simulations to three dimensional lab experiments and simulations to idealised planetary atmosphere simulations with the latter two types of simulations using the same model numerics.

The simple configuration we have chosen to use as a model of the atmosphere is based on the Held-Suarez model (Held and Suarez, 1994). This model is sufficiently simple that it is relatively inexpensive to run but captures many of the dominant

features of the dynamics which are present in both the atmosphere and the annulus experiment. The model was originally designed as a benchmark test for dynamical cores. Since then, it (and variants on the original setup) has been used extensively as an idealised testbed for many aspects of atmospheric dynamics leading to one of its creators, Isaac Held, to compare it to the fruit fly used in biology as a simple system to study as part of a hierarchy of models (Held, 2005). The Held-Suarez model is a global, dry atmospheric model on a uniform, smooth sphere. The model is forced via Newtonian relaxation of the temperature field to a specified radiative-convective profile and Rayleigh damping of the velocities is used near the surface to represent boundary layer friction. Other details are left to the choice of the individual modeller - for example whether the model is hydrostatic and what kind of boundary is specified at the model top. The original configuration uses Earth like values for the planet size, rotation rate and thermodynamic properties of the atmosphere.

A number of authors have used simple models, similar to the Held-Suarez configuration, with heating via Newtonian relaxation to approach the problem of thermal equilibration by eddies in Earth's atmosphere. As noted in chapter 1, many of the early studies of baroclinic adjustment focused on QG models as the original argument of Stone (1978) was based on the stability criterion of the two layer QG model. However, recently more attention has been given to primitive equation models which are a step closer to the real atmosphere in the hierarchy of models. Schneider and Walker (2006) used a model with thermal relaxation towards a statically unstable radiative profile coupled with a simple convective adjustment scheme to support their assertion that supercritical states, $\xi > 1$, cannot be accessed by the primitive equation model. However, their argument differs from the baroclinic adjustment hypothesis of Stone (1978) as it is based on estimates of the eddy fluxes of potential vorticity and surface potential temperature rather than invoking any dependence on the baroclinic stability of the system.

More recent studies of Held-Suarez-like primitive equation systems have shown that under certain circumstances the criticality of primitive equation systems with

Newtonian heating can be continuously varied above one (Zurita-Gotor, 2008; Zurita-Gotor and Vallis, 2009; Jansen and Ferrari, 2012; Chai and Vallis, 2014). Schneider and Walker (2006) and Chai and Vallis (2014) carry out their simulations on spherical Earth-like planets whereas the other studies use channel models on a β-plane. Zurita-Gotor and Vallis (2013) extended these studies to use an idealised gray radiation model rather than Newtonian heating. They found that the vertical transport is an important factor in setting the criticality and this was only comparable between the Newtonian heating and gray radiation models when an unstable profile was used for relaxation in the Newtonian case.

We base our simulations on the standard Held-Suarez setup but with a few differences. The main difference is that we use an unstable profile inspired by the conductive temperature field in the annulus for our Newtonian relaxation. This is combined with the convective adjustment parameterisation scheme that was tested in the annulus in section 4.4.1. With a view to comparing the results with those from the annulus we focus on spanning a similar range of thermal Rossby number by varying the planetary rotation rate. By doing so we produce simulations across a wider range of rotation rates than most previous authors. Details of the modifications to the original Held-Suarez setup are outlined below. As in previous chapters our primary aim is to understand the thermally equilibrated state which emerges and here we have the additional goal of comparing the results to the findings from the annulus. We also note that, as in our annulus simulations and in contrast to the work of previous authors outlined above, our model solves the full, non-hydrostatic Navier-Stokes equations rather than the hydrostatic primitive equations. However, given that none of the systems in our simulations deviate too far from Earth's atmospheric conditions we would expect the hydrostatic primitive equation approximations to hold well.

7.1 Model setup

We begin with ENDGame configured for the Held-Suarez test, which is a standard configuration in the UM. Mayne et al. (2014) carried out the Held-Suarez test using

ENDGame at moderate resolution (144 longitude points, 90 in latitude and 32 vertical levels) and found the results to be consistent with those in the literature for other models. It should be noted that Mayne et al. (2014) used a dry static adjustment scheme to parameterise convection. This should not be necessary for the original Held-Suarez test as the temperature is relaxed towards a statically stable radiative-convective equilibrium and so convection is already implicitly accounted for. Hence, we do not include a convection parameterisation scheme in simulations where a stably stratified relaxation field is used. Heng et al. (2011) showed, using a spectral dynamical core, that differences between runs with and without the adjustment scheme were negligible when a stable relaxation profile was used and we found the same is true for our model. We carry out some runs using the setup and parameters of Held and Suarez (1994) for comparison with the more novel setup outlined below.

7.1.1 A conductive relaxation profile

In the interest of comparing the results of these atmosphere-like simulations with the previous results from the annulus, the major modification we make to the Held-Suarez model setup is the relaxation profile. In the annulus, in the absence of dynamics, heat is transferred through the system by conduction. Mapping the configuration of heating in the annulus to a spherical shell of thickness d=10km with inner radius equal to the radius of Earth, a=6371km, produces the conductive equilibrium profile shown in figure 7.1. Here the top and bottom boundaries are thermally insulating aside from an isothermal hot region at $r = a$ and $\phi < 20°$ and an isothermal cold region at $r = a + d$ and $\phi > 70°$. The temperature difference between this heat source and sink is 115K. The conduction equation is then solved using a simple Jacobi iteration with an anisotropic diffusion coefficient which is 5000 times larger in the horizontal than the vertical to produce a similar rate of heat transport in the horizontal and vertical directions despite the large aspect ratio of the atmosphere.

We use this solution to the conduction equation as inspiration for a temperature relaxation profile in the model. The model architecture of the UM does not readily

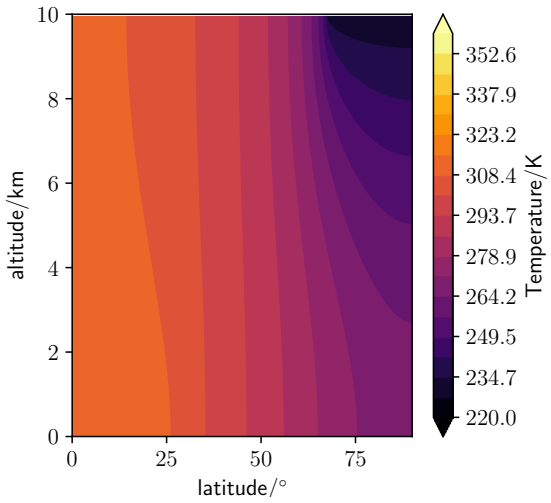


Figure 7.1: The solution to the thermal conduction equation in a quarter of a spherical shell with inner radius a and thickness $d = 10$km with an isothermal heat source on the bottom boundary for latitude, $\phi < 20°$ and an isothermal heat sink on the top boundary for $\phi > 70°$. The temperature difference between the heat source and sink is 115K. An anisotropic diffusion coefficient is used which is 5000 times larger in the horizontal than the vertical.

allow the relaxation profile to be read from a file and so we approximate the above field using an analytical function. We use this as a relaxation profile for potential temperature so that we are relaxing to a profile which is unstably stratified in the vertical. The conductive profile is approximated using the function

$$\theta_{eq} = \max\left\{\frac{T_{top}}{\Pi}, T_s + \Delta_H\left(\sigma^{1/10} - 1 - \frac{\sin^2\phi}{\sigma^{1/10}}\right)\right\} \tag{7.1}$$

where $\sigma = p/p_0$, T_{top} is a constant stratospheric temperature set equal to 200K and Δ_H is the applied temperature difference between the pole and equator at the surface which is equal to 60K throughout this work. Although the initial conditions are specified in σ co-ordinates, the model levels are height based as discussed in chapter 3. T_s is the surface temperature of the equator which is set equal to 315K. The presence of the isothermal stratosphere is required for model stability and means that the conductive profile extends only to a certain altitude which sets a radiative constraint on the tropopause height. This height is dependent on latitude. When the thermal relaxation timescale, τ, is long, there is some flexibility for the dynamics to affect the tropopause height. The relaxation profile is unstable to

convection everywhere in the troposphere, although more so at the pole and equator than in the extra-tropics. Figure 7.2 shows the conductive profile of potential temperature given by equation 7.1 compared to the profile of the classic Held-Suarez setup. The crucial difference is the unstable stratification in the conductive profile.

Although this unstable stratification can cause grid scale convection we use a parameterisation scheme for convection in most of our simulations where the unstable relaxation profile is used. We employ the same convective adjustment scheme described in section 3.2.8 in these simulations. The convective timescale, τ_c, is set to 4hrs. The combination of an unstable profile and a convective adjustment scheme is somewhat similar to the setup of Schneider and Walker (2006) although their equilibrium temperature profile is considerably more unstable than ours and they use a rescaled convective lapse rate to mimic latent heat release by moist convection compared to the dry adiabatic lapse rate used by our convection scheme. An unstable relaxation profile has also been studied in a two layer primitive equation model by Zurita-Gotor and Vallis (2009) where a convection scheme was not used but grid scale convection did occur. As pointed out by Zurita-Gotor and Vallis (2013) the main difference between relaxing toward a stable, radiative-convective state as opposed to an unstable state is that in the unstable state convection acts sporadically, only when the stratification becomes unstable. When the radiative equilibrium profile is stable it is implied that convection is happening at all points and at all times and thus the heat transport in the vertical by the resolved dynamics is reduced.

7.1.2 Parameter variation

We focused on changing the rotation rate of the simulations as we did when simulating the annulus. The rotation rate was varied between $1/16\Omega_E$ and $4\Omega_E$ where Ω_E is the Earth's rotation rate. We also gave some consideration to the effect of changing the time constant, τ, of the Newtonian relaxation. This was varied between 1day and 50days. As we have seen in the annulus, a fast rotation rate stiffens the fluid which inhibits advective heat transport and causes the flow form to tend to the conductive solution. A shorter relaxation time is expected to have

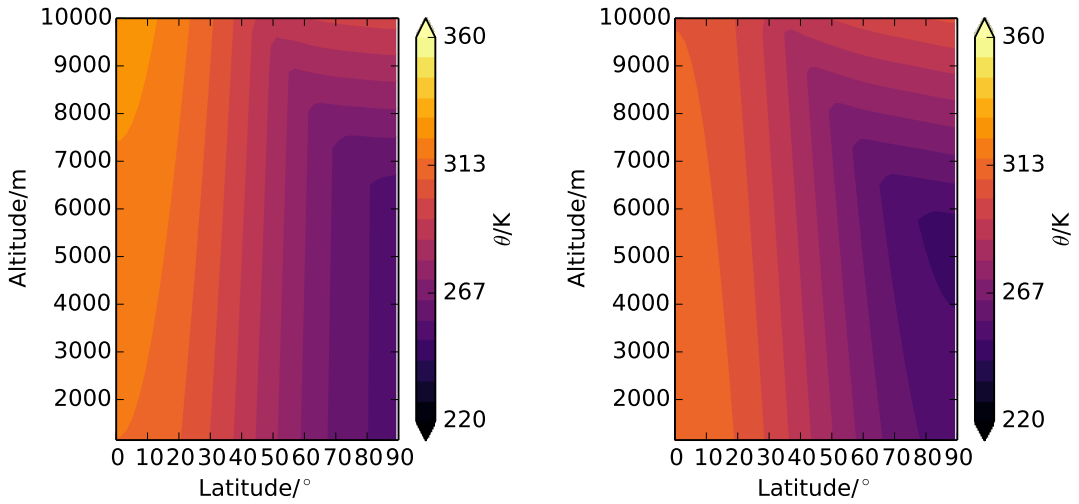


Figure 7.2: The left hand panel shows the radiative-convective relaxation profile for potential temperature in the standard setup of Held and Suarez (1994). The right hand panel shows the unstable conductive profile described by equation 7.1.

a similar effect. We used the same relaxation timescale for the entire flow given that our system was inspired by the tendency of the annulus flow to the conductive solution. As in Held and Suarez (1994) we used a linear damping of the velocities on a timescale of 1day up to a height of $\sigma = 0.7$ to represent boundary layer friction.

Following Zurita-Gotor (2008) we also tested the effect of using a different forcing timescale for the eddies and the mean flow. The equation for the temperature forcing in this case was modified to

$$\frac{D\theta}{Dt} = -\frac{1}{\tau}(\theta - \theta_{eq}) - \frac{1}{\tau}(\gamma - 1)(\overline{\theta} - \theta_{eq}) \tag{7.2}$$

and hence the forcing timescale was γ times greater for the mean flow than for the eddies. For most of our simulations $\gamma = 1$ unless specified otherwise. By setting a long relaxation time for the eddies and a short timescale for the mean flow we were able to strongly force the mean flow without damping out the eddies. This is a convenient numerical tool but is not necessarily physically justified. We found that, in general, forcing the flow in this way made little difference to the mean state compared to forcing the eddies on the same timescale as the mean flow.

We ran all simulations for 1200 days. The first 200 days were discarded as spin up time and the following 1000 days were used to produce time averages. We used

2° resolution in both latitude and longitude and 38 vertical levels up to a height of 40km with approximately 15 levels between the surface and the tropopause.

7.2 Zonal mean diagnostics

We begin by considering the zonal mean fields. The temperature, zonal wind and meridional overturning circulation are shown for a number of different rotation rates for τ =1day and τ =50days in figures 7.4 and 7.3. From here we may already draw some qualitative parallels with the simulations of the annulus experiment. The overturning streamfunction field consists of cells which increase in number and decrease in width with rotation rate. When the relaxation time constant is reduced to 1 day (so the flow is forced very strongly towards the applied profile) only one overturning cell is observed at all rotation rates. We also see that the overturning circulation becomes weaker as rotation rate is increased but it is stronger for lower τ. The isentropes in the troposphere, below about 200hPa, steepen as rotation rate increases and are steeper for shorter relaxation time.

The simulation with $\Omega = 1.0\Omega_E$ and $\tau = 50$ days is the most comparable of those shown in figure 7.4 to the terrestrial atmosphere. In this simulation the width of the thermally direct Hadley cell is approximately 30° which is comparable with what is seen in Earth's atmosphere. In total there are three cells in each hemisphere which is also consistent with observations of Earth's atmosphere. The sense of the motion in each cell is given by the sign of the streamfunction - a positive overturning streamfunction denotes clockwise motion while a negative streamfunction means the motion is anti-clockwise. The corresponding plot of potential temperature in figure 7.3 shows that, as in Earth's atmosphere, the slope of the isentropes and hence the baroclinicity is higher in the extratropics than in the tropics.

We can estimate a dynamical timescale, τ_D, from the thermal wind, U, and the length scale, a, given by the size of the planet. Hence

$$\tau_D = \frac{a}{U} = \frac{\Omega a^2}{R\Delta_H} \tag{7.3}$$

Substituting in the values for R, a and Δ_H which are constant across our simulations we find that $\tau_D \approx 2\Omega^*$days where $\Omega_E = 7.29 \times 10^{-5}\mathrm{s}^{-1}$ is the Earth's rotation rate and $\Omega^* = \Omega/\Omega_E$. When this dynamical timescale is similar to or larger than the thermal forcing timescale, τ, the dynamics become inefficient and the flow is set by the radiative-convective or conductive-convective equilibrium of the relaxation profile. Hence, for $\tau = 1$day the mean state is expected to be dominated by the effect of the conductive-convective equilibrium imposed by the thermal relaxation profile.

7.3 Criticality

We now consider the criticality of the flows and how this changes with rotation rate and relaxation time. We compute the criticality using the definition of Schneider and Walker (2006)

$$\xi = -\frac{f}{\beta}\frac{\partial_y \overline{\theta}_s}{\Delta_v} \tag{7.4}$$

where $\Delta_v = -2\overline{\partial_p \theta}^s (\overline{p}_s - \overline{p}_t)$[1]. s denotes that the quantity is calculated at the surface although we use the near surface layer at 700mb in our calculations to avoid boundary layer effects on the isentropes. $\overline{p}_t$ is the pressure at the tropopause which we define according to the WMO definition. This states that the tropopause is at the lowest level where lapse rate decreases below 2 K/km provided that the average lapse rate between this level and all higher levels within 2km does not exceed 2 K/km. This is appropriate as none of the thermal structures in our simulations deviate too far from an Earth-like atmosphere. As a reference latitude for calculating f and β we take the latitude, ϕ, where the eddy potential temperature flux, $\overline{v'\theta'}\cos(\phi)$ reaches a maximum on the 700mb level. We average quantities over the baroclinic zone which is defined as the range of latitudes within which the eddy potential temperature flux is within 30% of its maximum value. Hence, the reference latitude and baroclinic zone are located at different latitudes for different simulations.

[1]Other authors (Jansen and Ferrari, 2013b; Chai and Vallis, 2014) have noted the factor of two is not necessary as the value of criticality varies with latitude and the criticality can be varied smoothly. We retain the factor of two here but agree that the exact value of the criticality is not special

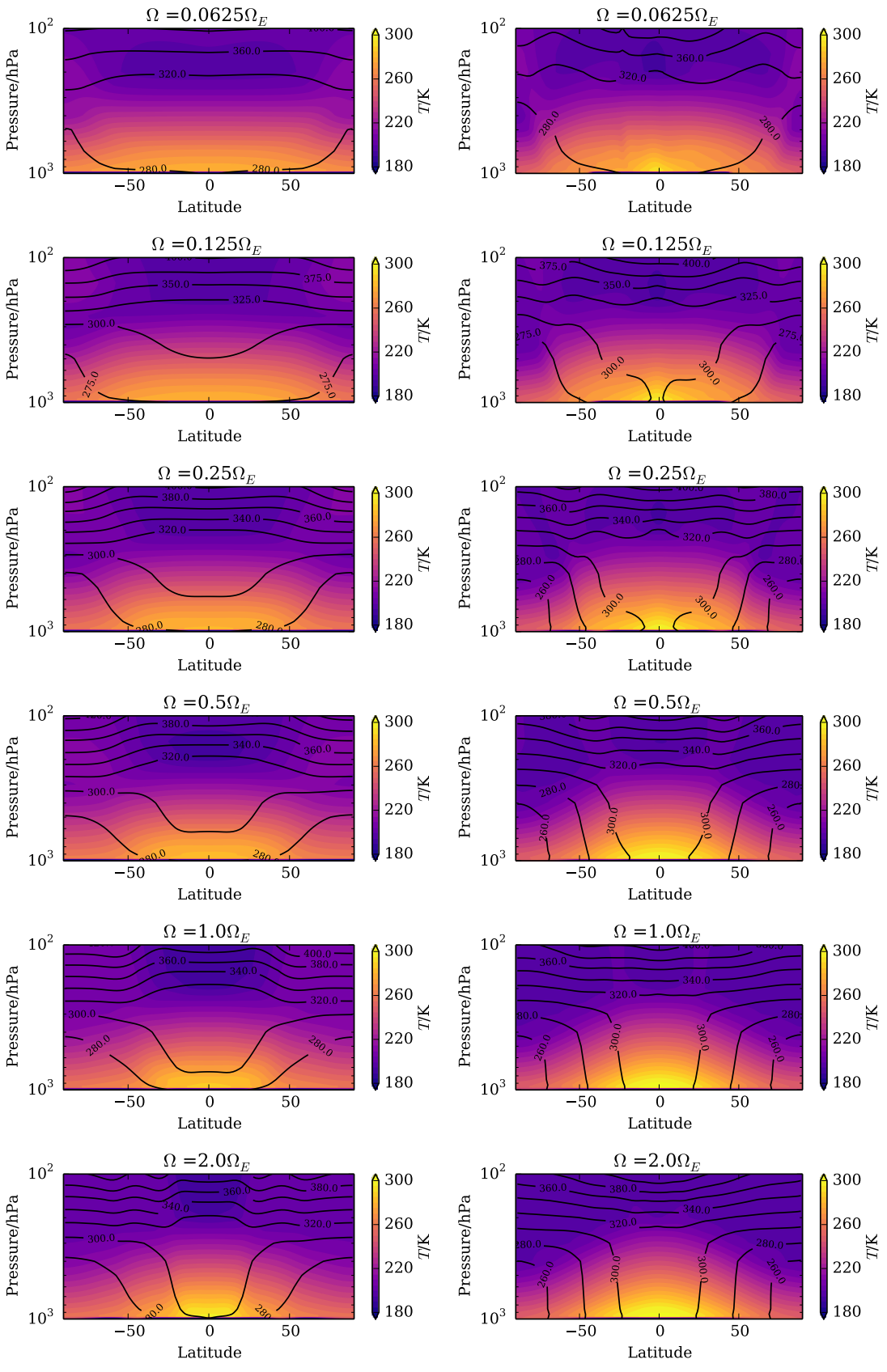


Figure 7.3: The zonally and temporally averaged temperature field (shading) and potential temperature (contours) for simulations where the thermal relaxation time is 50days (left hand column) and 1day (right hand column). Rotation rate increases down the columns.

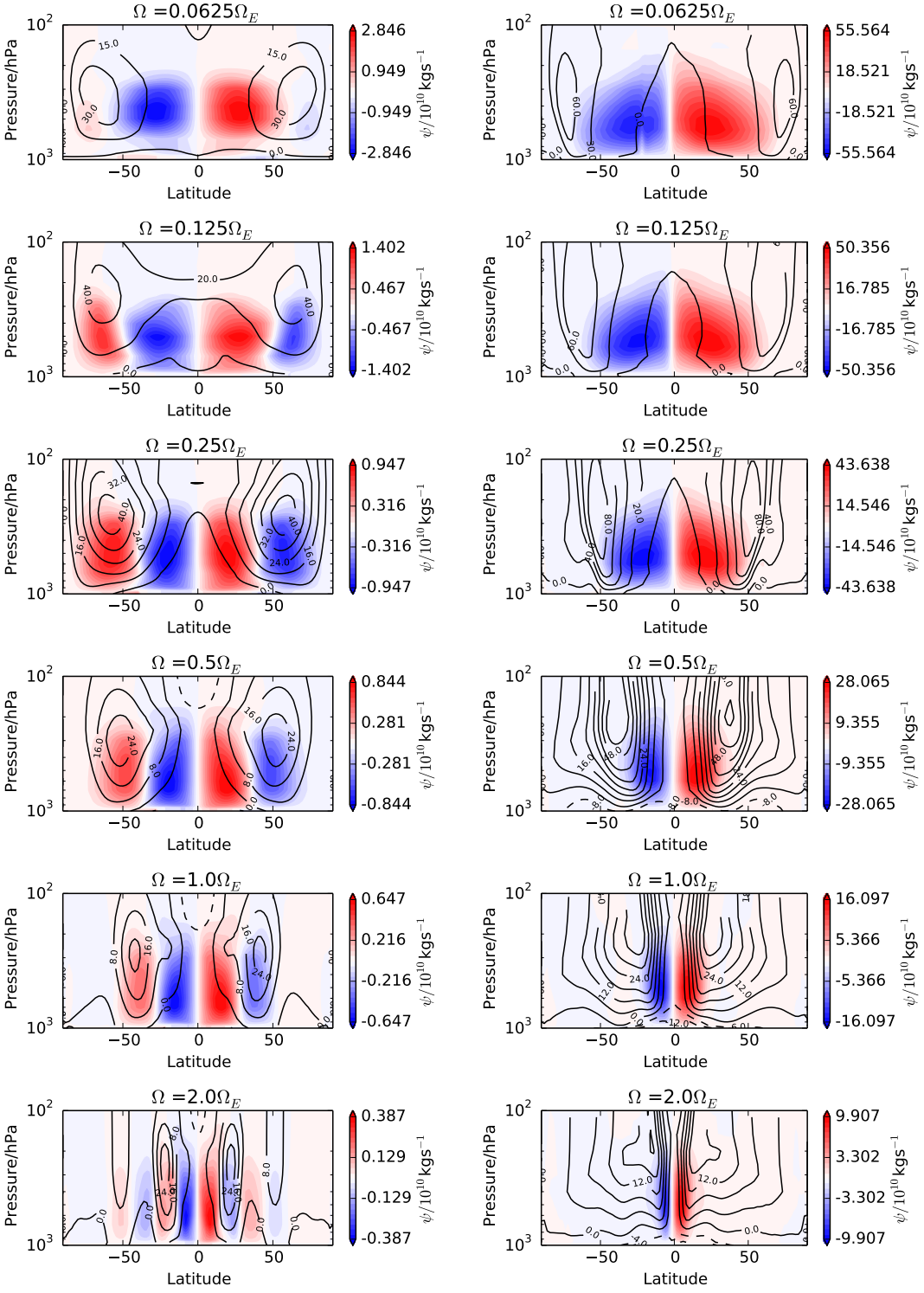


Figure 7.4: The zonally and temporally averaged meridional overturning streamfunction (shading) and zonal wind (contours) for simulations where the thermal relaxation time is 50days (left hand column) and 1day (right hand column). Rotation rate increases down the columns. The wind is given in units of ms^{-1}.

Figure 7.5 shows the trend in supercriticality and the horizontal and vertical temperature contrasts as a function of thermal Rossby number for a range of simulations. All simulations have the same equator to pole temperature difference in the relaxation profile. The horizontal thermal contrast (top row) is normalised by that of the equilibrium state. For $\tau = 1$ day the horizontal thermal structure of the atmosphere is very close to that of the relaxation profile at all rotation rates and as τ increases the meridional thermal contrast is reduced. The increase in the meridional thermal gradient with rotation rate is in the same sense as that observed in the annulus although here the simulations are far less isothermal at the highest thermal Rossby numbers.

The bulk stability (middle row) exhibits a different trend with rotation rate to that seen in the baroclinic zone of the annulus (see section 4.3). At high Ro_{th} it is approximately constant or slightly increasing and subsequently decreases sharply at a value of Ro_{th} which has some dependence on the relaxation timescale. Simulations with short relaxation timescales decrease more sharply towards zero - the potential temperature gradient of the dry adiabat. The strong thermal relaxation destabilises the flow and this is compensated by the convection scheme which relaxes towards the dry adiabat. It is notable that, in the absence of the convective adjustment parameterisation, the simulations with grid scale convection alone yield very similar results.

The trend in bulk stability with rotation rate is somewhat similar to that seen in the the annulus when the convective adjustment scheme was used there. In that case the enhanced convection due to the parameterisation scheme damped out large changes in the stratification with rotation rate. Similarities are particularly evident in the simulations here with large τ and also the one where we relax towards the stable Held-Suarez state, HS40 in the right hand column. The significance of the similarity is debatable but it is worth noting that we found the stratification to be modified in the annulus depending on how the convection is represented. Although we find here that the stratification does not change when the parameterisation scheme is used compared to when there is only grid scale convection, neither

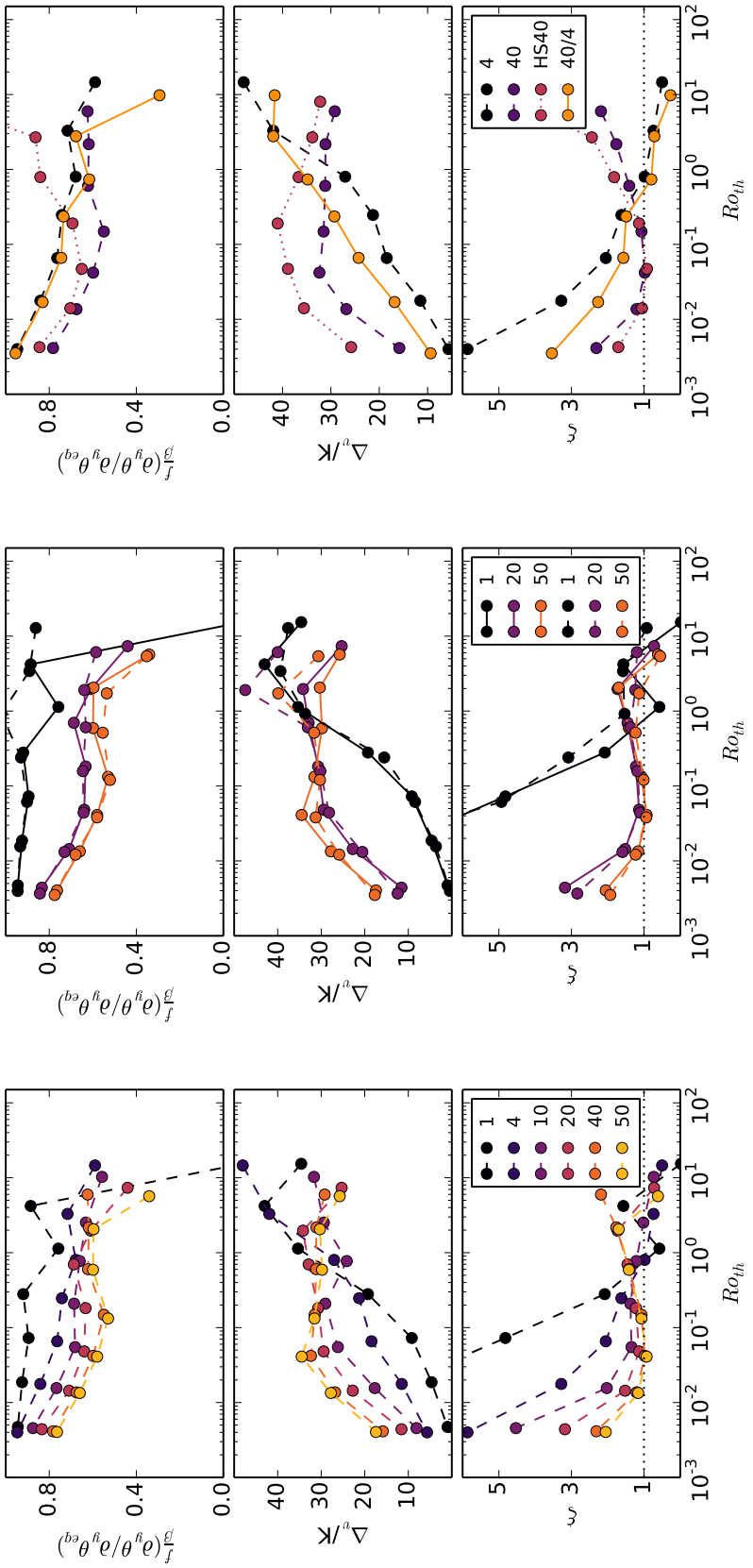


Figure 7.5: The meridional temperature contrast normalised by the equilibrium state value, $\partial_y\theta/\partial_y\theta_{eq}$, bulk stability, Δ_v, and criticality, ξ. The left hand column compares simulations with different relaxation timescales, shown in units of days in the legend. The central column compares simulations with parameterised convection (solid lines) and with only grid scale convection (dashed lines). The right hand column shows the results for the standard Held Suarez setup (HS40, dotted line), a simulation with eddies relaxed on a 40 day timescale and the mean state relaxed on a 4 day timescale (40/4) and the simulations with τ =4, 40 days from the left hand column for comparison.

situation is very realistic. The resolution is too low to resolve convection in any amount of detail and the parameterisation scheme is very simple and does not account for the effect of rotation on convection.

Despite the differences in the vertical and horizontal temperature contrasts individually, for slow relaxation timescales these effects combine to give criticalities very similar to those we observed in the annulus. For $0.1 < Ro_{th} < 1$ the criticality takes a value of approximately one (or slightly higher at the largest thermal Rossby numbers) and then begins to increase smoothly as thermal Rossby number increases further. For large τ the range of criticalities (up to a maximum of about 3) is similar to that seen in the annulus but for small τ the flow becomes dominated by convection reacting to the destabilisation of the flow by the strong thermal relaxation and the criticality becomes very large as the bulk stability is strongly reduced.

To compare further with the criticality in the annulus flows we plot the criticality as a function of the ratio of the deformation radius to the horizontal length scale of the flow (taken to be the planetary radius, a, in this case) as in figure 5.12. This is shown in figure 7.6. The similarity between the plot on the top left of figure 7.6 and figure 5.12 is striking. As the plot on the top right of figure 7.6 shows, criticality increases as τ decreases for a given rotation rate at small R_D/a. For $R_D/a < 0.2$ this may be accounted for by the scaling of Jansen and Ferrari (2012) where

$$\xi \approx \left(\frac{1}{\tau f}\right)^{1/4} \left(\frac{R_D}{a}\right)^{-3/4} \tag{7.5}$$

and hence $f\tau\xi^4 \approx (R_D/a)^{-3}$. Jansen and Ferrari (2012) also found this scaling broke down at around $R_D/a \approx 0.2$ and attributed this to the breakdown of the scaling of Held and Larichev (1996) which is used to estimate the eddy diffusivity. In the annulus the scaling breakdown occurs at approximately the same value of R_D/a which is also approximately coincident with the transition between irregular/turbulent flow and large scale regular waves. We also noted in this region that a diffusive relation between eddy heat flux and mean gradient may be inappropriate as the fluxes did not appear to transport heat down gradient.

For $0.2 < R_D < 1$ the criticality plateaus at a value close to one before becoming more variable again. Generally this variation results in increasing ξ for simulations with large τ and a reduction in criticality for simulations with fast relaxation. At low rotation rates the flow is dominated by the mean overturning circulations and this is much stronger in simulations with low τ. A strong overturning circulation induces strong mixing and this reduces the isentropes to a sub-critical state. In the intermediate regime, where $R_D/a > 0.2$ but the meridional circulation does not dominate the heat transport, the criticality equilibrates to a value close to 1. This was also found in the annulus and is again suggestive of a baroclinic adjustment process which causes the system to equilibrate to a preferred mean state.

As a complementary measure of criticality figure 7.7 shows the Rhines scale as a function of the deformation radius for all simulations. For most simulations the Rhines scale is larger than the deformation radius suggesting that the atmosphere is marginally supercritical and becomes increasingly supercritical as the deformation radius is reduced with rotation rate. At the very lowest rotation rates the flows are subcritical as the mean overturning sets the isentropic gradient and heat transport. This suggests the possibility of an inverse cascade at high rotation rates where there is reasonable separation between the two scales but further investigation is required to ascertain whether this exists or not.

7.4 Energy transfer

We end this chapter by considering various diagnostics for the heat transport in this idealised atmospheric system and how they compare with the results from the annulus.

7.4.1 Equator to pole temperature difference

From figure 7.3 it is clear that the temperature of the equator at the surface increases with rotation rate and is also higher when the relaxation timescale is shorter. Figure 7.8 shows the trend in the equator to pole surface temperature difference normalised by that of the relaxation profile which is equal to 60K. The

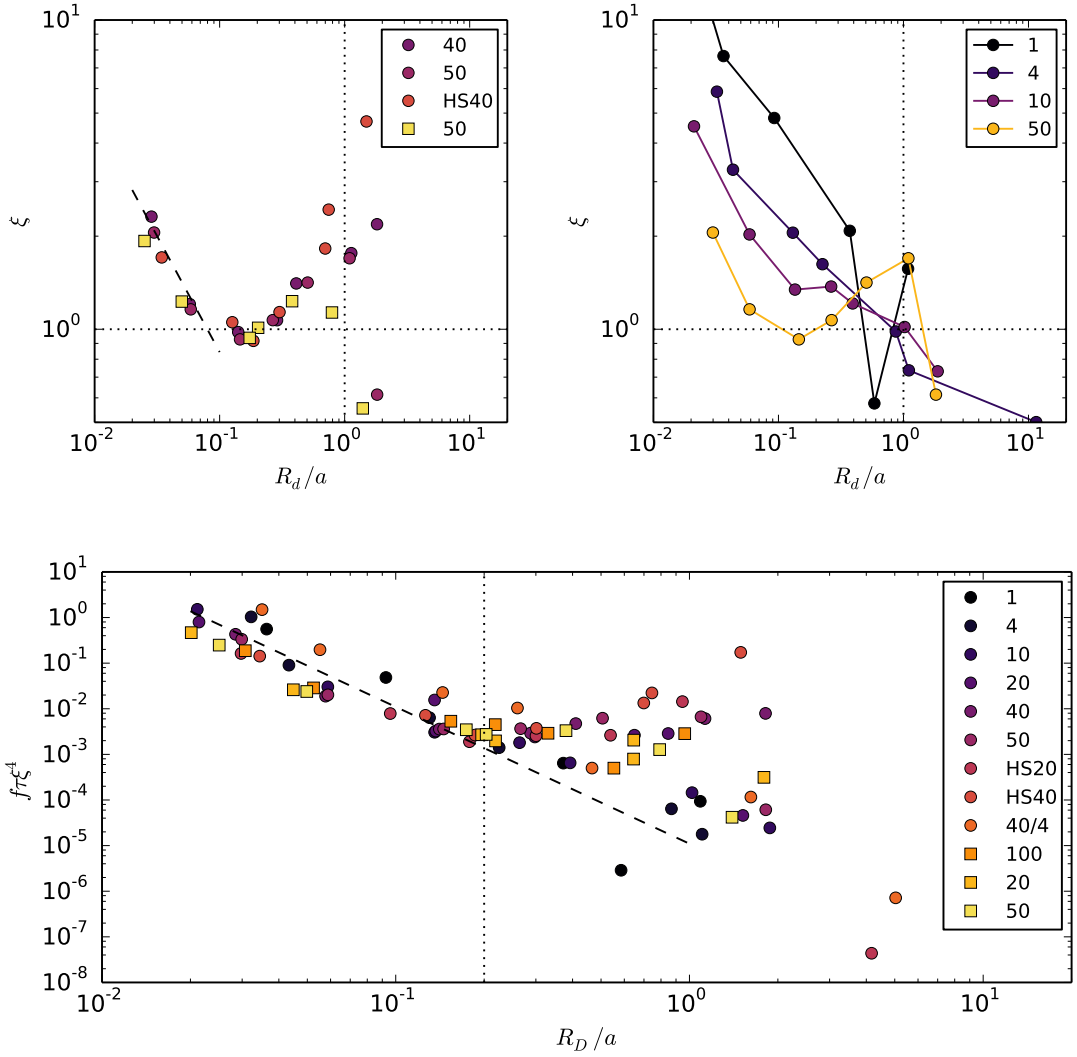


Figure 7.6: The criticality as a function of the non-dimensionalised deformation radius in the annulus. The top left panel shows only runs with long relaxation timescales and these may be compared with the same plot for the annulus data in figure 5.12. Square points represent runs without parameterised convection. The dashed line has a slope of -3/4 in accordance with the scaling of Jansen and Ferrari (2012). The top right panel shows the dependence of the criticality on the relaxation timescale, τ, which is given in units of days in the legend. The bottom panel shows all experiments scaled according to the full scaling of Jansen and Ferrari (2012), see main text for details. Here the dashed line has a slope of -3.

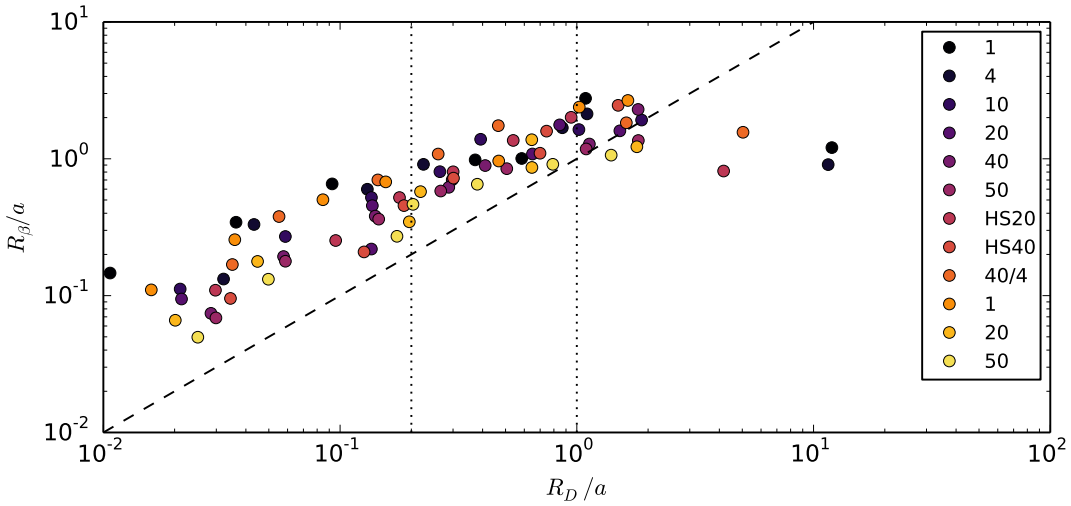


Figure 7.7: The Rhines scale vs. the Rossby deformation radius, both normalised by the radius of the Earth. The dashed line shows where the two are equal and colours are used to represent the same sets of simulations as in the bottom panel of figure 7.6.

stronger the forcing, the closer the temperature difference comes to the applied temperature difference. The exception to this is for $\Omega = 4\Omega_E$ for the shortest relaxation times where the temperature difference drops sharply. This may be due to numerical instability in these simulations where the model is forced very strongly towards the unstable profile.

The equator to pole temperature difference is a marker of the efficiency of heat transport by the flow with lower temperature differences indicating more efficient heat transport. The general trend with rotation rate is a rapid increase in temperature difference at low and high rotation rates with a plateau region at intermediate values of Ω. Wang et al. (2018) attributed a similar result to the possibility of a baroclinic adjustment mechanism causing the plateau as eddy activity resists the change in forcing over some range.

We also note that temperature differences are much lower for a given rotation rate and relaxation timescale in simulations where the flow is relaxed towards an unstable conductive state rather than the standard Held-Suarez radiative convective profile. In relaxing towards the Held-Suarez state, which is convectively neutral, we are effectively assuming that convection is acting everywhere at all times. A caveat

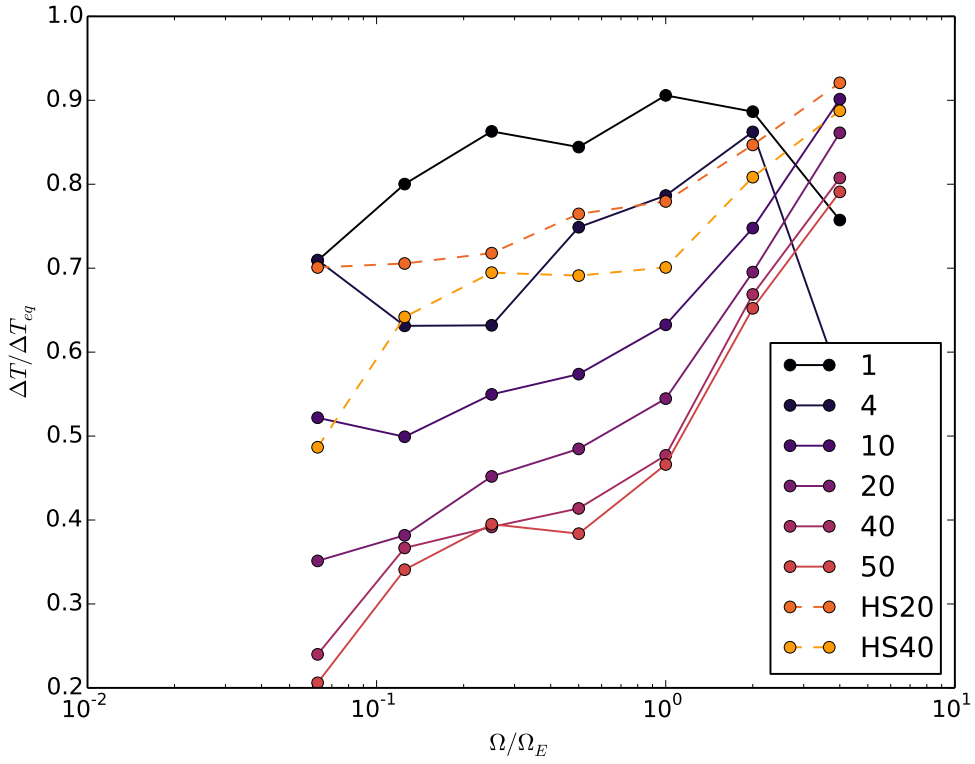


Figure 7.8: The surface equator to pole temperature difference, ΔT, normalised by that of the equilibrium profile, ΔT_{eq} =60K as a function of rotation rate. Different colours represent different thermal relaxation times with the numbers in the legend showing the relaxation timescale in days. Solid lines represent simulations where the temperature is relaxed towards an unstable conductive state and convection is parameterised and dashed lines show simulations relaxed towards the standard Held-Suarez radiative-convective state for comparison.

is that the implicit convection in the Held Suarez model is moist and thus the lapse rate is shallower than the dry adiabat used in our convective adjustment scheme. When we relax towards the unstable conductive state, convection acts sporadically which allows for higher heat transport efficiency by the dynamics. The difference between the two is less apparent at higher rotation rates where the temperature field is strongly constrained by the equilibrium profile in all cases.

7.4.2 Heat fluxes

Quantifying the heat flux due to the mean circulation and the eddies provides another way of understanding the heat transport in the system. Here we calculate

the peak integrated meridional fluxes across all latitudes as

$$F_{max} = \max\left(2\pi a\cos(\phi)\int\left[\frac{\overline{F}c_p}{g}\right]dP\right) \tag{7.6}$$

where F is either the mean flux $\overline{v}\overline{T}$ or the eddy heat flux $\overline{v'T'}$.

Figure 7.9 shows the heat fluxes due to the mean circulation and those due to the eddies for simulations with different thermal relaxation timescales, simulations with/without a convective parameterisation and simulations with different relaxation profiles. We plot these as a function of R_D/a as we found this to be a relevant parameter for scaling the criticality in the annulus and in these simulations.

Panels (a) to (f) of figure 7.9 show simulations with increasing thermal relaxation timescale. For $\tau = 1$ day the mean component of the heat flux dominates at all rotation rates. As the thermal forcing weakens the eddy component becomes stronger and tends to dominate for all but the lowest rotation rates. The zonal mean component of the flux decreases monotonically with rotation rate whilst the eddy flux increases up to a peak within the range $0.2 < R_D/a < 1$ and subsequently drops off as rotation rate increases further. For τ =50 days the mean circulation is very weak and the heat transport is almost entirely due to the eddies.

This weakening of the mean circulation is also observed in simulations where convection is not parameterised but not in the simulations where the Newtonian cooling relaxes towards a statically stable radiative convective profile. This highlights the role of convection in the various simulations. Where τ is large and we relax to an unstable profile, the weak thermal forcing does not destabilise the atmosphere very strongly and thus the convection scheme does not act. When convection is not parameterised the grid scale convection is inefficient at transporting heat. Conversely, in simulations where the relaxation profile is stable, or τ is short and an unstable profile is used, convection occurs implicitly at all times in the former case or frequently in the latter case and hence the mean overturning is stronger. In the simulations where convection is not parameterised the heat flux due to the zonal mean flow actually increases with rotation rate.

The trend in the eddy heat flux is very similar across all simulations. Furthermore, we note that the differences in the strength of the zonal mean heat flux do not seem to manifest themselves in changes in the equilibrium criticality which is perhaps unsurprising as the total heat flux is generally dominated by the eddy component. For $R_D/a < 1$ the trend in total heat flux is fairly similar for all simulations, it stays approximately constant as rotation rate increases and then drops off for $R_D/a < 0.2$. Where convection is strong the total flux remains constant for $R_D/a > 1$ as the increase in eddy flux compensates for the reduction in zonal mean flux. In simulations where the zonal mean flux is very weak the total flux increases as the eddy flux in this regime.

Comparing these results to those from the annulus we note some differences and similarities. In both cases the heat transport is generally dominated by the eddy fluxes except at the lowest rotation rates (or for small τ in these simulations) and the strength of the overturning circulation is reduced with rotation rate. However, the change in the eddy meridional flux with rotation rate is quite different in each case. In the annulus the meridional flux does not plateau in the region $0.2 < R_D/a < 1$, it is approximately constant for all but the lowest rotation rates. Here the behaviour is more intuitive as the eddy fluxes decrease as the deformation radius becomes smaller and hence the eddy diffusivity is reduced. This may in part be due to the weak thermally driven circulation in the annulus resulting from the partially resolved convection. This results in a comparatively weak zonal flow at low rotation rates which may be compensated for by eddy fluxes. Furthermore, due to the imposed boundary fluxes in the annulus there are tighter constraints on the total heat flux through the system which may mean it is less sensitive to the rotation rate.

7.4.3 Lorenz cycles

Lorenz (1955) provided a simple means of analysing the energy budget in the atmosphere by formulating the Lorenz energy cycle. We shall briefly consider the Lorenz cycle for our simulations here as a function of R_D/a. The cycle consists of reservoirs of zonal mean available potential energy (AZ), zonal mean kinetic

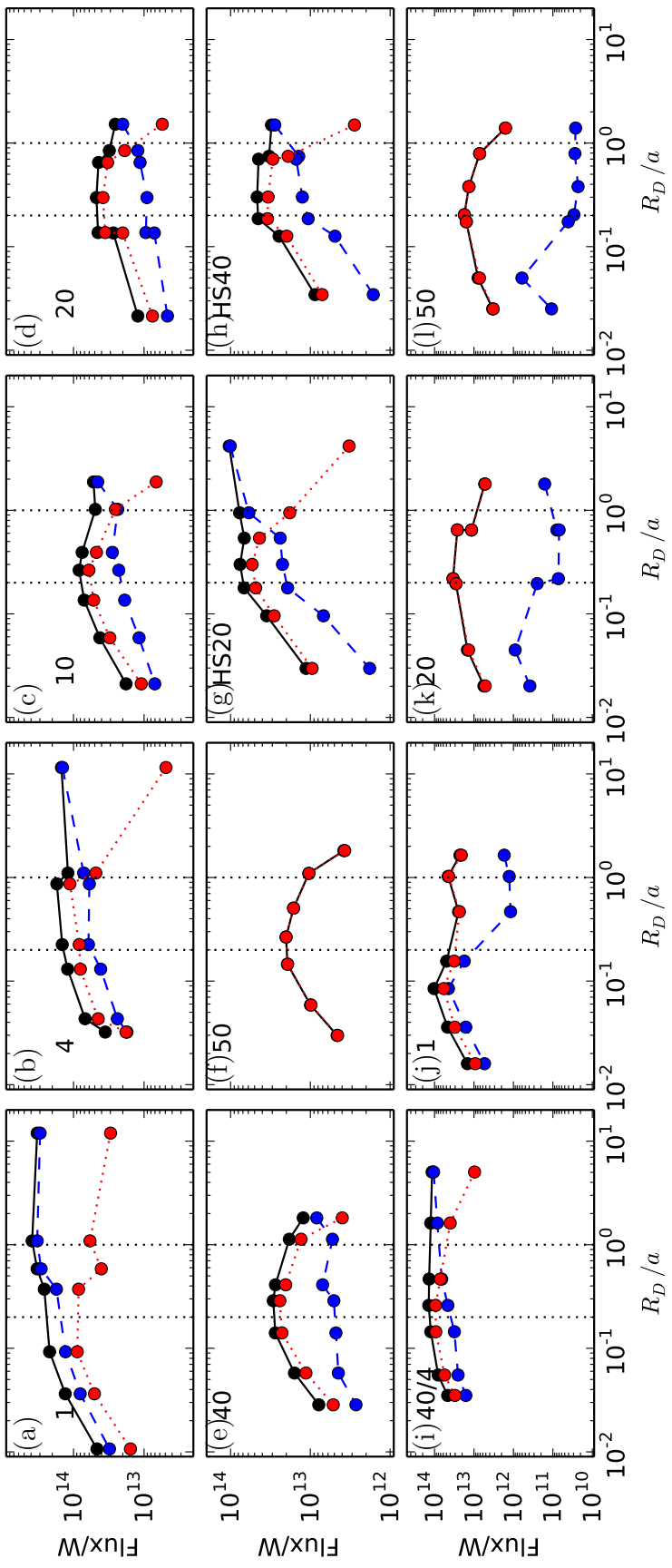


Figure 7.9: Meridional heat fluxes due to different components of the flow in different atmosphere-like simulations. The black lines represent the total heat flux, the red dotted line shows the heat flux due to the eddies and the blue dashed line represents the zonal mean component of the heat flux. Panels (a) to (f) show simulations where the thermal relaxation time, τ, is changed. The value of τ for each panel is shown in units of days. Panels (g) and (h) show simulations where the relaxation profile is the radiative-convective profile of Held and Suarez (1994) and τ=20 days and 40 days respectively. Panel (i) represents a simulation where the relaxation time scale is 40 days for the eddies and 4 days for the mean flow. Panels (j) to (l) show simulations without a convective parameterisation scheme.

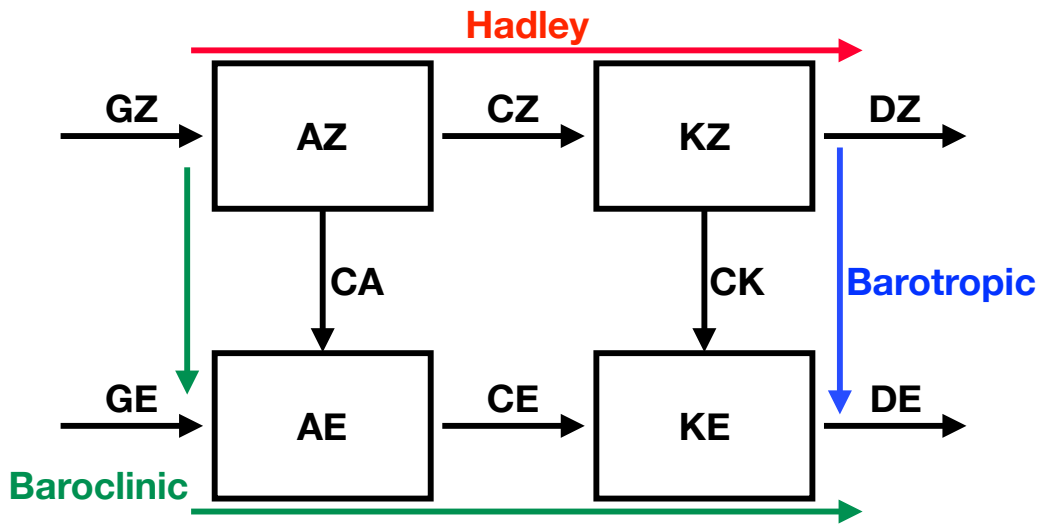


Figure 7.10: A schematic of the Lorenz energy cycle (Lorenz, 1955). The energy reservoirs represent zonal mean kinetic energy (KZ), mean available potential energy (AZ), eddy kinetic energy (KE) and eddy available potential energy (AE). The black arrows represent transfers between these reservoirs which are positive in the directions shown. The main pathways for barotropic and baroclinic instability and the mean overturning circulation (labelled Hadley) are also shown. GZ and GE are diabatic generation terms and DE and DZ are dissipation terms.

energy (KZ), eddy kinetic energy (KE), eddy available potential energy (AE) and the transfers between them. The cycle is shown schematically in figure 7.10. The transfer of zonal mean potential energy to zonal mean kinetic energy (CZ) is carried out by the mean overturning circulation. Barotropic instability feeds off the kinetic energy of the zonal mean circulation and so is represented by the transfer term CK. Baroclinic instability involves a conversion of zonal mean potential energy to eddy kinetic energy and so is represented by the pathway of CA to CE. GZ and GE are diabatic generation terms and DE and DZ are dissipation terms.

We found the trend in the globally and temporally averaged Lorenz cycle terms with rotation rate to be quite similar for all our simulations. Figure 7.11 shows an example of the change in the time averaged terms of the Lorenz cycle as a function of R_D/a for a simulation with $\tau = 50$days and parameterised convection. For $R_D/a > 1$ the zonal kinetic energy is the dominant term in the energy budget whilst for $R_D/a < 0.2$ the zonal potential energy dominates and the other terms

(KZ, KE, AE) decrease as rotation rate decreases further. This suggests that the dynamics become inefficient at reducing the potential energy of the mean state at high rotation rates. Between these two regimes, where we found the criticality to be approximately constant, there is a transition where the kinetic energy of the zonal mean state decays sharply.

We find that, in this example, the baroclinic transfer terms (CE and CA) dominate at all rotation rates although at the lowest rotation rate they are similar in magnitude to CZ. This is consistent with the trend in the meridional fluxes. For $Rd/a \leq 1$ CZ and CK are negative and reach maximum amplitude at $R_D/a \approx 0.5$. This is also where the baroclinic transfers reach a maximum. A negative value of CK indicates that eddies are driving and strengthening the mean flow by a transfer of momentum whilst a negative value of CZ indicates that the thermally indirect cells are stronger than the Hadley cell. These results are broadly consistent with those of Read et al. (2018) although they found that CZ was stronger at the lowest rotation rates. However, they used a statically stable relaxation profile within their Newtonian scheme. We have already noted that weak forcing towards an unstable profile or forcing to an unstable profile in the absence of a convection parameterisation results in a very weak overturning circulation.

7.5 Discussion

Using a simple atmospheric model we have produced simulations of an atmosphere with properties inspired by the annulus experiment studied throughout the previous chapters of this thesis. These simulations were based on the setup of Held and Suarez (1994). The main modification we made to the original setup was to use an unstably stratified state as our equilibrium profile for the Newtonian relaxation heating formulation. This was used either in conjunction with a convective adjustment scheme or grid scale convection only. The unstably stratified equilibrium profile was produced with reference to the solution of the conduction equation in the annulus. The rationale behind this approach was to produce a set of Earth-like simulations which could be compared with the results from the annulus. Relaxing

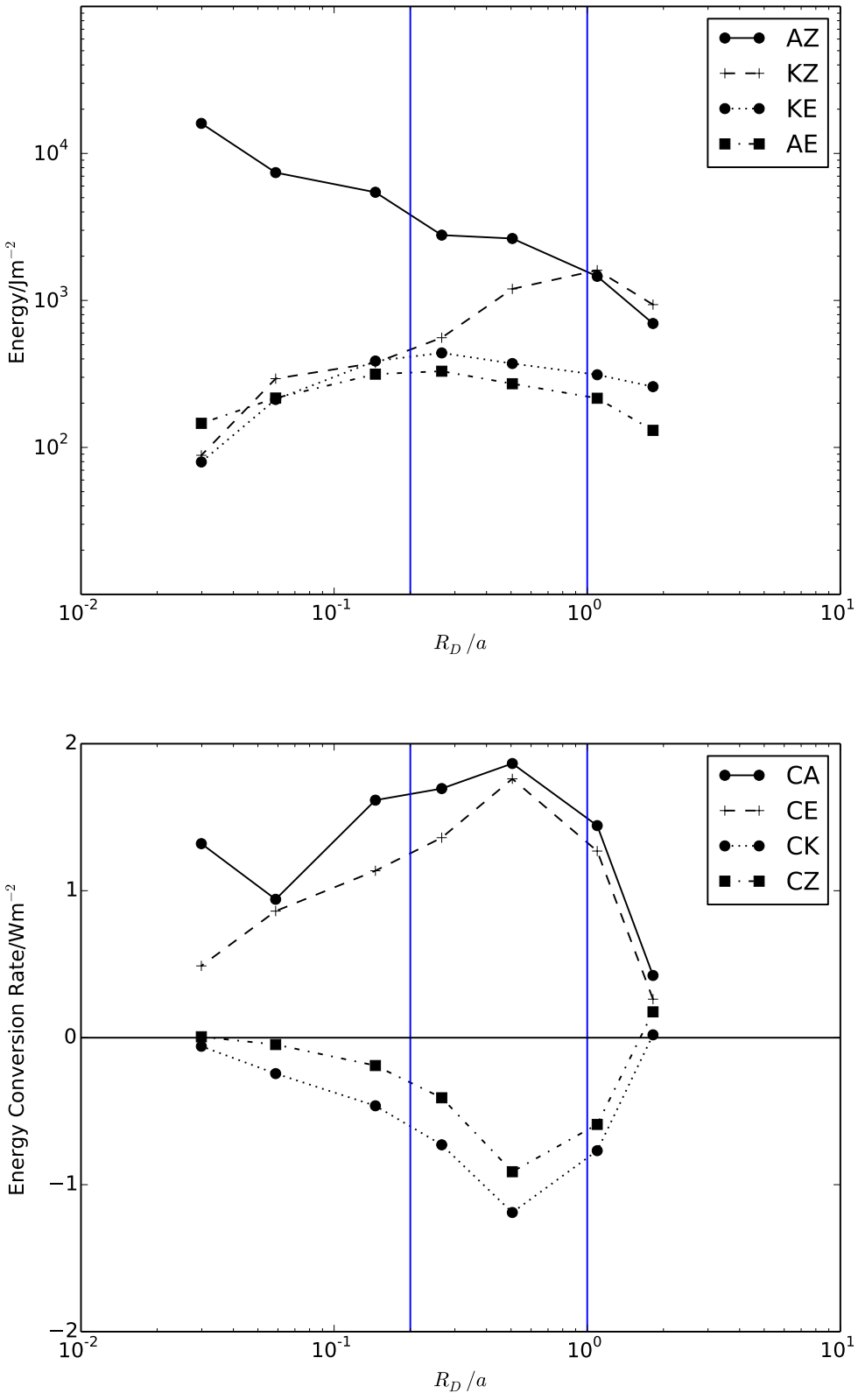


Figure 7.11: The energy reservoirs (top panel) and transfer terms (bottom panel) from the Lorenz cycle of Lorenz (1955) as a function of R_D/a. These are taken from a simulation with $\tau = 50$days and parameterised convection which is shown in panel f in figure 7.9.

the potential temperature field towards an unstable profile allows for more realistic, sporadic convection rather than the implication that convection is always acting as is the case for a stably stratified equilibrium profile.

Our results show that, in agreement with the previous results of Zurita-Gotor (2008), Zurita-Gotor and Vallis (2009), Jansen and Ferrari (2012), and Chai and Vallis (2014), we are able to smoothly vary the criticality above and below one using different combinations of forcing. This is at odds with the results of Schneider and Walker (2006) and we attribute this to the smaller range of forcing explored in their simulations.

When the ratio of deformation radius to domain size is less than 0.2, we find that the scaling of Jansen and Ferrari (2012) is a good predictor for the criticality in our simulations and this was also true for the simulations of the annulus. We find that the scaling works well for all simulations regardless of whether convection is parameterised or what relaxation profile is used or how strong the forcing is. This theory relies on the diffusivity scaling of (Held and Larichev, 1996) which only formally holds at high criticalities and so it is unsurprising that it breaks down when the criticality becomes close to one. Furthermore, the validity of a diffusive closure in general may be called into question when the size of the eddies approaches the domain size. This was supported in the annulus by evidence that the eddy fluxes are not anti-correlated with the mean thermal gradients in this regime.

At the lowest rotation rates the mean overturning becomes an important factor in determining the thermal structure of the flow but the behaviour of the system between these two extremes remains an open question. We suggest that the large scale, regular baroclinic waves observed in the annulus and known to occur in similar, idealised atmospheric models (Wang et al., 2018) are a key ingredient for the heat transport and setting the equilibrium thermal structure in the intermediate regime. However, it is unclear how or whether these structures manifest themselves in real atmospheres. The parallels which can be drawn between the flow in the annulus and these atmosphere-like flows is an encouraging sign of the utility of the annulus experiment in providing insights useful for understanding the atmosphere.

In the quasi-geostrophic models which have traditionally been used to study the problem of thermal equilibration, the stratification of the atmosphere is fixed and this presents a major difference between the models used here and the even more simplified quasi-geostrophic framework. We observed in both the annulus and the planetary simulations that the changes in vertical thermal contrast are of the same order as the changes in the meridional contrast.

However, these simplified experiments are still a far cry from a realistic atmosphere. We have already discussed the limitation that partially resolving convection or using a highly simplified convection parameterisation scheme puts on the system. As in the annulus, a convective parameterisation which captures the influence of rotation on convection would be an improvement. Another obvious factor relevant to the convection which is potentially important for the Earth's atmosphere is moisture. Although Schneider and O'Gorman (2008) found that in Earth-like climates the addition of moist convection did not greatly affect the thermal equilibration in the extra-tropics. The simple Newtonian heating formulation used here may also put unrealistic constraints on the atmospheric equilibration. Using a more realistic gray-radiation model, Zurita-Gotor and Vallis (2013) found that the atmosphere did not generally adjust to marginal criticality for typical atmospheric parameters. In comparing their model to the model with Newtonian relaxation used by Zurita-Gotor and Vallis (2011) they found that the two were fairly similar in the case where the Newtonian relaxation was towards a statically unstable state, as used in this chapter. In this case the relaxation does not imply that convection is acting all the time so the dynamical vertical heat transport is stronger.

We shall not cease from exploration
And the end of all our exploring
Will be to arrive where we started
And know the place for the first time.

— T.S. Eliot, *Little Gidding*

8 Conclusion

The aim of this thesis was to use a new approach to provide insights useful for understanding the impacts of various instabilities on the dynamical equilibration of the thermal structure of the atmosphere. This new approach involved developing a numerical model to complement the study of a novel configuration of a lab experiment. In particular we were interested in the way that baroclinic eddies may contribute to setting the atmospheric mean state and under what circumstances the existing paradigms of baroclinic adjustment and geostrophic turbulence may provide useful descriptions of this behaviour. The new experiment is a variation on the classical rotating annulus of Hide and Mason (1975). It was designed to provide a better representation of the distribution of heating and cooling in the atmosphere than previous, similar experiments. In chapter 2 we used an existing, two dimensional numerical model to provide an initial insight into the experimental flow and ensure that these design criteria were satisfied. We found that the flow in the experiment consisted of a stably stratified baroclinic zone sandwiched between two freely convecting regions. Thus, the experiment may be thought of as an analogue to the Earth's atmosphere where vigorous convection takes place in the tropics and, to some extent, in the polar regions and the mid-latitude atmosphere is baroclinic.

8.1 Overview of main results

Following this initial characterisation of the flow in two dimensions the primary aim of the work detailed here was to develop a numerical model of the new lab experiment in three dimensions which could also be used to simulate atmosphere-like flows so that the two may be more seamlessly compared than in previous work. To this end, we adapted ENDGame, the dynamical core of the Met Office Unified Model, to enable the simulation of the experimental flows. To our knowledge this is the first time that part of an operational forecasting model has been used to simulate lab experiments but the adaptation was not without difficulty. In particular, the model was found to be quite susceptible to numerical instability without the use of an appropriate monotone filter and a small timestep. The requirement on the timestep meant that the model was quite expensive to run and this negated much of the benefit of using a semi-Lagrangian scheme which is expected to be stable for relatively long timesteps.

The geometry of our annulus experiment presents a particular challenge to the modeller as the small inner cylinder means there is significant convergence of the grid at small radii and the large diameter of the experiment means a large range of scales are present in the flow. The convergence of the grid meant that, at large radii, scales two orders of magnitude greater than the Kolmogorov length scale were the smallest that could be resolved in the azimuthal direction. At small radii the high resolution required a small timestep for stability. Furthermore, the presence of the sloping bottom caused the vertical resolution to vary with radius in the interior and also limited the minimum depth of flow that could be simulated. A more systematic study of simulations with different resolutions would be required to elucidate the precise effect of these various factors on the flow. By comparing runs without a sloping bottom at two different resolutions we found that the stratification over the heat source was the property most affected by the resolution. Therefore, we suggested that a convective parameterisation, ideally one that captures the effect of rotation on the convection, may be a useful improvement to be added to the model in the future. Running at much higher resolution than

that used here would be prohibitively expensive without major improvements in numerical stability or computer hardware.

Despite these limitations of the model, qualitative comparison between the experiment and simulations was good in many respects. The same flow regimes were found within similar thermal Rossby number ranges and the trends in stratification with thermal Rossby number were similar when heat loss from the boundaries was parameterised in the simulations. However, the stratification in the simulations was much weaker than in the experiments at low rotation rate. The total temperature variance spectra on the top surface of the flow were found to be broadly similar although with a weaker zonal component than in the experiments.

The most profound disagreement between the experiments and simulations was found when comparing the total heat transport characterised by the mean temperature difference between the hot and cold plate. In simulations the heat transport was found to become significantly more efficient as thermal Rossby number decreased whilst in the experiment it remained approximately constant. Introducing a parameterisation for convection removed this spurious increase in heat transport and so we suggest that it may be an artefact of unresolved convection which weakens the thermally direct overturning. The question of how partially resolved convection affects the simulated flow is pertinent since numerical weather prediction models are now able to run operationally at resolutions in the so-called 'grey zone' where convection is partially resolved. Although convection in these realistic weather and climate models is more complex than what we have modelled, not least because moisture, clouds and precipitation play an important role, our results suggest that under resolving small convective scales may have a significant effect on heat transport. Further investigation is required to confirm and quantify the nature of this effect, we discuss this further in section 8.2.

For our analysis of the simulation results we chose to focus on the criticality parameter as a diagnostic of the mean state since this has been used extensively in the existing literature. We found that the variation of the criticality could be characterised by a number of regimes described by the ratio of the Rossby

deformation radius, R_D, to the width of the baroclinic zone, a. When the Rossby radius was of a similar size to, or larger than, the baroclinic zone the criticality was generally larger than one but it was not well defined in that regime. This was because the interior of the fluid was approximately isothermal and so both the vertical and radial temperature gradients were close to zero. When $R_D/a < 0.2$ the criticality varied according to the scaling suggested by Jansen and Ferrari (2012) which is based on assumptions about eddy size derived from geostrophic turbulence theory and a diffusive eddy flux closure. In this regime we found evidence for the existence of a significant inverse cascade at the highest rotation rates only. At slightly lower rotation rates, where the scaling still holds, it is possible that the flow is in the weakly nonlinear regime described by Chai and Vallis (2014) where eddy scale increases with criticality without involving an inverse cascade.

When $0.2 < R_D/a < 0.6$ the criticality remained approximately constant at a value which appeared to depend somewhat on the applied heat flux, which in turn sets the applied temperature difference. In this region of approximately constant criticality there is evidence that the eddy fluxes do not behave diffusively and so it is unsurprising that the diffusive closure of (Jansen and Ferrari, 2012) breaks down. The apparent equilibration to a constant value in this regime is consistent with a baroclinic adjustment paradigm although the precise dynamical mechanism for this remains unknown and poses a future challenge for theorists. It seems very likely that, in the annulus, the near constant criticality in this intermediate regime is a result of the presence of large scale baroclinic waves and so a more systematic experimental campaign to elucidate the properties of these waves - particularly how they affect heat transport through the flow - would be useful.

We also carried out simulations using an idealised model for a planetary atmosphere and found that the trends in the criticality were the same in these simulations as in the annulus. The scaling of Jansen and Ferrari (2012) held for runs with and without parameterised convection, with different thermal relaxation times and different thermal relaxation profiles. Recently, the closely related scaling

of Jansen and Ferrari (2013a)[1] was used by Komacek et al. (2019) to develop a predictive framework enabling the lapse rate and equator to pole temperature difference on terrestrial exoplanets to be calculated from parameters that can be derived from telescope observations. They suggest that their scaling applies for any atmospheres rotating sufficiently quickly that baroclinic effects dominate the atmospheric dynamics. They show this by comparing the theoretical scaling to results from a more realistic GCM than that used for our idealised simulations. Our results suggest that the theoretical basis of their scaling does not hold well for $\Omega/\Omega_E < 1$. However, it remains to be seen how well our findings extend to more realistic models of the atmosphere.

Finally, an unexpected result of this work was the apparent applicability of SQG dynamics to at least some aspects of the flows in the annulus. We found that the potential vorticity structure of the flow was such that the potential vorticity gradients in the interior of the fluid are comparatively weak but strong gradients appear on the boundaries due to the temperature gradients there. This is similar to the structure of the Eady model (Eady, 1949). In addition to this we found that the rate of decay with depth of the kinetic energy and buoyancy spectra was consistent with the decay constants predicted by SQG theory. However, the spectra themselves did not clearly exhibit the slopes predicted by SQG theory. An exact match between this theory and simulations of the annulus would be unexpected given the theory is heavily idealised. To our knowledge SQG-like flows have not previously been produced in experiment and so this result gives some insight into how a future experiment might be designed to study SQG dynamics specifically.

8.1.1 Science questions

To summarise, we provide answers to the questions which were posed in section 1.4.

1. **Can the novel annulus configuration be used as an analogue for Earth's atmosphere?**

[1] The scaling of Jansen and Ferrari (2013a) is the specific case where the fluid relaxes towards a statically neutral state, the scaling of Jansen and Ferrari (2012) is for the general case.

The novel annulus configuration fulfils its design criteria by supporting a flow which contains a baroclinically unstable zone sandwiched between two freely convective regions. This is analogous to the mid-latitude baroclinic zone between the convecting tropics and the polar cell in Earth's atmosphere. Furthermore, the mean overturning in the boundary layers plays a reduced role compared with the classical annulus and so baroclinic instability may exert greater influence on the equilibration of the mean state. However, unlike in the classical annulus, free convection is present in our system and this drives the thermally direct overturning circulation and also has an influence on the equilibrated state.

2. **Can the ENDGame dynamical core be used to successfully simulate a laboratory experiment?**

   We have managed to adapt ENDGame to produce a model for the lab experiment. The main qualitative features of the flows in the annulus experiment are replicated in the simulations. However, quantitative agreement was not generally achieved and we attribute this, at least in part, to the insufficient resolution of the free convection. Our results suggest that, for heat transport to be accurately represented by the model, convection must be well resolved or parameterised. To investigate this more thoroughly a systematic study of resolution sensitivity and closer matching of the simulation parameters to particular case study experimental flows would be useful as well as more experimental data for comparison in general.

3. **How does heat transfer in the annulus scale with different experimental parameters and specifically how does this relate to baroclinic eddy activity?**

   We focused on systematically changing the rotation rate of the simulations and also considered sets of simulations with different applied heat fluxes at the hot plate. As in previous studies we chose to focus on the criticality parameter as a measure of the equilibrated state. We found that the criticality

varied smoothly as rotation rate was changed and identified a number of regimes of different behaviour. At the highest rotation rates the scaling of the criticality was consistent with geostrophic turbulence theories, specifically the scaling of Jansen and Ferrari (2012) which suggests the criticality scales as $(R_D/a)^{-3/4}$ and that eddies transport heat diffusively. Within this regime the deformation radius was much smaller than the domain size and there was scale separation between the deformation radius and the Rhines scale. At moderate rotation rates, within the regular wave regime, the criticality saturated to an approximately constant value suggesting that baroclinic adjustment may be a more relevant closure in that regime where the diffusive closure breaks down.

4. **Is an inverse energy cascade from small to large scales observed and under what conditions does it emerge/is it suppressed?**
   We used third order structure functions to infer the existence of an inverse cascade in the annulus when $\Omega \geq 0.631$rad/s. We also observed eddy driven zonal jets for $\Omega = 1$rad/s when the applied temperature difference was low. We showed that, at these high rotation rates, the eddy energy containing scale was well predicted by the Rhines scale. These observations all imply that an inverse cascade is present at the highest rotation rates. At lower rotation rates (0.2rad/s$<\Omega<$0.6rad/s) the scaling $R_\beta/R_D \approx \xi$ was still observed to hold without evidence for an inverse cascade suggesting the weakly nonlinear regime discussed by Chai and Vallis (2014) could be active.

5. **How do phenomena observed in the lab experiment scale to a more atmosphere like configuration of the model?**
   Qualitatively, various features of the flows in the lab experiment were also observed in the idealised atmospheric simulations. For example the steepening of the isotherms with rotation rate and the reduction in strength but increase in the number of cells present in the overturning streamfunction. However, our most encouraging result is that the behaviour of the criticality parameter as a function of R_D/a seems to be consistent between the two systems.

8.2 Future work

We have already made some suggestions for how this work could be extended and improved upon in the future. One of the biggest limitations of this study is the relatively small amount of experimental data currently available for comparison with the simulations. Using the current experimental setup PIV analysis can be used to obtain the horizontal velocity fields on three different levels within the flow. This could then be used to compute the kinetic energy spectra and structure functions for comparison with our results in chapter 6.

Further thermal measurements would also be useful. In particular, a measure of the temperature at different radii in the baroclinic zone would make computation of the radial temperature gradient and hence the criticality possible. Better spatial coverage of the convective zone would also be useful to validate the representation of convection in the experiment. In particular, measurements of the temperature near the sidewalls could be used to diagnose the role of the boundaries in heat transport. In chapter 5 we found that the mean vertical heat flux was strongest in the sidewall boundary layers. Another method which could be used to increase spatial coverage of the thermal data is particle imaging thermometry. This involves using thermochromic liquid crystals as tracer particles to simultaneously measure temperature and velocity.

A more detailed analysis of the heat fluxes in and out of the domain in the experiment would enable more thorough calculations of total heat transport through the fluid. This could also be used for validation of the parameterisation of heat loss in the simulations. Preliminary calculations of this type were demonstrated by Scolan and Read (2017). Additional experimental data would be useful for model validation more generally as would a more systematic study of the simulation's resolution sensitivity. At this stage it would also be relatively simple to adapt the numerical model to simulate other, similar, annulus experiments.

As already discussed, the addition of a more sophisticated parameterisation scheme for convection might go some way towards improving agreement between the experiment and the simulations. This is necessary because it is prohibitively

expensive to run the simulations at much higher resolution than used here and parameterisation may also help mitigate any problems due to insufficiently resolving the convection. One option for this would be a mass flux, plume-based parameterisation (e.g. Cheinet (2003)) as this would account for the inhibition of convection as rotation rate increases. A combination of experimental data, parameterised simulations and simulations with only grid scale convection might then be used to better understand the behaviour of heat transfer for simulations in the 'grey zone' where convection is only partly resolved. As we have already said, this could provide insight into the behaviour of convection in numerical weather prediction models which are being run at increasingly high resolutions and hence partially resolving convection. Currently research is being undertaken to understand the key characteristics of convection at these resolutions so that scale aware parameterisations may be developed (e.g. Field et al. (2017), Tomassini et al. (2017), and Roode et al. (2019)).

We showed that the scaling of the criticality can be predicted using an eddy diffusive closure at high rotation rates in both the annulus and the idealised atmospheric model, but a similar theoretical scaling outside this regime is not known. Even if baroclinic adjustment provides an accurate closure at lower rotation rates, the idea that the flow equilibrates to a specific criticality does not in itself imply a mechanism by which this could occur.

A possible starting point for development of a theoretical description of the annulus flows would be the Eady model with appropriate modifications to include variable stratification and the β-effect. Alternatively, given that the interior potential vorticity is not identically zero in our simulations, an approach similar to that of Lapeyre and Klein (2006) where the dynamics are treated as a superposition of surface controlled SQG and advection of interior PV could be useful. However, these approaches are based on the quasi-geostrophic equations and so cannot provide a universal description of the dynamics as the quasi-geostrophic approximation breaks down for lower rotation rates and uses a constant stratification, thus precluding a potential mechanism for equilibration.

Weakly nonlinear theories have previously had some success in describing the large scale regular waves which form in the annulus in the regime where criticality is approximately constant (Read et al. (2015) and references therein). The underlying concept behind these theories is the assumption that the background flow is only weakly unstable so only a few modes of instability can grow. An important question is what sets the dominant wavenumber selected by the system and how is the heat transport related to this. This question is also pertinent in nonlinear baroclinic adjustment theory (although this is derived within a quasi-geostrophic system) which suggests the criticality is set by the dominant heat transporting wave (Cehelsky and Tung, 1991; Welch and Tung, 1998). A systematic campaign of experimental and computational work within the regular wave regime might be used to ascertain whether wavenumber selection in the annulus bears any resemblance to nonlinear baroclinic adjustment theory. Furthermore, one could look to Mars for a realistic planetary setting to validate theories pertaining to the dynamics of the regular wave regime. The atmosphere of Mars is closer to the dry approximation than that of Earth and its larger Rossby and Burger numbers mean it is more clearly within the regime where diffusive eddy behaviour breaks down. To our knowledge, no studies of the robustness of the criticality in the Martian atmosphere have taken place at the time of writing.

Another setting where the results presented here could be relevant is in Earth's oceans. As mentioned in chapter 1 baroclinic instability is an important agent of heat and momentum transfer in the oceans as well as the atmosphere (e.g. Karsten and Marshall (2002)). However, unlike in the atmosphere where the criticality is generally close to one, the ocean equilibrates to a supercritical state and this is accompanied by greater scale separation between the deformation radius and Rhines scale and hence an inverse energy cascade (Scott and Wang, 2005). Our results suggest that this is simply because the ocean and atmosphere lie within different regimes of equilibration due to their different characteristic values of R_D/a. This argument was previously made by Jansen and Ferrari (2012) who suggested that the root of the difference is the thermal expansion coefficient of the fluid which is larger

for air than seawater, resulting in a smaller deformation radius in the ocean. The results presented here could offer a basis for designing new or validating existing parameterisations of oceanic eddies based on a diffusive closure.

Finally, the ultimate aim of idealised modelling, whether it be in an annulus experiment or in a numerical model, is to provide a better understanding of the dynamics of the atmospheres of Earth and other planets. To this end, as well as using more simplified theoretical approaches, one would need to test how well the results presented here extend to more complex, realistic atmospheric models. A first step might be to include more complexity in the existing idealised atmosphere simulations. For example, a gray or more complex radiation scheme could be used or a more sophisticated convection parameterisation. Eventually it would be of interest to see whether the criticality behaves in the same way in sophisticated GCMs with radiative transfer and moisture present. If it does, this could lead us towards a means of predicting the equilibrated mean state of an atmosphere from external parameters. The recent work of Komacek et al. (2019) has already suggested that this might be possible. Ultimately, to fully understand the mechanisms which control the dynamics of the atmosphere and how these various phenomena interact we require a full hierarchy of models, from the highly idealised to the highly complex and realistic. The benefit of having used the Met Office UM in this study is that we would be able to assess this full hierarchy from within the same model.

Appendices

A

The form of the diffusive term used in MORALS

The diffusive term, **D**, used in the momentum equation (Equation (2.1)) consists of a radial component,

$$D_u = \Delta^2(\nu, u) + \frac{1}{r}\frac{\partial(ru)}{\partial r}\frac{\partial \nu}{\partial r} + \frac{\partial w}{\partial r}\frac{\partial \nu}{\partial z}, \tag{A.1}$$

an azimuthal component,

$$D_v = \Delta^2(\nu, v), \tag{A.2}$$

and a vertical component,

$$D_w = \tilde{\Delta}^2(\nu, w) + \frac{\partial u}{\partial z}\frac{\partial \nu}{\partial r} + \frac{\partial w}{\partial z}\frac{\partial \nu}{\partial z}. \tag{A.3}$$

The diffusion operators, $\Delta^2(\nu, A)$ and $\tilde{\Delta}^2(\nu, A)$, are given by

$$\Delta^2(\nu, A) = \frac{1}{r}\nabla \cdot \left(\nu r^2 \nabla\left(\frac{A}{r}\right)\right) \tag{A.4}$$

$$\tilde{\Delta}^2(\nu, A) = \nabla \cdot (\nu \nabla A) \tag{A.5}$$

where A is a component of the velocity vector.

B

Details of tests for cylindrical geometry

B.1 Barotropic instability test in a cylinder

This test was used to set up a barotropically unstable flow in the annulus. The inviscid, isothermal fluid was initialised with a radially dependent azimuthal velocity with an inflection point. All boundaries were thermally insulating and free slip. The radial and vertical velocities were set to zero and the azimuthal velocity was set to

$$u = \frac{u_0 s}{\sqrt{1+s^2}} \tag{B.1}$$

where $u_0 = 50\text{ms}^{-1}$ is the magnitude of the velocity and $s = a(r - r_m)/r_i$ is a scaled radial co-ordinate. r_m is the radius at the centre of the annular domain, r_i is the inner radius and a is a scale factor to moderate the width of the sheared region. The initial azimuthal velocity profiles for different values of a are shown in figure B.1. The initial pressure field, p, is calculated by substituting this velocity profile into the radial component of the momentum equation in cylindrical co-ordinates. Assuming the initial conditions are in the steady state,

$$\frac{1}{\rho}\frac{\partial p}{\partial r} = 2\Omega u + \Omega^2 r + \frac{u^2}{r}, \tag{B.2}$$

which can be solved analytically via substitution for ρ using the ideal gas equation (equation 3.4).

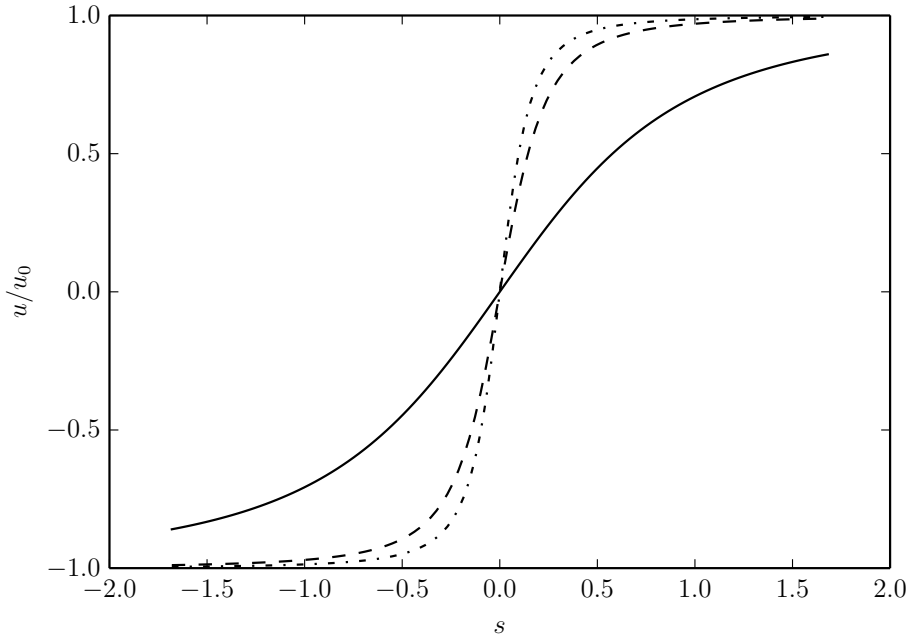


Figure B.1: The normalised azimuthal velocity, u/u_0, as a function of scaled radial co-ordinate, s, for different values of the parameter a. The solid line gives the velocity profile for $a = 1$, the dashed line represents $a = 4$ and $a = 6$ is given by the dashed-dotted line. The smaller the value of a, the greater the width of the shear zone.

For these simulations 90 gridpoints were used in the azimuthal direction, 120 in the radial direction and 70 in the vertical. The inner radius was placed at 450km and the radial resolution was 12.5km. The total height of the domain was 32km with no grid stretching in any direction.

B.2 Baroclinic instability test in a cylinder

This test is based on the Jablonowski-Williamson baroclinic wave test (Jablonowski and Williamson, 2006). The original version of this test in spherical co-ordinates is included in the UM as an option for initialising the model. The test involves applying a perturbation to an initially steady zonal velocity field to trigger a baroclinic wave.

The initial conditions in cylindrical geometry are derived as follows. The inviscid

primitive equations in the required cylindrical co-ordinates are given by

$$\frac{Du}{Dt} + \frac{uv}{r} = \frac{-RT}{r}\frac{\partial \ln(p)}{\partial \theta} - 2\Omega v - \frac{1}{r}\frac{\partial \phi}{\partial \theta} \tag{B.3}$$

$$\frac{Dv}{Dt} - \frac{u^2}{r} = -RT\frac{\partial \ln(p)}{\partial r} + 2\Omega u + \Omega^2 r - \frac{\partial \phi}{\partial r} \tag{B.4}$$

$$\frac{\partial \phi}{\partial \sigma} = \frac{-RT}{p}\frac{\partial p}{\partial \sigma} \tag{B.5}$$

$$\frac{d\theta_v}{dt} = 0 \tag{B.6}$$

$$\frac{\partial}{\partial t}\left(\frac{\partial p}{\partial \sigma}\right) + \frac{1}{r}\frac{\partial}{\partial \theta}\left(\frac{\partial p}{\partial \sigma}u\right) + \frac{1}{r}\frac{\partial}{\partial r}\left(\frac{\partial p}{\partial \sigma}rv\right) + \frac{\partial}{\partial \sigma}\left(\frac{\partial p}{\partial \sigma}\dot{\sigma}\right) = 0 \tag{B.7}$$

$$p = \rho RT \tag{B.8}$$

where ϕ is the geopotential, $\sigma = p/p_s$ is a pressure based vertical co-ordinate with $p_s = 1000\text{hPa}$ being the surface pressure. θ_v is the potential temperature, c_p is the heat capacity at constant pressure and ρ is the density. Equation B.7 is the continuity equation for a generalised vertical co-ordinate, σ.

An initial, non-divergent, steady state velocity field is chosen where

$$u = u_0\frac{r}{r_0}\sin\left(\frac{\pi r}{r_0}\right)\ln(\sigma)\exp\left(-\left(\frac{\ln(\sigma)}{2}\right)^2\right), \tag{B.9}$$

$$v = w = 0. \tag{B.10}$$

u_0 and r_0 are constants.

The geopotential may be derived from the radial momentum equation. In the steady state this reduces to

$$\frac{\partial \phi'}{\partial r} = \frac{u^2}{r} + 2\Omega u + \Omega^2 r \tag{B.11}$$

which, after substitution of the chosen velocity profile, may be integrated over r at constant σ to give

$$\phi' = \int\left(\frac{u^2}{r} + 2\Omega u + \Omega^2 r\right)dr + \phi_0 \tag{B.12}$$

where ϕ_0 is the constant of integration and a $'$ denotes deviations from the horizontally averaged state. The horizontally averaged geopotential is $\langle\phi\rangle = gz(p)$

where g is the acceleration due to gravity. ϕ_0 may be calculated by noting that averaging the deviations over the horizontal gives zero,

$$\int_{r_1}^{r_2} \phi' r dr = 0. \tag{B.13}$$

where r_1 and r_2 are the inner and outer radii of the cylindrical annulus respectively.

The horizontally averaged temperature profile is given by $\langle T \rangle = T_0 - \Gamma z$ where Γ is the vertical lapse rate and deviations from this are calculated assuming an initially stead state. From the hydrostatic relation the deviations are given by

$$T' = \frac{-\sigma}{R} \frac{\partial \phi'}{\partial \sigma}. \tag{B.14}$$

The initial azimuthal velocity and temperature fields used with the cylindrical geometry are shown in figure B.2. A baroclinic wave is triggered by a local Gaussian perturbation to the zonal velocity field as in Jablonowski and Williamson (2006). Simulations were carried out with a rotation speed equal to that of the Earth and a timestep of 10 minutes. The domain used had a height of 32km and an inner radius of 6250km and an outer radius of 9400km. The resolution was 124, 185 and 70 gridpoints in the azimuthal, radial and vertical directions respectively.

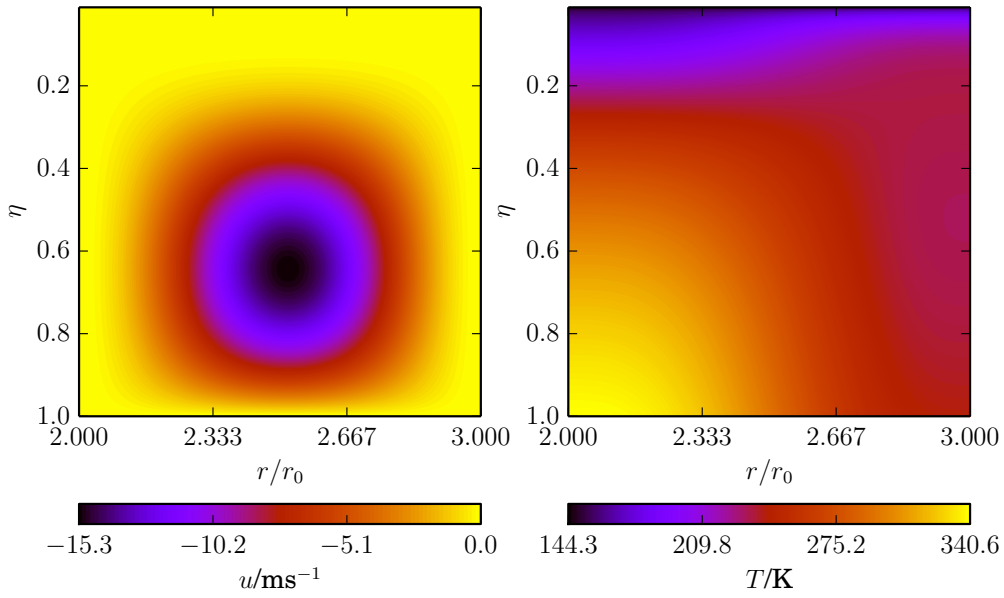


Figure B.2: The initial conditions used for the Jablonowski-Williamson baroclinic wave test in the cylindrical geometry. The initial state is axisymmetric and shown here in the r, z plane. The initial azimuthal velocity field is shown on the left and the initial temperature field is plotted on the right.

Bibliography

Afanasyev, Y. and J. Wells (2005). "Quasi-two-dimensional turbulence on the polar beta-plane: laboratory experiments". In: *Geophysical & Astrophysical Fluid Dynamics* 99.1, pp. 1–17.

Ahlers, G., S. Grossmann, and D. Lohse (2009). "Heat transfer and large scale dynamics in turbulent Rayleigh-Bénard convection". In: *Rev. Mod. Phys.* 81, pp. 503–537.

Allen, T. (2018). *Semi-Lagrangian Advection*. Tech. rep. 018. UK Met Office.

Andrews, D. G. (2000). *An introduction to atmospheric physics*. Cambridge University Press, p. 229.

Arakawa, A. and V. R. Lamb (1977). "Computational Design of the Basic Dynamical Processes of the UCLA General Circulation Model". In: *Methods in Computational Physics: Advances in Research and Applications*. Vol. 17, pp. 173–265.

Augier, P. and E. Lindborg (2013). "A New Formulation of the Spectral Energy Budget of the Atmosphere, with Application to Two High-Resolution General Circulation Models". In: *Journal of the Atmospheric Sciences* 70.7, pp. 2293–2308.

Bailon-Cuba, J., M. S. Emran, and J. Schumacher (2010). "Aspect ratio dependence of heat transfer and large-scale flow in turbulent convection". In: *J. Fluid Mech.* 655, pp. 152–173.

Barry, L., G. C. Craig, and J. Thuburn (2000). "A GCM Investigation into the Nature of Baroclinic Adjustment". In: *Journal of the Atmospheric Sciences* 57.8, pp. 1141–1155.

Bastin, M. and P. Read (1999). "The effect of sloping boundairies on baroclinic instability in two related internally heated, rotating fluid systems". In: *Physics and Chemistry of the Earth, Part B: Hydrology, Oceans and Atmosphere* 24.5, pp. 481–486.

Bell, M. J. and A. A. White (1988). "The Stability of Internal Baroclinic Jets: Some Analytical Results". In: *J. Atmos. Sci.* 45.18, pp. 2571–2590.

Benton, E. R. and A. Clark (1974). "Spin-Up". In: *Annual Review of Fluid Mechanics* 6.1, pp. 257–280.

Blumen, W. (1978). "Uniform Potential Vorticity Flow: Part I. Theory of Wave Interactions and Two-Dimensional Turbulence". In: *Journal of the Atmospheric Sciences* 35.5, pp. 774–783.

Bretherton, F. P. (1966). "Critical layer instability in baroclinic flows". In: *Quarterly Journal of the Royal Meteorological Society* 92.393, pp. 325–334.

Campagne, A., B. Gallet, F. Moisy, and P.-P. Cortet (2014). "Direct and inverse energy cascades in a forced rotating turbulence experiment". In: *Physics of Fluids* 26.12, p. 125112.

Capet, X., P. Klein, B. L. Hua, G. Lapeyre, and J. C. McWilliams (2008). "Surface kinetic energy transfer in surface quasi-geostrophic flows". In: *Journal of Fluid Mechanics* 604, pp. 165–174.

Castaing, B., G. Gunaratne, F. Heslot, L. Kadanoff, A. Libchaber, S. Thomae, X.-Z. Wu, S. Zaleski, and G. Zanetti (1989). "Scaling of hard thermal turbulence in Rayleigh-Bénard convection". In: *J. Fluid Mech.* 204, pp. 1–30.

Castrejón-Pita, A. A. and P. L. Read (2007). "Baroclinic waves in an air-filled thermally driven rotating annulus". In: *Phys. Rev. E* 75 (2), p. 026301.

Cehelsky, P. and K. K. Tung (1991). "Nonlinear Baroclinic Adjustment". In: *J. Atmos. Sci.* 48.17, pp. 1930–1947.

Celani, A., M. Cencini, A. Mazzino, and M. Vergassola (2004). "Active and passive fields face to face". In: *New J. Phys.* 6.

Chai, J. and G. K. Vallis (2014). "The Role of Criticality on the Horizontal and Vertical Scales of Extratropical Eddies in a Dry GCM". In: *Journal of the Atmospheric Sciences* 71.7, pp. 2300–2318.

Charney, J. G. (1947). "The dynamics of long waves in a baroclinic westerly current". In: *J. Met.* 4.5, pp. 136–162.

Charney, J. G. and N. A. Phillips (1953). "Numerical Integration of the Quasi-Geostrophic Equations for Barotropic and Simple Baroclinic Flows". In: *Journal of Meteorology* 10.2, pp. 71–99.

Charney, J. G. and M. E. Stern (1962). "On the Stability of Internal Baroclinic Jets in a Rotating Atmosphere". In: *J. Atmos. Sci.* 19, pp. 159–172.

Chavanne, a. X., F. Chilla, B. Castaing, B. Hebral, B. Chabaud, and J. Chaussy (1997). "Observation of the ultimate regime in Rayleigh-Bénard convection". In: *Phys. Rev. Lett.* 79.19, p. 3648.

Cheinet, S. (2003). "A Multiple Mass-Flux Parameterization for the Surface-Generated Convection. Part I: Dry Plumes". In: *Journal of the Atmospheric Sciences* 60.18, pp. 2313–2327.

Chillà, F. and J. Schumacher (2012). "New perspectives in turbulent Rayleigh-Bénard convection". In: *Eur. Phys. J. E* 35.

Cho, J. Y. N. and E. Lindborg (2001). "Horizontal velocity structure functions in the upper troposphere and lower stratosphere: 1. Observations". In: *Journal of Geophysical Research: Atmospheres* 106.D10, pp. 10223–10232.

Cushman-Roisin, B. and J.-M. Beckers (2011). *Introduction to geophysical fluid dynamics : physical and numerical aspects*. Academic Press, p. 828.

Davidson, P. (2015). *Turbulence: An Introduction for Scientists and Engineers*. Oxford University Press.

Duck, P. and M. Foster (2001). "Spin-up of homogeneous and stratified fluids". In: *Annual review of fluid mechanics* 33.1, pp. 231–263.

Eady, E. T. (1949). "Long Waves and Cyclone Waves". In: *Tellus* 1.3, pp. 33–52.

Farnell, L. and R. Plumb (1975). "Numerical Integration of Flow in a Rotating Annulus I: Axisymmetric Model". In: *Geophysical Fluid Dynamics Laboratory,UK, Meteorological Office*, pp. 1–39.

Fein, J. S. and R. L. Pfeffer (1976). "An experimental study of the effects of Prandtl number on thermal convection in a rotating, differentially heated cylindrical annulus of fluid". In: *J. Fluid Mech.* 75 (01), pp. 81–112.

Field, P. R., R. Brozková, M. Chen, J. Dudhia, C. Lac, T. Hara, R. Honnert, J. Olson, P. Siebesma, S. de Roode, L. Tomassini, A. Hill, and R. McTaggart-Cowan (2017). "Exploring the convective grey zone with regional simulations of a cold air outbreak". In: *Quarterly Journal of the Royal Meteorological Society* 143.707, pp. 2537–2555.

Frierson, D. M. W. (2008). "Midlatitude Static Stability in Simple and Comprehensive General Circulation Models". In: *Journal of the Atmospheric Sciences* 65.3, pp. 1049–1062.

Frierson, D. M. W., I. M. Held, and P. Zurita-Gotor (2006). "A Gray-Radiation Aquaplanet Moist GCM. Part I: Static Stability and Eddy Scale". In: *Journal of the Atmospheric Sciences* 63.10, pp. 2548–2566.

Fultz, D., R. R. Long, G. V. Owens, W. Bohan, R. Kaylor, and J. Weil (1959). "Studies of Thermal Convection in a Rotating Cylinder with Some Implications for Large-Scale Atmospheric Motions". In: *Studies of Thermal Convection in a Rotating Cylinder with Some Implications for Large-Scale Atmospheric Motions*. Boston, MA: American Meteorological Society, pp. 1–104.

Funfschilling, D., E. Brown, A. Nikolaenko, and G. Ahlers (2005). "Heat transport by turbulent Rayleigh–Bénard convection in cylindrical samples with aspect ratio one and larger". In: *J. Fluid Mech.* 536, pp. 145–154.

Galperin, B., J. Hoemann, S. Espa, G. Di Nitto, and G. Lacorata (2016). "Anisotropic macroturbulence and diffusion associated with a westward zonal jet: From laboratory to planetary atmospheres and oceans". In: *Physical Review E* 94.6, p. 063102.

Goldstein, R. and S. Tokuda (1980). "Heat transfer by thermal convection at high Rayleigh numbers". In: *Int. J. Heat Mass Transfer* 23.

Gomes-Fernandes, R., B. Ganapathisubramani, and J. C. Vassilicos (2015). "The energy cascade in near-field non-homogeneous non-isotropic turbulence". In: *Journal of Fluid Mechanics* 771, pp. 676–705.

Greenspan, H. P. and L. N. Howard (1963). "On a time-dependent motion of a rotating fluid". In: *Journal of Fluid Mechanics* 17.3, pp. 385–404.

Grossmann, S. and D. Lohse (2001). "Thermal convection for large Prandtl numbers." In: *Physical Review Letters* 86, pp. 3316–9.

Grossmann, S. and D. Lohse (2000). "Scaling in thermal convection: A unifying theory". In: *J. Fluid Mech.* 407, p. 30.

— (2002). "Prandtl and Rayleigh number dependence of the Reynolds number in turbulent thermal convection." In: *Phys. Rev. E* 66.

— (2004). "Fluctuations in turbulent Rayleigh–Benard convection: The role of plumes". In: *Phys. Fluids* 16, p. 4462.

— (2011). "Multiple scaling in the ultimate regime of thermal convection". In: *Phys. Fluids* 23, p. 045108.

Held, I. M. (1978). "The Vertical Scale of an Unstable Baroclinic Wave and Its Importance for Eddy Heat Flux Parameterizations". In: *Journal of the Atmospheric Sciences* 35.4, pp. 572–576.

— (2005). "The Gap between Simulation and Understanding in Climate Modeling". In: *Bulletin of the American Meteorological Society* 86.11, pp. 1609–1614.

Held, I. M. and V. D. Larichev (1996). "A Scaling Theory for Horizontally Homogeneous, Baroclinically Unstable Flow on a Beta Plane". In: *Journal of the Atmospheric Sciences* 53.7, pp. 946–952.

Held, I. M., R. T. Pierrehumbert, S. T. Garner, and K. L. Swanson (1995). "Surface quasi-geostrophic dynamics". In: *Journal of Fluid Mechanics* 282, pp. 1–20.

Held, I. M. and M. J. Suarez (1994). "A Proposal for the Intercomparison of the Dynamical Cores of Atmospheric General Circulation Models". In: *Bulletin of the American Meteorological Society* 75.10, pp. 1825–1830.

Heng, K., D. M. W. Frierson, and P. J. Phillipps (2011). "Atmospheric circulation of tidally locked exoplanets: II. Dual-band radiative transfer and convective adjustment". In: *Monthly Notices of the Royal Astronomical Society* 418.4, pp. 2669–2696.

Hide, R. (1953). "Some experiments on thermal convection in a rotating liquid". In: *Q. J. Roy. Meteor. Soc.* 79.339, pp. 161–161.

Hide, R. and P. J. Mason (1970). "Baroclinic Waves in a Rotating Fluid Subject to Internal Heating". In: *Philosophical Transactions of the Royal Society A: Mathematical, Physical and Engineering Sciences* 268.1186, pp. 201–232.

Hide, R. and P. J. Mason (1975). "Sloping convection in a rotating fluid". In: *Adv. Phys.* 24.1, pp. 47–100.

Hignett, P., A. White, R. Carter, W. Jackson, and R. Small (1985). "A comparison of laboratory measurements and numerical simulations of baroclinic wave flows in a rotating cylindrical annulus". In: *Quarterly Journal of the Royal Meteorological Society* 111, pp. 131–154.

Hignett, P. (1982). "A note on the heat transfer by the axisymmetric thermal convection in a rotating fluid annulus". In: *Geophysical & Astrophysical Fluid Dynamics* 19.3-4, pp. 293–299.

Hignett, P., A. Ibbetson, and P. D. Killworth (1981). "On rotating thermal convection driven by non-uniform heating from below". English. In: *Journal of Fluid Mechanics* 109.-1, p. 161.

Hughes, G. O. and R. W. Griffiths (2008). "Horizontal Convection". In: *Annual Review of Fluid Mechanics* 40.1, pp. 185–208.

Hyun, J. M. (1985). "Convection in a rotating cylinder with its sidewall having a finite thermal conductance". In: *Geophysical & Astrophysical Fluid Dynamics* 34.1-4, pp. 83–98.

Ilicak, M. and G. K. Vallis (2012). "Simulations and scaling of horizontal convection". en. In: *Tellus A* 64.

Jablonowski, C. and D. L. Williamson (2006). "A baroclinic instability test case for atmospheric model dynamical cores". In: 132, pp. 2943–2975.

Jansen, M. and R. Ferrari (2012). "Macroturbulent Equilibration in a Thermally Forced Primitive Equation System". In: *Journal of the Atmospheric Sciences* 69.2, pp. 695–713.

— (2013a). "Equilibration of an Atmosphere by Adiabatic Eddy Fluxes". In: *Journal of the Atmospheric Sciences* 70.9, pp. 2948–2962.

— (2013b). "The Vertical Structure of the Eddy Diffusivity and the Equilibration of the Extratropical Atmosphere". In: *Journal of the Atmospheric Sciences* 70.5, pp. 1456–1469.

Juckes, M. N. (2000). "The Static Stability of the Midlatitude Troposphere: The Relevance of Moisture". In: *Journal of the Atmospheric Sciences* 57.18, pp. 3050–3057.

Karsten, R. H. and J. Marshall (2002). "Constructing the Residual Circulation of the ACC from Observations". In: *Journal of Physical Oceanography* 32.12, pp. 3315–3327.

Kim, M. C. and C. Kyun Choi (2006). "The onset of Taylor–Görtler vortices during impulsive spin-down to rest". In: *Chemical Engineering Science* 61.19, pp. 6478–6485.

King, E. M., S. Stellmach, and J. M. Aurnou (2012). "Heat transfer by rapidly rotating Rayleigh–Bénard convection". In: *J. Fluid Mech* 691, pp. 568–582.

King, E. M., S. Stellmach, J. Noir, U. Hansen, and J. M. Aurnou (2009). "Boundary layer control of rotating convection systems." In: *Nature* 457, pp. 301–304.

Kolmogorov, A. N. (1941). "The local structure of turbulence in incompressible viscous fluid for very large Reynold's numbers". In: *C. R. Acad. Sci. USSR* 30, pp. 301–305.

Komacek, T. D., M. F. Jansen, E. T. Wolf, and D. S. Abbot (2019). "Scaling Relations for Terrestrial Exoplanet Atmospheres from Baroclinic Criticality". In: *The Astrophysical Journal* 883.1, p. 46.

Lambert, H., N. Lewis, and I. Boutle (2017). *The Lambert-Lewis Convection Scheme.* Tech. rep. 041. UK Met Office.

Lamriben, C., P.-P. Cortet, and F. Moisy (2011). "Direct Measurements of Anisotropic Energy Transfers in a Rotating Turbulence Experiment". In: *Physical Review Letters* 107.2, p. 024503.

Lapeyre, G. and I. M. Held (2003). "Diffusivity, Kinetic Energy Dissipation, and Closure Theories for the Poleward Eddy Heat Flux". In: *Journal of the Atmospheric Sciences* 60.23, pp. 2907–2916.

Lapeyre, G. and P. Klein (2006). "Dynamics of the Upper Oceanic Layers in Terms of Surface Quasigeostrophy Theory". In: *Journal of Physical Oceanography* 36, pp. 165–176.

Lapeyre, G. (2017). "Surface Quasi-Geostrophy". In: *Fluids* 2.1, p. 7.

Larichev, V. D. and I. M. Held (1995). "Eddy Amplitudes and Fluxes in a Homogeneous Model of Fully Developed Baroclinic Instability". In: *J. Phys. Oceanogr.* 25.10, pp. 2285–2297.

Lindborg, E. (1999). "Can the atmospheric kinetic energy spectrum be explained by two-dimensional turbulence?" In: *Journal of Fluid Mechanics* 388, S0022112099004851.

Lindzen, R. S. (1994). "The Eady Problem for a Basic State with Zero PV Gradient but $\beta \neq 0$". In: *Journal of the Atmospheric Sciences* 51.22, pp. 3221–3226.

Lorenz, E. N. (1955). "Available Potential Energy and the Maintenance of the General Circulation". In: *Tellus* 7.2, pp. 157–167.

Mahrer, Y. (1984). "An Improved Numerical Approximation of the Horizontal Gradients in a Terrain-Following Coordinate System". In: *Monthly Weather Review* 112.5, pp. 918–922.

Malkus, W. V. R. (1954). "The Heat Transport and Spectrum of Thermal Turbulence". In: *P. Roy. Soc. Lond. A Mat.* 225, pp. 196–212.

Mason, P. J. (1975). "Baroclinic waves in a container with sloping end walls". In: *Philosophical Transactions of the Royal Society of London A: Mathematical, Physical and Engineering Sciences* 278.1284.

Mayne, N. J., I. Baraffe, D. M. Acreman, C. Smith, N. Wood, D. S. Amundsen, J. Thuburn, and D. R. Jackson (2014). "Using the UM dynamical cores to reproduce idealised 3-D flows". English. In: *Geoscientific Model Development* 7.6, pp. 3059–3087.

Mayne, N. J., I. Baraffe, D. M. Acreman, C. Smith, M. K. Browning, D. S. Amundsen, N. Wood, J. Thuburn, and D. R. Jackson (2013). "The unified model, a fully-compressible, non-hydrostatic, deep atmosphere global circulation model, applied to hot Jupiters". In: *Astronomy & Astrophysics* 561, A1.

Min Hyun, J. and J. Chun Hyun (1987). "Heatup of an Initially Isothermal Fluid in an Enclosure with Semi-Conducting Boundaries". In: *Journal of the Physical Society of Japan* 56.3, pp. 942–948.

Mushref, M. A. (2010). "Fourier-Bessel Expansions with Arbitrary Radial Boundaries". In: *Applied Mathematics* 1, pp. 18–23.

Nastrom, G. D. and K. S. Gage (1985). "A Climatology of Atmospheric Wavenumber Spectra of Wind and Temperature Observed by Commercial Aircraft". In: *Journal of the Atmospheric Sciences* 42.9, pp. 950–960.

Neitzel, G. P. and S. H. Davis (1981). "Centrifugal instabilities during spin-down to rest in finite cylinders. Numerical experiments". In: *Journal of Fluid Mechanics* 102.-1, p. 329.

Otero, J., R. W. Wittenberg, R. A. Worthing, and C. R. Doering (2002). "Bounds on Rayleigh–Bénard convection with an imposed heat flux". In: *Journal of Fluid Mechanics* 473, pp. 191–199.

Park, J. S. and J. M. Hyun (2008). "Review on open-problems of spin-up flow of an incompressible fluid". In: *Journal of Mechanical Science and Technology* 22.4, pp. 780–787.

Pedlosky, J. (1964). "An initial value problem in the theory of baroclinic instability". In: *Tellus* 16.1, pp. 12–17.

Pérez-Pérez, E., P. Read, and I. Moroz (2010). "Assessing eddy parameterization schemes in a differentially heated rotating annulus experiment". In: *Ocean Modelling* 32.3-4, pp. 118–131.

Pfeffer, R. L., G. Buzyna, and R. Kung (1980). "Relationships Among Eddy Fluxes of Heat, Eddy Temperature Variances and Basic-State Temperature Parameters in Thermally Driven Rotating Fluids". In: *Journal of the Atmospheric Sciences* 37.12, pp. 2577–2599.

Pfeffer, R. L. and Chiang (1967). "Two kinds of vacillation in rotating laboratory experiments". In: *Monthly Weather Review* 95.2, pp. 75–82.

Phillips, N. A. (1951). "A simple three-dimensional model for the study of large-scale extratropical flow patterns". In: *J. Met.* 8.6, pp. 381–394.

Pierrehumbert, R. T., I. M. Held, and K. L. Swanson (1994). "Spectra of Local and Nonlocal Two-dimensional Turbulence". In: *Pergamon Chaos, Solitons & Fractals* 4.6, pp. 1111–1116.

Puits, R. du, C. Resagk, and A. Thess (2013). "Thermal boundary layers in turbulent Rayleigh–Bénard convection at aspect ratios between 1 and 9". In: *New Journal of Physics* 15.1, p. 013040.

Rahm, L. and G. Walin (1980). "On thermally forced stratified rotating fluids". In: *Journal of Fluid Mechanics* 97.04, p. 807.

Read, P. L. (1986). "Regimes of axisymmetric flow in an internally heated rotating fluid". In: *Journal of Fluid Mechanics* 168, pp. 255–289.

Read, P. L., N. P. J. Thomas, and S. H. Risch (2000). "An Evaluation of Eulerian and Semi-Lagrangian Advection Schemes in Simulations of Rotating, Stratified Flows in the Laboratory. Part I: Axisymmetric Flow". In: *Monthly Weather Review* 128.8, pp. 2835–2852.

Read, P. L. (2003). "A combined laboratory and numerical study of heat transport by baroclinic eddies and axisymmetric flows". In: *Journal of Fluid Mechanics* 489, pp. 301–323.

Read, P. L., E. P. Pérez, I. M. Moroz, and R. M. B. Young (2015). "General Circulation of Planetary Atmospheres: Insights from Rotating Annulus and Related Experiments". In: *Modeling Atmospheric and Oceanic Flows: Insights from Laboratory Experiments and Numerical Simulations*, pp. 7–44.

Read, P. L., F. Tabataba-Vakili, Y. Wang, P. Augier, E. Lindborg, A. Valeanu, and R. M. B. Young (2018). "Comparative terrestrial atmospheric circulation regimes in simplified global circulation models. Part II: Energy budgets and spectral transfers". In: *Quarterly Journal of the Royal Meteorological Society* 144.717, pp. 2558–2576.

Read, P. (2011). "Dynamics and circulation regimes of terrestrial planets". In: 59.10, pp. 900–914.

Rhines, P. B. (1975). "Waves and turbulence on a beta-plane". In: *Journal of Fluid Mechanics* 69.3, pp. 417–443.

Roode, S. R., T. Frederikse, A. P. Siebesma, A. S. Ackerman, J. Chylik, P. R. Field, J. Fricke, M. Gryschka, A. Hill, R. Honnert, S. K. Krueger, C. Lac, A. T. Lesage, and L. Tomassini (2019). "Turbulent Transport in the Gray Zone: A Large Eddy Model Intercomparison Study of the CONSTRAIN Cold Air Outbreak Case". In: *Journal of Advances in Modeling Earth Systems* 11.3, pp. 597–623.

Rossby, H. (1965). "On thermal convection driven by non-uniform heating from below: an experimental study". In: *Deep-Sea Res.* 12, pp. 9–16.

Salmon, R. (1978). "Two-layer quasi-geostrophic turbulence in a simple special case". In: *Geophysical & Astrophysical Fluid Dynamics* 10.1, pp. 25–52.

— (1980). "Baroclinic instability and geostrophic turbulence". In: *Geophysical & Astrophysical Fluid Dynamics* 15.1, pp. 167–211.

Schmalzl, J., M. Breuer, and U. Hansen (2004). "On the validity of two-dimensional numerical approaches to time-dependent thermal convection". In: *Europhysics Letters (EPL)* 67.3, pp. 390–396.

Schneider, T. (2006). "The General Circulation of the Atmosphere". In: *Annu. Rev. Earth Planet. Sci.* 34, pp. 655–688.

Schneider, T. (2004). "The Tropopause and the Thermal Stratification in the Extratropics of a Dry Atmosphere". In: *Journal of the Atmospheric Sciences* 61.12, pp. 1317–1340.

— (2005). "Zonal Momentum Balance, Potential Vorticity Dynamics, and Mass Fluxes on Near-Surface Isentropes". In: *Journal of the Atmospheric Sciences* 62.6, pp. 1884–1900.

Schneider, T. and P. a. O'Gorman (2008). "Moist Convection and the Thermal Stratification of the Extratropical Troposphere". In: *Journal of the Atmospheric Sciences* 65.11, pp. 3571–3583.

Schneider, T. and C. C. Walker (2006). "Self-Organization of Atmospheric Macroturbulence into Critical States of Weak Nonlinear Eddy–Eddy Interactions". In: *Journal of the Atmospheric Sciences* 63.6, pp. 1569–1586.

Scolan, H. and P. L. Read (2017). "A rotating annulus driven by localized convective forcing: a new atmosphere-like experiment". In: *Experiments in Fluids* 58.6, p. 75.

Scott, R. K. (2006). "Local and nonlocal advection of a passive scalar". In: *Physics of Fluids* 18.11, p. 116601.

Scott, R. B. and F. Wang (2005). "Direct Evidence of an Oceanic Inverse Kinetic Energy Cascade from Satellite Altimetry". In: *Journal of Physical Oceanography* 35.9, pp. 1650–1666.

Shah, M. M. (2012). "Improved method for calculating evaporation from indoor water pools". In: *Energy and Buildings* 49, pp. 306–309.

Shepherd, T. G. (1987). "A Spectral View of Nonlinear Fluxes and Stationary-Transient Interaction in the Atmosphere". In: *Journal of the Atmospheric Sciences* 44.8, pp. 1166–1179.

Shishkina, O., S. Grossmann, and D. Lohse (2016). "Heat and momentum transport scalings in horizontal convection". In: *Geophysical Research Letters* 43, pp. 1219–1225.

Shishkina, O., R. J. A. M. Stevens, S. Grossmann, and D. Lohse (2010). "Boundary layer structure in turbulent thermal convection and its consequences for the required numerical resolution". In: *New Journal of Physics* 12.7, p. 75022. arXiv: 1109.6870.

Shishkina, O. and S. Wagner (2016). “Prandtl-number dependence of heat hransport in laminar horizontal convection.” In: *Physical Review Letters* 116, p. 024302.

Shraiman, B. I. and E. D. Siggia (1990). “Heat transport in high-Rayleigh-number convection”. In: *Phys. Rev. A* 42, pp. 3650–3653.

Smith, K. S., G. Boccaletti, C. C. Henning, I. Marinov, C. Y. Tam, I. M. Held, and G. K. Vallis (2002). “Turbulent diffusion in the geostrophic inverse cascade”. In: *Journal of Fluid Mechanics* 469, pp. 13–48.

Staniforth, A., A. A. White, and N. Wood (2010). “Treatment of vector equations in deep-atmosphere, semi-Lagrangian models. I: Momentum equation”. In: *Quarterly Journal of the Royal Meteorological Society* 136.647, pp. 497–506.

Staniforth, A. and J. Côté (1991). “Semi-Lagrangian Integration Schemes for Atmospheric Models—A Review”. In: *Monthly Weather Review* 119.9, pp. 2206–2223.

Staniforth, A. and N. Wood (2013). “Exact axisymmetric solutions of the deep- and shallow-atmosphere Euler equations in curvilinear and plane geometries”. In: *Quarterly Journal of the Royal Meteorological Society* 139.673, pp. 1113–1120.

Steffen, M. (1990). “A simple method for monotonic interpolation in one dimension”. In: *Astronomy & Astrophysics* 239.11, pp. 443–450.

Stevens, R. J. A. M., E. P. van der Poel, S. Grossmann, and D. Lohse (2013). “The unifying theory of scaling in thermal convection: the updated prefactors”. In: *J. Fluid Mech.* 730, pp. 295–308.

Stevens, R. J., R. Verzicco, and D. Lohse (2010). “Radial boundary layer structure and Nusselt number in Rayleigh–Bénard convection”. In: *Journal of Fluid Mechanics* 643, p. 495. arXiv: 0905.0379.

Stewartson, K. (1957). “On almost rigid rotations”. In: *Journal of Fluid Mechanics* 3.1, pp. 17–26.

Stone, P. H. (1978). “Baroclinic Adjustment”. In: *Journal of the Atmospheric Sciences* 35.4, pp. 561–571.

Stone, P. H. and L. Branscome (1992). “Diabatically Forced, Nearly Inviscid Eddy Regimes”. In: 49.4, pp. 355–367.

Sukhatme, J. and R. T. Pierrehumbert (2002). “Surface quasigeostrophic turbulence: The study of an active scalar”. In: *Chaos: An Interdisciplinary Journal of Nonlinear Science* 12.2, pp. 439–450.

Sukhatme, J. and L. M. Smith (2009). “Local and nonlocal dispersive turbulence”. In: *Physics of Fluids* 21.5, p. 056603.

Sukoriansky, S., N. Dikovskaya, and B. Galperin (2007). “On the Arrest of Inverse Energy Cascade and the Rhines Scale”. In: *Journal of the Atmospheric Sciences* 64.9, pp. 3312–3327.

Sun, C., L.-Y. Ren, H. Song, and K.-Q. Xia (2005). “Heat transport by turbulent Rayleigh–Bénard convection in 1 m diameter cylindrical cells of widely varying aspect ratio”. In: *Journal of Fluid Mechanics* 542, p. 165.

Tang, Y., H. W. Lean, and J. Bornemann (2013). “The benefits of the Met Office variable resolution NWP model for forecasting convection”. In: *Meteorological Applications* 20.4, pp. 417–426.

Tomassini, L., P. R. Field, R. Honnert, S. Malardel, R. McTaggart-Cowan, K. Saitou, A. T. Noda, and A. Seifert (2017). “The “Grey Zone” cold air outbreak global model intercomparison: A cross evaluation using large-eddy simulations”. In: *Journal of Advances in Modeling Earth Systems* 9.1, pp. 39–64.

Tulloch, R. and K. S. Smith (2006). "A theory for the atmospheric energy spectrum: depth-limited temperature anomalies at the tropopause." In: *Proceedings of the National Academy of Sciences of the United States of America* 103.40, pp. 14690–4.

Ullrich, P. and C. Jablonowski (2012). "Operator-Split Runge–Kutta–Rosenbrock Methods for Nonhydrostatic Atmospheric Models". In: *Monthly Weather Review* 140.4, pp. 1257–1284.

Valente, P. C. and J. C. Vassilicos (2015). "The energy cascade in grid-generated non-equilibrium decaying turbulence". In: *Physics of Fluids* 27.4, p. 045103.

Vallis, G. K. (1988). "Numerical studies of eddy transport properties in eddy-resolving and parameterized models". In: *Journal of the Royal Meteorological Society* 114, pp. 183–204.

Vallis, G. K. (2006). *Atmospheric and oceanic fluid dynamics: fundamentals and large-scale circulation.* Cambridge University Press.

Vallis, G. K. and M. E. Maltrud (1993). "Generation of Mean Flows and Jets on a Beta Plane and over Topography". In: *Journal of Physical Oceanography* 23.7, pp. 1346–1362.

van der Poel, E. P., R. J. A. M. Stevens, and D. Lohse (2011). "Connecting flow structures and heat flux in turbulent Rayleigh-Bénard convection." In: *Physical Review E* 84, p. 045303.

van der Poel, E. P., R. J. A. M. Stevens, and D. Lohse (2013). "Comparison between two- and three-dimensional Rayleigh–Bénard convection". In: *Journal of Fluid Mechanics* 736.February 2014, pp. 177–194.

Vettin, F. (1857). "Meteorologische Untersuchungen". In: *Annalen der Physik und Chemie* 176.1, pp. 99–110.

Vincze, M., S. Borchert, U. Achatz, T. von Larcher, M. Baumann, C. Liersch, S. Remmler, T. Beck, K. D. Alexandrov, C. Egbers, J. Fröhlich, V. Heuveline, S. Hickel, and U. Harlander (2015). "Benchmarking in a rotating annulus: a comparative experimental and numerical study of baroclinic wave dynamics". In: *Meteorologische Zeitschrift* 23.6, pp. 611–635.

von Larcher, T., S. Viazzo, U. Harlander, M. Vincze, and A. Randriamampianina (2018). "Instabilities and small-scale waves within the Stewartson layers of a thermally driven rotating annulus". In: *Journal of Fluid Mechanics* 841, pp. 380–407.

Walin, G. (1971). "Contained non-homogeneous flow under gravity or how to stratify a fluid in the laboratory". In: *Journal of Fluid Mechanics* 48.4, pp. 647–672.

Wang, Y., P. L. Read, F. Tabataba-Vakili, and R. M. B. Young (2018). "Comparative terrestrial atmospheric circulation regimes in simplified global circulation models: I. from cyclostrophic super-rotation to geostrophic turbulence". In: *Quarterly Journal of the Royal Meteorological Society.*

Warn-Varnas, A., W. W. Fowlis, S. Piacsek, and S. M. Lee (1978). "Numerical solutions and laser-Doppler measurements of spin-up". In: *Journal of Fluid Mechanics* 85.04, p. 609.

Weidman, P. D. (1976). "On the spin-up and spin-down of a rotating fluid. Part 2. Measurements and stability". In: *Journal of Fluid Mechanics* 77.04, p. 709.

Weiss, S. and G. Ahlers (2011). "Heat transport by turbulent rotating Rayleigh–Bénard convection and its dependence on the aspect ratio". In: *Journal of Fluid Mechanics* 684, pp. 407–426.

Welch, W. T. and K.-K. Tung (1998). "On the Equilibrium Spectrum of Transient Waves in the Atmosphere". In: *Journal of the Atmospheric Sciences* 55.17, pp. 2833–2851.

Weng, H.-Y. and A. Barcilon (1988). "Wavenumber transition and wavenumber vacillation in Eady-type baroclinic flows". In: *Quarterly Journal of the Royal Meteorological Society* 114.483, pp. 1253–1269.

White, A. A., A. Staniforth, and N. Wood (2008). "Spheroidal coordinate systems for modelling global atmospheres". In: *Quarterly Journal of the Royal Meteorological Society* 134.630, pp. 261–270.

Williams, G. P. (1969). "Numerical integration of the three-dimensional Navier-Stokes equations for incompressible flow". In: *Journal of Fluid Mechanics* 37.4, pp. 727–750.

Williams, G. P. (1974). "Generalized Eady waves". In: *Journal of Fluid Mechanics* 62.4, pp. 643–655.

Wood, N., A. Staniforth, A. White, T. Allen, M. Diamantakis, M. Gross, T. Melvin, C. Smith, S. Vosper, M. Zerroukat, and J. Thuburn (2014). "An inherently mass-conserving semi-implicit semi-Lagrangian discretization of the deep-atmosphere global non-hydrostatic equations". In: *Quarterly Journal of the Royal Meteorological Society*.

Wood, N., A. A. White, and A. Staniforth (2010). "Treatment of vector equations in deep-atmosphere, semi-lagrangian models. II: Kinematic equation". In: *Quarterly Journal of the Royal Meteorological Society*.

Wordsworth, R. D., P. L. Read, and Y. H. Yamazaki (2008). "Turbulence, waves, and jets in a differentially heated rotating annulus experiment". In: *Physics of Fluids* 20.12, p. 126602.

Wright, S., S. Su, H. Scolan, R. Young, and P. Read (2017). "Regimes of Axisymmetric Flow and Scaling Laws in a Rotating Annulus with Local Convective Forcing". In: *Fluids* 2.3, p. 41.

Xu, X., K. M. Bajaj, and G. Ahlers (2000). "Heat transport in turbulent Rayleigh-Bénard convection". In: *Physical Review Letters* 84.19, p. 4357.

Young, R. M. B. and P. L. Read (2008). "Flow transitions resembling bifurcations of the logistic map in simulations of the baroclinic rotating annulus". In: *Phys. D* 237.18, pp. 2251–2262.

Young, R. M. B. and P. L. Read (2017). "Forward and inverse kinetic energy cascades in Jupiter's turbulent weather layer". In: *Nature Physics* 13.11, pp. 1135–1140.

Zurita-Gotor, P. and R. Lindzen (2007). "Theories of baroclinic adjustment and eddy equilibration". In: *The Global Circulation of the Atmosphere*. Princeton University Press, pp. 22–46.

Zurita-Gotor, P. (2007). "The Relation between Baroclinic Adjustment and Turbulent Diffusion in the Two-Layer Model". In: *Journal of the Atmospheric Sciences* 64.4, pp. 1284–1300.

— (2008). "The Sensitivity of the Isentropic Slope in a Primitive Equation Dry Model". In: *Journal of the Atmospheric Sciences* 65.1, pp. 43–65.

Zurita-Gotor, P. and R. S. Lindzen (2006). "A Generalized Momentum Framework for Looking at Baroclinic Circulations". In: *Journal of the Atmospheric Sciences* 63.8, pp. 2036–2055.

Zurita-Gotor, P. and G. K. Vallis (2009). "Equilibration of Baroclinic Turbulence in Primitive Equations and Quasigeostrophic Models". In: *Journal of the Atmospheric Sciences* 66.4, pp. 837–863.

— (2011). "Dynamics of Midlatitude Tropopause Height in an Idealized Model". In: *Journal of the Atmospheric Sciences* 68.4, pp. 823–838.

— (2013). “Determination of Extratropical Tropopause Height in an Idealized Gray Radiation Model”. In: *Journal of the Atmospheric Sciences* 70.7, pp. 2272–2292.